HARNESSING FLOW-INDUCED FLUTTER OF FLAPPING FLAGS FOR HEAT TRANSFER, MIXING, AND ENERGY HARVESTING

By

Aaron Joshua Rips

A dissertation submitted to Johns Hopkins University in conformity with the requirements for the degree of Doctor of Philosophy

Baltimore, Maryland

July 2019

Abstract

Fluid-structure interaction is ubiquitous in natural and engineering systems. While in engineering applications, these aeroelastic phenomena have historically been considered as detrimental, in Nature there are widespread instances of biological systems designed specifically to take advantage of fluid-structure interaction phenomena. This research explores the notion of utilizing fluid-structure interaction to achieve a range of engineering objectives. In particular, we look at flow-induced flutter of highly flexible bodies such as flags, membranes, and filaments. We use fully-coupled fluid-structure interaction (FSI) CFD simulations to first explore two related engineering applications: heat transfer enhancement in forced-convection channel-flow heat exchangers, and mixing enhancement in low Reynolds number micromixers operating in the inertial microfluidic regime Re=O(1-100). In both applications, we show that the addition of a flapping membrane into a channel (or duct) flow can dramatically improve system performance for either heat transfer or mixing. Simulations are used to explore the flow physics underlying this improvement in performance. We then explore the use of inverted flags (flags where the leading edge is free, and the trailing edge is fixed) to harvest energy via flow-induced flutter. This study focuses on the use of multi-flag arrangements as a way to improve overall system performance. We also describe the design, fabrication and testing a 1ftx1ft cross-section low-Reynolds number (maximum speed of 20 m/s) wind tunnel which was developed in provide comprehensive validation data for the FSI simulations.

Primary Reader and Advisor: Professor Rajat Mittal

Secondary Readers: Professor Claire Hur and Professor Jung-Hee Seo

Acknowledgements

First and foremost, I would like to thank my advisor Professor Rajat Mittal for his guidance and support throughout my PhD, and indeed throughout my time at Hopkins. Prof. Mittal taught my undergraduate Fluid Mechanics 1 course during sophomore year, and his courses both as an undergraduate and particularly as a Master's student ultimately motivated me to seek a PhD. Throughout my time as a graduate student he instilled a fascination with the complexity and beauty of fluid dynamics, as well as a respect for the tools and scientific rigor we use to understand that complexity. His ability to instill intellectual curiosity in those around him on nearly any topic makes him an excellent teacher, and his insight, patience, and guidance makes him an excellent mentor. It has been a privilege to work together, and I am grateful and honored to have him as my advisor.

I would also like to thank various members of the Johns Hopkins Mechanical engineering faculty community for their help and support throughout my undergraduate and graduate career at Hopkins: Prof. Charles Meneveau, Prof. Andrea Prosperetti, and Prof. Joseph Katz who provided valuable advice, mentorship, and excellent teaching; Dr. Jung-Hee Seo for unparalleled insight into the complexities of the computational side of the work; Dr. Claire Hur for guidance in the experimental side of Fluid Dynamics; and finally Dr. Kerri Phillips and Dr. Tom Dragone for their mentorship, excellent teaching, and for showing me the path to a career that lies at the nexus between physics and aerospace engineering. They have all been inspirational and I am very grateful. And I would also like to thank the Hopkins Mechanical Engineering community more broadly for a consistently excellent standard of teaching, fostering intellectual curiosity, and

creating a challenging yet supportive environment. I truly could not have asked for a better academic environment for my undergraduate and graduate studies.

I would like to thank my lab mates Dr. Chi Zhu and Karthik Menon for their insight, support, and friendship. I am grateful to the entire Fluids PhD student community at Hopkins, it is a valuable gift to have been able to work with people that are so capable and passionate about their work. I am also grateful for their friendship and support, and for creating a warm and welcoming group friends in the midst of the trials and stress of being a PhD student. And I am of course forever grateful to my family whose love and support have been invaluable. There is a direct path between my childhood birthday parties and completing a PhD in Fluid Dynamics and going on to work at NASA, and I could not have accomplished any of this without their love, guidance, and support.

Finally, to the Johns Hopkins community in general. Clearly I am biased, but I could not imagine a better environment for fostering curiosity and academic excellence. At many points during my academic career I have been reminded of a quote from my favorite science educator:

"Everyone you will ever meet knows something you don't"

– Bill Nye the Science Guy

Perhaps nowhere is that more viscerally true than at Johns Hopkins University.

Dedication

To my family Noelle, David, and Lev Rips. A love for learning is the greatest gift I could have ever received, thank you.

Table of Contents

Table of Figures

Chapter 1

Introduction

1.1 Utility vs. Nuance: The duality of flow-induced flutter

Fluid-structure interaction is ubiquitous in natural and engineering systems. While in engineering applications aeroelasticity has historically been considered as detrimental, in nature there are widespread instances of biological systems designed specifically to utilize and take advantage of particular fluid-structure interaction phenomena. The classic engineering example taught to all undergraduate mechanical engineering students is of the infamous collapse of the Tacoma Narrows bridge in 1940, wherein the image seen in FIG. 1.1 of the galloping bridge moments before the bridges collapse serves as a lesson of the destructive potential of aeroelasticity. In many engineering applications fluid-structure interaction is a significant concern; in civil engineering for instance, considerable effort is invested in mitigating the vortex induced vibrations of tall buildings and other structures such as smokestacks and antennas caused by vortex shedding (Dowell et al., 1989; MATSUMOTO, 1999).

(a) (b)

FIG. 1.1 – (a) Image of the Tacoma Narrows bridge exhibiting very large torsional deflection due to aeroelastic flutter taken prior to its collapse in 1940. (b) Image of a hummingbird in hovering flight prior to drinking from a flower. Thrust generation and flight control authority of small flyers (including hummingbirds) often relies on FSI phenomena.

In aerospace engineering, there is rich variety of aeroelastic phenomena which were classified by Collar (1946). Many of these phenomena create significant challenges. Some threaten the structural integrity of a vehicle, as is the case with resonant aeroelastic flutter (Garrick & Reed III, 1981) wherein structures such as an airplane wing can be excited at frequency near its structural resonant frequency, leading to positive feedback and eventual damage or failure. Others can threaten the operation of a vehicle as with aeroelastic control reversal where aeroelastic deformations of a wing or control surface can create flow conditions such that control inputs have opposite results compared with the expected behavior of the undeflected case. The goal of studying those fluid-structure interactions is to eventually mitigate or eliminate them. For example, currently, significant research effort aims to understand the flow-induced flutter of airfoils with the hope that more complete understanding of the underlying fluid-structure interactions would motivate better engineering strategies and designs that redress these issues.

However, in nature, there are wide-ranging examples of fluid-structure interactions as beneficial, and even central to achieving a design goal. The flight of animals at low Re numbers (small birds and insects) often relies in part on the flexibility of the wings, one example being hummingbird wings. In fact, locomotion (i.e. swimming or flying) in fish, insects and birds takes advantage of flow-induced deformation and even flutter of flexible structures to improve performance. Prior studies into biological flow-induced flutter phenomena have examined topics such as wing flutter (Michelin & Llewellyn Smith, 2009; Tang, Yamamoto, & H. Dowell, 2003); as well as fish locomotion and insect flight (Lighthill, 1975; SHOELE & ZHU, 2010; Shoele & Zhu, 2012; Shoele & Zhu, 2013). One such case studied by others in our group is the marine invertebrate *Aplysia*, or the "sea hare", which was investigated in the work by Zhou & Mittal (2018). As is common to these marine invertebrates, this animal has a large flexible, membranous wing-like structure called a parapodia which they flap to create thrust. It is important to note that the parapodia are not controlled throughout the chord, but instead only an area at the root of the membrane is actuated. The rest of the structures deformation is due to a combination of the forces from the actuated part of the membrane and the surrounding fluid forces. Yet it was shown that the specific deformations of the parapodia due to the fluid-structure interactions aided in the creation of the thrust generating vortical structures, indicating that the *Aplysia* has evolved an anatomy that takes advantage of these fluid-structure interactions.

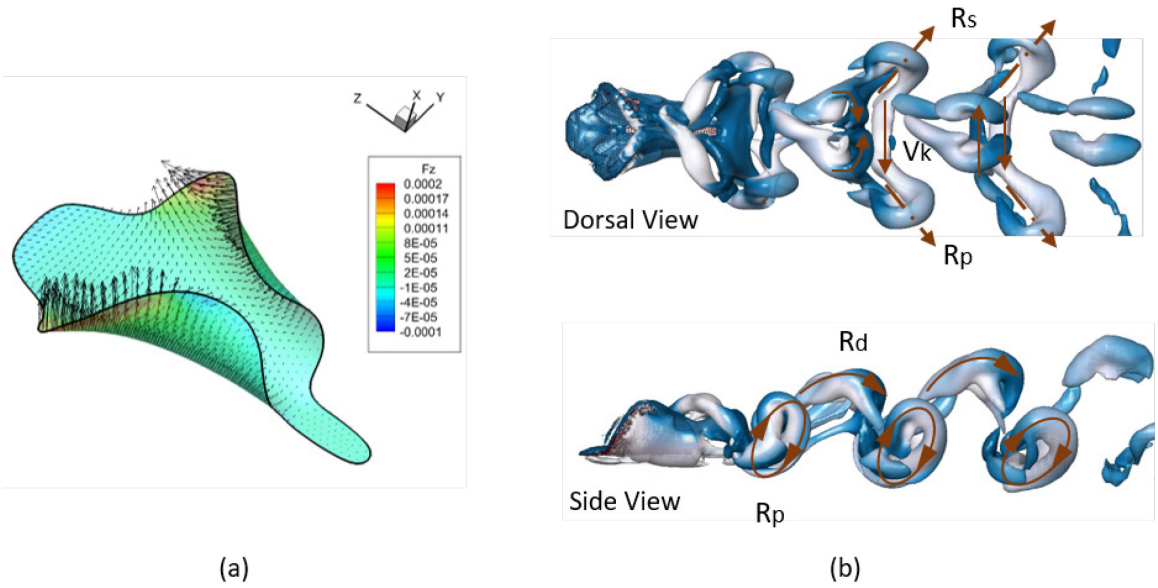

FIG. 1.2 – Simulation results of a marine invertebrate called Aplysia from work by Zhou & Mittal (2018). (a) shows the forces on the flapping membrane and (b) shows the vortical structures shed by the membrane.

Beyond locomotion there are many other examples of biological processes which are designed to utilize fluid-structure interactions. In the cases of phonation (Mittal, Erath, & Plesniak, 2013) or heart valves (Seo et al., 2014), the anatomy of the biological structures has evolved to take advantage of fluid forces to improve performance. In the case of phonation, the vocal folds are not actively driven, but instead vibrate due to the flow passing over them. In the case of heart valves, the entire system is designed to utilize flow-induced deformations, by way of the flexible membranous valves, to accomplish complex plumbing without external forcing or control.

While historically FSI problems have been studied by the engineering community as a failure mode, more recently research has begun to examine methods and applications which can exploit these FSI phenomena. Many examples of these sorts of efforts have so far focused on the study of pitching and heaving airfoils as energy harvesters (Kinsey & Dumas, 2008), and while these systems certainly aim to take advantage of FSI phenomenon, they still mostly use rigid structures. However, as we can see from the examples from nature, there are likely numerous engineered systems which

could be designed to take advantage of flow-induced flutter of flexible bodies. Exploring a subset of such systems that harness flow-induced flutter to accomplish some useful thermo-fluidic task is the goal of this research. We examine three applications: heat transfer, energy harvesting, and mixing. In these applications flow-induced flutter of highly flexible membranes provides a novel engineering solution to an existing problem.

1.1.1 The Flapping Flag Phenomenon

Flapping flags have been extensively studied in recent years, in part because they represent the archetype of a complex dynamic aeroelastic phenomenon, called flutter (Shelley & Zhang, 2011). Flutter can perhaps be best conceptualized by understanding the so called "Collar triangle" (Collar, 1946), which classifies aeroelastic phenomena based on the relative importance of three key pieces of physics, each manifested by a force on a given structure. Those physics are the dynamics caused by inertial forces, the structural mechanics caused by elastic forces, and the fluid mechanics caused by the aerodynamic forces. Flutter is a case where all three of these physical phenomena are active and are coupled. It is defined as "*an unstable, self-excited structural oscillation at a definite frequency where energy is extracted from the [flow]-stream by the motion of the structure*" (Dowell et al., 1989).

Flapping flags are a classic example of this because they represent this phenomenon without the otherwise typically accompanying structural damage and destruction. Furthermore, they represent a subset of a much larger class of FSI problems, as discussed by Shelley & Zhang in their 2011 annual review paper on flapping flags: "*The flapping of flags is a subset of a more general class of fluid-structure problems that concern the interaction of flexible sheets or bodies with high-speed fluid flows*"(Shelley & Zhang, 2011). They go on to mention that the study of the flapping flag problem can aide in the understanding of many other more complicated systems.

Prior research on flow-induced flapping of flexible filaments or flags has focused on the problem as both a dynamical system and as a fluid dynamics problem (Shelley & Zhang, 2011). Considerable attention has been paid to the "regular flag" configuration, wherein the leading-edge is fixed and the trailing-edge is free. Single regular flags have been studied experimentally (Christophe Eloy, Kofman, & Schouveiler, 2012; Shelley, Vandenberghe, & Zhang, 2005; J. Zhang et al., 2000), analytically (Alben & Shelley, 2008; Alben, 2015; C. Eloy, Souilliez, & Schouveiler, 2007; Shoele & Mittal, 2016b; Theodorsen, 1935; WATANABE et al., 2002), and computationally (Shoele & Mittal, 2014; Zhu & Peskin, 2002). These studies have examined many features of this system.

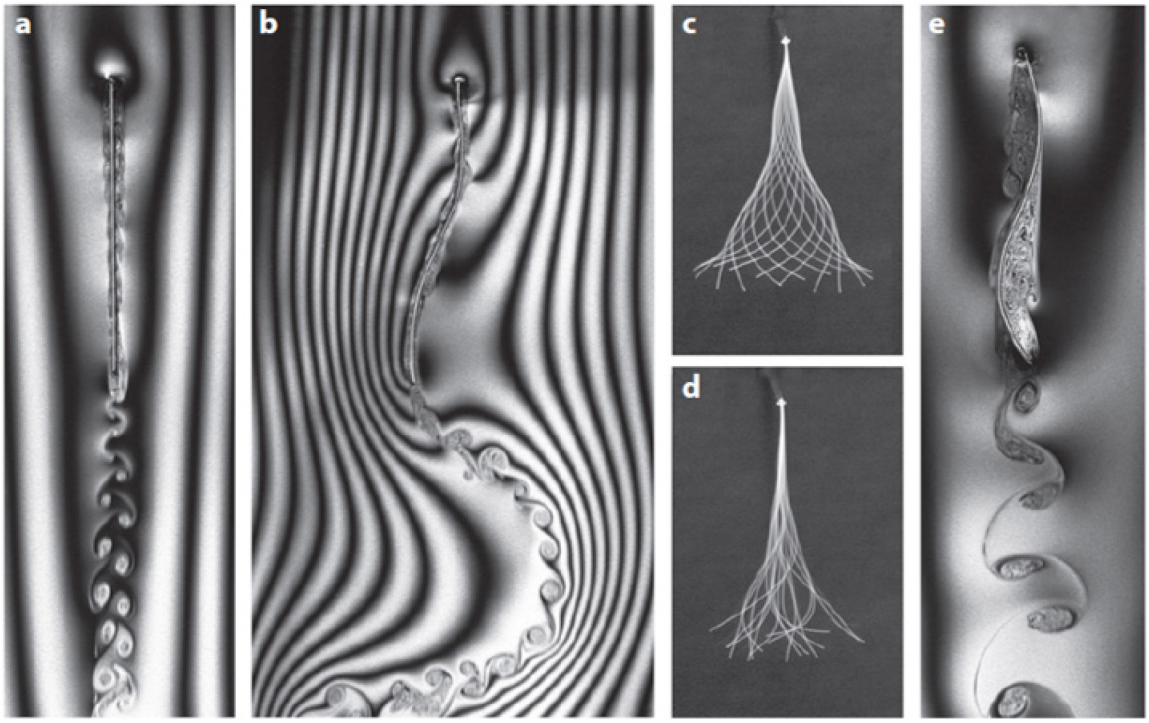

FIG. 1.3 – From Shelley and Zhang 2011 annual review paper (Shelley & Zhang, 2011): (a,b) Soap film flow visualization of the wake structure downstream of a flexible filament showing (a) The stretched-straight state and (b) Flapping. (c-d) flapping envelopes showing (c) coherent flapping and (d) aperiodic flapping. (e) The flow around a stiff metal wire bent permanently into the shape of a flapping filament.

Perhaps the most interesting feature of flapping flags in the context of this study is the rich variety of behaviors that is observed. This is shown in the FIG. 1.3 (Shelley & Zhang, 2011). In these figures, there are three key states for the flapping flag instability: (a) the stretched straight state, (c) the coherent flapping state, and (d) the aperiodic flapping state. Furthermore, flapping flags exhibit a wide variety of nonlinear phenomena. For example, the transitions between these behaviors regimes often exhibit bi-stability and hysteresis (Christophe Eloy et al., 2012). This rich variety of behaviors may be desirable from an engineering perspective as it allows the system to be tuned to a state that produces favorable behavior for a given objective. Furthermore, even within each flapping state regime there can be multiple flapping modes. This was shown both analytically and via a numerical experiment by Shoele & Mittal (2014) as shown in FIG. 1.4.

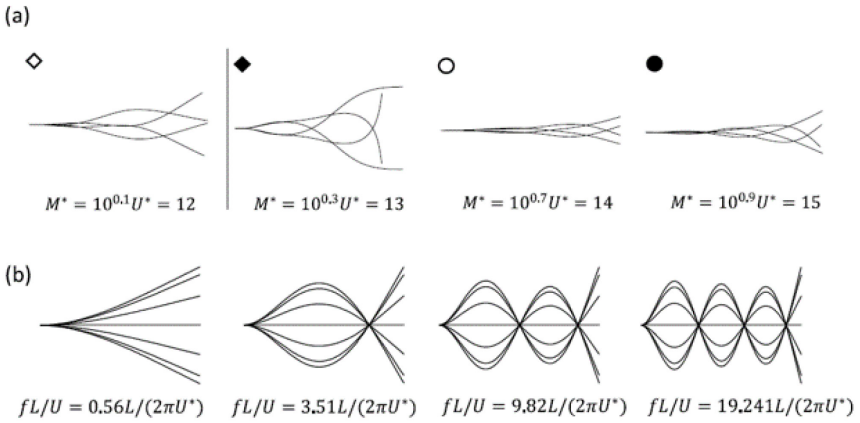

FIG. 1.4 – Figure showing the flow-induced flutter modes and the corresponding vibration modes in a vacuum of flag at different points in the U, M* parameter space (Shoele & Mittal, 2014).*

Here we can see the top row showing various flutter modes and the bottom row shows the various possible in-vacuo flutter modes for a flag or membrane clamped at one edge. As will be shown later in this work, flags can settle on different modes in this parameter space of the reduced velocity U*, the mass ratio M*, and even the Reynolds number. Another significant feature of the flapping flag problem that makes it interesting for engineering applications, is the ability of flapping flags to undergo very large deformations with relatively minimal drag forces. This is advantageous

for applications that involve mixing heated fluid or scalar species, where it is desirable to stretch and fold fluid regions, while still incurring the minimum additional energy losses.

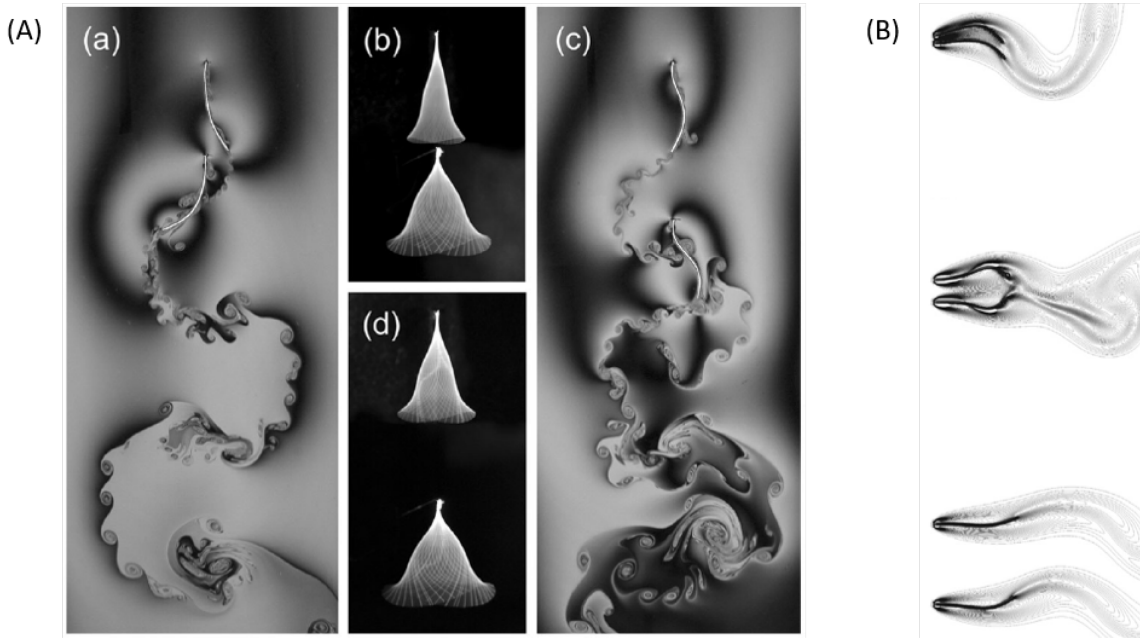

FIG. 1.5 – Examples of prior work investigating multi-flag configurations. (A) shows experimental soap film studies of tandem flags (Ristroph & Zhang, 2008) and (B) shows a numerical simulation of abreast flags (Favier, Revell, & Pinelli, 2015).

Additionally, multi flag configurations have also been studied in both tandem configurations (ALBEN, 2009; Jia & Yin, 2008; S. KIM, HUANG, & SUNG, 2010; Ristroph & Zhang, 2008) as well as side-by-side (or abreast) configurations (Farnell, David, & Barton, 2004; Favier et al., 2015; J. Zhang et al., 2000; Zhu & Peskin, 2003). Examples results from these studies are shown in FIG. 1.5. In the side-by-side configuration, Zhang, et al. (2000) and Zhu & Peskin (2003) were again able to identify distinct regimes based on separation distance. For close proximity ($d/L < 0.2$) the flags flap in-phase in so-called synchronized flapping; further apart ($0.2 < d/L < 1.0$) and the flags flap anti-phase in the so-called clapping regime, and finally, at large enough distances, the flapping of the two flags become decoupled.

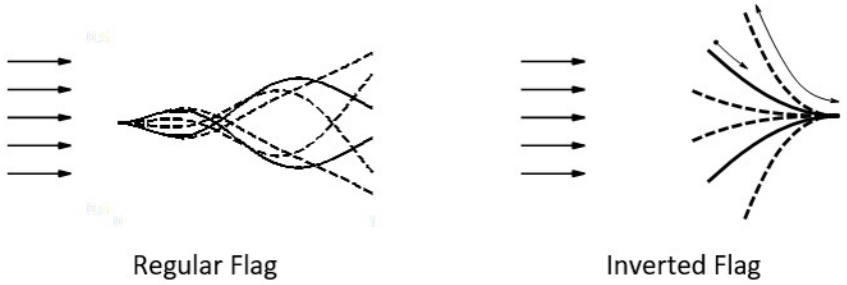

FIG. 1.6 – A regular flag (fixed leading edge, free trailing edge) and an inverted flag (free leading edge, fixed trailing edge)

So far, we have discussed the beneficial aspects of what is called the "regular" flapping flag, wherein the leading edge is fixed and the trailing edge is free. However, there is another configuration called the "inverted" flapping flag wherein the leading-edge is free and the trailing-edge is fixed. This system only produces interesting and potentially useful flutter phenomena for flags which are much stiffer than what is typically considered for regular flags. While considerable attention had been paid to the regular flag configuration, "inverted flag" configurations, wherein the leading edge is free and the trailing edge is fixed, are relatively new. The concept was first studied in earnest by Kim et al. (2013). They showed, and others since have confirmed that these flags can flutter with large amplitude at lower reduced velocities thereby making them useful for low-speed applications. They argued that for the particular application of electromechanical energy harvesting, the more unstable nature of the inverted system and the larger achievable flapping amplitudes could lead to better energy harvesting performance. Further studies have shown significantly improved energy harvesting potential of inverted flapping flags over regular flags (Orrego et al., 2017; Shoele & Mittal, 2016a).

There have been numerous studies of multi-flag configurations involving regular flags, however, multi-inverted flag configurations have only recently been the subject of investigation. One such example is recent experimental work by Cerdeira, et al. (Huertas-Cerdeira, Fan, & Gharib, 2018). They used high speed videography to examine the side-by-side configuration (aka Abreast

configuration) at various flag distances, reduced velocities, and flag length ratios, and showed that flag proximity can in fact increase the flutter amplitude.

The phenomenological study of the flapping flag problem has characterized a rich variety of behaviors across a range of configurations. As discussed, these flow-induced flutter phenomena, and aeroelastic fluid-structure interactions in general, can have both beneficial and detrimental effects. It is the goal of this work to examine the beneficial effects. We explore novel applications where flow-induced flutter of thin elastic membranes, flags, and plates can be exploited for enhancing heat transfer and mixing, and to harvest energy from the flow.

1.2 Motivating Applications

In this work we primarily study flutter phenomena in two types of flapping flags (or membranes): the regular flag and the inverted flag. The inverted flag-study is motivated by the possibility of harvesting energy from the flutter using for instance, piezo-electric membranes. For the regular flags we are motivated by two applications: heat transfer enhancement and mixing enhancement. We examine this system in the context of two such engineering applications: low Reynolds number micro-mixers at inertial microscales for use in microfluidic devices, and heat transfer in a forced-convection channel-flow type heat-exchangers for both large industrial scales such as air cooled condensers for power plants and other industrial applications, as well as small scales such as high performance electronics cooling.

1.2.1 Microfluidic Mixing

Mixing enhancement at the so-called inertial scale Reynolds numbers i.e. $O(1)<Re<O(100)$ (Amini, Lee, & Di Carlo, 2014) has wide ranging applications in both chemical and biomedical engineering. Recent interest in this arena has been driven by the development of lab-on-a-chip (LOC) devices, micro-total-analysis systems (μTAS), micro-scale bioreactors and other low cost,

field deployable, chemical or biological microfluidic devices (Cai et al., 2017; Capretto et al., 2011; Lee et al., 2011; Lee et al., 2016; Nguyen & Wu, 2004; Stone, Stroock, & Ajdari, 2004; Jun Zhang et al., 2016). The wide-ranging need for these devices has driven considerable research as various technological advancements, particularly in terms of manufacturing technology, have made such systems possible (Alam et al., 2018). Many of these potential applications involve creating low cost, field deployable, replacements for existing laboratory testing as can be seen in the cartoon of a lab on a chip in FIG. 1.7. The practical applications of these systems in many cases involve improvements to diagnosis of diseases and health conditions in areas without ready access to the infrastructure that is needed for traditional laboratories. As such, microfluidic devices are generally required to be cost efficient, energy efficient, simple to operate, and simple to fabricate on a large scale. Furthermore, with miniaturization often come new challenges and design requirements. These engineering goals drives improvements into all aspects of these devices.

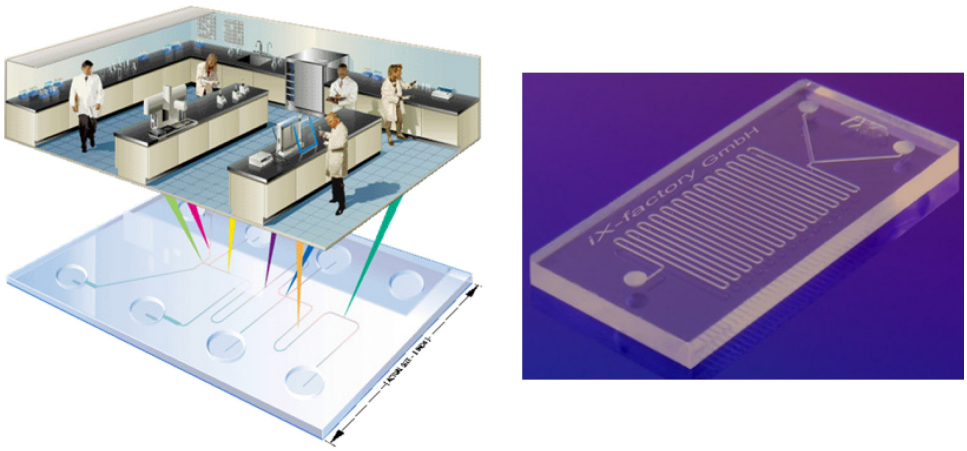

(a) (b)

FIG. 1.7 – (a) cartoon showing the so called "lab on a chip" concept. (b) Image showing a standard mixing and reaction chamber using a zig-zagging channel design.

Microfluidic devices often involve many different operations and subcomponents including pumps, mixers, separators, sorters, reactors, and others. One of these subsystems, the micromixer, is the focus of much of the research presented in the first part of this dissertation. The requirements

and engineering goals for the microfluidic device overall also apply to micromixers in particular. Goals for mixers include fast mixing, low energy expenditure, low design complexity, ease of manufacture and operation, robustness to malfunction, and small overall footprint. While in principal even a straight channel could be an effective mixer given sufficient channel length and pumping power, the cutting-edge nature of microfluidic devices typically requires more clever solutions wherein achieving rapid mixing in a small space with minimal pumping power is critical.

The need for rapid mixing is made even more crucial because in many cases, the mixed fluid is subject to some kind of chemical reaction or other assay. This means that the faster the fluids can be mixed, then less channel length would be required for a reaction chamber. Also, faster mixing means less time until the fluids are homogenously mixed which could be especially important if there is some time component to the reaction. In such cases, ideally all the fluid would start reacting at the same time, making rapid mixing of crucial importance.

1.2.1.1 Inertial Reynolds Number Regime

As discussed, these microfluidic devices used for analysis or synthesis in biological or chemical applications, often require fast mixing. However, in many applications, high throughput requires increased operational flow rates, which increases Reynolds and Peclet numbers, thereby reducing molecular diffusion-based mixing. However, the Reynolds number of these flows still remains too low to take advantage of mixing due to turbulence or other intrinsic fluid-dynamic instabilities (e.g. vortex shedding, as will be shown). The challenge then is to create devices which can accomplish efficient mixing without relying on these mechanisms. There is one regime in particular where this interplay is acute, wherein the Reynolds number is high enough to decrease molecular transport by increasing the Peclet number, while simultaneously the Re number is too low to access highly efficient mixing phenomena such as vortex shedding or turbulent mixing.

This regime is called the "inertial microfluidic" range that typically extends from Re~1 to Re~100. It exhibits interesting fluid dynamics, as it is a regime in which both the inertia of the flow and the viscosity are both finite and play an active role in the fluid dynamics and mixing. This leads to a number of interesting phenomena in this regime, and as such this Reynolds number range has seen significant research interest, particularly in recent years with the newfound focus on microfluidic devices.

1.2.1.2 Active and Passive Mixers

Within this context, inertial micromixers, as with all micromixers, may be categorized as "active" or "passive." Wherein active mixing involves addition of energy beyond the pumping power required to move the fluid, and/or additional control or actuation to be externally applied to the system. Whereas, passive mixers use no external forcing or energy besides what is provided by the pump.

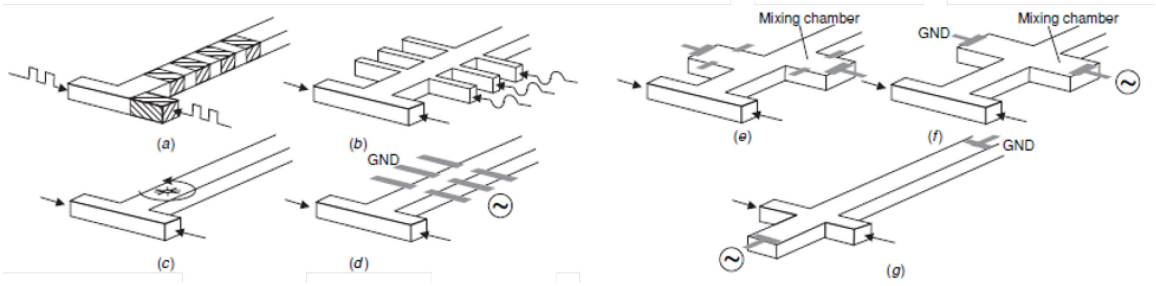

FIG. 1.8 – Schematics of various active mixer designs from Nguyen & Wu (Nguyen & Wu, 2004).

Active mixing comes in a wide variety of forms, some of which are shown in a schematic from the 2004 review paper by Nguyen & Wu (2004) in FIG. 1.8. Active mixing can come in the form of pressure perturbations (Afzal & Kim, 2015; Glasgow & Aubry, 2003; Xia & Zhong, 2013), or can be mechanical (Khatavkar et al., 2007; K. S. Ryu et al., 2004), electromagnetic (Oddy, Santiago, & Mikkelsen, 2001; Tai et al., 2006), acoustic (Ahmed et al., 2009; Van Phan et al., 2015), or can use piezoelectric energy (Cui et al., 2016), as well as many other approaches. Active mixers introduce

spatial and temporal variations into the flow which enhance mixing. This approach can be very effective, but it adds significant complexity, which increases cost and decreases system reliability.

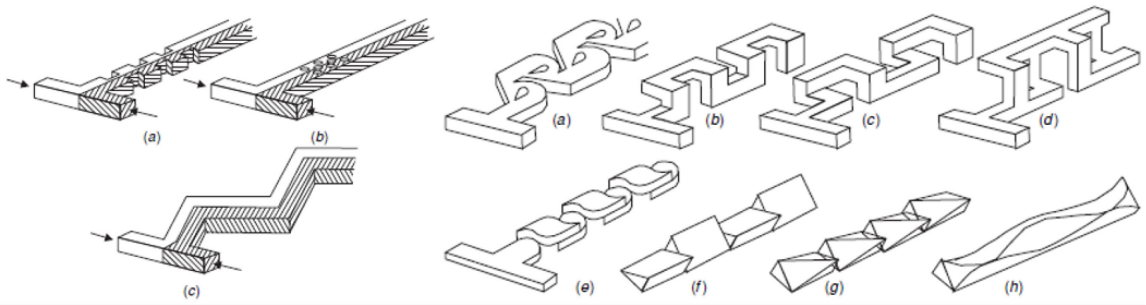

FIG. 1.9 – Schematics of passive mixers from Nguyen & Wu (Nguyen & Wu, 2004). (A) shows 3 major categories of passive mixing strategies, while (B) shows a number of previously investigated passive mixers for "intermediate Re numbers" which they define as Re = O(10-100).

Passive mixers require no external forcing, but instead, use only the energy of flow (i.e. pumping power) to induce mixing. FIG. 1.9 shows a variety of schematics of passive mixers for channel flow configurations (Nguyen & Wu, 2004). Here, (A) shows three major passive mixing strategies and (B) shows several previously studied passive mixer designs for so called "intermediate Re number" which they define as Re = O(10-100). The use of complex channel paths (curved, sinusoids, zig-zags, and square wave shapes etc.) is a common passive mixing technique (Afzal & Kim, 2012; Hossain, Ansari, & Kim, 2009; Lee et al., 2016). Other devices such as the so-called chaotic advection mixers use obstacles to introduce complex, spatially varying velocity gradients into the flow as a way to enhance mixing (Stroock et al., 2002). While these passive mixers have a simpler design, they usually underperform compared to active mixers (Nguyen & Wu, 2004; Wu & Nguyen, 2005). This is because these passive mixers are also always "static" and do not introduce any temporal fluctuations into the flow. Furthermore, these passive mixers also incur large pressure losses and this manifests as increased pumping power as well as higher channel pressures, both of which are undesirable in microfluidic systems (Nguyen & Wu, 2004).

In our low Re mixing work, we explore a new approach to inertial micromixing; one that exploits flow-induced flutter of membranes to enhance mixing. These "flutter mixers" may be considered passive in that they do not require any energy input or external control beyond the pumping power that drives the flow. However, their effect is akin to active mixers in that they introduce complex spatial as well as temporal fluctuations into the flow. These flutter micromixers have several desirable traits: first, as will be show later, the flutter instability occurs over a wide range of Reynolds numbers relevant to inertial micromixing and their mixing performance improves with increasing Reynolds number. Second, the structural parameters (density and elasticity) of the fluttering element can in-principle be chosen to optimize the flutter for a given mixing application. Third, the device complexity should be lower than active mixers. Finally, as will be shown, significant mixing enhancement can be accomplished over very short channel lengths with a relatively small attendant pressure loss.

Previous studies examined the use of membrane flutter in channels to enhance heat transfer in heat-sinks appropriate for electronic cooling applications (Herrault et al., 2012; Rips et al., 2017; Shoele & Mittal, 2014). The Reynolds numbers for these applications is typically O(1000) or higher (Herrault et al., 2012) where membrane flutter is guaranteed, although the simulations did show sustained flutter at a Reynolds number of 50. Past experimental work on flapping flags/membranes/filaments has also been at O(1000) or higher Reynolds numbers (Ait Abderrahmane et al., 2012; Dessi & Mazzocconi, 2015; CHRISTOPHE ELOY et al., 2008; Gibbs et al., 2014; D. Kim et al., 2013; Shelley & Zhang, 2011; Taneda, 1968; J. Zhang et al., 2000) whereas a significant number of computational modeling studies have employed inviscid models (Alben, 2008; ALBEN, 2008; Alben & Shelley, 2008; Alben, 2015; Argentina & Mahadevan, 2005; Doaré, Sauzade, & Eloy, 2011; C. Eloy et al., 2007; Kornecki, Dowell, & O'Brien, 1976; Theodorsen, 1935). Even modeling studies employing viscous flow models have mostly focused on Reynolds number of O(100) or higher (CONNELL & YUE, 2007; Huang, Shin, & Sung, 2007; Zhu & Peskin, 2002). Thus,

much of the previous work is not directly relevant to the inertial micromixing regime where Reynolds numbers extend down to O(10) and viscous effects are much more significant.

The work focuses on flow-induced membrane flutter in the O(10-100) Reynolds number regime that is relevant for inertial micromixing, and provides a detailed description of the flutter dynamics, flow features, and mixing performance. We first employ flow simulations in a simple two-dimensional (2D) model of an inertial scale micromixer and examine the effect of key parameters such as Reynolds and Schmidt numbers, as well as reduced velocity and confinement ratio on the flutter dynamics, flow/vortex features, pressure losses and mixing quality. We also explore strategies for extending downwards the range of Reynolds number for which such mixers could be used. We compare the flutter mixer performance with an analogy to post mixers via a circular cylinder. As the final component of our 2D mixing analysis, we examine tandem configurations of flutter mixers with different membrane lengths to assess the potential utility of multi-flutter mixer designs.

We then use three-dimensional (3D) fully-coupled fluid-structure interaction simulations. We again explore the dependence of the 3D flags on the Reynolds number. We also perform a preliminary exploration of the parameter space which is unique to the 3D system, namely the flag aspect ratio and the spanwise gap between the flag edges and the sidewalls. We then compare the results of the 2D and 3D investigations both to understand the fidelity limitations of the 2D study, as well as to glean further understanding of both models of the system through their comparison.

1.2.2 Heat Transfer Enhancement

Another application which is in many ways related to mixing is forced-convection channel-flow heat-exchangers, which play a vital role in industrial and scientific systems. From applications with dedicated heat transfer goals (e.g. condensers, refrigeration, and industrial heat exchangers) to applications requiring waste heat disposal (e.g. electronic cooling), forced convection is used

when more passive methods cannot provide adequate heat flux. But even forced convection heat exchangers can reach performance saturation. Often these barriers act as the primary limiting factor on a design, and said systems are described as “heat limited”. Thus, heat transfer enhancement a critical issue for many technologies.

Heat transfer enhancement is not simply increased heat flux over some reference design. As with any notion of performance, heat transfer enhancement must be considered from an efficiency perspective. Forced convection heat exchangers have an implicit cost of performance which is the energy used to drive the flow, or more practically, the power required to drive the pump or the fan. Any notion of improved performance must be normalized by this input energy, essentially answering the question of whether the increased heat flux due to the device is worth its cost in pump power. To achieve this type of comparison, this work uses the Thermal Enhancement Factor (TEF) (Webb, 1981).

Many approaches to heat transfer enhancement in forced convection heat exchangers have been studied. Much like the work on mixers, these methods can be broadly categorized as either active or passive systems by whether they require external energy input or control to function. However, in the case of heat transfer applications, far more effort has been focused on passive devices. Examples of some general categories of passive methods can be seen in FIG. 1.10. (A) and (C) show examples of vortex generator methods (Jacobi & Shah, 1995) where small obstructions are placed on the channel walls to create streamwise vortices. (B) shows examples of ribbed channels (Tanda, 2004) which both increase the surface area of the wall, and increase heat transfer by creating a turbulent boundary layer.

Broadly speaking, one would expect active methods to outperform passive methods, usually by the introduction of some sort of unsteadiness. However, this increased performance usually

comes at the cost of practical considerations such as system complexity, ease of manufacture and maintenance, and probability of failure.

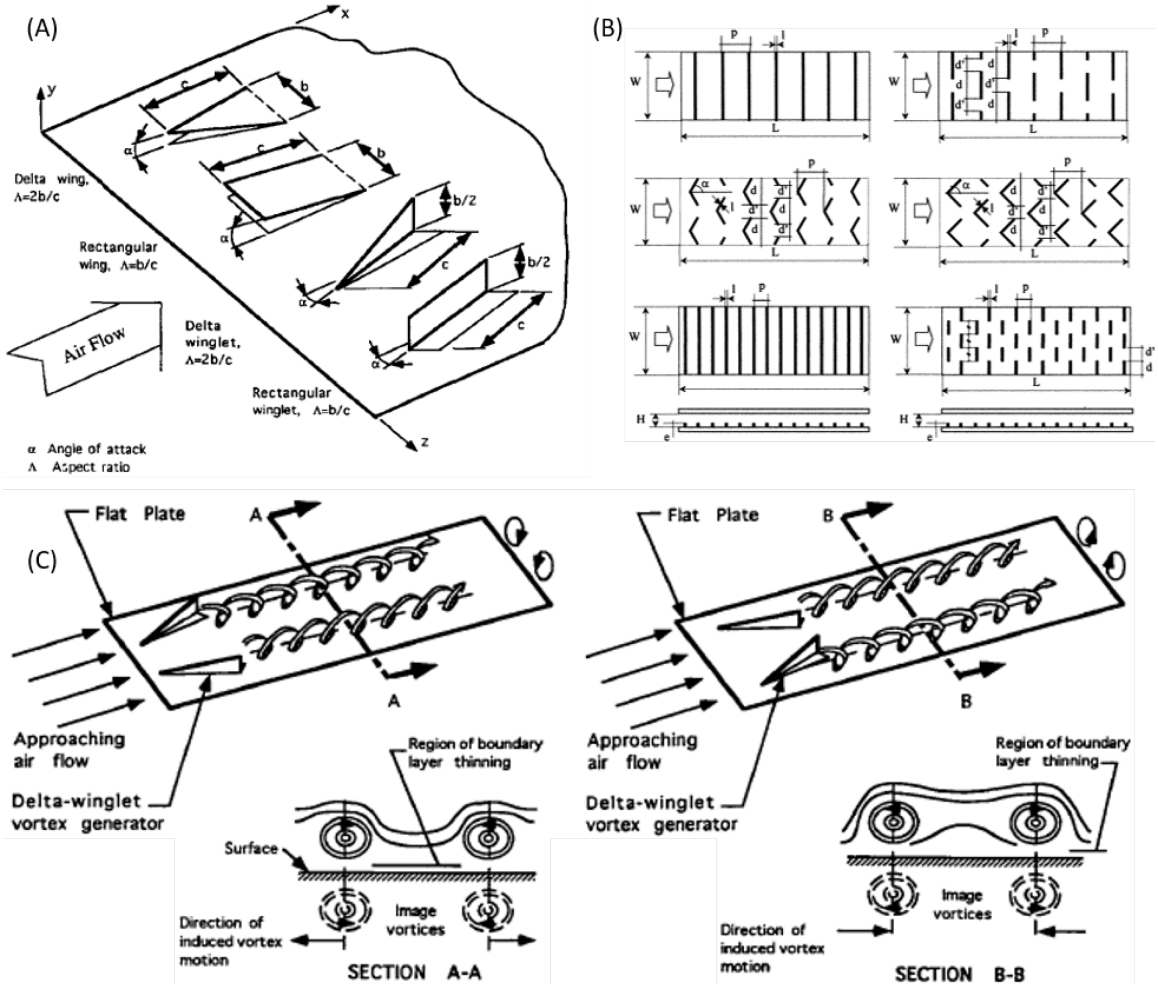

FIG. 1.10 – Examples of forced convection channel flow heat exchangers. (A) and (C) show examples of surface mounted vortex generators (Jacobi & Shah, 1995). (B) shows examples of ribbed channels with various rib patterns (Tanda, 2004).

An ideal system would generate unsteadiness with no external control or energy input. One such system is flapping flag heat transfer enhancement devices which have been shown in our prior 2D simulations (Shoele & Mittal, 2014) and experiments by the group of Ari Glezer at George Tech (Herrault et al., 2012) to dramatically improve heat transfer performance. The results of this prior 2D study are summarized in Appendix A. The notion is that the flag flaps in the flow,

disrupting the boundary layers of the smooth channel flow profile, thereby increasing the heat flux through the walls. The 2D simplification used in our prior simulations is clearly an idealized perspective. While the prior work shows the potential for significant performance improvements, these idealizations both regarding 2D simplification as well as the assumption of simple rectangular channels create uncertainty into the practicable realization of these performance gains. This is because existing forced convection channel flow heat exchanger designs come in a wide variety of channel shapes because of various practical engineering requirements.

Initially we explored the idea of using a prescribed motion method to impose the 2D flapping behavior of the flag onto the 3D system. To do this we modeled the 2D flapping dynamics as a traveling wave and imposed that behavior as a prescribed motion method on a 3D membrane. This would provide the 3D fluid dynamics and would allow us to explore system parameters which can only exist in 3D such as flag aspect ratio and spanwise confinement. However that investigation (Rips et al., 2017) assumes that the infinite span flapping behavior and the finite span flapping behavior is sufficiently comparable. However as has been shown in the literature (C. Eloy et al., 2007), there are considerable changes in the system dynamics and stability in going from 2D to 3D flags.

In the current work, we use a 3D, fully coupled fluid-structure-thermal (FST) interaction model to simulate, the behavior of the flapping membrane in the channel. This lends significant additional fidelity to the model and captures the flapping dynamics of the finite span membrane. It also allows for the study of designs and configurations in which the prescribed motion method would not be appropriate, namely non-rectangular channel geometries. There are multiple potential issues for a prescribed motion method with varying the channel shape. First, it seems at the outset that the flag dynamics would be sensitive to the channel shape, especially if the channel shape somehow interferes with the typical flapping envelope. Second, due to the complex interactions between the

vortical structures produced by the flag and the boundary layer, it is possible that these interactions may be sensitive to the channel geometry.

In this work we will first compare the high-fidelity 3D simulations to a 2D system comparable to the prior investigation. We will then investigate various 3D aspects of this system including channel shapes, flag aspect ratios, as well as other flag configurations. The goal is to evaluate the robustness of this device and its sensitivity to system parameters that would vary in practical applications; both to better understand its utility in industrial and scientific applications, and to fully examine the specific fluid dynamic mechanisms responsible for this design's significant heat transfer enhancement.

1.2.3 Energy Harvesting

One of the first engineering applications studied by the fluid-structure interaction community where a flow-induced flutter phenomenon would be utilized in a beneficial manner was piezo-electric energy harvesting (Allen & Smits, 2001). A variety of flutter-based energy harvesting devices have been studied using various approaches with varying success. Many initial attempts to design flutter energy harvesters focused on regular flags (Allen & Smits, 2001; Taylor et al., 2001; Li, Yuan, & Lipson, 2011; Michelin & Doaré, 2013). These studies showed energy harvesting success, however, it became apparent that regular flags have a significant limitation in that the deformation amplitude and local curvature are low compared to the length of the flag.

The earliest work on inverted flags for energy harvesting by (Akaydin, Elvin, & Andreopoulos, 2010) used a cylinder upstream of the inverted flag however, this only led to small amplitude deformations. A more thorough study of the inverted flag parameter space by Kim et. al. (2013) showed that inverted flags were in-fact much better candidates for piezo-electric energy harvesting because they experienced significantly greater flapping amplitudes. In light of the observations by Kim et al. (D. Kim et al., 2013) and the potential engineering applications of the inverted

configuration, a number of other recent studies have examined the single inverted flapping flag (J. Ryu et al., 2015; Sader et al., 2016). Following the work by Kim et al., Shoele & Mittal (2016a) were also able to show this effect using 2D fluid-structure-electromechanical interaction simulations, where the behavior regimes and vortex shedding phenomena of the inverted piezoelectric flapping flags were studied in detail. Furthermore, that work examined how the extraction of energy from the piezoelectric materials would affect the observed flapping behaviors.

In our study, we focus on the behavior and performance of multi-flag systems. This is partly because real world applications will likely consist of arrays of harvesters. Furthermore, multi-inverted flag configurations are valuable candidates for study since these configurations act as a surrogate for more complex fluid-structure interaction problems. In particular, they can serve as a model for problems featuring coupled large-scale deformation of relatively stiff bodies. Insights gained from the study of single-regular flags, multi-regular flags, single-inverted flags, and now multi-inverted flags can serve as a base towards understanding a broad group of fluid-structure interaction problems in the flow induced-flutter regime, with the single-flag studies demonstrating individual behaviors and the multi-flag studies demonstrating coupled group behaviors. Additionally, there are real-world problems for which multi-inverted flags serve as a simplified model besides piezoelectric energy harvesters. These include phenomena such as leaf flutter, fish schooling, and bird flocking where multiple moving/flexible bodies are affected due to the dynamics of the intervening flow.

Finally, as discussed above, the potential engineering applications for inverted flags will likely involve multiple flags working in close proximity. For example, prototype concepts for inverted flag electromechanical energy harvesting could use a bio-inspired tree-like structure to hold many piezo-electric harvesters. More broadly, the argument for these systems often involve ideas like economies of scale and ease of deployment, wherein a single energy harvester may not out perform its more conventional turbine-based counterpart, but a tree of harvesters could be a better solution.

For these engineering applications, understanding the coupled dynamics of multi-inverted flag systems is a key step towards real world deployment.

In this part of the study, we examine the fluid dynamics, flapping behavior, and energy harvesting potential of multi-inverted flag configurations in both the tandem and side by side configuration. For both configurations we perform a fine grain parametric sweep over the separation distance using coupled FSI numerical simulations. To develop insights and recommendations towards optimized multi-inverted flag energy harvesting, we explore three key motivating questions. First, we look for distinct behavior regimes based on separation distance. These systems are highly stochastic, so identification and segregation into discrete regimes can simplify our analysis. Second, we examine the fluid dynamics (the vortex shedding behaviors), and the fluid-structure interaction for both the individual flags and for the coupling between the flags. Understanding these dynamics could lead to insights which may assist in understanding more complex theoretical problems, and more complex real-world phenomena. Third, we use three key performance metrics: the phase shift, the RMS of the amplitude, and the flapping Strouhal number to better understand the energy harvesting potential of these coupled systems.

Chapter 2

Numerical Methods

In this research we use various computational fluid dynamics approaches which all fall into the category of immersed boundary methods (Mittal & Iaccarino, 2005). Immersed boundary methods are a valuable tool in CFD. They provide a highly generalized framework which is largely agnostic to the details of the geometry/boundary in the problem. This is accomplished by decoupling the shape of the fluid mesh from the geometries in the fluid. In the immersed boundary methods that we use in this work, the Eulerian fluid field is always represented on a Cartesian grid. The body in question is then represented by its own Lagrangian grid and is immersed within the fluid mesh. The challenge then is to impose boundary conditions for the immersed body onto the fluid grid which does not have nodes at the surface of the body.

Therein also lies the distinction between the various techniques used in this work. In this research we use different immersed boundary approaches depending on the specifics of the structure in question. If the structure is either stationary with respect to the flow, or if it is moving according to a prescribed motion, we use a sharp-interface approach which is at the core of the in-house code of our group ViCar3D (Mittal et al., 2008). The other situation is flow with flexible bodies subject to fluid-structure interactions. In this work, those bodies are either represented as 2D membranes or 1D filaments (for 3D and 2D simulations respectively). Their behavior is subject to their own structural governing equations which are driven by the force exerted by the fluid. In these cases, we use a diffuse-interface penalty method approach for simulating these flows.

In this section we will first describe the flow solver as this component is common to both our immersed boundary techniques followed by a description of the structural solver used to simulate the governing equations defining the bodies dynamics. We will describe the sharp-interface immersed boundary method used in our solver for standard rigid bodies. We will then explain the penalty method diffuse-interface immersed boundary method used for flexible bodies subject to fluid-structure interactions. In that section we will discuss the diffuse interface immersed boundary method, the penalty method FSI coupling. The last solver we discuss is the scalar solver used to model passively advected scalars such as heat or some other species in the flow. Finally, we will discuss the validation and verification of the various components of our solver. Included in that validation work is a description of the development of a medium-sized wind tunnel that was designed and built as part of the work in pursuit of this validation effort.

2.1 Numerical solvers

2.1.1 The Flow Solver

One of the primary benefits of immersed boundary methods is the simplification of the flow solver for configurations that involve complex geometries and/or moving boundaries. Because the flow solver is agnostic to the geometry and position of the boundary, we are able to use Cartesian grids and finite differencing for our discretization scheme. To discuss this numerical method, first we must describe the underlying physics being modeled. Here the fluid is described according to the incompressible Navier-Stokes equations:

$$\frac{\partial \mathbf{u}}{\partial t} + \nabla \cdot (\mathbf{u}\mathbf{u}) = -\frac{1}{\rho}\nabla p + \frac{1}{\nu}\nabla^2 \mathbf{u} + \mathbf{f} \tag{2.1}$$

$$\nabla \cdot \mathbf{u} = 0 \tag{2.2}$$

Where $\boldsymbol{x}$ is the position vector in the fluid domain, $\mathbf{u}$ is the velocity vector, p is the dynamic pressure, ρ is the fluid density, ν is the dynamic viscosity of the fluid and $\mathbf{f}$ is the penalty method coupling force which will be discussed in a later section. Eqn. (2.1) describes the conservation of momentum of the fluid and Eqn. (2.2) describes the conservation of mass in the fluid. These equations can be non-dimesionalized according to the following characteristic scales: L is some characteristic length (either the flag length or the channel width in our simulations), U is some characteristic velocity (the mean velocity of the channel flow $\bar{U}$, or the far field velocity U_∞), and ρ is the fluid density. Then the characteristic time scale is L/U, and the characteristic pressure scale is ρ/U^2. Using these scales, the Navier-Stokes Equations (2.1) and (2.2) can then be expressed in their nondimensional forms:

$$\frac{\partial u_i}{\partial t} + \frac{\partial (u_i u_j)}{\partial x_i} = -\frac{\partial p}{\partial x_i} + \frac{1}{\mathrm{Re}} \frac{\partial}{\partial x_j}\left(\frac{\partial u_i}{\partial x_j}\right) + \mathbf{f} \tag{2.3}$$

$$\frac{\partial u_i}{\partial x_i} = 0 \tag{2.4}$$

where $i; j = 1, 2, 3$, and the same variable names u and p are used for the nondimensionalized variables for convenience. Here Re is the Reynolds number defined as $\mathrm{Re} = UL/\nu$. These equations are then discretized on a Cartesian mesh in a semi-staggered approach. Here, the variables u_i and p are stored at the cell centers, and in addition, face centered velocities U_i are also computed and stored. These additional face centered velocities are needed in support of a fractional step approach used to decouple the calculations for the pressure and momentum.

The fractional step method used here splits up the solution of the Navier-Stokes equations into several steps. First, an advection-diffusion equation is solved iteratively for an intermediate velocity variable u_i^*. Here, the convective and diffusive terms are discretized using finite-central differencing according to an Adams-Bashforth approach for the convective term and a Crank-

Nicholson approach for the diffusive term so as to achieve second order accuracy in time according to:

$$u_i^* = u_i^n + \frac{\Delta t}{2} \cdot \left[\left(3C_i^n - C_i^{n-1} \right) + \frac{1}{\mathrm{Re}} \left(D_i^n + D_i^* \right) + \mathbf{f} \right] \tag{2.5}$$

$$C_i = \frac{\delta \left(U_j u_i \right)}{\delta x_j} \ , \ D_i = \frac{\delta}{\delta x_j} \left(\frac{\delta u_i}{\delta x_j} \right) \tag{2.6}$$

where C_i and D_i are the convective and diffusive terms respectively, $\frac{\delta}{\delta x_i}$ is a second order central difference, and superscripts represent the relative timestep. This equation is solved using a Gauss-Seidel Line-SOR method. The intermediate cell-centered velocity u_i^* is then interpolated onto the face centers to create U_i^* which is then used to calculate the pressure at the new time step. This is accomplished by requiring that the divergence of the velocity at the new time step be zero (according to Eqn. (2.4)), which is done by setting the divergence of the momentum equation equal to zero, which creates the Pressure Poisson Equation:

$$\frac{\delta}{\delta x_i} \left(\frac{\delta p^{n+1}}{\delta x_i} \right) = \frac{1}{\Delta t} \frac{\delta U_i^*}{\delta x_i} \tag{2.7}$$

where Neumann boundary conditions are used for the pressure at any boundary. Herein we can see the benefit of the semi-staggered approach of keeping face-centered velocities as the first derivative of the intermediate velocity because the discretization of the first derivative of u_i^* would be subject to even-odd decoupling as it is one order lower than the discretization needed for the pressure. With the semi-staggered method, the velocities can be taken at the immediate cell faces, and the pressure can be taken at the adjacent cell centers, eliminating the even-odd decoupling issue as all the values are taken from neighboring locations meaning no neighbor-skipping is needed. In general, this Pressure Poisson Equation (PPE) is solved using a Bi Conjugate Gradient approach

for most of the work presented in this thesis. A much more detailed discussion on the method can be found in Zhu et al. (2017).

Once the new pressure p^n is calculated, it is used to correct the intermediate velocities calculated earlier. This correction step is performed to calculate both u_i^n and U_i^n as the face-centered velocities are needed for the convective term in the momentum advection diffusion equation. It is calculated according to:

$$u_i^{n+1} = u_i^* - \frac{1}{\Delta t}\left(\frac{\delta p^{n+1}}{\delta x_i}\right)_{cc} \tag{2.8}$$

$$U_i^{n+1} = U_i^* - \frac{1}{\Delta t}\left(\frac{\delta p^{n+1}}{\delta x_i}\right)_{fc} \tag{2.9}$$

where the subscripts denote cell-centered and face-centered. The boundary conditions for pressure are always taken to be Neumann boundary conditions. The boundary conditions for the velocity at the outer boundaries are problem specific but are typically subject to a ghost cell approach to preserve the spatial accuracy of the solver. The momentum boundary conditions for anything that isn't the outer domain boundaries depend on whether the sharp interface method is being used (solid and prescribed motion bodies) or if the diffuse interface penalty method is used (FSI bodies). These methods will be discussed in following sections. The pressure equation is solved using a B-Conjugate Gradient (BiCGSTAB) method (Zhu et al., 2017).

2.1.2 Structural Solver

This work examines both two-dimensional (2D) and three-dimensional (3D) systems which have one-dimensional (1D) filaments, and two-dimensional (2D) membranes respectively. In principle the solution procedure is very similar for the 1D and 2D structural solvers. However, there are sufficiently significant differences in the calculation, especially in handling of the tension force in the membrane. Therefore, the 2D and 3D methodologies will be presented separately. In general,

both solvers use finite differencing to solve their governing equations. This method was chosen over the more conventional finite element methods because the bodies in question always had a uniform, and typically rectangular shape. Finite-differencing methods have the benefit that they are generally far simpler to implement than finite-element methods.

2.1.2.1 2D Structural Solver

In the 2D flow configuration with a 1D filament, the structure is defined using a 1D Lagrangian curvilinear grid whose grid points are defined using the coordinate s which represents the path along the filament. The filament is assumed to be massive, zero-thickness, and inextensible with its dynamics governed by:

$$m_s \frac{\partial^2 \mathbf{X}}{\partial t^2} = \frac{\partial}{\partial s}\left(\sigma \frac{\partial \mathbf{X}}{\partial s}\right) - \frac{\partial^2}{\partial s^2}\left(\gamma \frac{\partial^2 \mathbf{X}}{\partial s^2}\right) + m_s \mathbf{g} - \mathbf{F} \tag{2.10}$$

where m_s is the excess mass per unit area, $\mathbf{X}(s,t) = (x,y)$ is the Cartesian coordinates of a point on the filament at a given time, σ is the tension in the membrane, γ is the bending rigidity, $\mathbf{g}$ is the acceleration due to gravity and $\mathbf{F}$ is the coupling force associated with the penalty forcing method which will be discussed in a following section. To create a non-dimensional form of this equation, we first identify the two key non-dimensional parameters for the structural system; the mass ratio M* and the reduced velocity U*:

$$M^* = \frac{\rho_f L}{m_s}, \qquad U^* = UL\sqrt{\frac{m_s}{k_b}} \tag{2.11}$$

Where ρ_f is the fluid density, L is the characteristic length of the system (typically the filament length), m_s is the excess mass of the filament defined as $m_s = m_m - \rho_f h_s$ where m_m is the filament mass and h_s is the filament thickness. U is the characteristic fluid velocity and k_b is the bending rigidity. A nondimensional expression for the bending rigidity can then be developed as:

$$K_b = \frac{k_b}{\rho_m U^2 L^3} = \frac{Eh^2}{12\left(1-\nu^2\right)\rho_m U^2 L^3} \tag{2.12}$$

Where E is the Young's Modulus of the filament, h is the thickness, and ν is the Poisson's ratio for the filament. The governing equation for the position of the filament can then be nondimensionalized with $\rho_m U^2$ for the term containing the tension σ, $\rho_m U^2 L^2$ for the term containing the bending rigidity γ, and $\rho_m U^2 / L^2$ for the term containing the Lagrangian coupling force; resulting in the following equation:

$$\frac{\partial^2 \mathbf{X}}{\partial t^2} = \frac{\partial}{\partial s}\left(\sigma \frac{\partial \mathbf{X}}{\partial s}\right) - \frac{\partial^2}{\partial s^2}\left(\frac{M^*}{U^{*2}} \frac{\partial^2 \mathbf{X}}{\partial s^2}\right) + Fr \frac{\mathbf{g}}{\mathrm{g}} - \mathbf{F} \tag{2.13}$$

Where Fr is the Froude number defined as $Fr = \mathrm{g}L/U^2$, and $\mathrm{g} = |\mathbf{g}|$. Note that for convenience the dimensionless quantities use the same notation as their dimensional counterparts. Also, in many of the problems explored in the following chapters, gravity is assumed to play an insignificant role, and thus Fr is very small and assumed to be 0. To calculate the tension σ we use the assumption that the filament is inextensible which follows the work of Tornberg & Shelley (2004) and Huang & Sung (2007) and is expressed as:

$$\frac{d}{dt}\left|\frac{\partial \mathbf{X}}{\partial s}\right| = 0 \tag{2.14}$$

This constraint is then used to derive an equation for σ by first taking a derivative of Eqn. (2.13) and then taking the inner product with $\partial \mathbf{X}/\partial s$ (Shoele & Zhu, 2012). This leads to the following Poisson equation for σ:

$$\frac{\partial \mathbf{X}}{\partial s} \cdot \frac{\partial^2}{\partial s^2}\left(\sigma \frac{\partial \mathbf{X}}{\partial s}\right) = \frac{1}{2}\frac{\partial^2}{\partial t^2}\left(\frac{\partial \mathbf{X}}{\partial s} \cdot \frac{\partial \mathbf{X}}{\partial s}\right) - \frac{\partial^2 \mathbf{X}}{\partial t \partial s} \cdot \frac{\partial^2 \mathbf{X}}{\partial t \partial s} - \frac{\partial \mathbf{X}}{\partial s} \cdot \frac{\partial}{\partial s}\left(F_b + F\right) \tag{2.15}$$

$$F_b = -\frac{\partial^2}{\partial s^2}\left(\frac{M^*}{U^{*2}}\frac{\partial^2 \mathbf{X}}{\partial s^2}\right) \tag{2.16}$$

Where F_b is the bending force. Free end boundary conditions are defined as:

$$\sigma = 0 \ , \ \frac{\partial^2 \mathbf{X}}{\partial s^2} = (0,0) , \ \frac{\partial^3 \mathbf{X}}{\partial s^3} = (0,0) \tag{2.17}$$

All fixed end boundary conditions used in this work are clamped boundary conditions defined as:

$$\mathbf{X} = \mathbf{X}_0 , \ \frac{\partial^2 \mathbf{X}}{\partial s^2} = (-1,0) \tag{2.18}$$

To numerically solve these governing equations, the filament is discretized with staggered grids where the tension is defined at the centroid of the element and all other variables are defined at the nodes.

2.1.2.2 3D Structural Solver

The structural solver for the 3D system with a 2D membrane is in many ways similar to that of the 2D system with a 1D filament. The major differences lie in the expression for the governing equation as it must be solved in two directions. The structure is defined using a curvilinear Lagrangian grid with (s_1, s_2) coordinates which represents the path length along the membrane which can be understood to be the streamwise and spanwise directions if the membrane is stationary and undeflected. The membrane is assumed to be massive, zero-thickness, and elastic. Its dynamics are subject to the following governing equation for its position $\mathbf{X}$:

$$m_s \frac{\partial^2 \mathbf{X}}{\partial t^2} = \sum_{i,j=1}^{2}\left[\frac{\partial}{\partial s_i}\left(\sigma_{ij}\frac{\partial \mathbf{X}}{\partial s_j}\right) - \frac{\partial^2}{\partial s_i \partial s_j}\left(\delta_{ij}\frac{\partial^2 \mathbf{X}}{\partial s_i \partial s_j}\right)\right] + m_s \mathbf{g} - \mathbf{F} \tag{2.19}$$

where m_s is the excess mass per unit area, $\mathbf{X}(s_1, s_2, t) = (x, y, z)$ is the Cartesian coordinates of a point on the membrane at a given time, δ is the bending and twisting coefficients, **g** is gravity, and **F** is the coupling force associated with the penalty method. σ is the in-plane tension in the membrane and is defined as:

$$\sigma_{ij} = 4c_{ij}^{T}\left(\frac{\partial \mathbf{X}}{\partial s_i}\cdot\frac{\partial \mathbf{X}}{\partial s_j} - \frac{\partial \bar{\mathbf{X}}}{\partial s_i}\cdot\frac{\partial \bar{\mathbf{X}}}{\partial s_j}\right) \tag{2.20}$$

Where c_{ij}^{T} are the tension coefficients for the membrane, specifically c_{11} in the s_1 direction and c_{22} in the s_2 direction. The dynamics equation, equation (2.19), can be nondimensionalized to create the following:

$$\frac{\partial^2 \mathbf{X}}{\partial t^2} = \sum_{i,j=1}^{2}\left[\frac{\partial}{\partial s_i}\left(\sigma_{ij}\frac{\partial \mathbf{X}}{\partial s_j}\right) - \frac{\partial^2}{\partial s_i \partial s_j}\left(\frac{M^*}{U^{*2}}\frac{\partial^2 \mathbf{X}}{\partial s_i \partial s_j}\right)\right] + Fr\frac{\mathbf{g}}{\mathrm{g}} - \mathbf{F} \tag{2.21}$$

Note that just as before, the same variable names have been used for the nondimensional values for convenience. In all of the 3D studies in this work, gravity is negligible and thus Fr=0. For the 3D membrane, we do not use an inextensibility constraint, and instead the expression for the in-plane tension is discretized and calculated along with the other terms. At the fixed leading edge, a simply supported boundary condition is used:

$$\mathbf{X} = (0, 0, s_2), \quad \frac{\partial^2 \mathbf{X}}{\partial s_1^2} = 0 \text{ at } s_1 = 0 \tag{2.22}$$

At the free boundaries (the trailing edge and the side edges) the boundary conditions are:

$$\frac{\partial^2 \mathbf{X}}{\partial s_1^2} = 0, \quad \frac{\partial^3 \mathbf{X}}{\partial s_1^3} = 0 \text{ at } s_1 = S_1 \tag{2.23}$$

$$\frac{\partial^2 \mathbf{X}}{\partial s_2^2} = 0, \quad \frac{\partial^3 \mathbf{X}}{\partial s_2^3} = 0 \text{ at } s_1 = 0 \text{ or } S_2 \tag{2.24}$$

and $\sigma_{ij} = 0$ on the free edges.

2.1.3 Sharp Interface Immersed Boundary Method

For stationary rigid bodies, or any bodies that are subject to simple prescribed motion, we use a sharp-interface immersed boundary method. This method is the cornerstone of the in-house code ViCar3D and has been described in detail in a number of publications including (Mittal et al., 2008; Seo & Mittal, 2011). In the work presented in this thesis, this method is used in a number of cases from non-rectangular channel walls, to immersed cylinders. As it is not the focus of the research presented herein, only an abbreviated description of how it works will be discussed.

In this method, the goal is to apply boundary conditions to the fluid such that no-slip, no-penetration is prescribed exactly at the location of the desired surface, regardless of the grid being used. To accomplish this, the body is represented using a closed triangular mesh. Then, the fluid cells are tagged as either inside the body or outside the body, with a further specification for those cells that are inside the body but have no additional cells between them and the surface, called ghost cells. Quickly tagging the points in this manner is complicated, but in general it is accomplished by taking the dot product between a vector extending from a given surface triangular element and a fluid cell center, with the vector defining the normal of that surface element. Depending on the sign of that dot product the cell can be determined if it is inside or outside the body as can be seen in FIG. 2.1 (a) from the Mittal et. al., (2008). The procedure for finding which of the internal points are closest to the boundary is also complicated, but it is noted that this procedure need only happen once for stationary bodies, and while it does happen at every time-step for moving bodies, the body CFL number requires that the body move a finite jump per time step, meaning the points that need to be re-searched to determine if they are ghost cells is limited to those just around the body in the direction that the body was last moving. Furthermore, points that were inside the body in the

previous timestep but are newly in the fluid in the current time step are called freshcells and must be identified and assigned appropriate velocities and pressure as well.

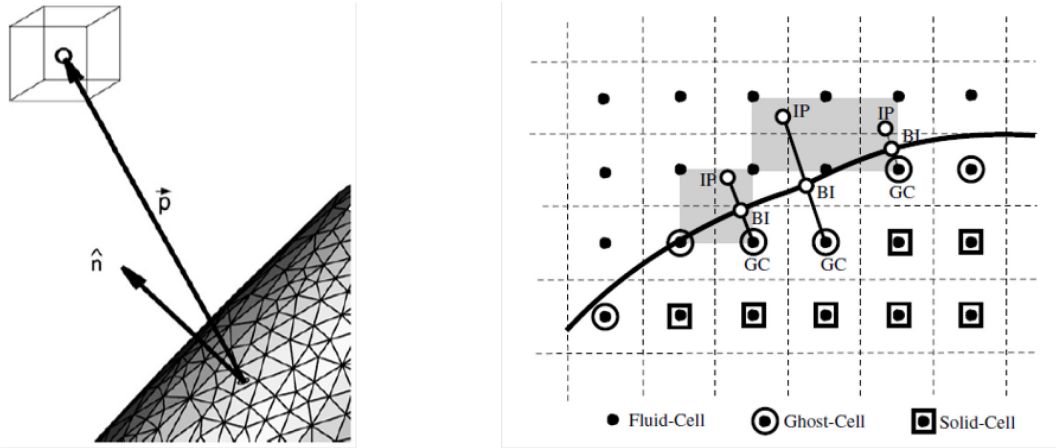

(a) (b)

FIG. 2.1 – Figures from Mittal, et. al., 2008 showing (a) the method for identifying points inside or outside a surface, and (b) the method for calculating the proper velocity for the ghost cell points to satisfy the sharp-interface boundary conditions.

Identification of the ghost cells is key to this method, as that is where the boundary conditions for the surface are applied. The notion is that there must be some value for the velocity at a ghost cell such that the velocity at the interface (between that ghost cell and other neighboring fluid cells) is exactly zero. This is accomplished by first extending a line segment from the ghost cell to the boundary such that the length of the line is minimized and then finding the point on the boundary closest to the ghost cell which is called the body intercept point (BI). Then, another line segment is drawn from BI into the fluid that is colinear with the line GC-BI and is the same length as GC-BI. The end of this segment is called the image point IP and likely falls somewhere between fluid cell centers. At this point, we know that the velocities must be zero at BI and we are looking for velocities at GC that would satisfy this. To find this velocity we can then use linear interpolation using the values at BI and IP to estimate GC. This requires the variable in question be defined at IP

which is accomplished via trilinear interpolation. Then, the calculated values of GC act as a field boundary condition for the given equation being solved with this method.

2.1.4 Fluid Structure Interaction and the Penalty Method

In the case of flexible bodies whose motion is subject to fluid-structure interaction forces, we use a penalty method approach which represents the solid boundary using a set of smoothened delta forcing functions. These forces act to enforce the boundary conditions in a small region around the surface of the body, defined by the size and shape of delta functions being used. The entire coupling procedure between the fluid to the structure hinges on the proper calculation of those forces. This method offers both advantages and disadvantages over a sharp interface method. The advantages of this penalty method mostly involve simplification of the coupling between the fluid and structural solvers. In the penalty method, the boundary conditions from the structure on the fluid don't actually act as boundary conditions. Instead they act as a source term in the momentum equation. The benefit of this is that no special treatment is required at or near the boundary. This bypasses significant complexity and some computational cost associated with the calculation of sharp interface boundary conditions.

Furthermore, the coupling procedure is far simpler with a penalty method. There are multiple available options for fluid-structure coupling. In principle the coupling for large amplitude deformations like flapping flags should be two-way, meaning the two solutions are interdependent at every time step, because the dynamics of the system are typically similarly dependent on both the fluid and the structure. In the simplest FSI implementations, this requirement is ignored and only one-way coupling is used. This trivializes the coupling issue as the solutions need only be solved sequentially, but comes at the expense of both fidelity and stability for the overall system. On the opposite end of the spectrum, the two solutions can be totally coupled. In practice in a code such as ours, this would manifest as co-iterations between the structural and fluid solvers at every

time step. Here each iteration of the solver would generate corrections to the boundary conditions for the other solver, prompting a new iteration of both solvers until the two solutions agreed to some tolerance. The stability and fidelity of this method is very strong, however it comes at the cost of significant computational expense, as each coupling iteration would multiply the overall computational cost. This means that if the solvers needed five iterations per time step to converge to some tolerance, the total computation time could be five times longer. Whereas, the simplicity of the of the penalty method means only one iteration is needed per solver, per time step.

However, the penalty method also comes with certain disadvantages which must be considered in order to use it effectively. First, it suffers from all the problems of any diffuse-interface immersed boundary method. The boundary does not identically satisfy no-slip, no-penetration, but instead these features are a function of the resolution. In general, slip and penetration are always present, but are minimized with sufficient resolution. Also, the boundary is not specifically defined, but instead acts as a narrow, but still fuzzy, field on the fluid which can change the dynamics if the resolution is not sufficient. These issues are problematic; however, they can be directly addressed to some degree via high resolution simulations, which was the solution taken in this thesis. While the increased resolution requirements are an acceptable cost, it has the side effect that there are no "cheap" preliminary simulations possible. That is to say that even simply testing ideas often requires significant computational cost as there is often no meaningful low-resolution version of a simulation.

These resolution requirements are an inconvenience. The true costs of the penalty method lie in significant stability constraints which leads to a very small time-step requirement. As will be described below, the calculation of the penalty force involves very large tunable coupling parameters which in some sense describe the stiffness of springs and dampers which "pull" the solutions of the fluid and structural solvers together. The very large magnitude of these penalty parameters leads to a "stiff" set of equations. Stable integration of these stiff equations results in

CFL numbers on the order of 10^{-2} or even 10^{-3}. Notwithstanding these shortcomings, the penalty method was chosen for its simplicity.

2.1.4.1 Penalty Method Coupling

In the penalty immersed boundary method, instead of an exchange of boundary conditions between the fluid and structural solvers, the two systems communicate via a common shared force field called the penalty force. In principle this force represents the required modifications for each solution to be in better agreement. This is not the same as the forces that the fluid is exerting on the structure or vice versa. This method is better conceptualized by imagining a series of springs and dampers connecting the fluid and the structure.

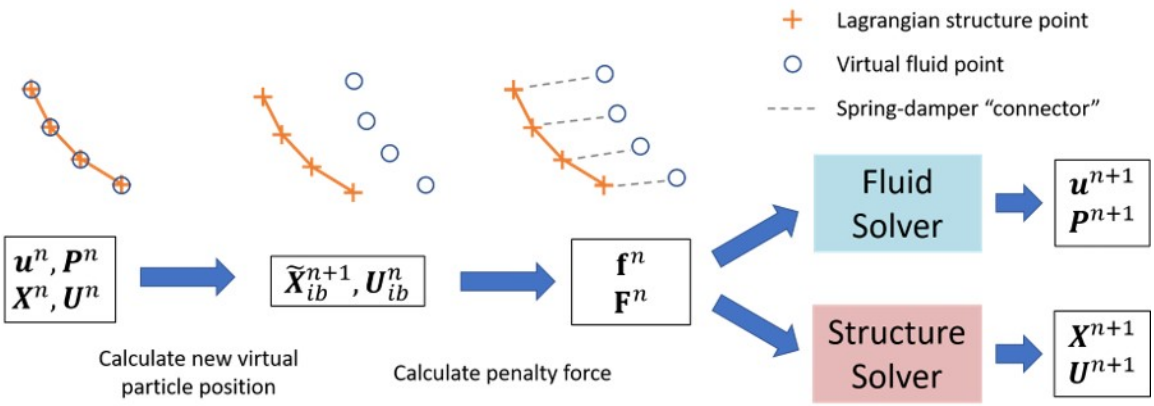

FIG. 2.2 – Flowchart type diagram describing the penalty method procedure.

FIG. 2.2 shows a flowchart diagram of the penalty method procedure. To implement this penalty method, two sets of structural points are tracked. The first set of points are the Lagrangian structure points on which the structural governing equations are solved. These points are assumed to not directly interact with the fluid, but instead interact via the second set of points. The second set of points are virtual, massless, fluid-following points which are assumed to move with the local fluid velocity. The two sets of points are connected using virtual springs and dampers. One side of each of these spring-damper connectors acts as a force on each Lagrangian node of the structural mesh. The other side of the spring interacts with the fluid. However, while the virtual springs and

dampers gain there force via connections to the virtual fluid following points, the delta functions used to force the fluid are actually evaluated at the locations of the Lagrangian structure points, so that the fluid and structure coincide spatially.

To begin the procedure, first a method is needed to translate between Eulerian fluid variables and Lagrangian structure variables. This is accomplished using Dirac delta functions. For example, to calculate the Lagrangian fluid velocity $\mathbf{U}(s,t)$ or the Lagrangian scalar concentration (or temperature) $\Gamma(s,t)$ at a given point on the structure grid $\mathbf{X}(s,t)$ we use the following expression:

$$\mathbf{U}(s,t) = \int_{\Omega_f} \mathbf{u}(\mathbf{x},t)\delta\left[\mathbf{x}-\mathbf{X}(s,t)\right]d\mathbf{x} \tag{2.25}$$

$$\Gamma(s,t) = \int_{\Omega_f} \phi(\mathbf{x},t)\delta\left[\mathbf{x}-\mathbf{X}(s,t)\right]d\mathbf{x} \tag{2.26}$$

where Ω_f is the fluid domain. A similar approach is used to translate from variables defined on the structural coordinate system back to the fluid coordinate system according to:

$$\mathbf{u}(\mathbf{x},t) = \int_{\Omega_s} \mathbf{U}(s,t)\delta\left[\mathbf{x}-\mathbf{X}(s,t)\right]ds \tag{2.27}$$

$$\mathbf{f}(\mathbf{x},t) = \int_{\Omega_s} \mathbf{F}(s,t)\delta\left[\mathbf{x}-\mathbf{X}(s,t)\right]ds \tag{2.28}$$

$$\mathbf{q}(\mathbf{x},t) = \int_{\Omega_s} \mathbf{Q}(s,t)\delta\left[\mathbf{x}-\mathbf{X}(s,t)\right]ds \tag{2.29}$$

where **f** is the coupling force density on the fluid, **F** is the coupling force density on the structure, **q** is the coupling source term for the scalar field in the fluid coordinate system, and **Q** is the coupling source term in the Lagrangian coordinate system. As noted above, these delta functions are centered at the Lagrangian structure points. The first step is to advect the virtual fluid following points according to the local fluid velocity. The virtual points' position and velocity are

denoted as $\mathbf{X}_{ib}(s,t)$ and $\mathbf{U}_{ib}(s,t)$ respectively. The velocity of the virtual point at the current time step is first calculated using the delta function in Eqn. (2.25) to create $\mathbf{U}_{ib}^{n}(s,t)$. Then an estimation of the new position of for the virtual point called $\tilde{\mathbf{X}}_{ib}^{n+1}$ is calculated:

$$\tilde{\mathbf{X}}_{ib}^{n+1} = \mathbf{X}_{ib}^{n} + \mathbf{U}_{ib}^{n}\Delta t \tag{2.30}$$

The velocity of the virtual point at the new estimated position $\tilde{\mathbf{X}}_{ib}^{n+1}$ is calculated using the delta function approach as:

$$\tilde{\mathbf{U}}_{ib}^{n+1}(s,t) = \int_{\Omega_f} \mathbf{u}(\mathbf{x},t)\,\delta\left[\mathbf{x} - \tilde{\mathbf{X}}_{ib}^{n+1}(s,t)\right] d\mathbf{x} \tag{2.31}$$

These values represent estimations of the structure's position at time step n+1. Using estimated points for the penalty method coupling force leads to greater stability than would be had by a fully explicit scheme. To calculate the coupling force, spring-damper connectors are imagined between the estimated virtual fluid following points and the structure. This manifests as the following equation for the Lagrangian coupling force:

$$\mathbf{F}(s,t) = \rho U\left(\frac{\kappa_1 U}{L}\int_0^t \left[\mathbf{U}_{ib}^{n}(s,t) - \tilde{\mathbf{U}}_{ib}^{n+1}(s,t)\right] d\tau + \kappa_2\left[\mathbf{U}_{ib}^{n}(s,t) - \tilde{\mathbf{U}}_{ib}^{n+1}(s,t)\right]\right) \tag{2.32}$$

where κ_1 and κ_2 are large negative tunable penalty parameters. A similar approach is taken to calculate the forcing for the scalar field:

$$\mathbf{Q}(s,t) = \rho U\left(\frac{\kappa_1 U}{L}\int_0^t \left[\Gamma_{ib}^{n}(s,t) - \tilde{\Gamma}_{ib}^{n+1}(s,t)\right] d\tau + \kappa_2\left[\Gamma_{ib}^{n}(s,t) - \tilde{\Gamma}_{ib}^{n+1}(s,t)\right]\right) \tag{2.33}$$

These coupling forces can then be applied to the fluid at the present location of the membrane (not at the estimated position) using the delta functions as shown in Eqn. (2.28). In the literature, considerable interest has been given to the calculation of the coupling force and in the specification and tuning of the penalty parameters. The formulation used here is very similar to the formulation

proposed by Goldstein et. al. (1993). A modification to this approach was used in some of the studies in this work:

$$\mathbf{F}(s,t)=\kappa_p \frac{\rho U^2}{L}\left(\left[\mathbf{X}_{ib}^{n}(s,t)-\tilde{\mathbf{X}}_{ib}^{n+1}(s,t)\right]-\Delta t\left[\mathbf{U}_{ib}^{n}(s,t)-\tilde{\mathbf{U}}_{ib}^{n+1}(s,t)\right]\right) \tag{2.34}$$

which can be shown as a special case of the formulation in Eqn. (2.32). This formulation has the benefit in that it relates the two penalty parameters according to $\kappa_1=\kappa_p$ and $\kappa_2=\kappa_p\Delta t$, which has been shown to be a beneficial relationship between the coefficients for the integral and proportional terms (Huang & Sung, 2009). This work by Huang & Sung also examined in detail the sensitivity of this type of solver to the penalty parameter choices; both in terms of stability and iterative convergence rate; as well as in terms of fidelity in canonical problems. Their work provided a starting point for the tuning of the parameters used throughout this work, and provided several key insights which were used in this study to tune our penalty parameters.

First, they confirmed that the time step size Δt is linked to the penalty parameters. In general, larger penalty parameters require smaller Δt. This is because in essence, larger penalty parameters mean stiffer coupling between the fluid and structure solutions, and stiffening the problem in principle should decrease its stability to time step size. If large steps are taken, the structure points and the virtual points can move farther apart, and the stiffness of the couplers will generate very large forces. It should be noted here that larger penalty parameters are associated with higher fidelity simulations, so in practice very small time steps are required for this type of penalty method. Second, they found that in the Goldstein type formulation, solutions for canonical problems were no longer sensitive to the first penalty parameter κ_2 if it was larger than O(10^4), and the second penalty parameter κ_2 should be only large enough to avoid oscillations at the onset of a simulation, but increasing it further does not significantly impact the system.

Building on their analysis, we conducted our own verification studies to better understand the sensitivity of our system to the penalty parameters and to ultimately choose proper parameters. Prior to each study presented in this paper, we conducted verification and sensitivity tests to pick our penalty parameters for a given problem. In general, we used a baseline setting of $\kappa_1 = -10^5$, $\kappa_2 = -150$, and $\Delta t = 10^{-4}$.

Finally, a special treatment was used for cases where there was a high probability of contact between flapping filaments or flags and any other bodies; be they the domain boundaries (in the case of channel walls), other rigid bodies in the flow, or other flexible filaments or membranes. According to lubrication theory, objects in a flow should not actually contact each other. In principle the pressure should be able to physically model the behavior during contact, however in practice this would require very high resolution in the space between the bodies. This would be far higher resolution than what is needed to model the behavior of the rest of the system, and far higher than what is practical. With poorer resolution than this requirement, the membranes will still feel forces due to the other body, however these forces will not ramp up quickly enough and the membranes are likely to pass through each other due to their inertia. To combat this, artificial contact forces are generated using Dirac delta functions according to:

$$\mathbf{F}_c(s,t) = \kappa_c \int_{S_w} \delta\left[\mathbf{x}(s') - \mathbf{X}(s,t)\right] \frac{\mathbf{x}(s') - \mathbf{X}(s,t)}{\left|\mathbf{x}(s') - \mathbf{X}(s,t)\right|} ds' \tag{2.35}$$

where κ_c is a tunable contact penalty parameter, and the superscript ‘ denotes the other body.

2.1.5 Scalar Transport

Several of the studies discussed in this work involve transport of a passive scalar. In the forced convection heat transfer section that scalar is temperature, and in the mixing sections that scalar

could be any number of relevant species depending on the particular application. The passive scalar (denoted generically by ϕ) is governed by an advection-diffusion equation according to:

$$\frac{\partial \phi}{\partial t} - \mathbf{u} \cdot \nabla \phi = D \nabla^2 \phi + \mathbf{q} \tag{2.36}$$

where D is the diffusion coefficient and $\mathbf{q}$ represents any sources or sinks of scalar. In the case of the penalty method, the influence of the membrane or filament on the scalar field is communicated as sources and sinks. This equation can be written in nondimensional form according to:

$$\frac{\partial \phi}{\partial t} - \mathbf{u} \cdot \nabla \phi = \frac{1}{\mathrm{Re} \cdot \mathrm{Sc}} \nabla^2 \phi + \mathbf{q} \tag{2.37}$$

where Sc is the Schmidt number defined as $\mathrm{Sc} = \nu / D$ where ν is the kinematic viscosity of the fluid. Often the Peclet number is introduced as $\mathrm{Pe} = \mathrm{Re} \cdot \mathrm{Sc}$. In the special case of temperature, Sc is typically called the Prandtl number and is defined as $\mathrm{Pr} = \frac{\nu}{\alpha} = \frac{\mu / \rho}{k / (\rho c_p)} = \frac{c_p \mu}{k}$ where α is the thermal diffusivity, k is the thermal conductivity, and c_p is the heat capacity. The scalar is defined on the fluid cells and is solved at each time step. The convective term in Eqn. (2.37) is discretized using the SHARP scheme (Simple High Accuracy Resolution Program)(Leonard, 1988). This is used because it is well suited for cases with sharp gradients which can often happen in passive scalar fields. The diffusive term is discretized using central differencing.

2.2 Wind Tunnel Validation and the Hanging Banner

The various components of the solver discussed above have been verified and validated in many published studies. This includes the FSI solver, especially true for the 2D variant which was validated directly against canonical problems in Shoele & Mittal (2014) (Shoele & Mittal, 2014). More generally, throughout the community there exist a wide variety of FSI simulation techniques,

including body fitted approaches, immersed boundary approaches of various flavors, and monolithic finite element approaches. These various methods offer different benefits but also leads to different challenges. Even without the complex challenges that often accompany FSI solvers, validation and benchmarking is always required to ensure fidelity of any computational simulation technique.

Ideally, the FSI community should have canonical, shared validation studies which are supported by experimental studies but there are not many experimental FSI studies that are well-suited for validation (Dou et al., 2018). In the absence of these experiments, cross-code benchmarking has become the norm in this arena and the simulations of Turek & Hron (2006) for the configuration shown in FIG. 2.3 have become a popular case for such benchmarking. However, while this configuration is sufficient for 2D FSI cases, it is not sufficient to adequately test a 3D FSI code, or perhaps even a 2D FSI code involving complex deformations or filaments which are aligned normal to the incoming flow. This is because the Turek & Hron configuration leads to stationary, relative low amplitude oscillations which involve instantaneous filament positions which are generally aligned with the local flow velocities.

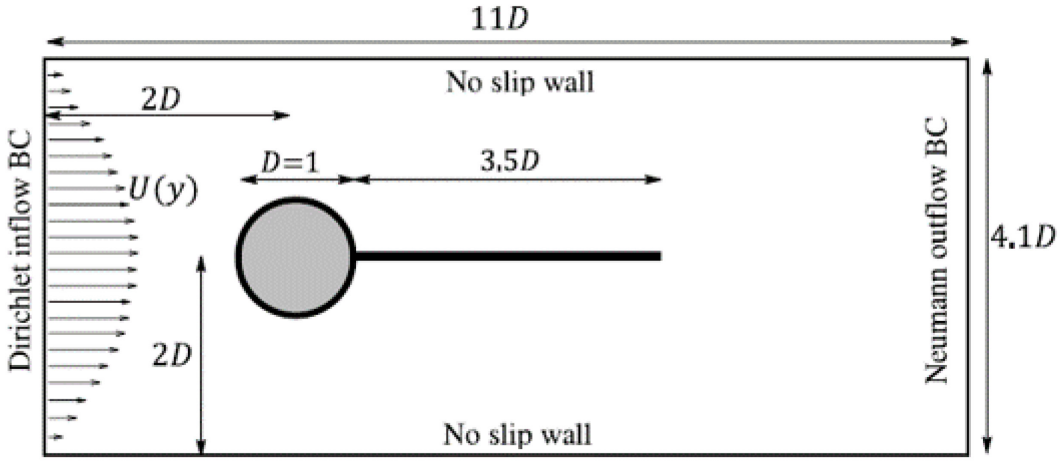

FIG. 2.3 – Canonical 2D FSI validation configuration from Turek & Hron (2006) (Turek & Hron, 2006)

An attempt was made here to address this unmet need for a canonical validation study for 3D FSI codes. We first identified a number of criteria for a potential FSI validation experiment. From the perspective of a computational fluid dynamicist, the following are the desirable features of a FIF validation experiment:

a) The configuration should be "canonical," i.e. relatively simple, with a limited set of parameters, and yet, capable of exhibiting a wide range of physical phenomena.

b) The FIF phenomena should occur over a broad range of Reynolds numbers, ranging from low O(1000) to >O(10^5) so as to allow validation of DNS, LES and RANS methodologies.

c) The configuration should generate considerable three-dimensional effects, yet be reducible to a nominally two-dimensional configuration to enable the deployment of "cheap" 2D simulations.

d) The material properties of the fluttering element, and the boundary conditions for the flow as well as the fluttering element, should be defined and cataloged in a precise manner.

e) Experiments should measure a sufficient set of quantities associated with both the fluttering element (frequency, mode shapes, etc.) as well as the flow so as to enable comprehensive validation.

2.2.1 Hanging Banner Configuration

Once these criteria were identified we considered various configurations to identify a simple system that might fit the above criteria. We performed a detailed literature survey on the existing experimental FIF studies involving highly flexible membrane like structures (Dou et al., 2018). While many of these experiments presented high quality data, and could be used for validation from a statistical perspective, none met all the criteria we described above. We decided on a new canonical configuration we call a "hanging banner" that we believe is well suited for the validation of FIF simulations.

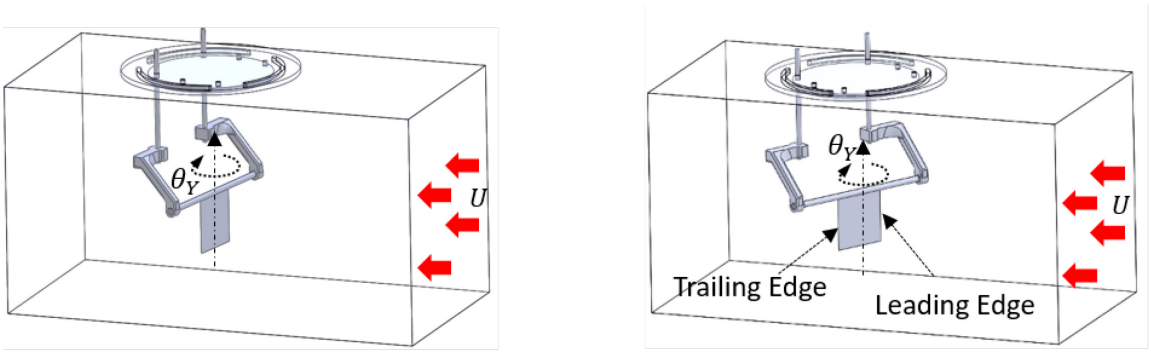

a) $\theta_y = 0°$ a) $\theta_y = 45°$

FIG. 2.4 – Schematic view of a hanging banner configuration. These images include the apparatus to hold the membrane in a wind tunnel test section, however the key features are the membrane and the set angle of the horizontal support: θ_y

FIG. 2.4 shows a schematic view of the hanging banner. This configuration consists of a rectangular elastic membrane that is suspended down from a horizontal support into a parallel, uniform flow. The are several key parameters of the system. In addition to the material parameters of the membrane M* and U*, the other key parameters are the Reynolds number, the membrane aspect-ratio, and the yaw angle of the membrane. The yaw angle is called θ_y in FIG. 2.4 and is the angle the fixed horizontal support makes with a plane normal to the incoming flow. We believe this configuration offers a number of advantages and is consistent with the five requirements set out above. It is a simple system; canonically the only required elements are the membrane and its orientation to a uniform flow. Also, experimental evidence which will be briefly described in a later section show that it exhibits a rich and wide range of behaviors at a variety of Re, M*, and U*.

Finally, the parameter θ_y allows the system to develop 3D behavior which is related directly to an adjustable parameter of the system. At $\theta_y = 0^\circ$ the system should behave in a quasi-2D manner and can be used to validate 2D simulations which would be used for more complex flows than what can be validated by the Turek and Hron case, such as flows not aligned with the filament. As θ_y is increased, the behavior should change in a dramatic but predictable manner. We have studied this

problem experimentally in a low Reynolds number wind tunnel which was built for this study and part of this dissertation research. There we observed a wide variety of 2D as well as 3D flutter dynamics that are quite sensitive to the yaw angle. Additionally, preliminary FSI simulations of this configuration using our immersed boundary solver were also performed. At present this provides a qualitative proof of concept of this idea, with plans to continue the validation of the solver using this method.

2.2.2 Wind Tunnel Design, Manufacture, and Testing

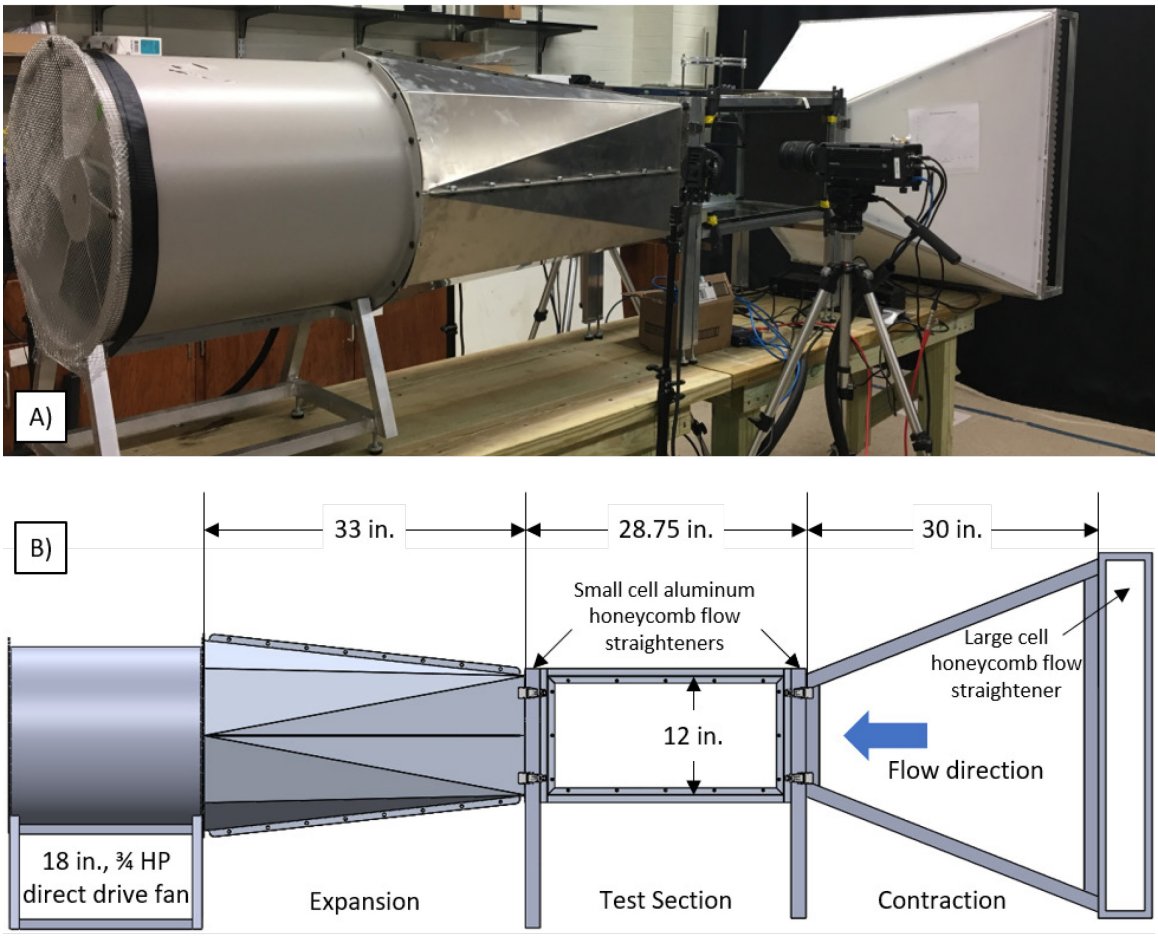

FIG. 2.5 – A) Picture and B) CAD schematic of a 20 m/s wind tunnel with a 1ftx1ft cross-section which was designed and manufactured in pursuit of the research presented in this thesis.

During the course of the research for this thesis, we designed, manufactured, tested, and operated a low speed wind tunnel. The general specifications are a 1ftx1ft cross-section at the test section, a 20 m/s maximum windspeed, and a modular construction which will allow for future expansion and augmentation. FIG. 2.5 A) shows a picture of the completed wind tunnel outfitted with a high-speed camera in a setup for hanging banner experiments. B) shows a side view of the wind tunnel design from a CAD model. The flow is from right to left, making this a suction type wind tunnel. The contraction has a half angle of 20° and the expansion has a half angle of 5°.

The wind tunnel is composed of three distinct sections: The contraction, the test section, and the expansion + fan sub-assembly. These three sub-assemblies can be easily disconnected using locking draw latches. The contraction section is made of welded 5052 aluminum angle extrusions to which HDPE sheets are riveted. 5052 was chosen as it retains strength after welding without needing to be heat treated, which was not an option given our manufacturing abilities. Foam tape was used to seal the seams between the aluminum rails and the HDPE sheets. The large rectangular section at the inlet of the contraction section holds a large cell, fiberglass honeycomb flow straightener section.

The test section is also made of welded aluminum square tube with thin wall aluminum angle pieces riveted in place to support the removable acrylic windows. The acrylic windows are outfitted with low profile press nuts to simplify the removal of the windows to access the experiment. The notion behind the operation of this wind tunnel is that the acrylic windows are replaceable depending on the needs of a given experiment. A user need only to laser cut a custom profile for their particular experiment onto a 2'x1' acrylic window blank, install their hardware onto the new window, and simply install the window back into the wind tunnel. Because the windows may need to bear the load of the experimental apparatus, they were chosen to be 3/8" thick with the option to go as thick as 3/4". Additionally, experimental apparatuses which need to be kept rigid, or which need to support more weight than is practical for the acrylic windows, are expected to clamp onto

the aluminum frame rails. Foam tape is used to seal and seat the interface between the windows and the aluminum frame. At each end of the test section is a welded aluminum mating frame which interfaces with identical aluminum mating frames attached to the contraction and expansion sections. Within these frames, small cell aluminum honeycomb flow straighteners are mounted.

The design and manufacture of the expansion section required a different approach from the aluminum frame with plastic panels approach used in the other sections. This is because the fan that was ultimately chosen to drive this wind tunnel has a circular cross-section, while the test section was chosen to have a square cross-section. Thus, a drafted section was required to transition between these cross-sections. The manufacturing requirements to fabricate such a drafted section were unavailable in the manufacture of this wind tunnel, so instead, a modular sheet metal design was chosen.

The expansion is made of four bent sheet metal sections which are bolted together. Instead of drafting from a square to a circle, the sheet metal sections actually draft to a dodecagon, because the fan has a twelve-hole bolt pattern. These sections were manufactured by water jet cutting blanks, and then carefully making several bends using a press-brake to create the final shape. This expansion section is riveted to a welded aluminum mating frame on the test section end, and is bolted to the fan on the fan end. The fan rests on a welded aluminum support frame and the outlet of the fan is covered using a wire mesh grate to protect against prying fingers. Protection against expelled debris in the event of a catastrophic failure of the testing apparatus was deemed unnecessary as the test section has a honeycomb flow straightener at its outlet. A key design constraint for this wind tunnel beyond the wind speed and flow quality was cost and the entire wind-tunnel was fabricated and assembled for a cost of about $1700.

While this wind tunnel was designed for the hanging banner validation experiments, more generally this wind tunnel was designed as a workhorse to potentially use for a variety of aerodynamic experiments involving fluid structure interactions. As such, careful calibration and

analysis was performed of the wind tunnel itself to identify its flow speed range and to examine the turbulent statistics within the channel. During said testing a number of modifications were made to the design to ensure more laminar flow through the test section. These modifications include the honeycomb flow straighteners as well as mounting the entire wind tunnel on modular wooden tables which elevate the inlet off the ground, eliminating an observed asymmetry due to ground effect inflow.

2.2.3 Hanging Banner – Wind Tunnel Experiments

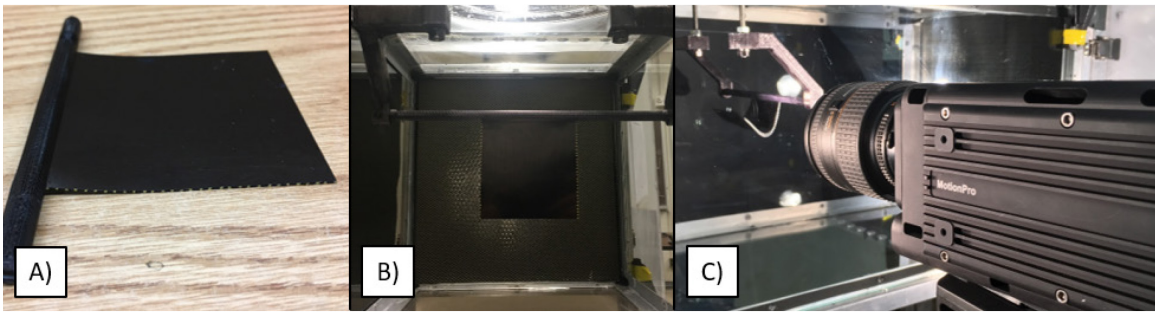

FIG. 2.6 – Images showing the implementation of the hanging banner experiment using the FPCL wind tunnel.

With the wind tunnel complete and functional, a number of experiments for hanging banners were devised. As that work is not central to this thesis, it will only be briefly summarized. Some of those experimental results were used to perform a proof of concept validation with the 2D version of our FSI code. Those data will be described in slightly more detail. FIG. 2.6 shows three images of the experimental setup for the hanging banner configuration. To experimentally investigate the hanging banner, an experimental apparatus was designed to hold a membranous banner (seen in A) in the center of the channel at a fixed yaw angle. This apparatus consisted of two 3D printed arms or “stings” which are attached to a lockable rotating plate mounted in the top window of the test section. To capture the position of the banner as a function of time, the membrane was painted black. Cases were then run with a series of high reflectivity white dots were painted on its edge, as well as cases where the entire edge was painted white.

To characterize the material properties of the membrane, detailed material testing of the purchased material samples were conducted using specialized testing equipment for highly flexible membranes. During the experiment, the test section was illuminated using very bright LED lights, and a high-speed camera recorded the membrane edge. Particle tracking software was then run to transform these movies into time series for each of the dots painted on the membrane edge. A number of studies were run of this system including investigations at different flow speeds (investigating U* or Re dependencies), at different yaw angles, and with different aspect ratios.

2.2.4 Hanging Banner – 2D Simulations and Preliminary Comparisons

To being the investigation into the utility of the hanging banner configuration for validation studies, we examined the 2D hanging banner configuration, theoretically equivalent to the zero yaw angle case. We used the 2D FSI solver described above.

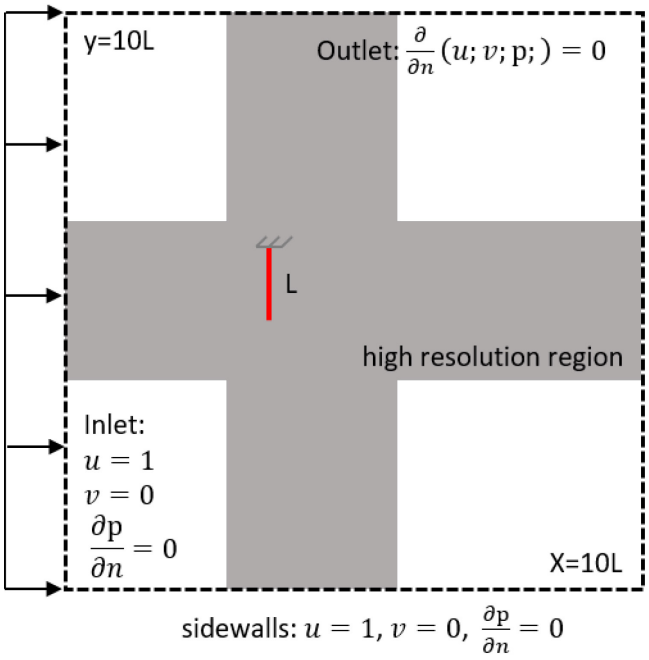

FIG. 2.7 – Schematic of the computational domain for the 2D hanging banner simulations.

FIG. 2.7 shows a schematic of the computational domain. The banner is placed in the center of a large domain. The inlet has a uniform inflow profile of u=1. The sidewalls are given mean flow

boundary conditions, and the outlet uses Neumann outflow boundary conditions. The domain is discretized using expanding meshes. A region around the banner is describe with a high-resolution uniform isotropic grid. The grid is then geometrically stretched in all directions away from the banner, with the downstream wake region having a very small stretching ratio. For these simulations, Re=400 and the structural solver was given a non-zero gravitational parameter as gravity is assumed to play a meaningful role in the dynamics for the banner case. The simulation was conducted at two U* values of 3 and 7 to attempt to compare distinctly different regimes.

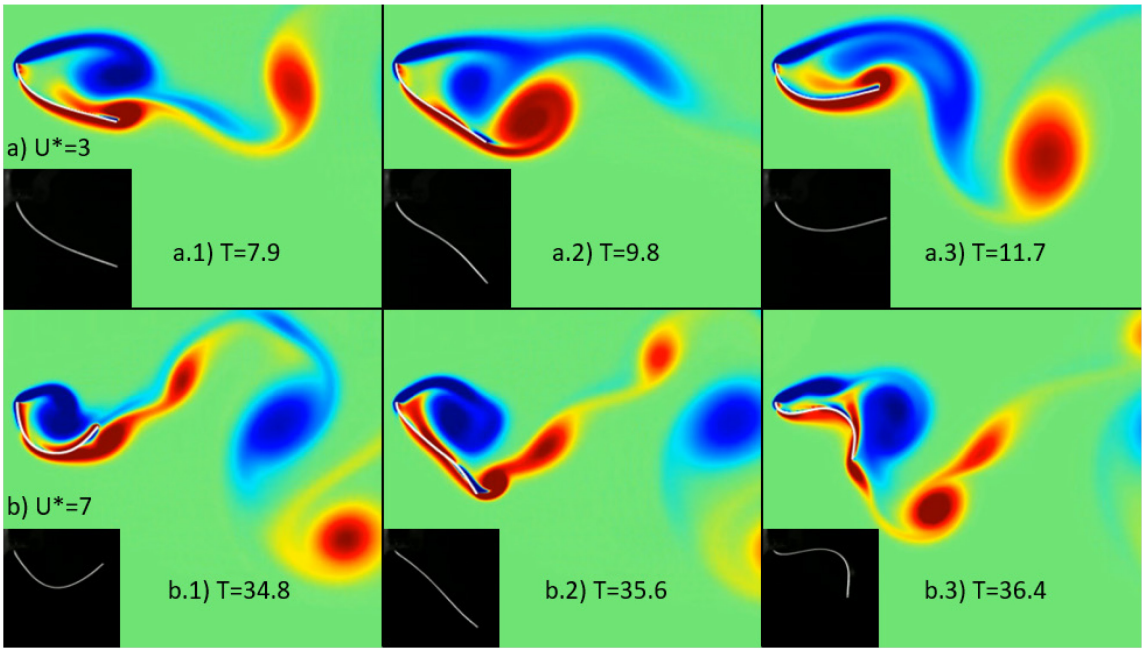

FIG. 2.8 – Snapshots comparing the simulation results (color contour plots) with the experimental results (black and white plots).

FIG. 2.8 shows snapshots comparing the simulations and the experiments. The top row shows U*=3 and the bottom row shows U*=7. The color contours show the vorticity of the flow in the simulation results. These results represent simple, preliminary, qualitative comparison. Nevertheless, even with this simple comparison, a significant aspect of the system was captured by both the simulations and the experiments. In the top row with the stiffer banners, both data show distinctive mode 1 flutter wherein the deformation in the chordwise direction is only bends in one

direction (with perhaps a subtle transition to mode 2 flutter seen in the top middle case for the experimental results). Whereas, in the second set of snapshots, both configurations are clearly showing mode 2 flutter, especially in the final snapshot. This transition is a measure of the stability of the system to the U* parameter, which is a key aspect that should be validated, especially if effects with varying U* are being investigated. Moreover, the transition between these flutter modes seems to have been captured. However, the coarseness of the U* step between these cases means a proper validation would require finer identification of this stability boundary. Finally, qualitatively these cases seem relatively similar. It should be noted that in viewing movies of the results, the experimental results do appear to have marginally more energetic flapping.

Chapter 3

Low Reynolds Number Mixing

As discussed in the introduction, the flow-induced flutter of flapping flags has significant potential as a low Reynolds number mixer. In particular, we examine the inertial microfluidics regime, which is typically Re = O(1-100), because in this regime, Re is sufficiently high to allow the flag to generate vortices which are crucial to its flapping, yet Re is still low enough such that many typical mixing mechanisms are unavailable. Furthermore, this is a regime of interest to many practical applications such as lab-on-chip technologies, μTAS (micro total analysis systems), and other chemical and biological microfluidic devices. To conduct our analysis of these so called "flutter mixers" we will examine the 2D single flag system to understand how flapping filaments behave at these low Re and how their behavior can act as a mixing enhancement device. We then examine a few multi-filament configurations to explore the impact of introducing multiple length scales to the flow. Finally, we examine the 3D flapping membrane as a flutter mixer to first understand 3D flapping at these low Re and to then understand how that behavior translates to mixing enhancement.

3.1 2D Mixing – Single Flag

Our 2D configuration provides a simplified framework to examine many aspects of flutter mixers. One of the challenges of studying flow-induced flutter is the wide array of parameters upon which the system depends. Complicating our analysis further is the fact that many of these

parameters are interdependent, meaning the system is often nonlinear, which means it is not sufficient to perform studies which sweep along only one parameter to capture the systems sensitivity to that parameter. Full studies of the flutter mixer parameter space are impractical no matter what tool is used to investigate them. However, 2D simulations, being considerably computationally less expensive than 3D simulations, provide the opportunity to investigate a broader range of the parameter space, as well as more nuanced studies which examine the counter play between multiple competing effects.

Our 2D studies primarily explore the system as a function of Re. To better understand other interlinked effects, we also examine filaments of various lengths also as a function of Re. This allows us to examine the effects of parameters such as confinement and the reduced velocity U*. Finally, we will examine the effect of varying only the Schmidt number without changing any other parameter. This allows us to examine relative roles of convection and diffusion in the mixing results we observe.

3.1.1 Computational Model

3.1.1.1 Configuration and Governing Equations

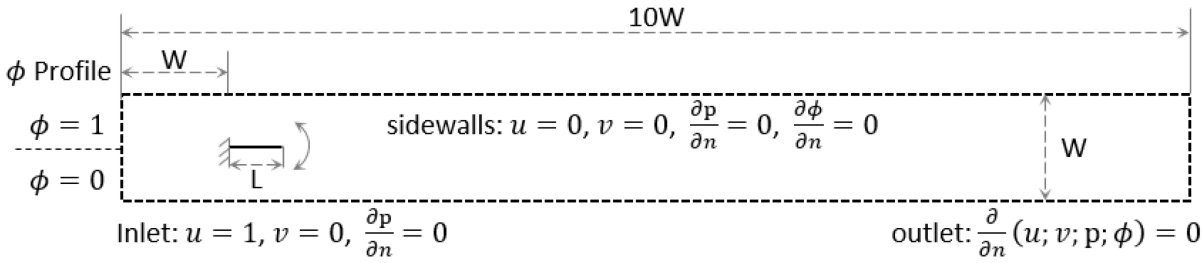

FIG. 3.1 – Schematic diagram of the computational domain (not to scale) showing the geometry and boundary conditions.

As shown in FIG. 3.1, in this study, we investigate the mixing enhancement associated with flow-induced flutter of a flexible membrane in a 2D channel of width W, length $10W$ and with a

mean flow velocity U. The membrane has length L and is placed on the center-line of the channel a distance W downstream of the entrance. This fluid-structure-scalar multiphysics system exhibits two-way coupling between the fluid and structure and one way coupling between the fluid and the scalar. As the governing equations and numerical methods of the solver were described in general in the Numerical Methods section, only a brief overview will be presented here for reference. The typical channel widths at which such flutter mixers could be fabricated and operated ranges from O(100) to O(1000) microns and the continuum approximation and no-slip conditions are acceptable at these scales (Tretheway & Meinhart, 2002). The flow is assumed to be governed by the incompressible Navier-Stokes equations. The membrane, which is assumed to be inextensible, is governed by the Navier equations expressed in terms of the position vector $\mathbf{X}$ and the tension ς of the membrane; and the scalar ϕ is governed by an advection-diffusion equation. The system's governing equations in the non-dimensional form are as follows:

$$\frac{\partial \mathbf{u}}{\partial t} + \nabla \cdot (\mathbf{uu}) = -\nabla p + \frac{1}{\mathrm{Re}} \nabla^2 \mathbf{u} + \mathbf{f} \tag{3.1}$$

$$\nabla \cdot \mathbf{u} = 0 \tag{3.2}$$

$$\frac{\partial \phi}{\partial t} + \mathbf{u} \cdot \nabla \phi = \frac{1}{\mathrm{Re} \cdot \mathrm{Sc}} \nabla^2 \phi \tag{3.3}$$

$$\frac{\partial^2 \mathbf{X}}{\partial t^2} = \frac{\partial}{\partial s}\left(\varsigma \frac{\partial \mathbf{X}}{\partial s} \right) - \frac{\partial^2}{\partial s^2}\left(\frac{M^*}{U^{*2}} \frac{\partial \mathbf{X}}{\partial s} \right) - M^* \mathbf{F} \tag{3.4}$$

$$\frac{\partial \mathbf{X}}{\partial s} \cdot \frac{\partial^2}{\partial s^2}\left(\varsigma \frac{\partial \mathbf{X}}{\partial s} \right) = \frac{1}{2} \frac{\partial^2}{\partial t^2}\left(\frac{\partial \mathbf{X}}{\partial s} \cdot \frac{\partial \mathbf{X}}{\partial s} \right) - \frac{\partial^2 \mathbf{X}}{\partial t \partial s} \cdot \frac{\partial^2 \mathbf{X}}{\partial t \partial s} - \frac{\partial \mathbf{X}}{\partial s} \cdot \frac{\partial}{\partial s}(\mathbf{F}) \tag{3.5}$$

For the fluid governing equations (3.1) and (3.2), $\mathbf{u}$ is the velocity field, t is time, p is pressure, Re is the Reynolds number defined as $\mathrm{Re} = UW/\nu$ where U is the mean inlet velocity, W is the characteristic length given by the width of the channel, and ν is the dynamic viscosity of the

fluid. Furthermore, $\mathbf{f}$ is a forcing function associated with the fluid-structure interaction penalty method which will be discussed in a following section. For the scalar equation (3.3), ϕ is the scalar concentration ranging from 0 to 1, and Sc is the Schmidt number defined as $\mathrm{Sc} = \nu / D$ where D is the mass diffusivity of the scalar. Equations (3.4) and (3.5) govern the position and tension of the membrane. The key non-dimensional parameters governing the structure are the mass ratio M^* and reduced velocity U^*:

$$M^* = \frac{\rho L}{m_s}, \qquad U^* = UL\sqrt{\frac{m_s}{k_b}} \tag{3.6}$$

In the above, k_b is the bending rigidity. m_s is the excess mass per unit length according to $m_s = m_m - \rho_f \mathrm{A}_s$ where m_m is the mass per unit length of the membrane, ρ_f is the density of the fluid, and A_s is the cross-sectional area of the membrane. For the cases studied here, $A_s \to 0$ (the limit of a thin element), so $m_s \sim m_m$. $\mathbf{F}$ is the force density induced by the element on the surrounding fluid associated with the fluid-structure interaction penalty forcing method. Equation (3.5) is a Poisson's equation for the tension, derived as described in Huang et. al. (2007) by applying an inextensibility constraint defined as $(\partial \mathbf{X} / \partial s) \cdot (\partial \mathbf{X} / \partial s) = 1$ to equation (3.4).

3.1.1.2 Parameters and Boundary Conditions

In this study the range of Reynolds numbers based on the channel width W is 10 to 200 and Sc was varied in large increments from 1 to 1000. Three membrane lengths were studied: $L=W/2$, $L=W$, and $L=2W$. Based on prior work on confined flapping membranes (Shoele & Mittal, 2014) M^* and U^* were chosen as 0.5 and 15 respectively for the initial set of simulations so as to generate large amplitude flutter at these Re numbers. Later sections of paper explore flags with different lengths as a way to modulate U^*. The final range of the non-dimensional parameters in the current study is as follows:

Re: 10-200; M^*: 0.25 - 1.0; U^*: 7.5 - 30; L/W: 0.5 - 2.0; Sc: 1 - 1000.

The developing flow in the channel has a uniform inlet boundary condition u(0,y,t)=1, Dirichlet no-slip boundary conditions on the sidewalls, Neumann boundary conditions at the outflow, and an initial value of u(x,y,0)=1 everywhere. The leading-edge of the membrane is fixed and the trailing edge is free, with the corresponding boundary conditions being:

$$\mathbf{X} = \mathbf{X}_0, \ \frac{\partial \mathbf{X}}{\partial s} = [1,0] \qquad \text{at } s = 0 \quad \text{(leading-edge: fixed)} \tag{3.7}$$

$$M = \gamma = 0 \qquad \text{at } s = L \quad \text{(trailing edge: free)} \tag{3.8}$$

where M is the bending moment along the membrane. The membrane is initially deflected slightly (by a 2.5° angle to the incoming flow) to accelerate the attainment of stationary state flutter. This method is common to all studies presented in this work and verification studies have been performed to ensure that the dynamics are not sensitive to this small initial perturbation. The inlet boundary condition for the velocity is U=1 and the initial condition for the scalar field ϕ is as follows:

$$\phi = 0 \qquad 0 < y < W/2 \quad \text{(bottom half of channel)} \tag{3.9}$$

$$\phi = 1 \qquad W/2 < y < W \quad \text{(top half of channel)} \tag{3.10}$$

3.1.1.3 Numerical Method

The governing equations were solved using the in-house code ViCar3D which uses a second-order fractional step method on collocated Cartesian grids (Mittal et al., 2008) which is described in some detail in the Numerical Methods section of this report. For this particular study, the 2nd-order Crank-Nicolson fully implicit scheme is used for convective and diffusion terms and the Pressure Poisson equation is then solved with the biconjugate gradient (BiCGSTAB) scheme (C. Zhu et al., 2017).

Given that the immersed boundary method used in this study has been described earlier in this report and in previous publications (Shoele & Mittal, 2014; Shoele & Mittal, 2016a), only a brief summary of the method is included here. The fluid and structure are coupled using a procedure which involves two sets of structure points. The first set are the Lagrangian points which define the membrane. The second set of points are virtual, massless, fluid following points which are assumed to be advected by the local fluid velocity. The coupling is then created by connecting these points via virtual spring-damper "couplers". The penalty momentum force $\mathbf{F}(s,t)$ can be characterized as a spring-damper system that "connects" the two sets of structure points according to the following equation:

$$\mathbf{F}(s,t) = -\mathrm{K}_p \frac{\rho U^2}{L}\left[\left(\tilde{\mathbf{X}} - \mathbf{X}\right) + \beta \Delta t\left(\tilde{\mathbf{U}} - \mathbf{U}\right)\right] \tag{3.11}$$

where K_p and β are tunable penalty constant, and Δt is the computational time step. Based on a prior sensitivity analysis (Shoele & Mittal, 2016a) and similar to much of the work presented in this work, these parameters were chosen as $K_p = -10^5$, $\beta = 150$, and $dt = 1.0\times10^{-4}$, in large part because these values were found to be sufficiently far from stability boundaries that are present in the penalty method.

The fluid and scalar equations are solved on uniform Cartesian grids in a 10W by W domain with dx=dy=0.008W resulting in 1280x128 grid points. Uniform grids were chosen to resolve the large gradients in the scalar field at high Schmidt numbers. The membrane grid employs 160 points/W which provides high resolution for the structural dynamics. The simulations were run for roughly 10 flow-through times (O(10^6) time steps) and statistics accumulated over the last 4 flow-through times.

3.1.1.4 Verification and Grid Convergence

The flow solver in ViCar3D has been extensively validated (Mittal et al., 2008; Seo & Mittal, 2011). Furthermore, the FSI model used in this study has been benchmarked in multiple papers (Shoele & Zhu, 2012; Shoele & Mittal, 2014; Shoele & Mittal, 2016a). The remaining components for this study which require validation is the grid convergence for the scalar field, thus additional tests have been conducted for the Re = 200, Sc = 100 and $L=W/2$ case to demonstrate grid convergence for the current problem. First, the default resolution was chosen according to prior work such that $dx = dy = 0.016$, $ds = 0.012$, and $dt = 0.0001$ (1280x128 fluid points and 160 points/W for the membrane). Then the fluid resolution in each direction and the structure resolution was increased by a factor of 1.5, leading to a total of 2.25 times more fluid points (1920x192 fluid points). Concurrently, the temporal resolution was doubled to $dt = 5\times10^{-5}$. The mixing index and head loss were computed and compared between the two grids; the head loss saw almost no change (<0.1%) and this was expected as the baseline resolution was based in our previous studies of a similar configuration (Shoele & Mittal, 2014). The mixing index also changed by at most 3% in the channel at the higher resolution, indicating that the simulations on the baseline grid are also quite adequately converged.

3.1.1.5 Data Analysis and Performance Metrics

To systematically evaluate the performance of these membranes, the mixing effectiveness as well as the loss of mechanical energy must be quantified. Mixing has been quantified by a variety of metrics in the past (Danckwerts, 1952; Kockmann et al., 2006; Liscinsky, True, & Holdeman, 1993). It can be shown that these metrics are all related to one another, and map the mixing performance differently. Here we use the so-called Mixing Index (M) which is defined at a given streamwise location as:

$$M(x) = 1 - \sqrt{\frac{\sigma(x)^2}{\sigma_{\max}^2}} \tag{3.12}$$

$$\sigma(x) = \sqrt{\frac{1}{W}\int_0^W \left(\phi(x,y) - \bar{\phi}_m\right)^2 dy} \tag{3.13}$$

Where $\sigma(x)$ is the standard deviation, ϕ is the scalar field ranging from 0 to 1, $\bar{\phi}_m$ is the mean of the field which is 0.5, and $\sigma_{\max}$ is the maximum deviation in the scalar field, which occurs at the inlet. Thus, the mixing index M is just the normalized variance of the scalar concentration. It ranges from 0 to 1 with M=0 indicating totally unmixed flow and M=1 indicating complete mixing.

The loss in mechanical energy is characterized by computing the non-dimensional head (H) and corresponding head loss (HL) through the channel:

$$\mathrm{H}^*(x) = \frac{\mathrm{H}(x)}{\rho U^2} = \int_0^H \left(p(x,y) + \frac{1}{2}u^2(x,\mathrm{y}) \right) dy \tag{3.14}$$

$$\mathrm{HL}^*(x) = \mathrm{H}^*(0) - \mathrm{H}^*(x) \tag{3.15}$$

3.1.1.6 Interface Identification

The mixing index is commonly used throughout the literature to characterize the mixedness of a flow with a scalar concentration. However, while it does provide insight into how well the system is being mixed, it does not provide direct insight into the mechanism responsible for the mixing. In particular, while mixing is the direct result of diffusion, most mixing enhancing systems do not directly affect the diffusion rate, as that is a material property. Instead, mixing enhancement is achieved in nearly all cases by increasing the surface area of the material interfaces (via stretching and folding induced by complex flow patterns) and across which, molecular diffusion can occur. The mixing index and other such parameters are unable to separate the "stretching and folding" process from the continuously occurring molecular diffusion. Ideally, the best indication of how

the flag is stretching the interface to create more surface area would be some sort of interface path length. Also, as with all our performance measures, we would like this metric to be a function of the streamwise coordinate so as to see how this behavior changes with the downstream changes in the flow field.

To create this new measure, we must consider that an interface between dyed and undyed fluid is simply a surface across which there is a strong gradient in the scalar concentration. Thus, we can find the interfaces by detecting peaks in the magnitude of the gradient of the scalar field. To do this, we first calculate the scalar gradient field $\nabla\phi(x,y)$. We then calculate the magnitude of the scalar gradient $\left|\nabla\phi(x,y)\right|$ and then normalize it by the local maximum scalar gradient:

$$\nabla\phi_*(x,y) = \left|\nabla\phi(x,y)\right| / \left\|\nabla\phi(x)\right\|_\infty \tag{3.16}$$

where the double bars indicate the L_∞ norm (i.e. the maximum) at that x location, and the single bars indicate the magnitude of the gradient field. We can then detect the interfaces by finding the peaks in $\nabla\phi_*$. We do this with a peak identification approach which controls for the prominence of the peaks. This allows us to ensure we only capture areas of sufficeintly high gradient.

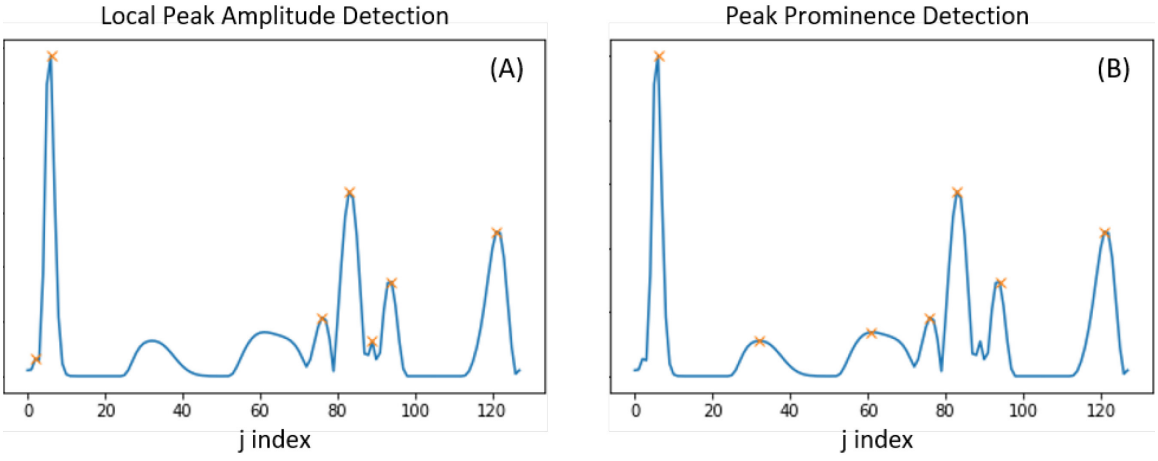

FIG. 3.2 – Example of peak identification procedure comparing a peak amplitude approach with a prominence approach.

There are several possible methods for locating peaks and filtering the detected peaks to capture only those that meet some criteria. FIG. 3.2 shows two possible approaches; a local amplitude approach and a "peak prominence" based approach. The plots shown in this figure are slices of normalized gradient field $\nabla\phi_*$ along the y direction at a particular x location. The symbols indicate the peaks detected by each approach. The local amplitude approach (A) is typically the standard method for peak identification, and it uses only the local information around the peak to make a detection by comparing a point to its neighboring points. This has the advantage of being computationally inexpensive, however it has drawbacks for our data. As can be seen in the figure, it captures very small peaks such as the first and fifth peaks from the left, while it is missing the two locations of high gradient between j=20 and j=70. Methods that detect peaks by examining the height of a peak only over it's local neighbors are essentially thresholding the signal based on the curvature of a peak. Therefore, the missed detections are clearly a result of the low order of the gradients being used to check this local curvature, making those peaks appear too flat. However, even if higher order gradients are taken (i.e. more distant neighbors are used to measure curvature), the over detection of the small sharp peaks would still occur.

To motivate using the prominence based approach, we can consider what we are interested in capturing. Namely, we are trying to detect peaks that represent large changes in the scalar field, i.e. the mean value of the pockets on each side of the peak are sufficiently far apart to enable effective scalar diffusion. The overall peak height is not an option, as there may be a realtively short peak which we do not want to capture embedded within a region of large non-zero background gradient. This would make its overall peak height large while its realtive or local peak height is small. Instead the prominence of the peak captures the relevant information. The prominece is measured as the height of a peak relative to the nearest highest valley. This essentially measures the relative height of a peak compared to the local background gradient magnitude. We threshold our prominence detection based on a percentage of the local maximum prominece. We can see in FIG. 3.2 that this

method succesfully identifies the two shallow peaks between j=20 and j=70, and does not identify the small sharp peaks which were the first and fifth of the previous detection method.

If we identify a peak, we mark the grid cell (or "pixel") that contains this as a "peak". This results in a field variable which is binary with either interface (one) or no interface (zero) which we call $\zeta(i,j)$ which is defined here in terms of the discrete indices i and j, as opposed to the domain directions x and y, so as to indicate that this variable only has meaning in a discrete sense. We can then simply count the number of peaks at any given x location by summation of ζ along a y line according to:

$$\text{\# of interfaces} = \sum_{j=1}^{N_y} \zeta(i,j) \tag{3.17}$$

Given that there should only be one interface, based on the incoming flow as a step function, any additional peaks on that y line must be the result of advective mixing due to the flag folding the interface. This counting approach is possible in 2D because if the interfaces are lines, then the cross-section of those lines at any given x location is a point. However, in 3D this would not work, as the cross-section of the interface surfaces would be lines. Counting those lines, even if possible, is not a good measure of the mixing in that it does not capture the total surface area of the interfaces, only how many surfaces there are. So as to later generalize to 3D, we define our new performance measure, the Interface Density (I_D), instead as the total number of pixels at a given i plane (i line in 2D) which is occupied by interfaces, normalized by the maximum interface density possible. In this way, the Interface Density is normalized such that it acts as a percentage of the maximum number of intefaces resolvable on the current grid. In 2D the maximum stratification is a Nyquist wave. This would appear as a striped pattern with every other cell having $\phi = 0$ and then $\phi = 1$. In this field, the boundaries between each cell represent an interface, meaning the total number of interfaces is equal to the total number of boundaries between cells, or the total number of cells – 1,

making the Interface Density in 2D very similar to an average. The 2D version of this calculation is:

$$I_p(i) = \frac{1}{N_y - 1} \sum_{j=1}^{N_y} \zeta(i, j) \tag{3.18}$$

To visualize this procedure, FIG. 3.3 shows snapshots of the scalar field ϕ, the normalized gradient of the scalar field $\nabla\phi_*$, and the binary interface field ζ.

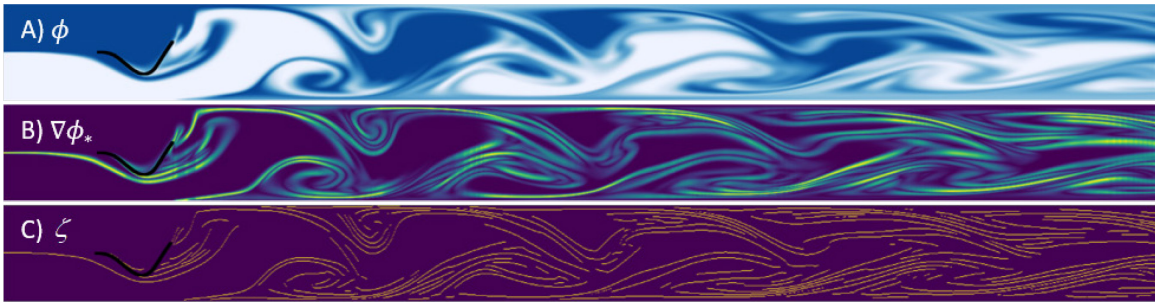

FIG. 3.3 – Snapshots of the scalar concentration field ϕ, the gradiient of the concetration at each x location $\nabla\phi_*$, and the binary interface indetification field ζ.

Here we can see that the gradient field clearly captures those locations between pockets of dyed and undyed fluid. Furthermore, it seems that the interface detection procedure we have devised, namely finding peaks with prominence over some threshold, seems to have fairly and successfully tagged pixels that are the centers of the streaks of scalar gradient magnitude. It is important to point out the difference between this peaks field and the scalar gradient field. It is tempting to simply integrate the gradient field magnitude $|\nabla\phi|$, or even our normalized gradient field $\nabla\phi_*$ to achieve the same result, but the goal of this measure is not to test the strength of the gradients, as there is no reason to suspect that the flag would be in any way directly impacting the strength of the gradients. Instead our supposition is only that the flag is generating more interfaces, or perhaps stated more acurately, it is stretching and folding the interface. Thus, we are only interested in the

path length and while integration of the $\nabla\phi$, would contain information about the path length, it would be contaminated by information regarding the interface strength as well.

3.1.2 Results

The results are organized as follows: we first present the effect of Reynolds number on the performance of the flutter mixer; this is followed by an examination of the effect of membrane length to identify the sensitivity to U* and confinement; followed by an examination of sensitivity to mass diffusivity on the mixing performance. Finally, we compare the performance of the flutter mixer to a conventional "post" mixer and provide an overview of the performance comparisons for all the cases.

3.1.2.1 Effect of Reynolds Number

The goal of this study is to investigate the mixing performance of these flutter mixers at inertial-scale Reynolds numbers and we initially examined the flutter characteristics for a membrane with length $L=W/2$ over the Reynolds number range from 25-200 which is relevant for inertial-scale micromixing applications. The Schmidt number for this study is fixed at 100, which lies squarely within the range of Schmidt numbers relevant for these applications (Nguyen & Wu, 2004).

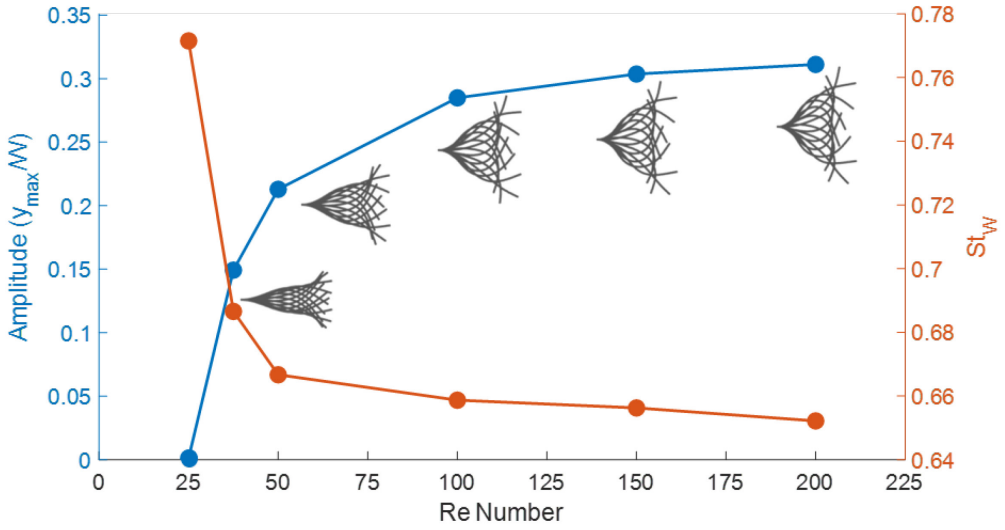

FIG. 3.4 – Flapping amplitude and Strouhal Number vs. Re number, measured from the maximum y component of the tip position.

FIG. 3.4 show the amplitude of the motion envelopes of the membrane as well as the trailing-edge amplitude and Strouhal number as a function of the Reynolds number. The plot shows that the amplitude is nearly zero at Re=25; low amplitude flutter is seen at Re=37.5 and substantial flutter is observed for Re=50 and beyond. The flutter amplitude exhibits an asymptotic behavior with Reynolds number, with the amplitude only growing from about y_{max}/W=0.285 to 0.33 between Re=100 and 200, indicating a saturation of the flutter behavior of this configuration with increasing Re number. The frequency of flutter (f_m) as characterized by the Strouhal number ($St_w = f_m W/U$) is nearly constant at a value of about 0.66 for cases with substantial flutter amplitude.

The saturation of the sensitivity to Re has been seen in past work. Shoele & Mittal (2014) showed that for confined flapping of 2D filaments in a channel flow, this threshold is at approximately Re=200. Our data seems to show a similar result for the L=W/2 flag length. Interestingly, this is likely not the result of confinement, or at least not directly so. The maximum tip excursion is only 0.33 even though the walls are 0.5 away from the centerline. Flapping flags and filaments can very easily come much closer to channel walls, so it is unlikely that this saturation has something to do with the presence of the boundary. Instead, it is clear from the flapping envelop

figures that the flapping mode shape itself has saturated. This is a much more likely candidate for the saturation mechanism, especially when we consider that the flag length is W/2, so the maximum excursion is more than 60% of the flag's overall length. This represents very high amplitude flapping for regular flags. Huang et al. (2007) found the maximum tip excursion for unconfined flags at Re=200 to be around 0.35. Those results were at slightly different U* and M* but they still seem to indicate these flags have reached their maximum deflection.

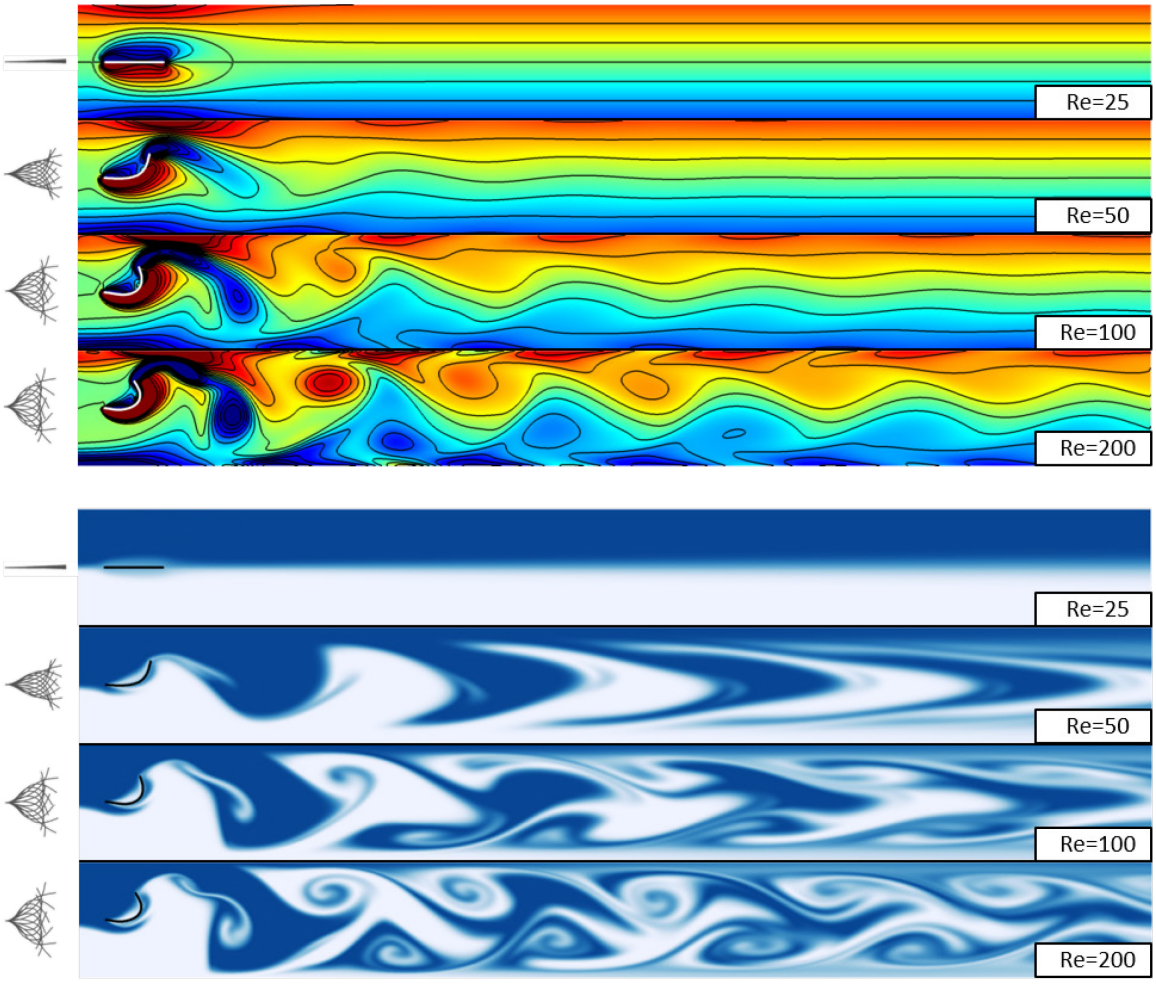

FIG. 3.5 – Contour plots of spanwise vorticity (top) and scalar concentration (bottom) for L=W/2 membrane at Reynolds numbers of 25, 50, 100, 200. The images to the left of the contour plots show the motion envelopes for the membrane through one cycle.

FIG. 3.5 shows contours of spanwise vorticity and scalar concentration for four selected cases. The spanwise vorticity figures show that for Reynolds numbers beyond 100, the essential features of the vortex topology include the rolling up of the shear layers on the membrane and shedding of compact vortices into the wake. These vortices arrange themselves in an inverse Karman vortex street, wherein the counter-clockwise rotating vortices are above the clockwise rotating vortices. Such vortex streets are typically seen in thrust generating flapping foils (H. Dong, Mittal, & Najjar, 2006). The literature on flapping membranes/flags seems to indicate that confinement changes the resulting vortex street from a standard Karman street to an inverse Karman street. This is discussed directly in Alben (2015) where they show a reverse Karman vortex street for confined flags using an analytical vortex sheet method over a range of confinement ratios. Similarly, the previous work of Shoele & Mittal (2014) found inverse vortex streets over a wide range of flutter amplitudes for Re=400 for a range of confinement ratios. In contrast, other papers (CONNELL & YUE, 2007; Huang et al., 2007; L. Zhu & Peskin, 2002) examining unconfined flapping membranes showed that, at least for the periodic flapping regime, the membrane creates a standard Karman vortex street.

For the Reynolds number of 50, the vortex rollup is not clearly visible, although individual counter-rotating vortices are still shed in the wake at each half of the flapping cycle. These vortices seem to dissipate rapidly in the near wake however their signature can be seen in the curvature of the vorticity isolines just downstream of the membrane. For the lowest Reynolds number of 25, there is no vortex shedding in the wake of the membrane, which remains stationary.

The characteristics of the scalar field (shown in FIG. 3.5) reflects the underlying vortex topology. For the Re=50 case, the vortex shedding is quite weak and the primary perturbation to the scalar field comes directly from the movement of the membrane. This movement generates nearly sinusoidal deformation of the scalar interface in the near wake of the membrane and as this deformed interface advects downstream, it is stretched along the streamwise direction due to the strain-rate associated with the developing parabolic channel flow profile. This stretching is

beneficial for mixing since it increases the interface length and sharpens the scalar gradients, thereby facilitating diffusive mixing.

For Reynolds number of 100 and higher, two factors significantly accelerate the mixing process. First, with a larger flapping amplitude, the perturbations in the scalar field generated directly by the membrane motion are larger. Furthermore, and more importantly, the compact vortices shed at the end of each half-stroke entrains scalar from one side of the channel and advect it to the other side. It is also observed that in addition to the continuous downstream stretching of the interface dues to the parabolic velocity field, the shed vortices continue to entrain mass thereby further enhancing the deformation of the scalar interface. This of course further accelerates the process of diffusive mixing. Thus, the flutter mixers are expected to continue to perform well beyond Reynolds numbers of 200, although intrinsic three-dimensional effects likely become important at these higher Reynolds numbers. Those 3D effects will be studied in a following section. To directly observe the effect of the flutter mixers we can examine the gradient field magnitude $|\nabla\phi|$ and the detected interface field ζ.

FIG. 3.6 shows snapshots of the scalar field ϕ, the magnitude of the gradient of the scalar field $|\nabla\phi|$ and the detected interface field ζ for Re 25, 50, 100, and 200. These combined visualizations provide complimentary information of the effects of convective mixing. The $|\nabla\phi|$ shows the global magnitude of the gradient instead of the local normalized magnitude as would be shown in $\nabla\phi_*$. This perspective gives a sense of how the interfaces diminish downstream as diffusion takes effect, thereby bringing the maximum and minimum values of ϕ closer together, meaning gradients wont be as strong. It also allows for the relative comparisson of interface sharpness between cases. Therefore, $|\nabla\phi|$ allows us to visualize the interface strength at a given location, whereas ζ shows the position of the interfaces, agnostic to their strength. This allows for

the visualization of the interface density and thus the degree to which the interface has been stretched.

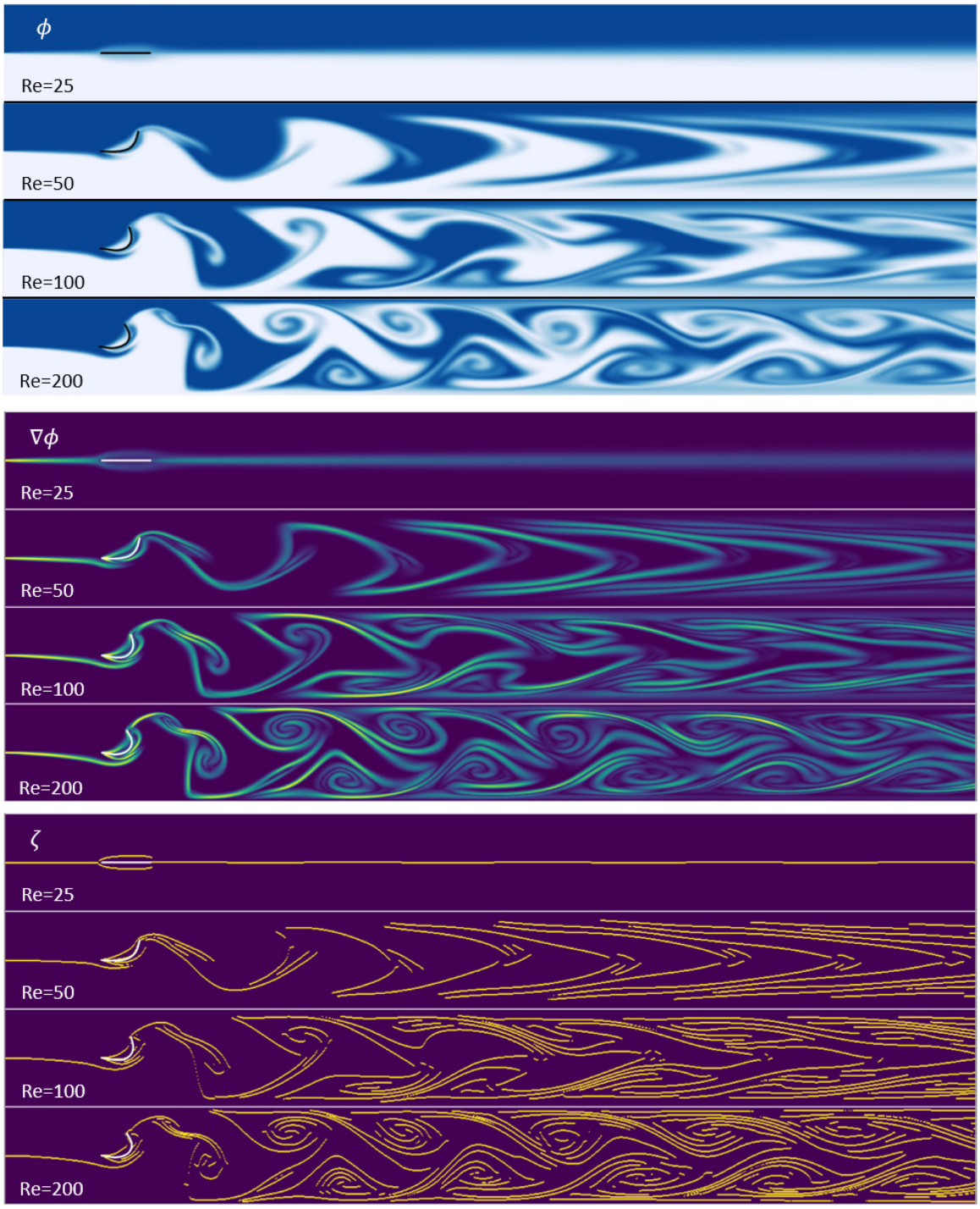

FIG. 3.6 – Scalar field ϕ, gradient field $\nabla\phi$, and interface field ζ for Re=25, 50, 100, and 200 with L=W/2 membranes.

Analyzing FIG. 3.6, we can more clearly observe the transition between the low Re mixing mechanism involving sinusoidal deformation of the interface seen in the Re=50 case, and the higher Re compact vortex shedding mechanism in Re=200. Furthermore, the $\nabla\phi$ snapshots show an increase in the gradient strength with increasing Re, as can be visualized by the brightness of the color contours. This is due in part to the Peclet number effects at play wherein at higher Re, the diffusion coefficient in the scalar advection-diffusion equation is smaller, This means that molecular diffusion will be less effective, and therefore large gradients will still be visible far downstream. The ζ field provides interesting insight into the result of this interface stretching. With increasing Re, not only is the density of the interface packing increasing, but the locations of these interfaces are changing as well. In the Re=50 case the interfaces are largely confined to the middle 80% of the channel, whereas in the Re=200 case they occupy the entire channel, and are perhaps most concentrated near the walls. This is important, because as can be seen in the scalar field for Re=50, the scalar in the boundary layers near the walls seemed to show very little mixing, which is problematic vis-à-vis the potential applications for this membrane length at this Re.

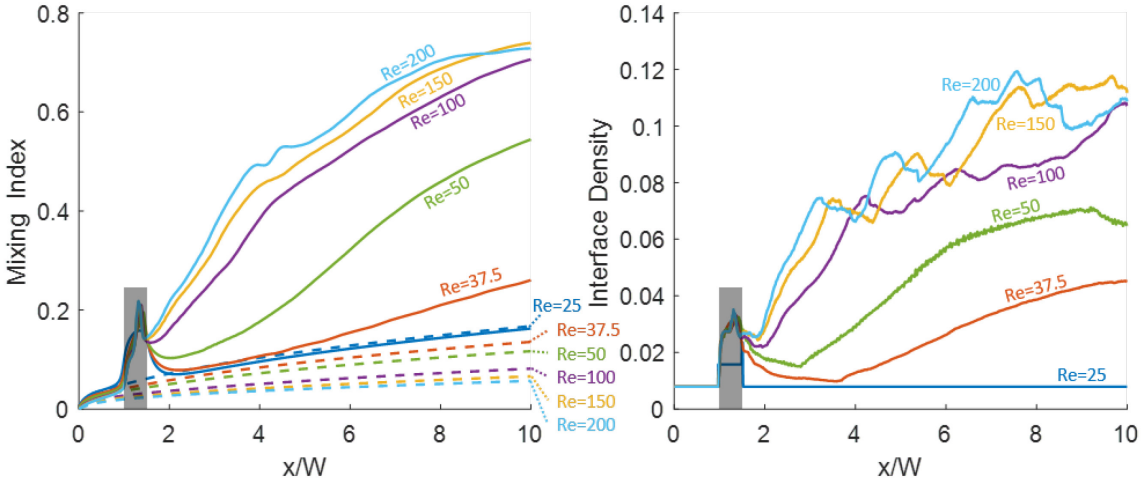

FIG. 3.7 – Plots of time averaged Mixing Index (left) and Interface Density (right) as a function of downstream location. The solid lines are the flapping membrane cases and the dashed lines are the empty

channel baseline cases for comparison. The shaded vertical bands represent the region occupied by the membrane.

FIG. 3.7 shows the mixing index and interface density results for the L=W/2 cases. The mixing index figure shows that between Re=25 and Re=100 the system transitions from no mixing improvement to behavior comprising very rapid mixing and a steep, linear increase in the mixing index immediately following the membrane, followed by a region where the mixing index slope get shallower but is still steeper than the empty channel baseline configuration. The Re=150 and 200 cases appear similar to the Re=100 case, with only a slight increase with higher Re. The slight dip in the Re = 200 case compared to the Re = 150 case may be the result of Pe number effects. If the effect of the membrane via interface stretching has mostly saturated by Re=150, then the Re=200 case could perform slightly worse.

However, the interface density figure shows interesting behavior which may contradict this Peclet number explanation. In general, the shapes of the interface density curves are similar to those of the mixing index curves. Crucially however, the changes in the interface density precede the changes in the mixing index. This spatial lag is due to the time it takes for diffusion to occur. That the mixing index shows such similarity, yet also lags behind the interface density shows a strong causal connection between how the membranes stretch the interfaces, and the mixing improvement. In comparing the Re 150 and 200 cases, it appears that the nonmonotonicity is seen at different locations downstream, with the Re=150 case showing this dips and rises spatially farther down the channel than the Re=200 case. This nonmonotonicity is surprising, but is likely related to the sometimes non-physical behavior of vortices in 2D, especially at Re in this range and higher. If these nonmonotonic patterns are real, then this result could in principle aide in the design of more complex flutter mixers for engineering applications by allowing designers and engineers to focus on multi-membrane configurations which maximize the interface stretching in the flow by picking spacings which take advantage of this nonmonotonicity.

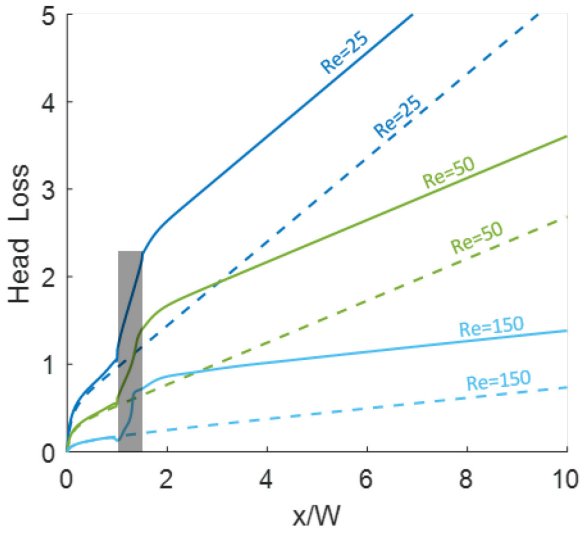

FIG. 3.8 – Head Loss for the L=W/2 cases. The solid lines are the flapping membrane cases and the dashed lines are the empty channel baseline cases for comparison. Only three selected cases are shown as the behavior of the intervening cases is largely similar. The shaded vertical bands represent the region occupied by the membrane.

Considering the head loss figure, it is clear that the flapping membrane accounts for a noticeable increase in head loss. However, it will be shown later that these are significantly smaller than the energy losses associated with another typical mixing enhancement method (Deshmukh & Vlachos, 2005) which is discussed in a later section. This increased head loss is in principle associated with the viscous drag on the membrane, the energy associated with the flapping of the membrane, and the vortex structures created by the membrane. However, is also noted that the head loss for the flutter mixer rapidly establishes a linear increase downstream of the membrane with a slope that matches that of the empty channel case. This implies that the kinetic energy (or dynamic pressure) term contributes very little to the increase in head loss, and almost all the head loss is associated with a decrease in the static pressure due to the membrane itself. Interestingly, the increase in the static pressure is still significant for the Re=25 case which did not exhibit flutter, suggesting that the viscous drag on the membrane is the dominant factor contributing to the additional pressure loss.

3.1.2.2 Effect of Membrane Length and Minimum Effective Reynolds Number

The lack of flutter at Re=25 for the $L=W/2$ case is not entirely surprising since it is known that viscous effects tend to damp the fluid-elastic instability (Shoele & Mittal, 2016b) and increase the critical reduced velocity at which flutter occurs. From the viewpoint of establishing the operational range of these mixers, it is useful to determine the lower limit of Reynolds numbers for which these micromixers can work. The reduced velocity can be rewritten as $U^* = U(L/t)\sqrt{\rho_s / E}$ where t is the thickness of the membrane and E is its Young's modulus. This suggests that the reduced velocity could be increased for a given Reynolds number by either increasing the length or reducing the thickness of the membrane. The same could be accomplished by reducing the elastic modulus or increasing the density of the membrane material. Here we explore the simple strategy of increasing the membrane length and have simulated two additional cases with $L=W$ and $2W$ at the low Reynolds numbers (Re<=25).

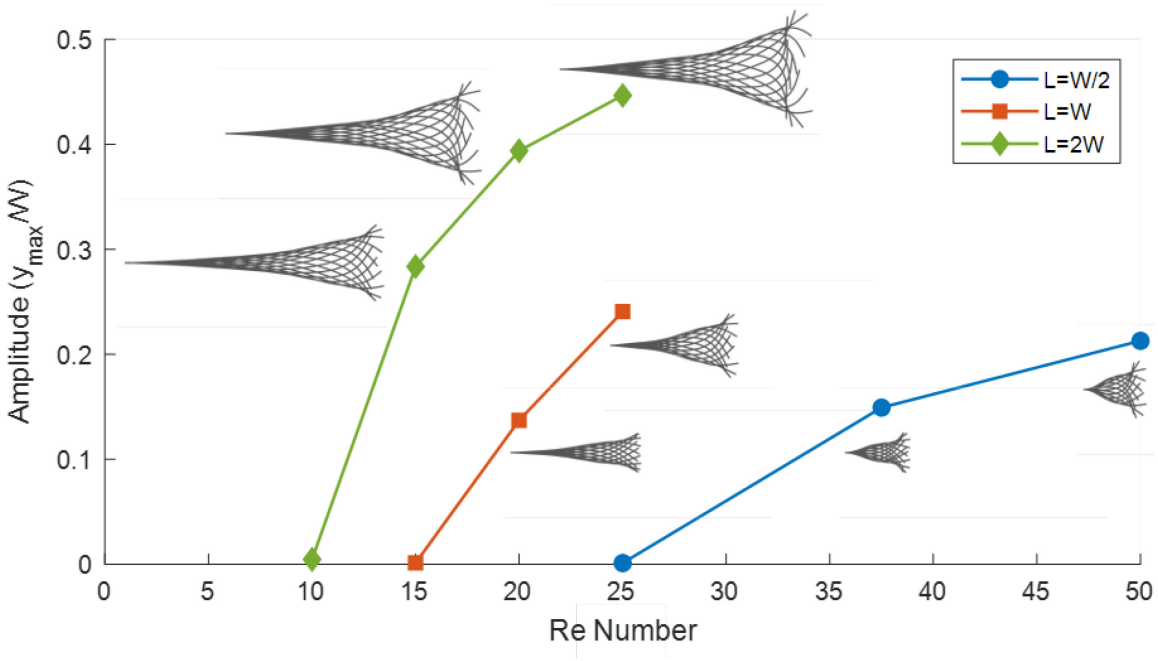

FIG. 3.9 – Flutter amplitude (y_{max}/W) and envelopes for the L=W/2, W, and 2W cases for low Reynolds numbers.

FIG. 3.9 includes the flutter amplitude for these cases and we note that minimum flutter amplitudes are y_{max}/W=0.14 at Re=20 for the L=W case and y_{max}/W=0.28 at Re=15 for the L=2W case. Thus, the longest membrane flutters with a significantly larger amplitude at Re=20 than the L=W/2 case reached even at Re=200. The behavior of the L=2W is an interesting result for a few reasons. It is noted that the amplitude is still smaller than the channel half height, however, as visualizations in FIG. 3.10 will show, it is clear that the membrane's amplitude is constrained by the confinement of the channel. One of the identified reasons that the L=W/2 Re=50 case showed such low mixing improvement was that it was not able to affect the flow in the boundary layers, as the flapping was constrained too close to the channel centerline. Here however, the higher amplitude flutter allows the tip of the flag to reach nearly to the wall. This could be beneficial as these cases are too low to exhibit vortex shedding, thus the only mixing improvement should be due to the interface deformation mechanism.

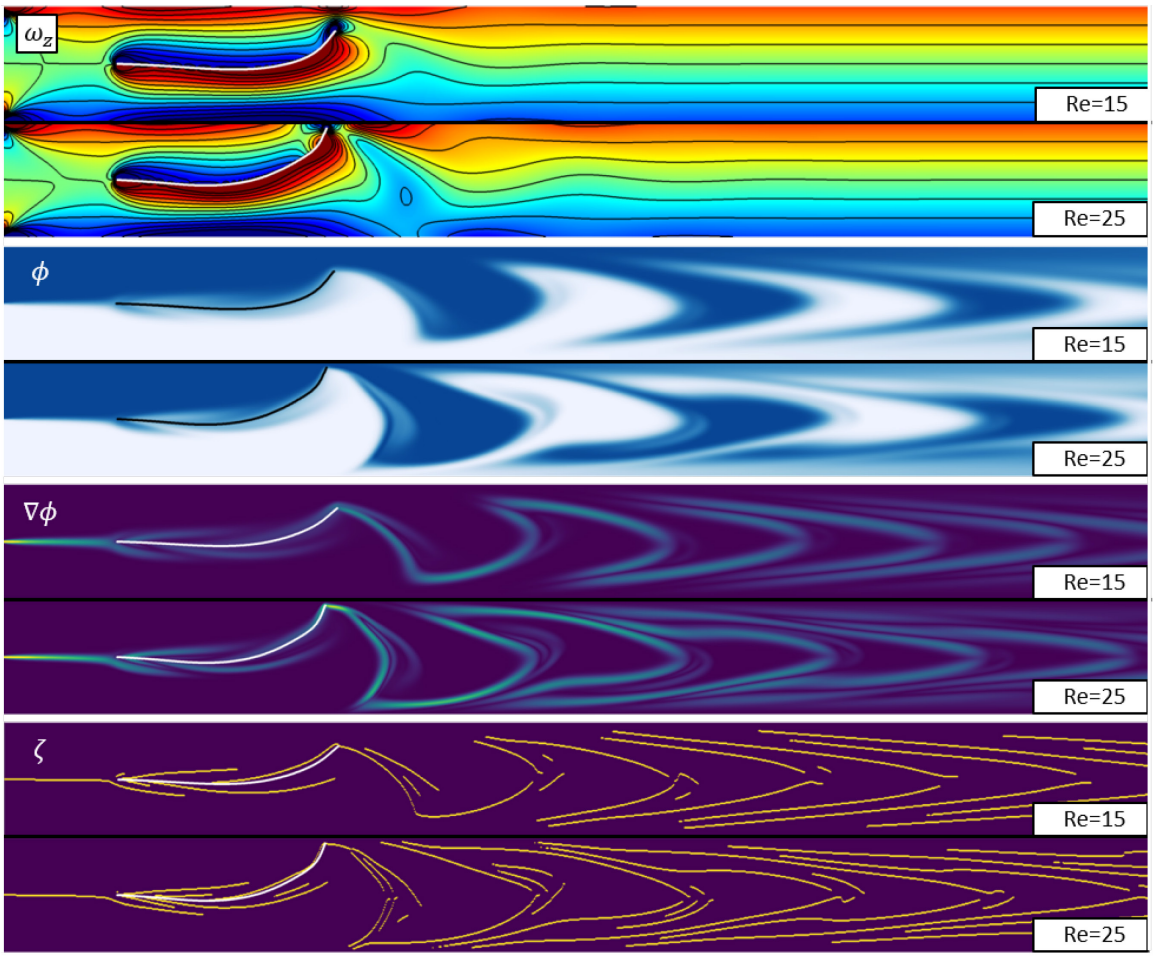

FIG. 3.10 – Spanwise vorticity (ω_z), scalar concentration (ϕ), Scalar Gradient ($\nabla\phi$), and interface field (ζ) for the L=2W, Re=15 and Re=25 cases.

To examine the effect of this high flapping amplitude, FIG. 3.10 shows the spanwise vorticity, scalar field, scalar gradient magnitude, and interface field for the *L*=2*W* Re=15 and Re=25 cases. The L=2W Re=15 case is the lowest Re number where flutter was observed in this study. It is noted that the overall features are quite similar to those for the *L*=*W*/2 membrane at Re=50 wherein no compact vortices are shed. As with the L=W/2 Re=50 case, the only mixing enhancement is due to the initial sinusoidal deformation of the scalar interface and the subsequent stretching by the parabolic flow profile. However, the effect of the increased flapping amplitude is clearly visible. Especially for the Re=25 case, the membrane tip nearly contacts the wall, and the resultant

deformation of the interface can be seen to stretch across the entire width of the channel. This leads to an interesting result which can be seen in the ϕ and the $\nabla\phi$ snapshots, where the regions of the channel near the walls are very well mixed, whereas the center of the channel still exhibits a streamwise periodic pattern. This is not the case for the Re=15 figures. Here the flapping amplitude is much lower. However, at y/L = 0.3 it is still almost double the mean tip excursion for the L=W/2, Re=37.5 case which exhibited flapping at the lowest Re for that flag length. Still, in the Re=15 case the sinusoidal perturbations are largely confined to the center of the channel, and the region near the walls shows almost no evidence of mixing.

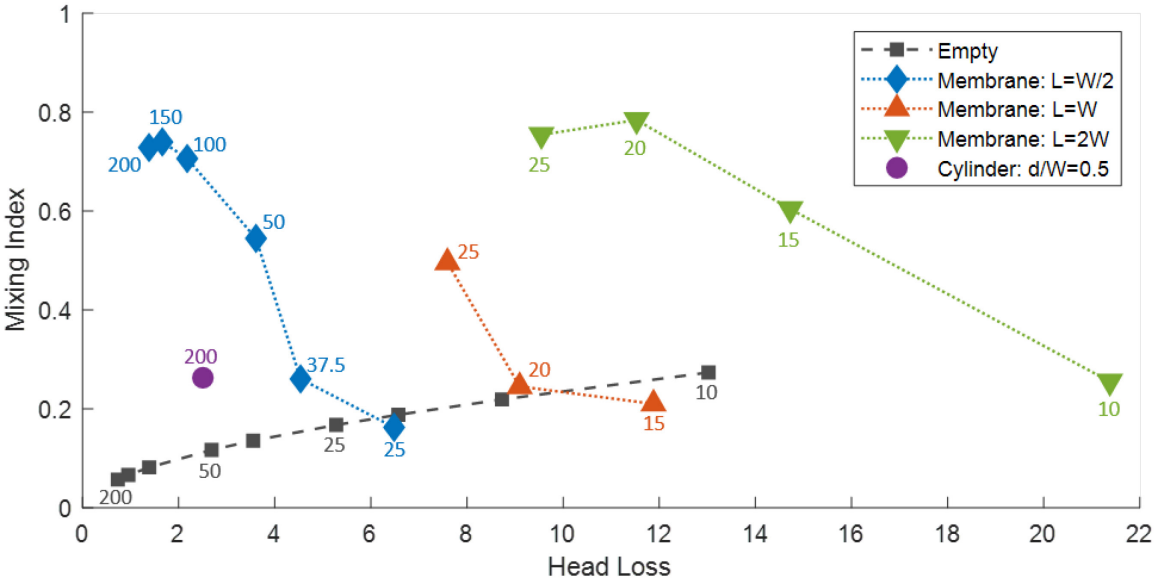

FIG. 3.11 – Performance comparison in terms of pressure drop and mixing index for the various cases studied in this paper. The Reynolds number for each case is noted on the plot. The point corresponding to the cylinder is discussed in a later section.

FIG. 3.11 summarizes the overall performance of the various cases examined in the current study at Sc=100. In this figure we plot the mixing index at the exit of the mixer (x/W=10) against the overall non-dimensional pressure loss. The plot clarifies the trends in the mixer performance of this system for various Reynolds numbers and membrane lengths. For the empty channel, mixing occurs exclusively due to molecular diffusion and the mixing index increases slowly with

decreasing Reynolds number (at fixed Schmidt number), signifying the Peclet number effect. Even at the lowest Reynolds number (highest mixing for the empty channel), the mixing index only reaches about 0.3 at the end of the channel.

In contrast, the cases with a membrane show increasing mixing performance with increasing Re number. For the channel with the flag ($L=W/2$), the mixing index rises rapidly with Reynolds number and reaches a peak of 0.78 at Re=150. This confirms that advective effects dominate the mixing process in the flutter mixer. The flutter mixer with $L=W$ has a mixing index at Re=25 that is nearly the same as that for $L=W/2$ and Re=50, although the pressure loss is nearly twice the value. Also, the Re=20 case for this membrane sees only marginally better mixing than the corresponding empty channel, while incurring a 30% larger head loss. Finally, the $L=2W$ case exhibits significant flutter and associate mixing enhancement down to a Reynolds number of 15 although, the associated pressure losses are quite significant. Interestingly, the Head Loss for the membrane cases still monotonically decreases with increasing Re. This is interesting because the higher Re cases show significantly more energetic flapping behavior, which should signify increased energy losses. However, as noted previously, the Head Loss appears to be almost entirely dominated by the viscous drag on the body, as shown by the large Head Loss for even the membranes that did not flap.

Finally, given the increase in pressure drop associated with increasing membrane length, other strategies for raising the reduced velocity at a fixed channel Reynolds number could, in principle, be explored, such as reducing the thickness or changing the material properties of the membrane. All of these strategies would likely not increase the pressure drop significantly, but might be challenging from a materials selection and/or fabrication viewpoint. Exploration of these strategies is outside the scope of the current study.

3.1.2.3 Effect of Schmidt Number

Mass diffusivities may vary over a large range in micromixing applications (Nguyen & Wu, 2004) and it is therefore useful to examine the effect of variations in this property on the performance of the flutter mixers. For this study, we fix the Reynolds number to 200 and vary the Schmidt number (Sc) from 1 to 1000. FIG. 3.12 shows snapshots of the scalar field at Sc =1, 10, 100, and 1000 (Nguyen & Wu, 2004). The observed behavior of the scalar is as expected: the flapping and vortex shedding only depends on the Reynolds number and is therefore the same for all these cases. However, the higher relative mass diffusivities at the lower Schmidt numbers (Sc=1,10) leads to extensive diffusive mixing across the complex scalar interfaces produced by vortex shedding and convection of the shed vortices. The Sc=100 and 1000 cases exhibit nearly identical scalar patterns indicting that beyond about Sc=100, the mixing is dominated by advection, at least within the channel length examine here.

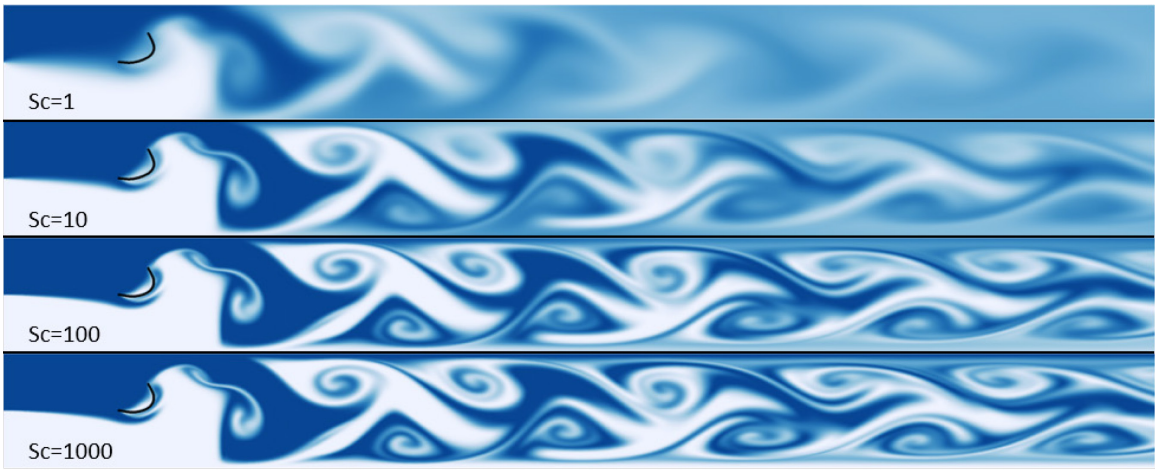

FIG. 3.12 – Contour plots show instantaneous snapshots of the scalar concentration field T *for Sc = 1, 10, 100, 1000.*

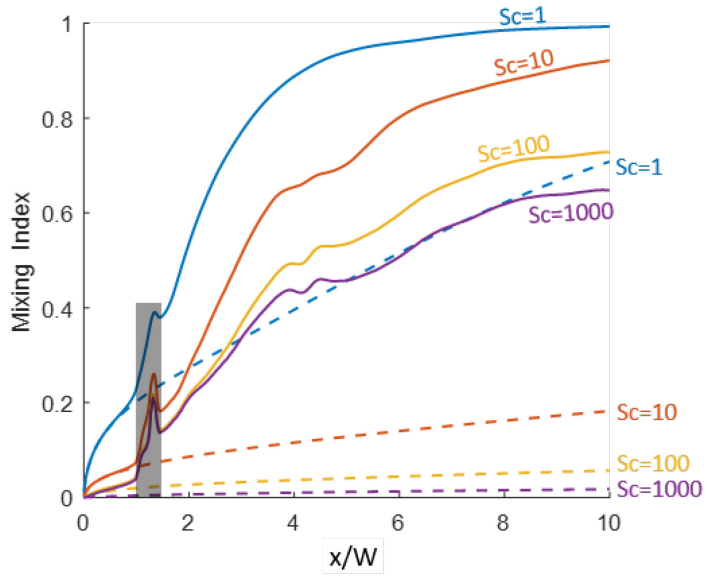

FIG. 3.13 – Plots of time averaged mixing index vs. downstream location for Re=200 and Sc =1, 10, 100, 1000. Shaded areas depict the extent of the membrane.

The plot of the time-averaged mixing index in FIG. 3.13 provides a more quantitative measure of the effect of Sc. Since the head loss depends only on the Reynolds number, its variation remains the same as that shown in FIG. 3.8. For the empty channel, the mixing performance increases significantly with reduction in Schmidt number due to the increase in mass diffusivity. For the flutter mixer with Sc=1.0, the scalars are almost fully mixed (M=0.99) by x/W=10, whereas for the highest Schmidt number of 1000, M=0.65 at x/W=10, which significantly exceeds the corresponding value for the empty channel (M=0.02). Overall, for the Sc = 1, 10, 100, and 1000 cases, the flutter mixer improves the mixing index by factors of 1.4, 4.1, 11.7, and 37.1, respectively, over their respective baselines. Thus, the introduction of the membrane significantly enhances the mixing performance for every case explored here, but the relative improvement is more pronounced for higher Sc.

3.1.2.4 Comparison with Bluff-Body Induced Mixing

To better understand the performance of the flutter mixer, it useful to compare it with other passive mixers. However, since there are so many different passive mixer designs (Cai et al., 2017;

Lee et al., 2011; Lee et al., 2016; Nguyen & Wu, 2004), it is difficult to establish a systematic approach to this comparison. In the current study, we choose to compare the flutter mixer to a mixer that employs a bluff-body to induce vortex shedding and mixing. Such mixers (sometimes called "post" micromixers) have been proposed before (Deshmukh & Vlachos, 2005) and the advantage of comparing with these mixers is that both use vortex formation and shedding as the primary mechanism for enhanced mixing.

The cylinder in the channel introduces the additional parameter (d/W), where d is the cylinder diameter. In the current study, we have simulated flow for d/W=0.25, 0.50 and 0.75 for the Re=200 and Sc=100 case. No vortex shedding is observed for the smallest and largest cylinders at this Reynolds numbers. For the smallest cylinder, the cylinder diameter-based Reynolds number $\mathrm{Re}_d = (d\,\bar{u}/\nu)$) is 50 and this is close to the critical Reynolds number for vortex shedding. For the largest cylinder, the flow and the vortex shedding instability is likely damped by the severe confinement effect of the channel walls(Sahin & Owens, 2004). The case with d/W=0.50, for which Re_d=100, does generate vortex shedding and provides data for comparison with the flutter mixer. Fortunately, this diameter is also quite comparable to the amplitude of the fluttering membrane with $L=W/2$ at this Reynolds number and this further facilitates the comparison between the two cases.

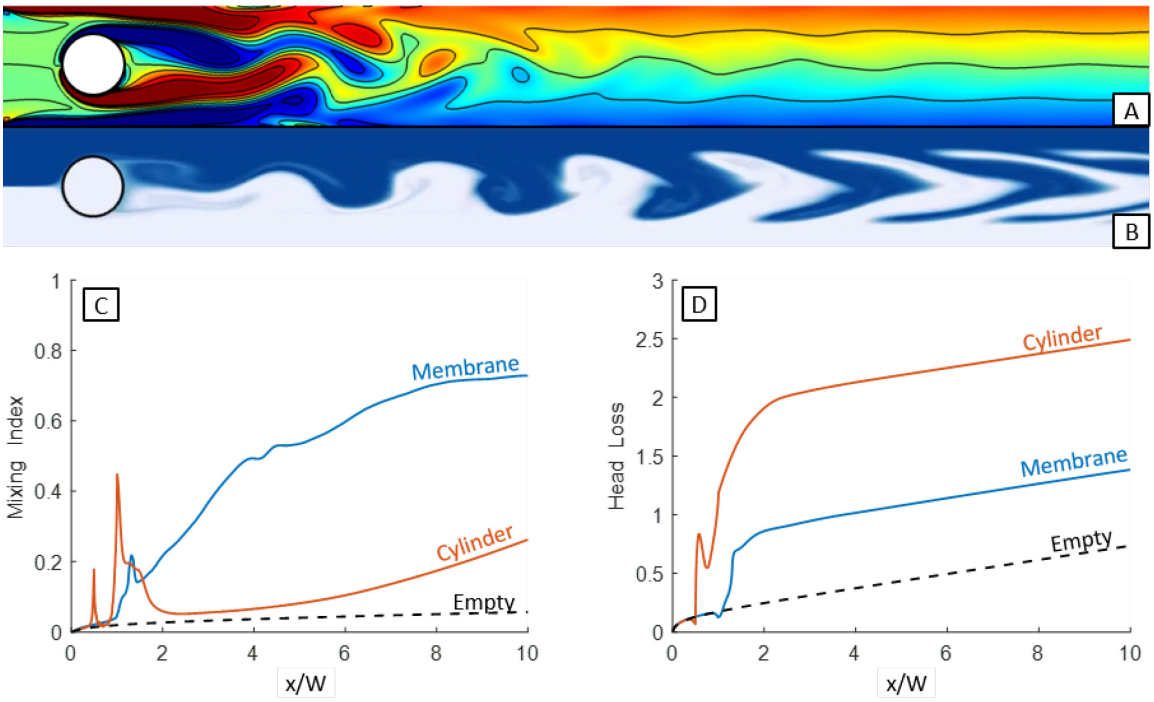

FIG. 3.14 – Comparison of a cylinder and the L=W/2 membrane case with snapshots of (A) the spanwise vorticity ω, (B) the scalar field ϕ, as well as plots of the (C) the Avg Mixing Index and (D) the Head Loss for the R=100, Sc=100 cases.

FIG. 3.14 shows the contours plots depicting the vortex shedding and scalar mixing for this mixer and these can be directly compared to the corresponding plots in FIG. 3.5. It is clear that although both cases exhibit vortex shedding patterns, the vortex topology and scalar transport are quite different. In particular, while the membrane releases vortices near the outer walls of channel and forms an inverse Karman vortex street (counterclockwise vortices on top and clockwise vortices on the bottom) where the shed vortices convect along the outer walls, the cylinder generates a conventional Karman vortex street with the vortices convecting near the middle of the channel. A consequence of this difference in the vortex topology is that the wake vortices of the membrane are more effective in inducing a downward advection of the scalar from the wall into the core of the fluid. In contrast, the cylinder wake vortices primarily perturb the scalar field near the channel

centerline and only have a marginal effect on the scalar concentration in the vicinity of the channel walls.

From a quantitative perspective (FIG. 3.14), the flutter mixer outperforms the post mixer both in terms of mixing and head loss by a significant margin. The flutter mixer shows a rapid increase in mixing between x/W=2 and 4 whereas, the cylinder mixer has a very slow increase in mixing index in this region (note that for this plot, we ignore the region with the cylinder where the mixing index is not meaningful). Consequently, the mixing index for the cylinder at x/W=10 is only 0.26 which is about 2.8 times smaller than that for the flutter mixer. Furthermore, the additional head loss for the cylinder is 1.76, which is 2.7 times higher than the flutter mixer at 0.65. This is in line with the fact that bluff-bodies exhibit a higher total drag than flexible bodies which deform to be streamlined with the flow (Shelley & Zhang, 2011). This difference in performance is clearly seen in the scatter plot seen in FIG. 3.11, wherein the post mixer at Re=200 shows better mixing than the empty channel, but underperforms significantly compared to the flutter mixer and also generates significant pressure loss. Thus, flow-induced flutter is a significantly more effective mixing mechanism than bluff-body vortex shedding.

3.1.3 Summary and Discussion of Single Flag Flutter Mixers

Computational modeling has been used to explore the fluid dynamics and mixing performance of an inertial-scale micromixer where mixing is enhanced by the flow-induced flutter of an elastic membrane. Simulations show that significant flutter and flutter-induced enhancement of mixing is achievable at channel Reynolds number as low as 15 and the mixing performance improves with Reynolds number. The enhanced mixing is associated with the shedding of vortices from the trailing-edge of the fluttering membrane and the organization of these vortices into an inverse Karman vortex street that generates significant cross-stream advection of the scalar and highly complex interfaces across which diffusive mixing can occur. The mixing mechanism in these flutter

mixers is stretching and folding of the interface and is found to be effective over a large range of mass diffusivities. Comparison of the flutter mixer with a "post" micromixer that employs bluff-body induced vortex shedding for mixing shows that the flutter mixer generates significantly higher mixing with much lower pressure loss.

The current 2D work also has limitations. First, the geometric model of the mixer is very simple (a straight channel) and two-dimensional. Actual micromixers have duct-like channels where three-dimensional flow effects are significant. Additionally, three-dimensionality could potentially affect the flutter of the elastic element and the flow field. While previous investigations have shown that the flutter-instability of such membranes is robust to three-dimensional effects (D. Dong, Chen, & Shi, 2016; Huang & Sung, 2010; Rips et al., 2017; Shoele & Mittal, 2016b), it is worthwhile to explore this using 3D computational models.

3.2 Multi-Flag Flutter Mixers

Motivated by the results of the single flag flutter mixer, we sought to examine other possible designs of a flutter mixer. One simple notion is motivated by other canonical passive mixers, which use repeated units of corrugations, or repeated units of posts. In the same way those arrangements see increases in mixing performance with multiple unitary elements, multiple membranes arranged in a sequence should also result in better mixing. We explore this notion by examining a two-flag tandem arrangement.

The difficulty in this type of study is the vast parameter space. Dual flag configurations automatically double the number of structural parameters. Furthermore, there are new geometric parameters regarding the spacing between membranes and the length ratio between the membranes. A brute force investigation of such a parameter space is impractical. Instead we chose to explore only a small fraction of this parameter space. Based on the observations of the single flag study, namely that interface stretching is essential to mixing enhancement for flutter mixers, we examined

which parameters might particularly benefit the system vis-à-vis interface stretching. Additionally, one potential issue with the observed behavior of these flags was how periodic their flapping behavior was. This highly periodic behavior created obvious periodic pockets of unmixed fluid in the downstream region which persisted for many flag lengths. This can be seen especially along the centerline of the channel. Thus, another goal should be to introduce more complexity to the dynamics to interrupt this periodicity and to enhance the stretching and folding of the material interfaces.

One way by which the dynamics could be so affected would be to introduce multiple length and time scales into the flow. There are multiple ways to affect this goal. Tuning the structural parameters could in principle induce the flags to flutter with different amplitudes and frequencies. However, this is not practical from an engineering or manufacturing perspective as using multiple materials or trying to effect the material properties of the flags with tweaks to the manufacturing process (such as adjusting the thickness of a membrane to change the bending stiffness) would likely be difficult, and prone to unforgiving manufacturing tolerances, precluding any fine tuning of the parameters. Instead, an easy parameter to vary is the membrane length. In principle, we should be able to pick membranes whose lengths are different in such a way that the interactions between them are complex and create a more broadband set of active wave numbers in the wake. We chose membrane length ratios which were not integers so as to eliminate simple super-harmonic type interactions between the flags. A simple implementation of this idea is membranes $L = W$ and $L = 2/3\,W$.

3.2.1 Problem Configuration

To investigate the multi-flag system, we chose three configurations keeping in mind our desired length ratio. We investigated a configuration of L=W, L=0.67W; L=0.67W, L=W; and L=0.83W, L=0.83W where the order of the lengths defines their order in the channel. The first two cases were

chosen so as to understand what effect the relative placement of the flags has on the mixing. The final case represents a control, where the total flag length is the same as the prior two cases, but the ratio between their flag lengths is unity. This set of simulations should allow us to differentiate to some degree between geometric coupling effects, and effects due to the hopefully non-linear interaction of length and time scales.

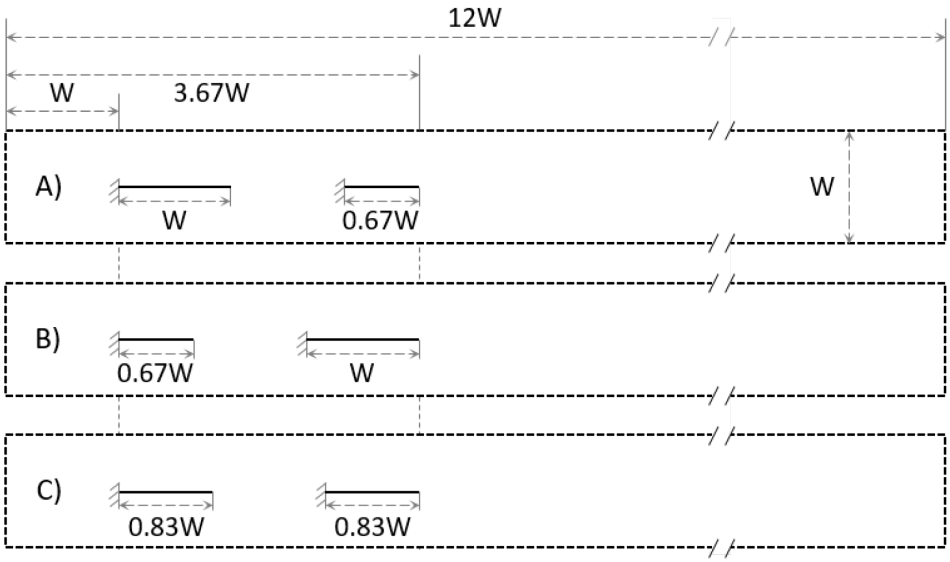

FIG. 3.15 – Schematic showing the three multi-flag simulation configurations.

FIG. 3.15 shows the three configurations we investigated. The flags were arranged such that the second flag always ended at the same downstream location, which also means that the spacing between them is always W. This allows us to make meaningful statements about downstream behavior after the flags, as all the flags end at the same location. The simulations were conducted at Re=200 and Sc=100. The computational domain is 12WxW and is discretized using a uniform Cartesian mesh of 1536x128 points. The membrane in discretized using 160 points per W. This high resolution was needed because several of the simulated flags are less than W long, but they still need to be adequately resolved. So the structure and fluid resolutions all stem from the requirements of the shortest flag. The cases were simulated using the same method described for the 2D single flag mixing study.

3.2.2 Results

Our goals of this analysis are to first demonstrate the potential performance of flutter mixers. The single flag investigations are valuable from the perspective of fundamentally understanding the fluid-structure interactions of the system, particularly at inertial-microscale Re. However, they do not provide a true sense of the mixing index improvement that could be obtained with flutter mixers. There is some notion of this potential insofar as the steep gradient in the mixing index plots just after the flag, but investigating the multi-flag configuration is closer to how these devices may be used in practical applications where several flags may be arranged in series.

We are then interested in understanding the dependence of the system on the geometric parameters we chose to investigate. The relative position and relative length of the membranes are the most easily accessible tuning parameters from a manufacturing perspective. If we can demonstrate sensitivity to these parameters it would make designing a well optimized system significantly less adhoc. To study these results, we will first calculate the mixing index and the interface density to understand the raw performance of these cases. We then examine the dynamics of the membranes based on their flutter amplitudes and their Strouhal numbers and investigate the flow physics via flow visualizations of the vorticity, the scalar concentration, scalar gradient magnitude, and the interface field. This analysis will provide context and explanation for the observed performance differences. Finally, we calculate the head loss and compare those results to the earlier mixing index results to understand relative the performance of these multi-flag flutter mixers.

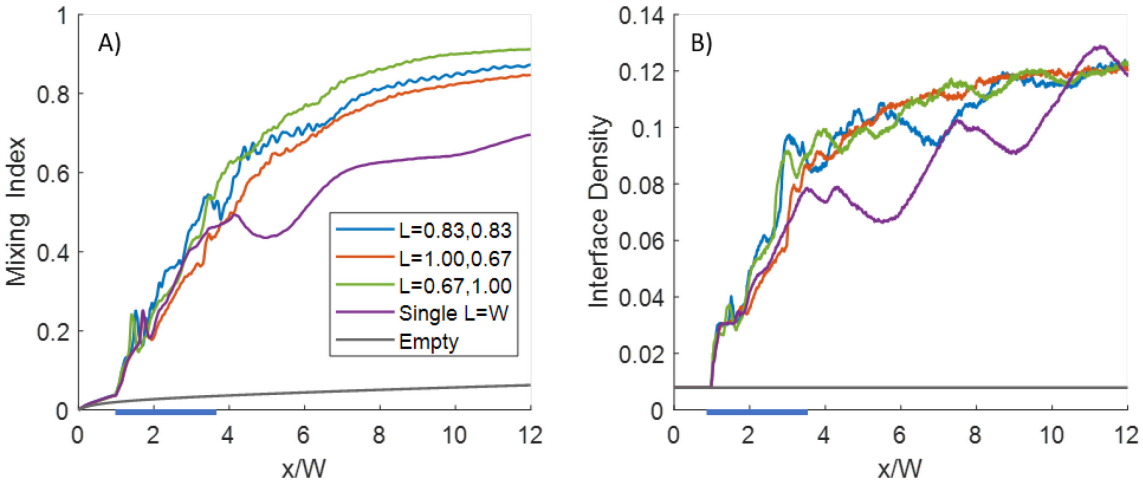

FIG. 3.16 – Plots of A) Mixing Index and B) Interface Density for the multi-flag configurations. Configurations with a L=W single flag and the empty channel configuration are also shown. The bars along the X axis show the region containing both flags.

FIG. 3.16 shows the mixing performance for the multi-flag cases in terms of the Mixing Index (MI) and the Interface Density (I_D). The behavior of MI is significantly different from the single flag configuration which is shown here for reference. It should be noted that while the Re and Sc are the same for this single flag simulation, it is not meant as a directly comparable case as the total length is not the same, instead it is meant as a reference for the behavior observed for the single flags. In comparison, the multi-flag cases are smoother and more monotonic. It was theorized that the cause of the nonmonotonic behavior in the single flag cases was the high degree of order in the organization of the vortices in the downstream region, likely a 2D specific artifact. That the multi-flag cases exhibit such smooth behavior with x/W suggests that whatever organization which may be in the instantaneous snapshots has been homogenized by the temporal-spatial averaging during the MI calculation, which suggests more stochastic shedding phenomena and vortex organization is taking place.

The MI is also much higher for all the multi-flag cases than the single flag case. Furthermore, among the multi-flag cases the MI varies by 8% between best case L=0.67,1.0 and the worst case L=1.0,0.67. This is an interesting result. Part of the goal of this analysis was to examine the effect

of asymmetric flag lengths on the performance vis-à-vis their introduction of multiple length and time scales. To show this, in principle, both the asymmetric cases should overperform the case with only a single length/time scale. This is clearly not the case as the symmetric case lies between the asymmetric cases. Instead, it will be shown in later figures that the flag-flag coupling has dramatically changed the flapping behaviors of both the leading and following flags in all cases, which apparently dominates the behavior. However, this data does contain evidence that the asymmetry has had some effect. Examining the Interface Density figure, we can see that the symmetric case shows evidence of the nonmonotonicity which had been linked to spatiotemporal organization of the wake region in the single membrane cases. Whereas, the asymmetric cases show smoother, monotonic behavior for the Interface Density wherein the interface in the channel appears to be very rapidly stretched immediately around the flags to reach some saturated condition, after which the Interface Density remains largely constant.

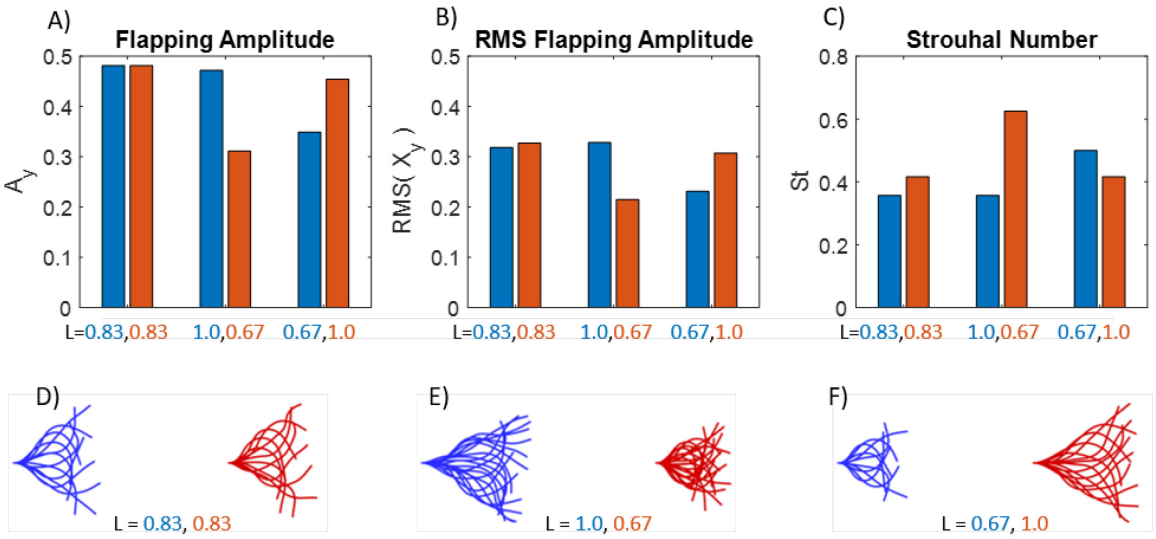

FIG. 3.17 – Plots showing the dynamics of the multi-flag configurations. A) is the time averaged maximum amplitude, B) is the RMS of the tip position of the flags, and C) is the channel width Strouhal number. D-E) show flapping envelopes for the cases.

FIG. 3.17 shows various measures of the dynamics of the multi-flag configurations. Here we can see that the confinement of the channel is clearly effect the L=0.83W and L=W flags in that their maximum tip excursions saturate around the channel half height (however, analyzing the time series show they never contact the walls). Interestingly, the combined mean tip excursion for the asymmetric cases is significantly less than that of the symmetric case. The RMS plot shows a similar result. If the RMS provides some notion of the flapping energy, one might expect that the most energetic case would provide the best mixing performance, however this data shows that is not the case as the best performing case L=0.67,1.0 is the middle performer with respect to the RMS and tip excursion.

However, in the St results, the L=0.67,1.0 case does stand out in that the average St between the membranes is higher than the other cases. Furthermore, the St are very similar for this case which is somewhat surprising considering the different flag lengths. It is possible that a lock on phenomenon may be at play in this case. This Is further justified by the flapping envelope figures. For all cases, only a small set of snapshots are plotted to provide a sense of the flapping behavior. For those cases which exhibited periodic flapping, such as the leading flag in the L=0.83,0.83 symmetric case and both flags in the L=0.67,1.0 case, the snapshots plotted comprise one cycle. The follower flag in the symmetric case, and both flags in the L=1.0,0.67 case exhibited highly aperiodic flapping behavior, so a sequence is plotted to give a sample of the mode shapes explored by this chaotic flapping behavior.

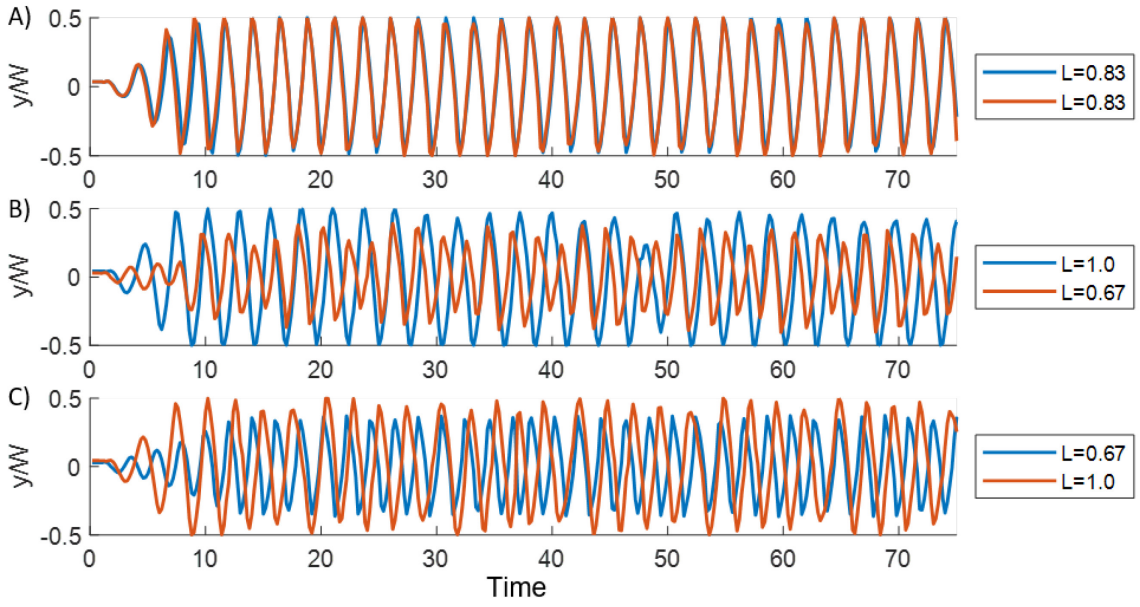

FIG. 3.18 – Time series of the tip y position for the multi-flag cases. The leader and follower are colored blue and red respectively.

The dynamics of these flags are very rich, and much of this richness is lost in the time averaged measures. FIG. 3.18 shows the y component of the flag tip as a function of time for each case. Examinations of these time series reveal a few key aspects of this system which are not apparent from the mean data. First, the symmetric case exhibits exactly in-phase flapping, even while the flapping RMS and St are slightly different. From the movies of the flag's behavior, it appears that the lock-on for the follower flag causes it to intermittently make small "corrections" to stay in-phase with the leader, leading to occasional atypical mode shapes. Alben (2009) examined wake-mediated synchronization of tandem flapping flags and showed that for certain separation distances, tandem flags would flap exactly in-phase. Interestingly, the L=0.83,0.83 case does not exactly fit Alben's result. Here, the separation distance between the flags is W, meaning the gap between them when normalized by their length is 1.2, however the nearest example which showed this phase locking in Alben's work was for gaps equal to the flag length. There are two possible explanations, it is possible that the confinement by the channel is modifying this wake-mediated synchronization,

or it is possible that this in-phase flapping behavior is subject to a lock-on phenomenon wherein the frequencies of one or both flags are being modified so as to flap in phase.

The second case L=1.0,0.67 shows complex behavior. Immediately one would assume that these flags are in the chaotic flapping regime based on the mode shapes they exbibit and the tip time series. However, the U* is too small for this to be the case on an individual flag level. Instead, it appears that this configuration is experiencing atypical flapping behavior due to the coupling between the flags. The leader flag appears largely unaffected in terms of the flapping period, though the flapping envelope and the time series show the flag has developed an asymmetric bias. Upon close inspection, the follower flag is flapping relatively periodically, however, it appears that there are multiple frequencies at play in its motion, as can be seen by a visible beating pattern in the data with a sequence which appears to have two large amplitude cycles followed by two smaller amplitude cycles.

The final case L=0.67,L=1 also shows a strong beating pattern, however in this instance it is between the flags. The flapping periods are such that for every 6 cycles taken by the leading L=0.67 flag, the follower takes exactly 5 cycles such that they are perfectly in phase approximately once every 11 nondimensional time units. This super harmonic lock-on is an interesting result and speaks to complicated, multi cycle interactions between the flags and the vortices they shed. Furthermore, the flapping amplitude for the L=0.67 flag is much larger than that of the L=0.67 from the previous case. Part of this is likely due to the fact that the shorter flag in case C is experiencing a cleaner inflow field as it is the leader in this case.

However, Ristroph & Zhang (2008) experimentally showed, and others corroborated, that tandem arrangements of flapping flags exhibit so called “inverted drafting” wherein the leading flag actually demonstrates higher flapping amplitudes than they would by themselves, and even higher amplitudes than the follower for certain configurations. This is most certainly partly responsible for the higher amplitudes of the L=0.67 flag. Alben (2009) showed using analytical

vortex sheet simulations that this inverted drafting phenomenon was due to wake-mediated coupling between the flags. They showed that for particular separation distances, vortices can add coherently in the wake. In those cases, the flags exhibited the same inverted drafting phenomenon as was seen in the experiments by Ristroph and Zhang. That wake mediated coupling mechanism is likely responsible for all the coupling phenomena seen in these results.

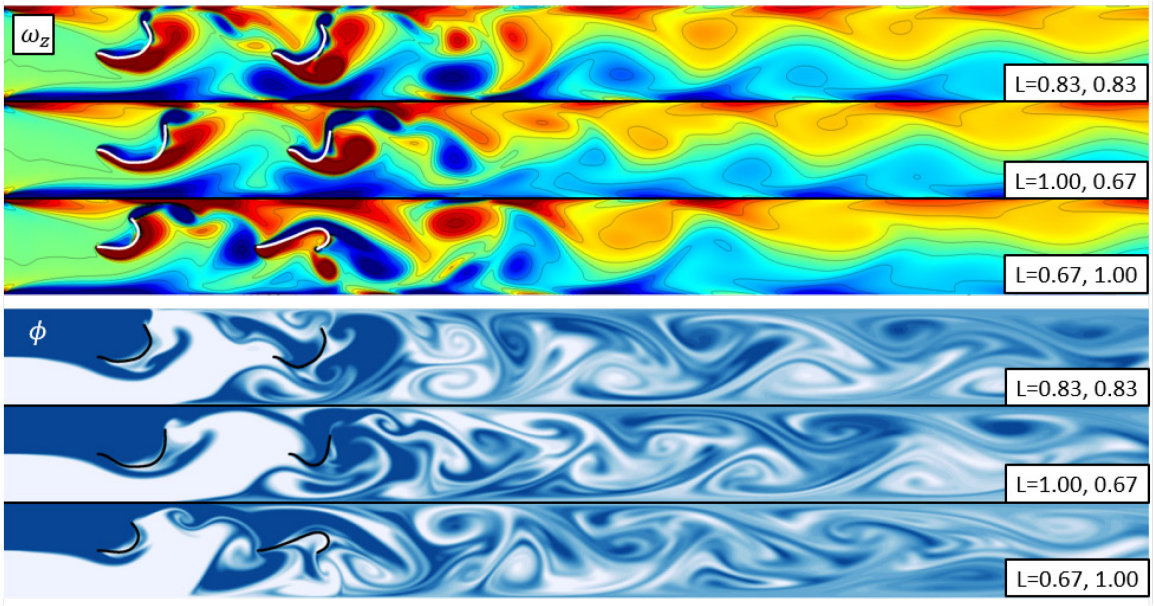

FIG. 3.19 – Snapshots of ω_z vorticity field and the scalar concentration field ϕ for the multi-flag cases.

To understand the fluid dynamic implications of these flapping behaviors, FIG. 3.19 shows snapshots of the vorticity and scalar concentration fields. Clearly the vorticity fields show far more complex behaviors than what was seen in the single flag cases. The region between the flags is interesting. The cases show significant differences in this region, particularly in the case of the L=1.0,0.67 case. For the other cases, we can see three distinct vortices which were shed by the leading flag, however we do not see these vortices for the L=1.0,0.67 case. In that case, the leading flag is larger than the other two cases, and so would create much larger vortices, however there is essentially not enough room before the follower flag for these larger vortices, which appears to either disrupt the vortices from the leader or stop them from being shed in the first place.

Also, the region just after the flags shows clustering of several vortices in all three cases. The complex interactions between the vortices shed by each flag create these clusters, and it is those interactions which are likely responsible for the sharp rise in the mixing index seen for all three cases. Beyond that complex region, these fields show different behavior between the cases, particularly in terms of the persistence of coherent vortices. The first two cases show similar behavior as was seen in the single flag configurations wherein large coherent vortices persist for many flag lengths downstream. However, this behavior is less apparent in the last case, which was the highest performing case. This can be seen by examining the vorticity isolines, which straighten out after several downstream flag lengths for the L=0.67,1.0 case but remain curved in the other two cases.

If we examine the scalar concentration fields, we can see the results of these differences. In all three cases, the region immediately after the flags is clearly exhibiting effective convective mixing. This can be seen because the flow appears streaky, yet those streaks still have high contrast meaning fluid is being advected but diffusion has not yet had the chance to smooth these streaks. This will be examined in more detail by looking at the scalar gradient field and the interface density field in FIG. 3.20. What is also interesting here is the behavior in the far wake. The first two cases show the same types of wake organization as was seen in the single flag cases with periodic organizations of pockets of fluid resembling vortices organized in a staggered pattern. However, the final case shows far less evidence of this behavior. Beyond appearing more mixed, this case also does not exhibit obvious spatial organization in this snapshot, and observations of the movies of this case show much more aperiodic behavior than the prior two cases. This is interesting as this case showed the greatest coherence in the frequency and phasing of the flapping dynamics.

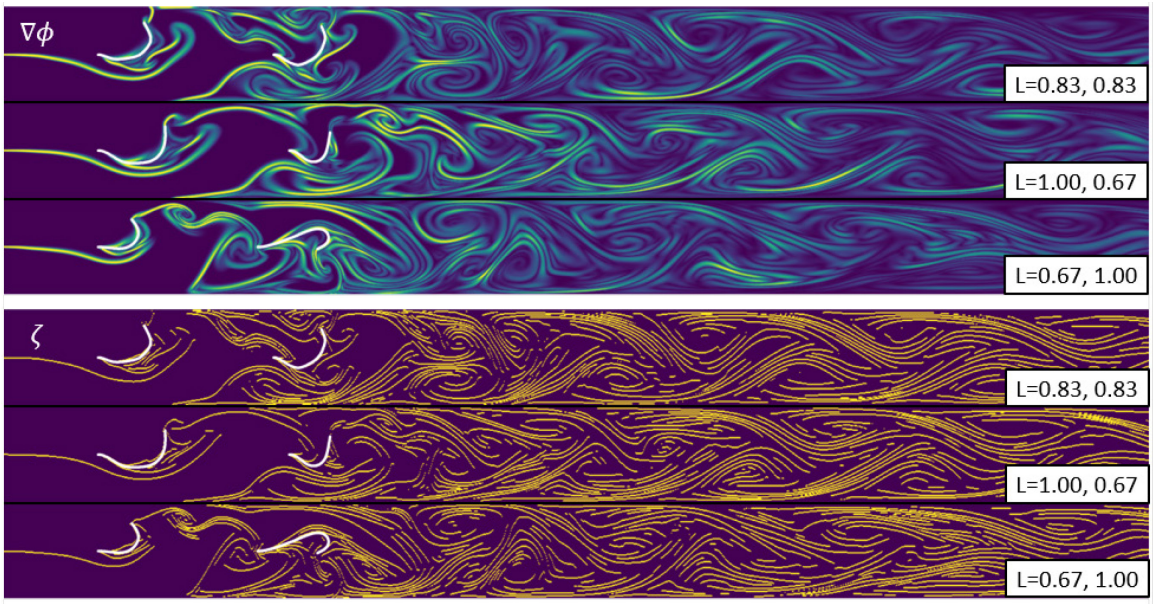

FIG. 3.20 – Snapshots showing the gradient of the scalar field $\nabla\phi$ and the detected interface field ζ for the multi-flag cases.

FIG. 3.20 shows the scalar gradient and the interface field which both show how all of these cases dramatically increase the advective mixing. The interface field shows that by the end of the second membrane, the domain is densely filled with interfaces. The patterns these cases exhibit in the scalar gradient fields are complex and show complicated and intricate interactions between multiple vortices. One interesting observation here is that for the L=0.83,0.83 case, and especially for the L=0.67,1.0 case, these indications of interface rollup or folding also appear in the space between the flags. It appears that due to the smaller size of the leading flags in those cases, there is enough room for the vortices to begin mixing the flow even before the start of the second flag, as was seen in the vorticity figures. The effect of this can be clearly seen looking back to FIG. 3.16 showing the time averaged Interface Density result. There, the L=1.0,0.67 case shows interface stretching is weaker and lags behind the other cases in the region between the flags. In principle a practical implementation of this technology could be designed to take advantage of these results by carefully choosing flag lengths and orders such that there is enough room before the next flag for vortices to be effectively shed.

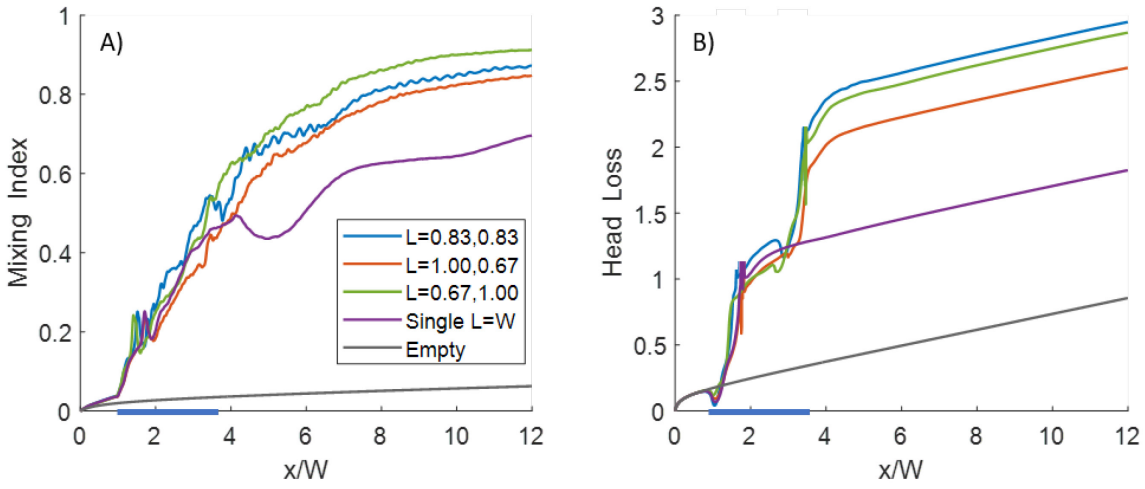

FIG. 3.21 – Plots of A) Mixing Index and B) Head Loss for the multi-flag configurations. Configurations with a L=W single flag and the empty channel configuration are also shown. The bars along the X axis show the regime containing both flags. Note that the spurious spikes in the Head Loss plot that occur just at the leading edge of each flag have been trimmed out for clarity.

To understand the performance of these systems from the perspective of energy expenditure, FIG. 3.21 plots the mixing index and the head loss. The mixing index figure is included again for reference. The head loss figure shows the expected behavior based on the single flag studies, wherein there is a sharp increase in the energy loss in the vicinity of the flag, after which the head loss progresses with the same slope as the empty channel case. However, the differences between the cases are interesting, and make selecting the "best" configuration more difficult. First, we can say that the L=0.67,1.0 categorically outperforms the L=0.83,0.83 case, as it has higher mixing and lower energy loss. However, comparing the L=0.67,1.0 and the L=1.0,0.67 cases is more difficult because while the L=1.0,0.67 case had the poorest performance in terms of the mixing index, it also shows the lowest energy loss; wherein the L=0.67,1.0 case had 8% better mixing index, but the L=1.0,0.67 case had 10% less head loss. The L=1.0,0.67 Head Loss result is particularly interesting. In principle, longer flags should have greater energy loss, especially considering the energy loss seems to be so dominated by viscous drag on the surface of the membranes. Thus one

would expect in all three case, the individual jumps for each flag would be different corresponding to their length, but the overall sum would be the same. However, this is not the case as the leading L=1.0 flag in L=1.0,0.67 case has slightly lower energy loss than the leading flag from the L=0.83,0.83 case. This discrepancy is responsible for the overall lower energy loss in that case, and may be a manifestation of the "inverted drafting" phenomenon which is not universal, but is instead dependent on the geometric parameters.

It is difficult to say which configuration is better. This is in large part due to the nature of the mixing index (or any measurement of mixing performance for that matter). The mixing index is not linear, in that it has a maximum at 1, and any performance improvements can only cause the system to asymptotically approach that value. Whereas, the head loss is ostensibly unbounded, or at least it is only bounded by a configuration which removes all kinetic energy from the flow causing the fluid to simply stop moving, which does not seem to have any real physical meaning in this type of a flow. Therefore, it is unclear how to directly compare these results relative to each other.

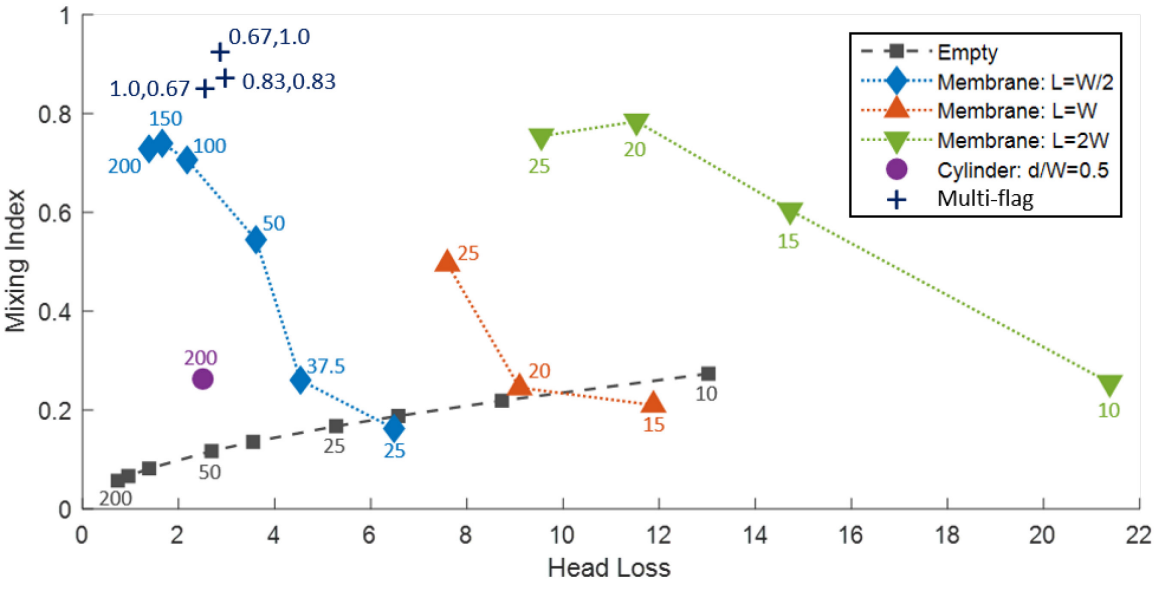

FIG. 3.22 – Performance comparison in terms of head loss and mixing index from the prior study with the added multi-flag cases. All the multi-flag cases are at Re=200.

We can however add our new results for the multi-flag flutter mixers to our performance scatter plot from the previous, single-flag flutter mixer study, as is shown in FIG. 3.22. Here we can see the significant improvement in mixing performance. The tandem flutter mixer has achieved very close to complete mixing in a very short channel length with only two flags. These cases are all at Re=200. Compared with the other Re=200 cases we can see they also have the highest overall Head Loss, but this Head Loss is still quite comparable to the best-performing "post mixer." Thus, this limited parameter study indicates the multi-flag configuration could be useful where rapid mixing is required over a short channel length, and that additional membranes added in tandem significantly improve the mixing performance.

Chapter 4

3D Mixing

The 2D mixing simulations provided an important initial assessment into the potential viability of flutter mixers for inertial microscale mixing enhancement. However, there are several limitations which restrict the fidelity and predictive utility of a 2D model towards the full 3D problem. As has been shown by others (Eloy, Souilliez, & Schouveiler, 2007), the 3D system is more stable than the 2D system, where narrower finite span flags were shown to be more stable than infinite span flags. This means the flapping amplitude of the flags could be lower depending on how close to the critical velocity the system is operating. Furthermore, spanwise confined flags also show different behavior. For instance, Doare et al. (2011) found that any appreciable gap between the sidewall and the spanwise edge of the flag leads to significant changes in the stability of the system, with confined finite span flags also showing greater stability than unconfined flags.

Beyond the potential differences in stability and dynamics between the 2D and 3D systems, the 3D system also has parameters and behavior that are absent in 2D. In the forced convection heat transfer section, we examined 3D flapping flags in channel flows at higher Reynolds numbers to examine their utility as heat transfer enhancement devices. In that work we showed that 2D and 3D confined flapping flags have several fundamental differences, both in terms of the flag's behavior as well as in terms of the fluid dynamics and the scalar field. Those simulations were conducted at significantly higher Re than what is examined here, namely Re=600. There it was shown that the flow phenomenon of primary importance in the 3D case was the production of strong streamwise

vortices, which cannot exist in 2D. Furthermore, it was shown that the flag dynamics were distinctly different, and that the overall system performance was only coincident between 2D and 3D at one location downstream of the flag, but was generally very different.

It is unclear how the comparison between 2D and 3D flapping flags will fair at the lower Re numbers of the inertial microfluidics regime that we study here. Usually decreasing the Reynolds number diminishes fluid dynamic instabilities. Furthermore, beyond the well-known differences between finite span 3D flags and infinite span 2D flags (Eloy et al., 2007), there are also considerable differences in flag flapping behavior at low Re, with large changes to the system stability as a function of Re, as was shown in the prior 2D mixing work. It is possible that these changes in stability at lower Re will exacerbate the differences between finite and infinite span flags, especially if the 2D and 3D configurations are pushed into different flapping modes and regimes.

Finally, it is possible that the 3D case can provide benefits to mixing which are not in the 2D model. We have conjectured that mixing enhancement mechanism of flutter mixers is interface stretching and folding due to large amplitude interface deformation and vortex production at low Re numbers. The notion here is that that the flapping flag advects the fluid in a way that deforms and stretches the interface in a particularly beneficial manner. Further, we have proposed that the flags are able to shed large vortices at lower Re numbers than other simple, passive vortex generation mechanisms such as bluff body shedding. For example, circular cylinder vortex shedding phenomena have a distinct and well known lower Re number limit for vortex shedding, and confinement such as would be seen in a channel flow has been shown to increase the stability of this vortex shedding phenomenon, further increasing the lower Re number limit (Sahin & Owens, 2004).

If this advection driven interface stretching mechanism is the key to flutter mixers' improved performance, it follows that this phenomenon would be more effective in 3D than 2D. This is because there is simply more room in three dimensions to pack the interfaces. This can be intuitively understood by considering randomly distributing a fixed number of interface locations in a 2D domain and in a 3D domain. Clearly the points could get farther apart in 3D than in 2D, meaning on average a distance metric would find higher norms in the higher dimension simply because there is an additional term in the norm for the higher dimension. While this is certainly a commonly understood aspect of changes in dimensionality, it has interesting implications on our 3D mixing system, specifically in that it is possible that given the same interface generation conditions, and assuming there is some lower limit to interface packing, then the 3D case can fit more interface length for any given streamwise position. On the other hand, 2D flows often exhibit non-physical behavior in terms of vortex persistence. This is due to the fact that there is one fewer dimension for the vortex to dissipate in. The effect would significantly increase the performance of the 2D system over the 3D system.

In this study, we examine the 3D flutter mixer in the inertial microfluidics regime. We seek to understand the fluid and structural dynamics of the baseline system and to identify what mechanisms if any are responsible for any increased mixing performance. We then examine the sensitivity of this system to decreasing the Re number from our starting point of Re=200 via a sweep ending at Re=50. We also examine the changes in behavior as a result of changes to the 3D specific parameters, namely the spanwise gap to the sidewalls and the aspect ratio by examining a flag with a narrower span in the same square channel as the prior baseline simulations. Finally, we examine the differences between the 2D system and 3D system in order to glean further understanding of the nuances of each system.

4.1 Problem Description

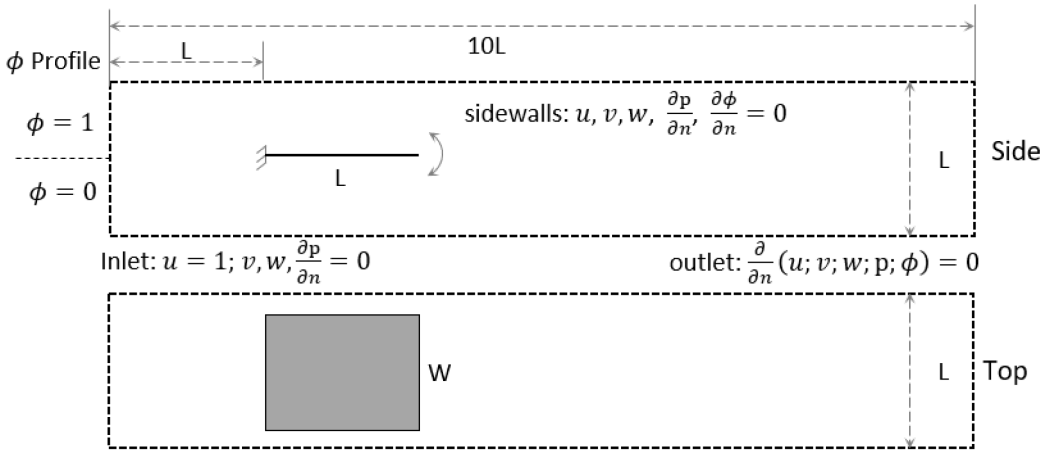

FIG. 4.1 – Schematic view of the 3D flutter mixer configuration.

To study the 3D flutter mixer in a channel type inertial micromixer, we consider a flapping flag immersed in a developing channel flow. FIG. 4.1 shows a schematic of the system depicting a top view and a side view. The flapping flag is considered to be a 2D membrane with negligible thickness compared to its length L and width W. It is a "normal flag" in that the leading edge is fixed and the trailing edge is free. The flag is placed near the entry of the channel to model the flow that would be seen in a T type or Y type mixer, for example. The inflow boundary condition is modeled as a uniform plug flow with U=1 where U is the velocity in the streamwise direction. The channel is considered to have no slip, no penetration boundary conditions on the walls and the outflow is generally modeled with zero-gradient boundary conditions. The species to be mixed is modeled as a passive scalar with a normalized concentration ϕ such that the fluid which is fully saturated with the species in question (i.e. fully dyed fluid) has a concentration of $\phi = 1$ and fluid that is completely undyed has a concentration $\phi = 0$. The inflow to the channel is a step function with $\phi = 1$ in the top half of the channel and $\phi = 0$ in the lower half. This inflow boundary condition is oriented such that the interface between the two halves is coplanar with the membranes surface.

This configuration is identical to the model used for the 2D study in terms of boundary conditions and initial conditions.

4.1.1 Numerical Methods

To compute the fluid and scalar fields as well as the structural position, we perform fully coupled 3D fluid-structure-scalar interaction simulations. The fluid is governed by the incompressible Navier-Stokes equations and is solved with finite differencing on cartesian grids using a fractional step method to advance so as to decouple the advection diffusion equation from the pressure Poisson equation. The structure is modeled as a plate with a Cartesian grid representing Lagrangian coordinates S_1 and S_2 in the chordwise and spanwise directions respectively. The equations for the position of the membrane are solved via finite differencing. We use a penalty method immersed boundary method to couple the fluid and structural solvers with two tunable parameters representing springs and dampers coupling the fluid and structure solutions. The scalar field is governed by an advection diffusion equation with a step inlet boundary condition and Neumann boundary conditions on the channel walls. The scalar solver is one way coupled from the fluid solution to the scalar solution. The details of the various solvers as well as the FSI coupling scheme is described in the numerical methods section earlier in this thesis.

4.1.2 Performance Measures

The performance of the system is measured with a few key metrics. First, the Mixing Index used previously in the 2D flutter mixer study is used again for the 3D mixing performance measure and is defined as:

$$M(x) = 1 - \sqrt{\frac{\sigma(x)^2}{\sigma_{\max}^2}} \tag{4.1}$$

$$\sigma(x) = \sqrt{\frac{1}{L^2}\int_0^z \int_0^y \left(\phi(x,y,z) - \bar{\phi}_m(x)\right)^2 dydz} \tag{4.2}$$

where $\sigma(x)$ is the standard deviation, ϕ is the scalar field ranging from 0 to 1, $\overline{\phi}_m$ is the mean of the field at that x plane and $\sigma_{\max}$ is the maximum deviation in the scalar field, which occurs at the inlet. The mixing index is essentially the normalized variance of the scalar concentration. It ranges from 0 to 1 with M=0 indicating totally unmixed flow and M=1 is completely mixed flow.

To fully understand the impact of a given mixing enhancement device, the energy losses must also be considered. This is because the mixing performance of these systems is sensitive to the Reynolds number. This is important because it means that if the Reynolds number was increased (e.g. if a stronger pump was used) then the mixing performance would change. Thus, if a particular system is improving the mixing performance over a reference design, but is also creating a significant increase in energy expenditure as compared to that reference design, it is possible that had the reference design been given that additional pump power, it might have actually overperformed the augmented test design. Furthermore, the practical considerations of microfluidic devices mean that even if a mixing enhancer is beneficial even when normalized by energy expense, it is still possible that the large increases in pump power requirement may not be feasible from a practical perspective. To quantify this loss in mechanical energy, we use the non-dimensional head (H*) and corresponding head loss (HL) through the channel:

$$H^*(x) = \frac{H(x)}{\rho U^2} = \int_0^Z \int_0^Y \left(p(x,y,z) + \frac{1}{2} u^2(x,y,z) \right) dydz \tag{4.3}$$

$$HL^*(x) = H^*(0) - H^*(x) \tag{4.4}$$

where p is the pressure, u is the streamwise velocity component, and ρ is the fluid density.

To locate and identify vortices in this 3D flow, we use the λ_2 vortex criterion. This is a vortex core identification method (Jeong & Hussain, 1995). To calculate this criterion, we construct the velocity gradient tensor ∇u. We can then decompose this tensor into its symmetric and

antisymmetric parts $\mathbf{S}$ and $\mathbf{Q}$. We then construct $\mathbf{S}^2 + \mathbf{Q}^2$ and order its eigenvalues $\lambda_1 \geq \lambda_2 \geq \lambda_3$. Finally, a point is only part of a vortex if two of the eigenvalues of $\mathbf{S}^2 + \mathbf{Q}^2$ are negative, so if λ_2 is negative we have successfully identified part of a vortex. A vortex is then defined as a connected region of negative λ_2. Plotting iso-surfaces of λ_2 shows a given 2D shell of a 3D vortex region.

4.1.3 Interface Identification and the Interface Density

The idea underlying all mixers is that flow fluctuations and/or vortices lead to stretching and folding of the flow. This leads to a lengthening of the interface between the two unmixed regions of the flow thereby allowing molecular diffusion to work effectively over a length scale much larger than the length scale of the underlying unmixed system. The mixing index defined earlier in the chapter provides one clear measure of the mixing effectiveness but it is a composite measure of interface lengthening and molecular diffusion and therefore dependent not only on the flag dynamics but also parameters associated with molecular diffusion (i.e. Reynolds and Schmidt numbers). As was the case in the 2D mixing investigation, it would be useful to extract from our simulations a direct and distinct measure of interface lengthening associated with the stretching and folding induced by the flag flutter, a measure that is somewhat independent of subsequent molecular diffusion effects. We described just such a measure in the 2D mixing section which we called the Interface Density, and we will use that measure again for our 3D investigation. However, there are non-trivial differences between the 2D and 3D calculations and normalizations of this measure.

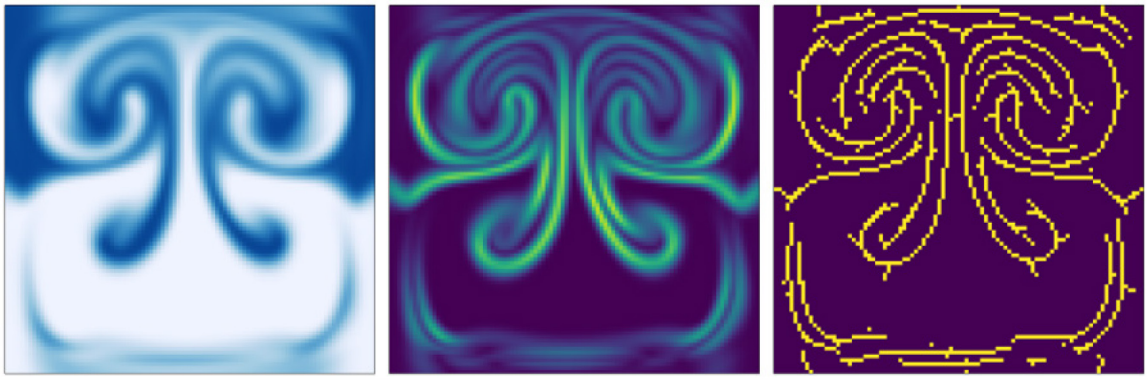

FIG. 4.2 – Example of the interface identification process showing the scalar concentration ϕ, the normalized magnitude of the scalar gradient $\nabla\phi^*$, and the interface field ζ.

The Interface Density is based on the notion of measuring the stretching of the interface length by counting or estimating the number of interface locations (pixels) generated in the discrete flow field across which molecular diffusion can act to effectively mix the two components of the flow. This value is then normalized against the maximum number of interfaces that are possible for that grid. FIG. 4.2 shows three contour plots of a snapshot of an x plane from one of our simulations. These plots provide a visual depiction of the calculations needed to create the interface density measure, showing the scalar concentration field ϕ, the normalized magnitude of the scalar gradient $\nabla\phi^*$, and the interface field ζ. Note that these figures have been displayed without the use of any interpolation or anti-aliasing procedures (which we commonly use in all other figures presented in this work). Each pixel on the plane is simply colored according the magnitude of the field variable at that location. This allows us to better visualize the resolution constraints at play. To perform the calculations for this measure, we first calculate the magnitude of the gradient of the scalar field at each streamwise location, and then normalize by the local maximum as follows:

$$\nabla\phi^*(x,y,z) = \left|\nabla\phi(x,y,z)\right| / \left\|\nabla\phi(x)\right\|_\infty \tag{4.5}$$

where the overbar indicates the average over that given x (streamwise) plane of data. In a finite Reynolds and Schmidt number calculation (as opposed to an inviscid model), molecular diffusion will tend to smear the gradients in the scalar field as the flow proceeds downstream. Given this, the above normalization step ensures that this overall reduction in scalar gradients is accounted for and eliminated, allowing our interface detection procedure a consistent signal level, independent of streamwise position.

We then proceed to determine the local maxima of this normalized gradient magnitude on each x plane. Essentially, we find peaks in the field which satisfy a "prominence" criteria based on their height relative to the neighboring valleys. This constraint allows us to ensure that we only count peaks that represent relatively large jumps in the local scalar concentration. This is because the diffusion across these interfaces (i.e. the mixing) is related to this gradient, so only sufficiently strong gradients will appreciably impact the mixing of the fluid. One of the key differences as compared to the 2D system is the procedure we used to find these peaks. In the 2D system, we could simply take each y line of values at a given x location and find the peaks of that set of data. However, for the 3D case it is not as easy to find peaks on each y-z plane of data. Instead, we treat each direction separately and combine the data. At any given x location, we first sweep along the y direction, identifying peaks for each z line. We then do the same for the z direction, identifying peaks for each y line. This raises a problem of how to combine these data for each direction.

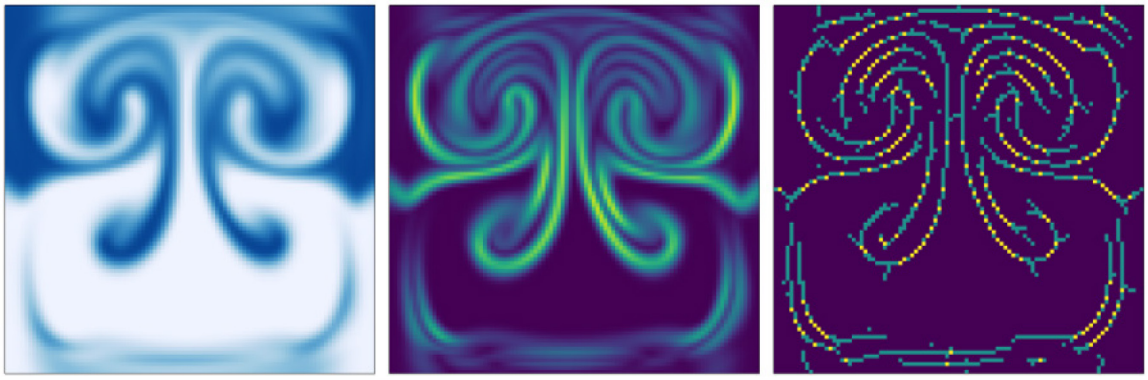

FIG. 4.3 – Interface detection procedure showing the additive interface detection mechanism where the interface pixels can have a value of 0 (no interface), 1 (interface allowing diffusion in only one direction), or 2 (interface allowing diffusion in both directions).

On the one hand, we could treat the directions with an "or", where we would tag each pixel in a binary sense as either an interface or not. If a given pixel was identified for either direction of sweeps then it would get tagged. This method results in the interface field shown earlier in FIG. 4.2. This method is reasonable for identifying where the interfaces are, but it does not actually fairly count the interfaces. To understand this issue, we must recognize that the diffusion we are trying to promote is on a cartesian grid. This means that any given pixel could be a location where diffusion is happening in either of two directions or in both directions. If we envision a field with vertical stripes of scalar concentration, then each pixel would be diffusing only in the horizontal direction. Similarly, if we envision horizontal stripes the pixels would only be diffusing vertically. However, if we then consider a field which is arranged in a checker board pattern, each pixel would be diffusing in both directions as all its neighbors have the opposite concentration. While the total concentration is the same for the stripes and the checkerboard, the checkerboard will clearly diffuse much more quickly.

By this logic, we combine the results of the sweeps in the y and z directions using an "and" function such that the pixels can have a value of: 0 (no interface), 1 (interface allowing diffusion

in only one direction), or 2 (interface allowing diffusion in both directions). This procedure results in the interface field shown in FIG. 4.3. Here we can see the locations of the flow which have interfaces which are mostly vertically or horizontally aligned have been tagged with $\zeta = 1$, while locations which have diagonal interfaces are tagged as $\zeta = 2$. To then come up with an overall measurement of the total interface length at any streamwise plane we construct the following interface density:

$$I_D(x) = \frac{1}{L^2} \sum_{z=0}^{L} \sum_{y=0}^{L} \zeta(x, y, z) \tag{4.6}$$

This is essentially an average over the given x plane. However, there is one final task required. It is necessary to normalize the interface density. In its current form it can take a value up to 2. However, it is useful to have the interface density normalized against the maximum density possible for a given resolution, thus the interface density is divided by 2. The only instance where this normalization is not used is when comparing with 2D systems, because in that scenario, the fact that the Interface Density can reach 2 for 3D and can only reach 1 for 2D has an important physical meaning.

4.2 Results

To explore the 3D flutter mixer, we first examine in detail a baseline case at Re=200, Sc=100. We then study the behavior of this system at Reynolds numbers of 50, 100, 150, and 200, all at Sc=100. This Reynolds number sweep is important because the applications for flutter mixers exist in the inertial microfluidics regime, typically Re=O(1-100), and fluid dynamics phenomena often show strong Reynolds number dependence in this regime, especially for systems that rely on vorticity. The Reynolds number sweep is also important in that it may shed light on different mechanisms at play in these flows, just as was the case in the 2D study where the Re sweep showed the sinusoidal interface deformation mixing mechanism at low Re and the vortex shedding mixing

mechanism at higher Re, thus providing a more complete picture of flutter mixers mixing enhancement.

We subsequently examine flags with a small aspect-ratio at various Reynolds numbers. Changes in a flag's aspect-ratio also simultaneously changes the spanwise gap between the flag and the sidewalls (we refer to this as spanwise confinement). Both the aspect-ratio and the spanwise confinement are parameters that only exist in 3D so cannot be modeled in a 2D study. Furthermore, as will be shown, the production of streamwise vorticity from the spanwise edges of the flag plays an important role in the mixing enhancement, so it is valuable to understand how the production of this streamwise vorticity might be modified and how the behavior and interaction of that streamwise vorticity would subsequently change. Finally, we compare the 3D results of the Re number study with the 2D model, which is an approximation frequently used to study channel flow type mixers, especially at these relatively low Re numbers.

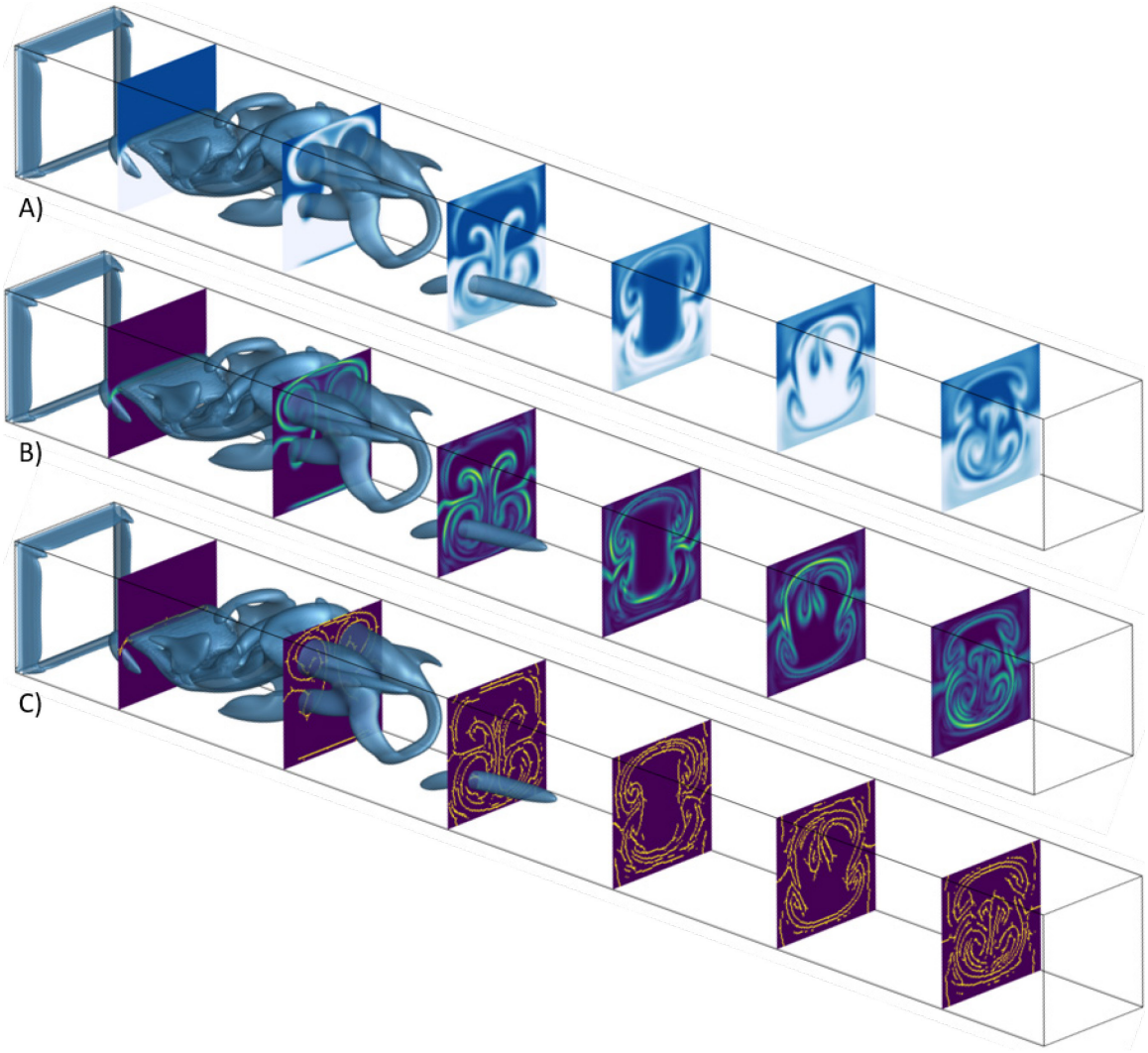

FIG. 4.4 – 3D visualizations of snapshots of A) scalar concentration ϕ, B) the normalized gradient magnitude $\nabla\phi^*$, and C) the Interface Field ζ for the Re=200 case. The isosurfaces in the flow show the λ_2 vortex identification criterion.

FIG. 4.4 shows 3D snapshots of the Re=200 case. In all three plots the isosurfaces in the flow are visualizations of the vortical structures in the flow by way of the λ_2 criterion. The color contours on the surfaces show A) the scalar field ϕ, B) the normalized magnitude of the gradient of the scalar field $\nabla\phi^*$, and C) the calculated local peaks in the scalar field as the interface field ζ. We can immediately see in the scalar field how vorticity shed from the flag is responsible for mixing the flow. In figure A), examining the cross-stream plane immediately downstream of the

flag, we can see a large, symmetric swirl pattern where it appears that the "white" fluid is being forced upwards creating a jet up into the "blue" fluid. At the center of the swirl patterns are large vortical structures as shown with the isosurfaces of the λ_2 criterion.

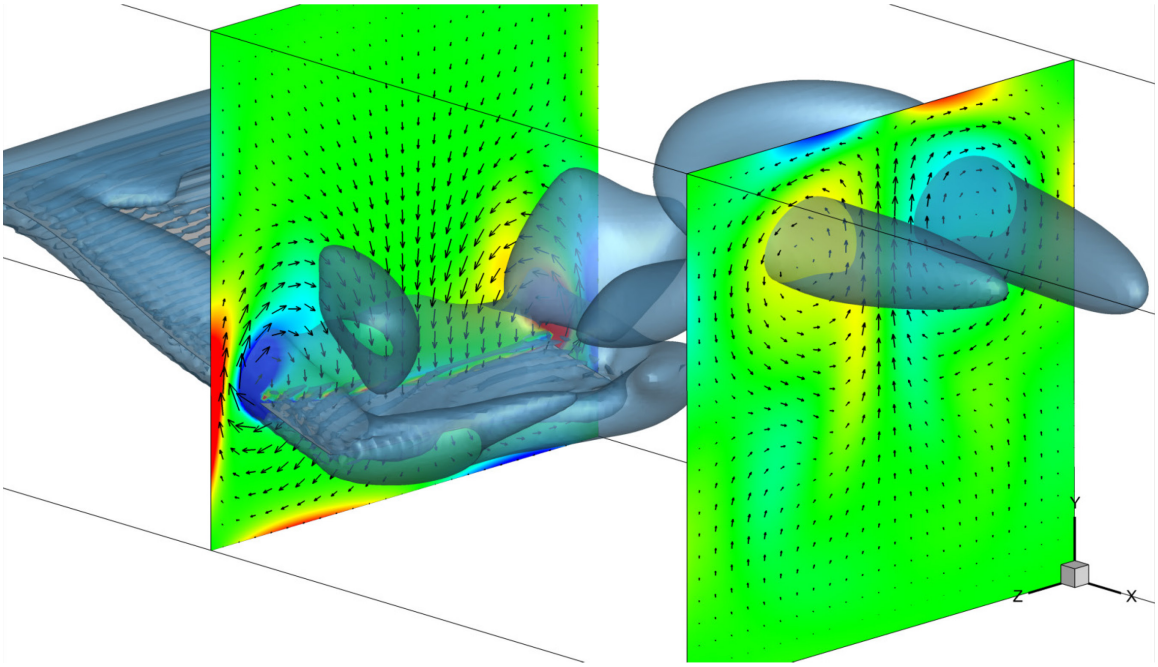

FIG. 4.5 – Zoomed in 3D snapshot of the Re=200 case. The color contours on the planes show the ω_z component of vorticity, the isosurfaces show the λ_2 criteria for vortical structures (at a higher threshold than FIG. 4.4), and the vectors on the cross-stream planes show the in-plane fluid velocity vectors.

As discussed in the chapter on 3D heat transfer enhancement, these streamwise vortices are the result of leakage flow around the sides of the streamwise membrane edges on each side of the flag. FIG. 4.5 shows a zoomed in view of the region around the flag and includes visualization tools to examine these vortices. The isosurfaces show the λ_2 criterion taken at a higher threshold than what was used in FIG. 4.4 so as to isolate the vortex cores, making the visualization less cluttered. The planes show color contours of the ω_z component of the vorticity, and the vectors show the in-plane fluid velocity vectors. This figure allows us to examine both the generation of this vorticity at the flag as well as the most recently shed vortical structure as it is advecting downstream.

Examining the behavior around the flag, we can see that as the flag flaps, the side in the direction the flag is moving becomes the pressure side and the opposite side becomes the suction side. Flow will seek to equalize this pressure drop by going around the streamwise edges from the pressure side to the suction side, which creates streamwise vorticity on each side of the flag as can be seen in the color contours. These vortices appear to be similar to leading edge vortices, as the flag is moving downwards as they are generated, and similar to tip leakage vortices as there is a considerable streamwise velocity affecting these vortices. These vortices are mirrored across the midplane of the flag, and once they are shed, they are clearly responsible for this jetting behavior. This can be seen in the downstream plane of FIG. 4.5 where the vorticity shed by the flag has created a distinct horseshoe shaped vortex, and the arms of that horseshoe vortex are close enough to jet fluid towards the wall, as indicated by the in-plane velocity vectors.

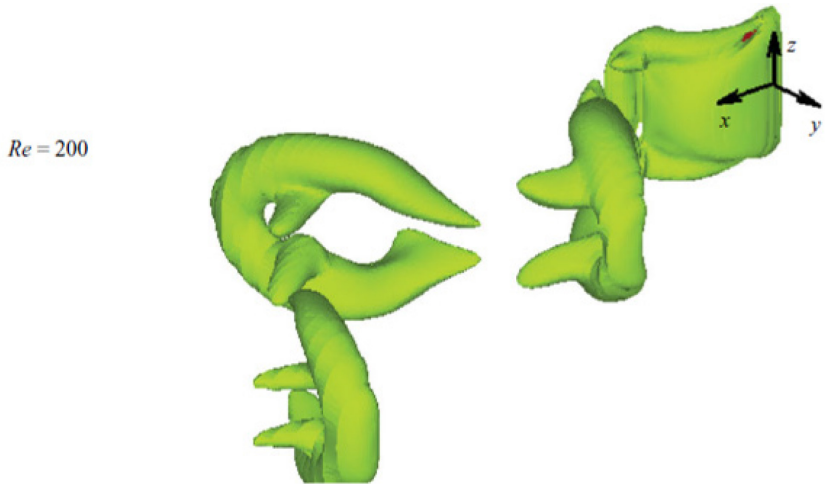

FIG. 4.6 – Snapshots of vortical structures from a 3D FSI simulation of a flapping flag at Re=200 taken from Huang & Sung (2010) for comparison. The key similarity to FIG. 4.5 is the presence of the horseshoe shaped vortices.

This horseshoe vortex shape has been seen previously in the literature for unconfined flapping flags. For example, Huang and Sung (2010) showed similar looking vortical structures shed from the flag, as can be seen in FIG. 4.6 from that paper. That simulation was at Re=200 as well and had

similar structural parameters to what is examined herein. Interestingly, in that study of unconfined 3D flapping flags, the horseshoe vortices are spreading out with a wake angle and the horseshoes are inclined the direction of the mean velocity. This behavior explains why the horseshoe vortices migrate to the channel walls in our confined simulation. One further difference is the orientation of these vortices, where it appears that confinement has rotated the vortices to be more in line with the streamwise direction. This rotation and alignment is due to the vortices interacting with their image vortices created by the presence of the wall.

There appears to be two major benefits of the jets created by these vortices. First, the advection of fluid from one half of the channel into the other half is of crucial importance towards mixing, as it will create pockets of opposite colored fluid in each layer of the incoming flow. Second, we can see at the centers of these vortices a clear swirl pattern of alternating blue and white fluid. The effect of this can be seen more clearly by examining figures B) and C) of FIG. 4.4 where we can clearly see densely packed sharp gradients in B) and the corresponding interfaces in C). This swirl pattern is beneficial in that it rapidly increases the interface length in the flow. It also tightly packs these striations, meaning that very quickly there will be pockets of very well mixed fluid.

In FIG. 4.4, we can see the continuation of this jetting process downstream of these initial instances of the jet. By the next cross stream plane, we can see there are two halves of the jet, after splitting due to impinging on the upper (or lower) channel walls. By this point those half jets, which are made up of very thin layers of alternating scalar, are re-colliding in the middle of the channel. In the next plane, and the subsequent planes as well, we can see a pattern emerging wherein the area along the edges of the channel has much higher concentration of interfaces and is subsequently much more mixed than the fluid in the core of the channel which appears to have an oscillatory pattern. This examination provides a clear phenomenological view of how the production of streamwise vortices plays a crucial role in the creation of the highly stratified layers along the channel walls.

4.2.1 Effect of Reynolds Number

The inertial microfluidics regime of Re=O(1-100) is unique in that both viscosity and inertia play an important role in the dynamics of the flow. This is especially true for systems which rely on vorticity, because the generation and persistence of vortices changes significantly in this Reynolds number regime. By examining the behavior of this system at a few Re numbers, namely Re=50, 100, 150, and 200, we can see the effects of this Re number sensitivity. For these studies, Sc=100, the flags are always length L and the spanwise gap is 0.2L meaning the flag aspect ratio is 0.6.

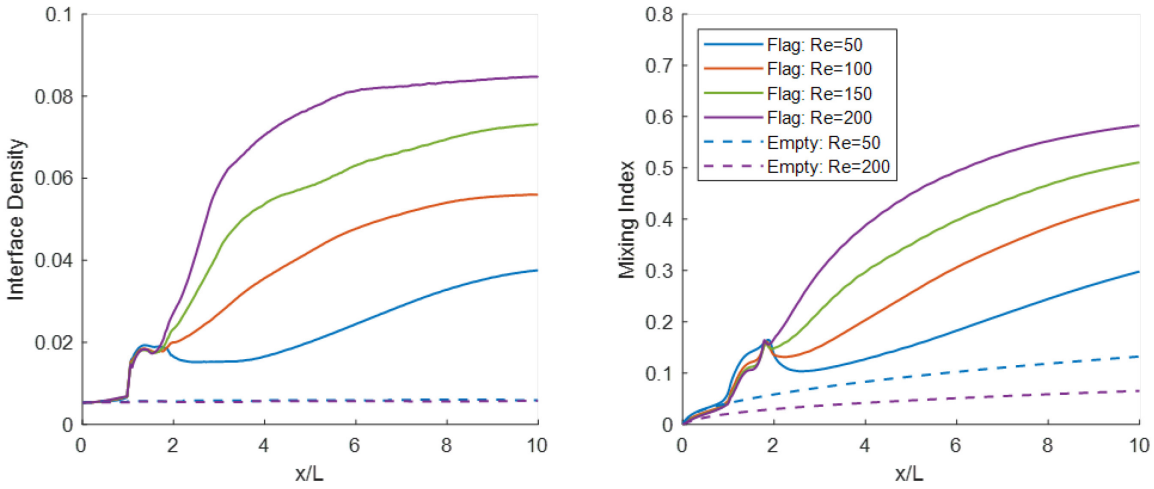

FIG. 4.7 – Time average of Interface Density and Mixing Index as a function of x/L for the four Re numbers simulated.

FIG. 4.7 shows the time-averaged Interface Density and the Mixing Index performance measures as a function of streamwise position x/L for each of the Re cases. Results for the empty channel are also included as a baseline for comparison, however only the Re = 50 and 200 empty channel cases are included so as to reduce clutter. For both performance measures we can see a very strong dependence on the Reynolds number. In the Interface Density plot we can that at the lowest Re case, i.e. Re=50, the increase in interface surface area is present but results in only a moderate improvement over the empty channel baseline. The empty channel baseline for the

interface density corresponds to the value at x/L=0 and represents a flat interface as wide as the channel.

For the Re=50 case, the addition of the flag increases the effective interface length by about 6.5 times before leveling off towards the exit of the computational domain. With increasing Re, this improvement rises as well, with Re=100 doing 10.5 times better, Re=150 doing 14 times better and Re=200 doing 16 times better by the end of the channel, as can be seen in FIG. 4.7 showing the Interface Density and Mixing Index at the end of the computational domain. There is also a change in the shape of the curve of Interface Density. With higher Re, the curves rise much more rapidly and by the Re=200 case, the stretching of the interface appears to reach a maximum very quickly, such that by x/L=6 the Interface Density curve has already flattened out. It should be noted that the behavior of neither of these measures in the vicinity of the flag itself (from x/L=1 to 2) are reliable, as the presence of the membrane inhibits the post processing calculations at those locations.

This rapid increase and subsequent plateau of the interface density is interesting in that it indicates that for Re=200, the continued stretching and folding of the interface ceases at around x/L=6 whereas for lower Reynolds numbers, stretching and folding of the interface continues beyond x/L=10. The Mixing Index plots show the same strong Reynolds number dependence that was seen with the interface index. However, the mixing index plots exhibit a continuous increase with streamwise distance. This is expected since mixing is a result of the combined effect of stretching and folding (i.e. advection) as well as molecular diffusion. Thus, even after the cessation of stretching and folding exhibited beyond x/L=6 for the Re=200 case, molecular diffusion continues to mix the two scalar fields.

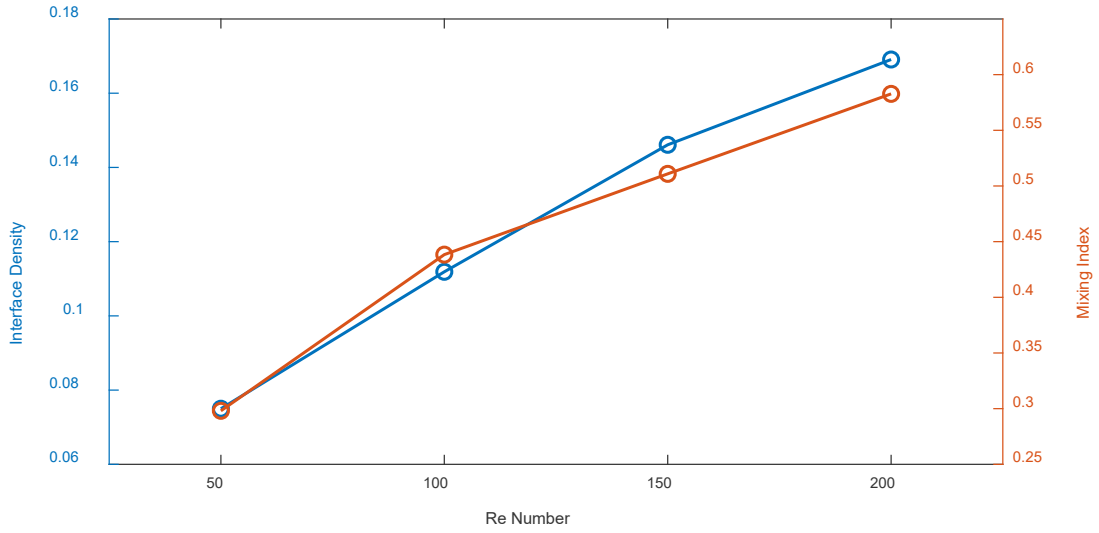

FIG. 4.8 – Interface Density and Mixing Index at the end of the computational domain as a function of Re.

This similarity between the Mixing Index and Interface Density is an important correlation, as it lends credibility to our proposed notion that flutter mixers improve the mixing performance over such a short distance as compared to other types of systems due to the very rapidly stretching and folding induced by the vortex structures generated by the flow-induced flutter. To further investigate this correlation, FIG. 4.8 shows the behavior of the Interface Density and Mixing Index at the end of the computational domain as a function of Re. Here we can see that if we ignore the magnitude of the two plots, their trends almost exactly collapse, showing this strong correlation. Also, it is interesting that the behavior seems to be almost linear with Re to first order. This result is not expected, as the mixing mechanism is likely to change throughout this regime. To better understand the mixing mechanism and underlying fluid dynamics we can examine snapshots of the system.

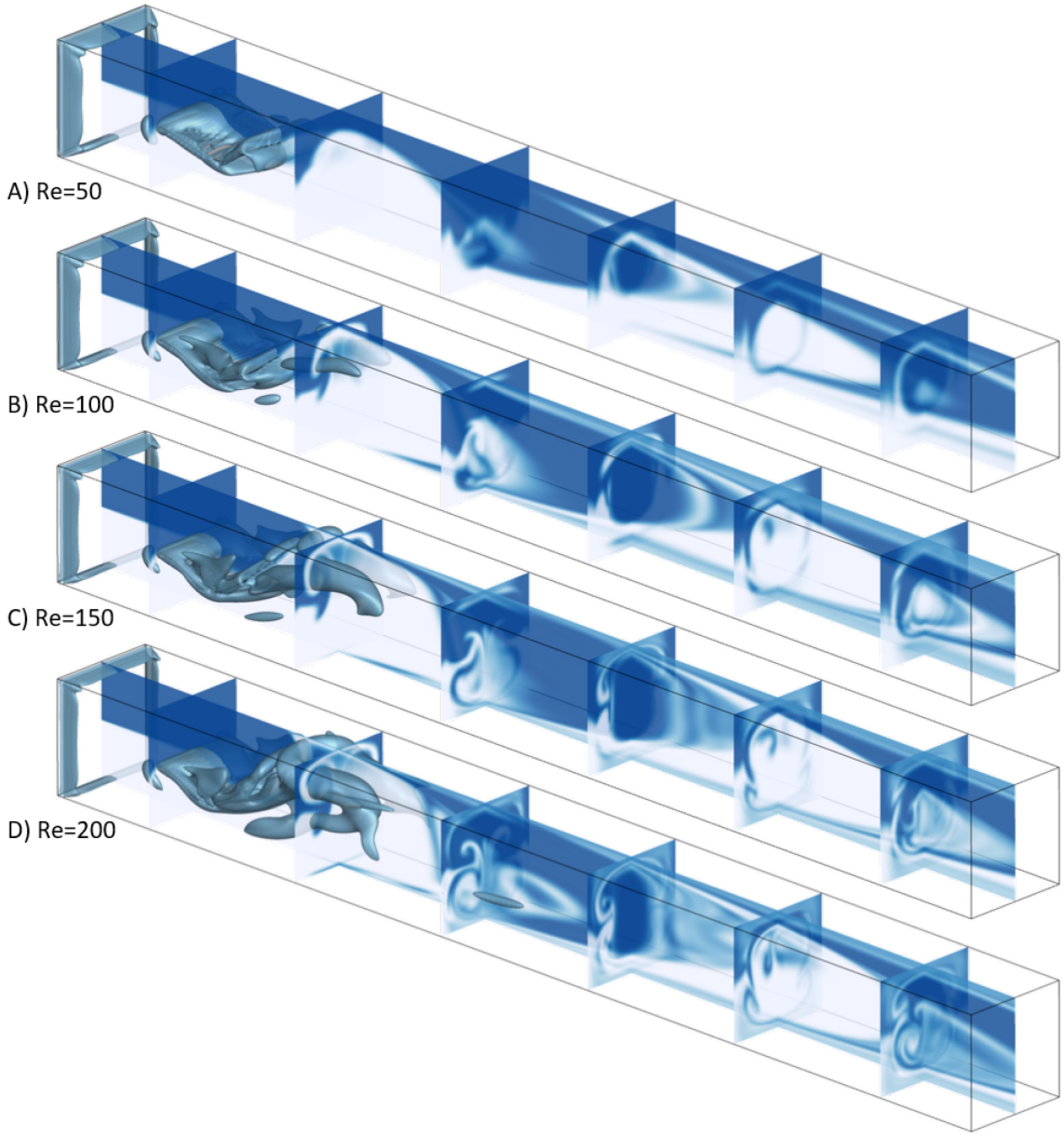

FIG. 4.9 – 3D visualizations of snapshots showing the scalar field ϕ for the four Re numbers simulated.

To better understand this dramatic change in performance with increasing Reynolds number we examine snapshots of the scalar field in FIG. 4.9. Here the contours on both the cross-stream planes and the streamwise midplane show the scalar field ϕ, and the isosurfaces are the λ_2 criterion for the vortical structures. The clearest result from these snapshots is that there appears to be a fundamental shift in the behavior between Re=50 and Re=100. In the Re=50 case we can observe

the flapping flag smoothly perturbing the interface in the streamwise mid plane view; this creates alternating pockets of dyed and undyed fluid in the streamwise direction. The cross-stream planes show that this region is largely confined to the center of the channel and that this region appears to get smaller with downstream distance.

This is very different from the behavior seen in the other three Reynolds number cases. Those cases all show the jetting behavior which was previously described in the analysis of the Re=200 case. Examining the first cross-stream plane after the flag, we can see that this jet pattern appears to get stronger at higher Reynolds numbers, which makes sense since the vortical structures being shed appear to be much stronger and more persistent at higher Reynolds numbers. Examining the next downstream plane, we can see the effect of this changing persistence of the vortical structures. In the Re=200 case we can see that the scalar still clearly shows the swirling patterns indicating that the vortices are still strong enough and induced a jet. This effect is weaker in the Re=150 case and for the Re=100 case, it appears that the jetting phenomenon is no longer active. Examining the final cross-stream plane for each case, we can see that the Re=200 case still shows evidence of the jetting behavior; the Re=150 case seems to have remnants of that behavior but it does not appear to be active at that downstream location. The Re=100 case has no evidence of the swirling patterns caused by the streamwise vortices and in fact appears much more similar to the Re=50 case at this point, despite having shown clear evidence of the vortex induced jetting mechanism earlier in the channel.

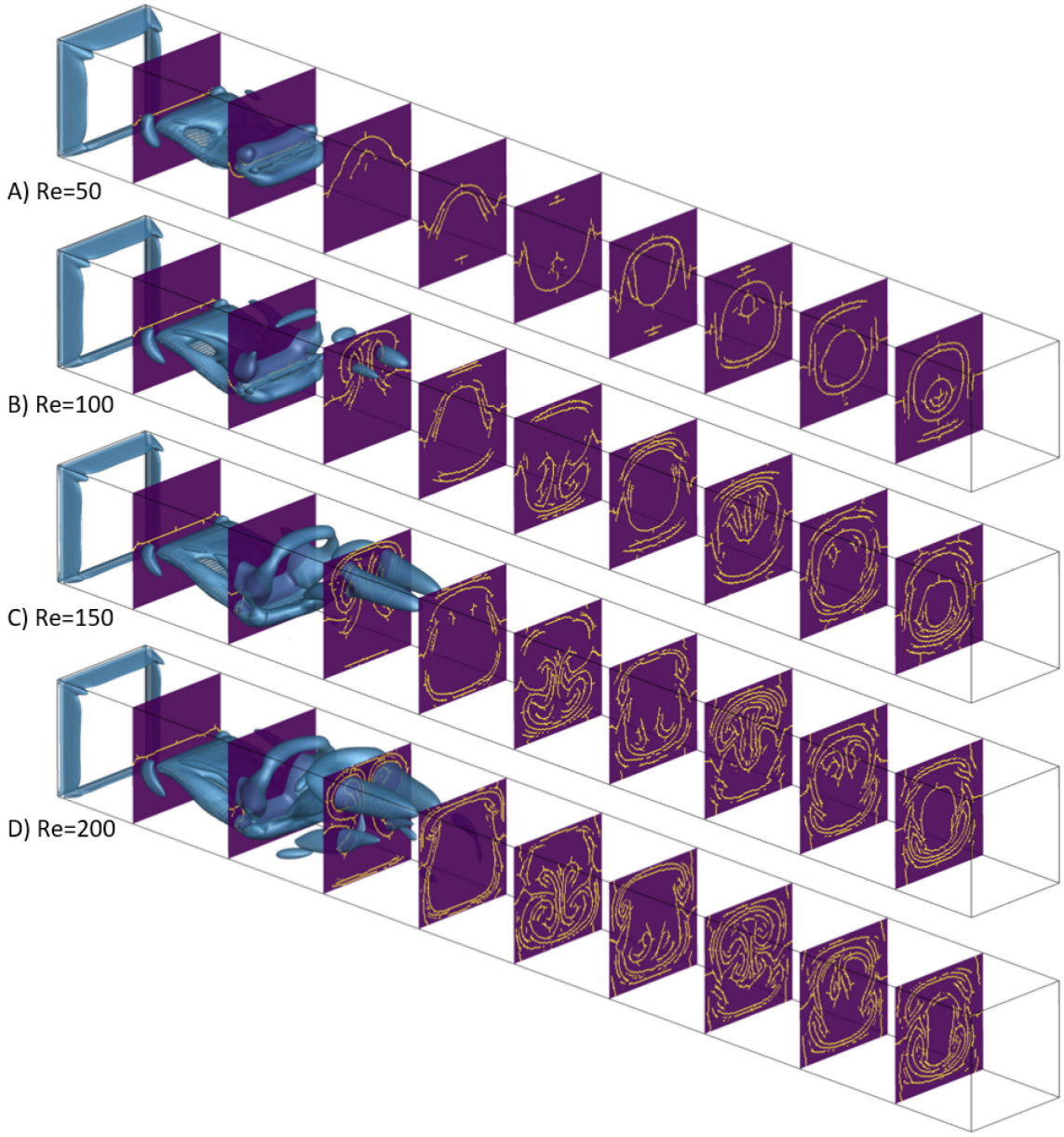

FIG. 4.10 – 3D visualizations of snapshots showing the interface field ζ for the four Re numbers simulated.

FIG. 4.10 shows 3D snapshots of the interface field ζ for each Re case, again showing isosurfaces of λ_2 vortical structures. The cross-stream planes showing the interfaces are placed more frequently, with interplane spacing of approximately L. This is to give a complete picture of the changes in the interfaces with downstream position. What can immediately be seen for the Re cases of 100, 150, and 200 is that the interface field appears to have a streamwise oscillating

behavior. It alternates between patterns indicating the presence of the plume-like jetting behavior, and areas that seem to have a band of densely packed interfaces around the periphery with an area of no interfaces in the center of the channel. For all three of those case, this central area devoid of interface appears to shrink with increasing x/L. The Re=150 case appears to be very similar to the Re=200 case. Interestingly however, the Re=100 case at first looks similar to the higher Re cases, but with increasing x/L appears more like the Re=50 case. The Re=50 case shows considerably different behavior. There is no indication of swirl driven by streamwise vorticity. Instead it appears that the interface is deformed from its initial flat shape into an arc which then extends around the periphery of the channel to eventually create interface rings in a shape that resembles the channel flow cross-stream profile in that it is vaguely super-elliptical. The difference in behavior in the Re=50 case as well as the observation that the Re=100 case becomes progressively more similar to the Re=50 case suggests that the presence and thus persistence of the hairpin vortices is what determines the interface profiles at that stage of the channel, which then determines the mixing performance.

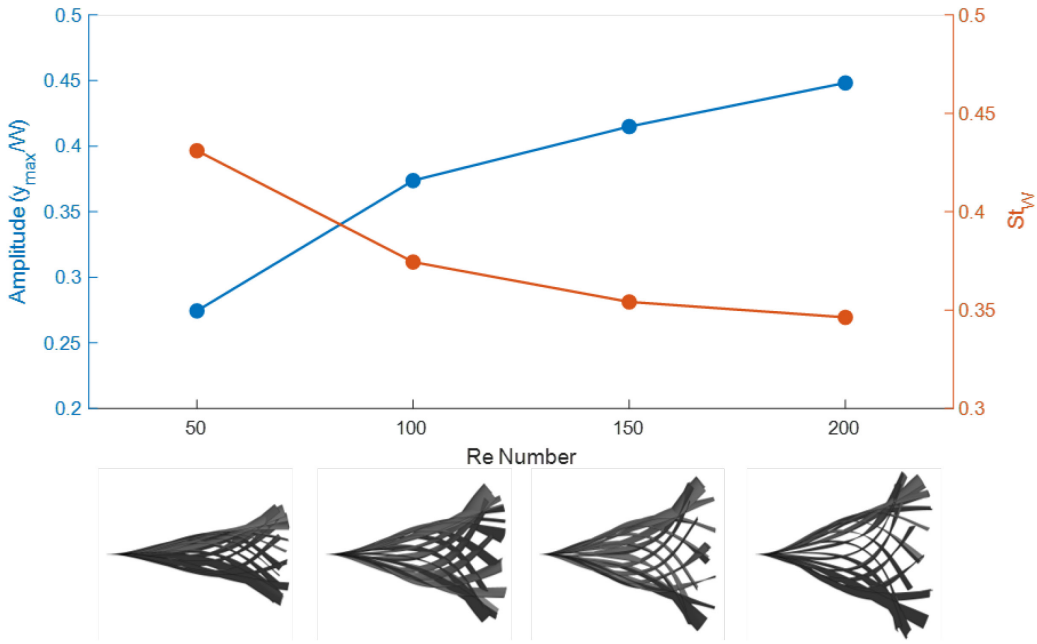

FIG. 4.11 – Flapping dynamics for the 3D flag simulations as a function of Re showing flapping half amplitude and the St number.

To better understand this transition in behavior, FIG. 4.11 shows the flapping dynamics of the flags at each Reynolds number in terms of the flapping half amplitude, the Strouhal number, and side views of the flutter envelopes. Here we can see further evidence of a transition occurring between Re=50 and Re=200. In general, we can see increasing amplitudes and decreasing flapping frequency with increasing Re number. This is in line with the behavior seen during the earlier 2D examination. However, from Re=50 to Re=100 there is a more significant jump in both the amplitude and the Strouhal number, with the subsequent Re cases showing smaller changes. Examining the envelope figures, we can possibly see the source of this change in behavior. The Re = 100, 150, and 200 cases all clearly exhibit 2-node flapping behavior, as described in prior work (Shoele & Mittal, 2014). This can be distinguished by the bulge in the outer envelope near the mid chord point of the flags. This bulge is only geometrically possible if the flag has an inflection point at a point closer to the fixed leading-edge than the bulge, indicating a node, and thus making this 2-node flapping. On the other hand, the Re=50 case only shows a slight bulged shape. This suggests

that while the Re = 50 case is still exhibiting the 2-node flapping, it is very close to the transition to 1-node flapping. As shown in the literature (Shelley & Zhang, 2011), these transitions in mode shape are typically accompanied by changes in the dynamics.

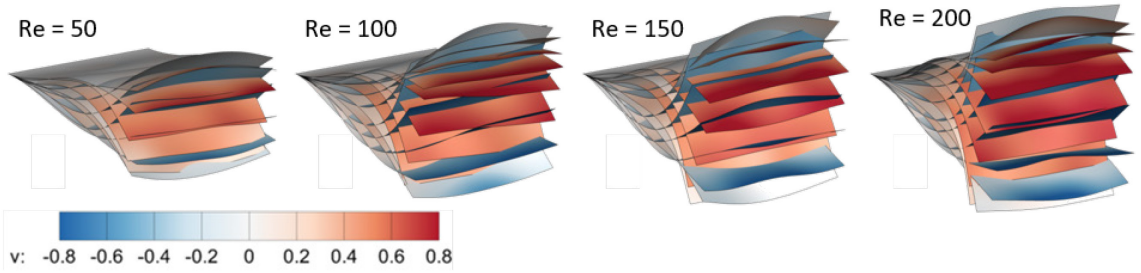

FIG. 4.12 – 3D views of the flapping envelopes for the four examined Re number cases showing approximately one flapping cycle. The color contours on the surfaces show the local y component of the flag's velocity, providing a sense of what direction each snapshot in the envelope is traveling.

One key point to note is that the amplitudes reported in FIG. 4.11 are the maximum for the entire trailing edge. However, as can be noted from the flapping envelope side views shown in FIG. 4.11, the 3D flags appear to exhibit significant spanwise deformations. To get a better understanding of this spanwise deformation, FIG. 4.12 shows a 3D view of the flapping envelopes for each Re number case. The surfaces are colored according to the v-velocity component to provide a sense of which direction each snapshot in each envelope is traveling. Here we can clearly observe the flags undergo considerable spanwise bending, particularly when the trailing edge is near its extrema y values and the flag is changing direction. Careful examination of the Re=200 figure shows the instance of maximum spanwise curvature at the top of the channel is colored red meaning it is still traveling upwards, showing the flag has not yet changed direction. To quantify the extent of this spanwise bending, we can calculate the difference in Y position between the corner points and the point at the centerline at the trailing edge of the flag. We found they differ by about 9%, 11%, 9%, and 6% for the Re 50, 100, 150, and 200 cases respectively.

4.2.2 Flag Aspect-Ratio and Spanwise Confinement

One of the primary challenges with numerically studying flapping flags is the vast parameter space governing their dynamics. This is further exacerbated when exploring 3D configurations, with the addition of two new geometric nondimensional parameters in the flag aspect ratio AR = W/L, and the spanwise confinement which can be considered as either the ratio of the span to the channel width (in this case W/L) or by the nondimensional distance between the spanwise edges and the sidewalls referred to as the spanwise gap which would be (L-W)/2. As discussed in the section on heat transfer enhancement, both of these parameters have been shown in prior work (Doaré et al., 2011; Eloy et al., 2007) to affect the stability of the system and both tend to make the flags more stable. This is of particular concern at these low Re numbers where the systems sensitivity to Re could mean that wider flags may flap while narrower flags do not. To examine this, we simulated the Re=50 and 200 cases again with flags having AR=0.5 instead of the 0.75 of the earlier tests. The Re=50 case was selected to understand if the increased stability of narrower flags would affect the low Re number behavior. Similarly, the Re=200 case was selected to examine how the cases compare when both AR cases exhibit large amplitude flutter.

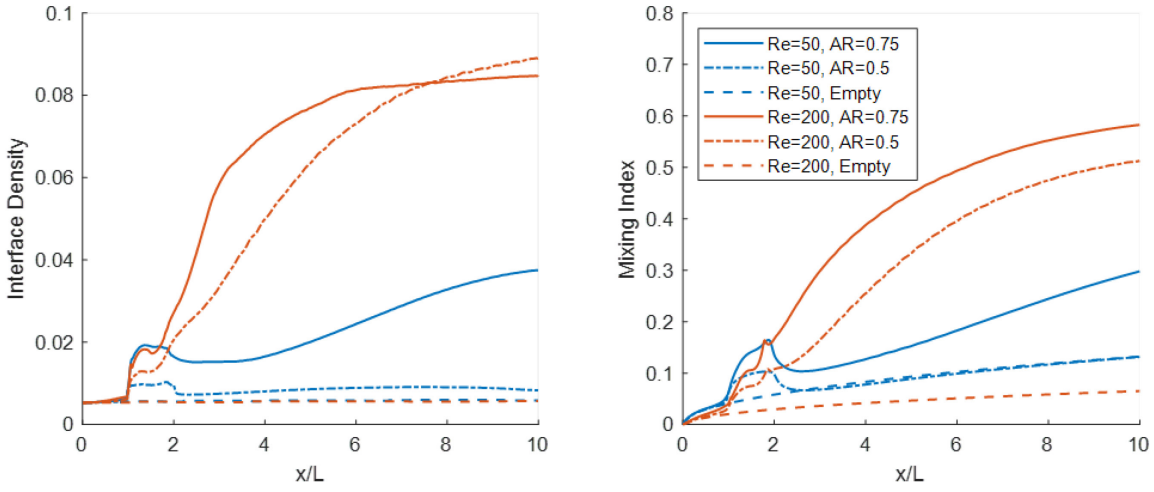

FIG. 4.13 – Time average of Interface Density and Mixing Index as a function of x/L for the two AR cases at Re=50 and 200.

FIG. 4.13 shows the performance comparison between the AR=0.5 and AR=0.75 cases in terms of the interface index and the mixing index for the Re=50 and 200 cases. What is immediately obvious is that the Re=50, AR=0.5 case did not create more interfaces in the flow. This suggests that the amplitude of flutter for this flag is likely very small which will be confirmed shortly by looking at the dynamics of these flags. The result of this is that there is essentially no improvement in the mixing index. In contrast, the Re=200, AR=0.5 case does show significant increase in interfaces, much like the corresponding AR=0.75 case, with a few key differences. The AR=0.75 case seems to asymptote much more quickly (i.e. the AR=0.5 case has a shallower slope of the Interface Density curve) which overall diminishes its performance in terms of the mixing index as can be seen in the MI plot. However, interestingly, the AR=0.5 case does not seems to saturate at a maximum interface stretching amount, or it does not saturate within the computational domain studied here and by the end of the channel, it appears that the AR=0.5 case has introduced slightly more interface surface area to the system. It is unclear from this figure what this means precisely, FIG. 4.14 and FIG. 4.15 showing the scalar concentrations and the interface field for these cases should shed more light. The Interface percentage is a valuable tool, but it is only designed to capture the moments before diffusion has had a chance to dampen the strengths of the peaks in the field. To better understand what is happening, and if this interface percentage result for the AR=0.5 case has physical significance, we can examine snapshots of the scalar field and the calculated interface field.

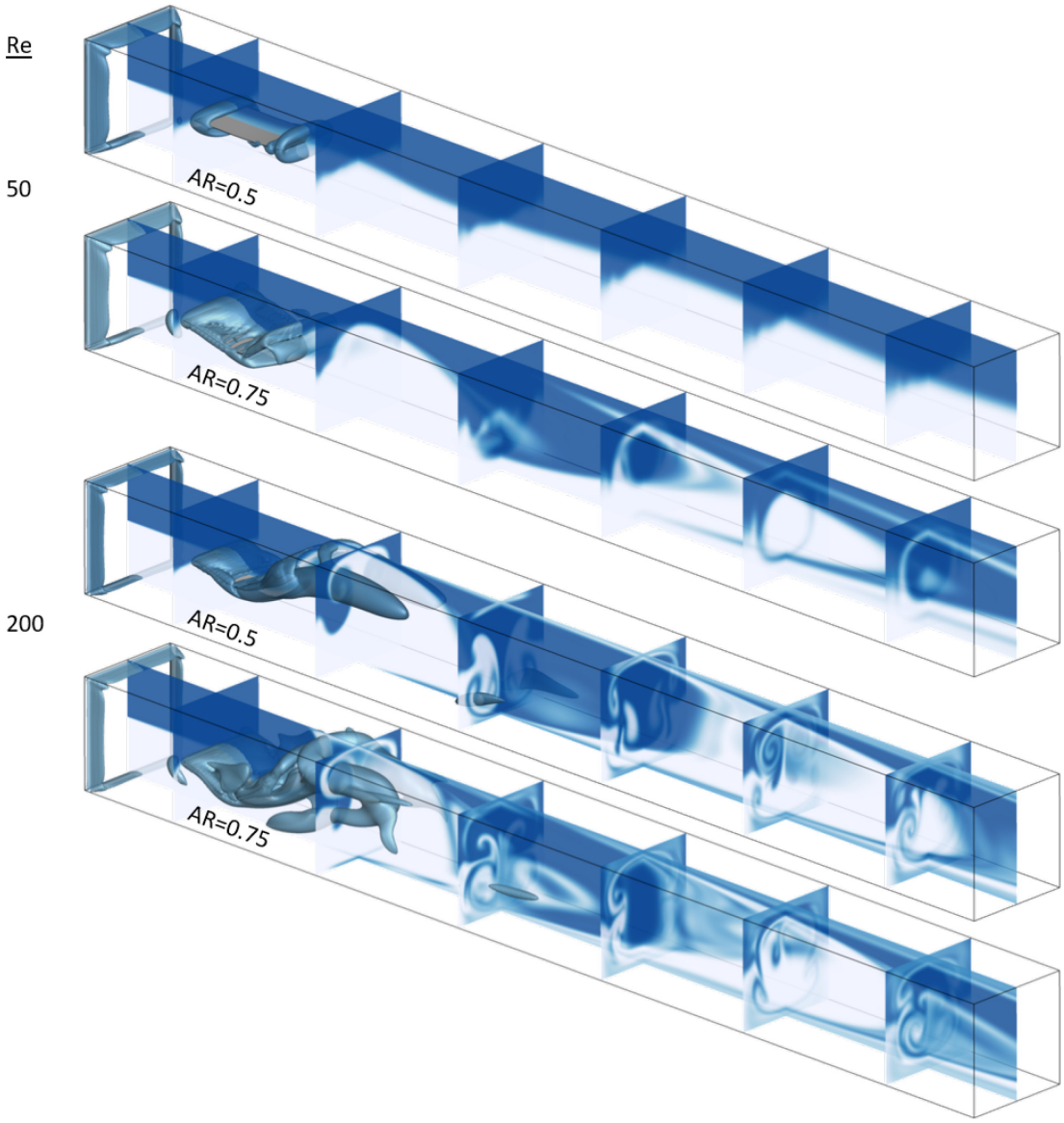

FIG. 4.14 – 3D visualizations of snapshots showing the scalar field ϕ for the two AR cases tested at Re=50 and 200.

FIG. 4.14 shows snapshots of the scalar concentration field for the AR=0.5 and 0.75 cases at Re=50 and 200. It is immediately clear that the Re=50, AR=0.5 case did not flap. This is not surprising, as it was already understood from the work by Eloy et. al. (2007) that narrower flags would exhibit increased stability. There is however a slight sinusoidal deformation to the interface in this case which we will examine in the following figure regarding the dynamics.

The Re=200 cases offer a significantly more interesting comparison. Here we can see both cases experienced flapping and both cases shed large streamwise vortices as visualized by the isosurfaces of the λ_2 criterion. However, it is clear that the wider AR=0.75 case shed significantly more vorticity and because of this the horseshoe shape of the vortex is preserved at this iso-surface threshold. Very interesting is how these differences seem to affect the scalar profiles at the later cross-stream planes. While the first plane after the flag shows largely comparable behavior, by the second plane we can see fundamental differences which may explain the differences in the interface percentage metric. In that second plane after the flag, the AR=0.5 case still shows a clear jet profile in the scalar concentration field, but without the indication of the two pieces of the jet recolliding in the center of the channel as can be seen for the AR=0.75 case. This is perhaps a result of decreased distance between the streamwise vortices that are causing this jet. Close inspection of the first plane after the flag shows that the jet pattern does not appear to interact with the sidewalls as it does in the AR=0.75 case. This difference alone could account for the changes in the performance.

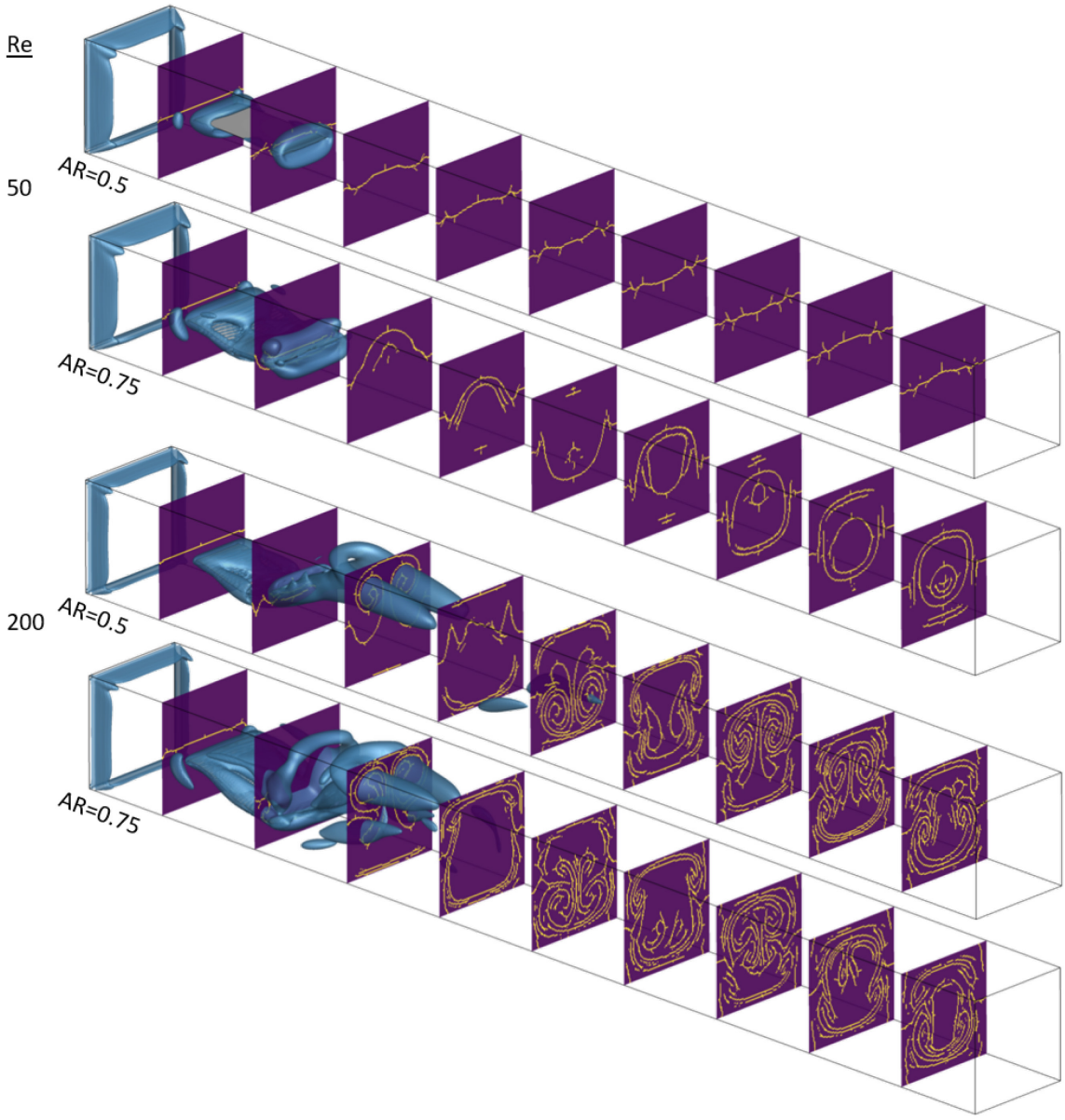

FIG. 4.15 – 3D visualizations of snapshots showing the interface field ζ for the two AR cases tested at Re=50 and 200.

FIG. 4.15 shows visualizations of the interface field for the AR cases. The comparison for the Re=200 cases more clearly shows the differences, especially in the planes showing the second plume downstream from the flag (the first plume pointing towards the lower wall). In the scalar concentration field figures, it was noted that the behavior here was different in that the AR=0.5 case did not seem to have the secondary jets re-colliding along the center plane of the channel. This

difference is much clearer in these interface field figures, and furthermore, we can see that instead the AR=0.5 case has a much more compact plume structure. Another interesting difference is the absence of central regions of unmixed fluid. It was previously noted that the AR=0.75 case exhibits pockets of unmixed fluid in the core of the channel, however, these pockets are not visible in the AR=0.5 case which is most likely due to the decreased inter vortex spacing. This difference may explain how the AR=0.5 case can exhibit slightly higher interface density, as the interfaces are more efficiently spatially distributed throughout the plane. The final key difference that helps explain the interface density result is that the streamwise vortex tubes in the AR=0.5 case appear much longer than in the AR=0.75 case. So much so that the third to last plane and second to last plane both exhibit the same sort of plume structure, meaning the vortex tubes must span across both planes.

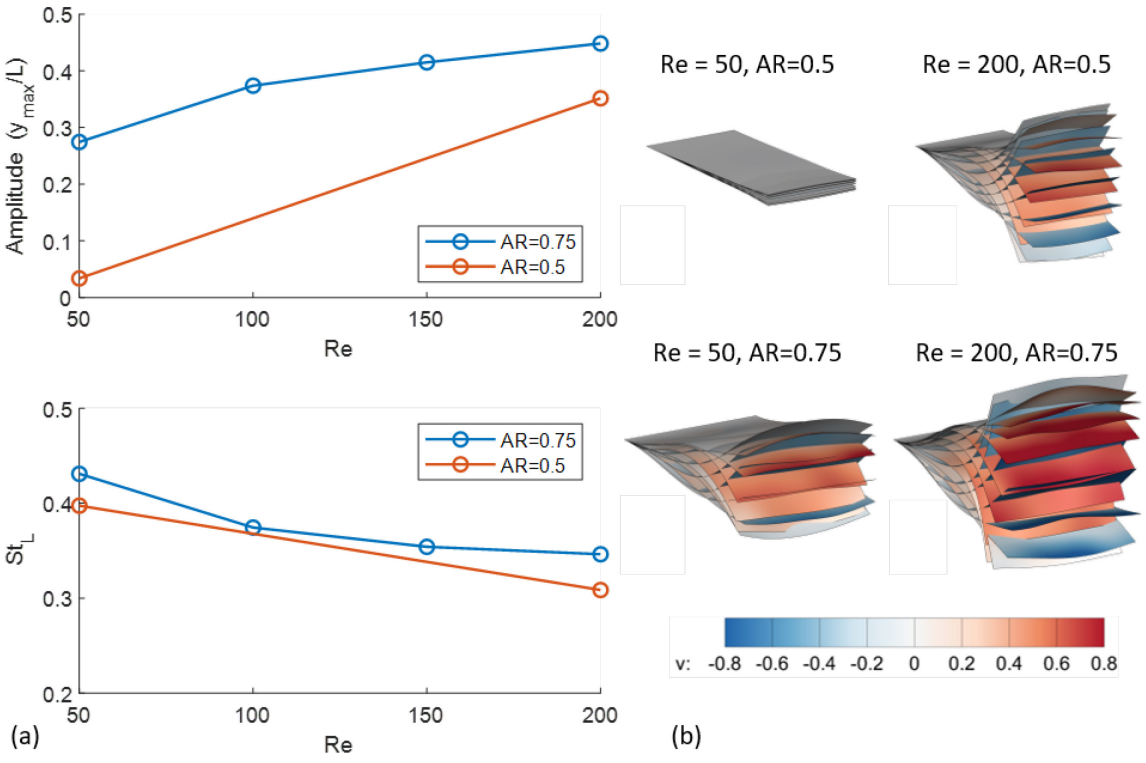

FIG. 4.16 – Comparison of flapping dynamics between the AR=0.5 cases and the AR=0.75 cases. (a) shows two figures comparing the Amplitude and St number. (b) shows 3D views of the flapping envelope where the

color of the surface represents the V component of velocity to give a sense of direction for each snapshot in the envelope.

FIG. 4.16 shows comparison of the flapping dynamics between the AR=0.5 and AR=0.75 cases using three approaches. (a) shows comparisons of the amplitude and the St number. There is a considerable difference in amplitude between the cases at Re=50 because the AR=0.5 case was essentially not flapping. Interestingly however, according to this figure, the Re=50 AR=0.5 case did not have zero amplitude, but instead had an exceedingly low amplitude. It is important to note here that the technique used to initiate flutter without waiting for it to develop naturally actually started this flag with a higher flutter amplitude than what is recorded here. Examination of the y position of the trailing edge of the flag shows that it decayed from the initial perturbation, but never actually stopped flapping, instead settling into the very small amplitude flutter recorded here at the St number reported in the second figure. While this behavior is interesting from a theoretical perspective, given the bi-stability of these regular flapping flags, it is very possible that this very low amplitude flutter would not have developed without the initial perturbation. Careful examination of the flapping envelope for this case shows evidence of very low amplitude 1-node flapping behavior. A final interesting point to note on this case which is essentially not flapping is that the calculated Strouhal number is very similar to that of the corresponding AR=0.75 case which did experience stationary flow induced flutter. This suggests that what little flutter is seen is in fact flow induced flutter and not simple ring down after the initial perturbation. That being said, the bistability exhibited by flapping flags almost ensures that this case would not have demonstrated this behavior without the initial perturbation.

The Re 200, AR=0.5 shows much more similar behavior to its AR=0.75 counterpart. The amplitude discrepancy here is much smaller than what was seen in the Re=50 case. Interestingly, there is still a small difference in the St number of a similar magnitude to the discrepancy seen in the Re=50 configuration. What is interesting here is that the narrower flag appears to be undergoing

considerably less spanwise bending than the AR=0.75 case as can be seen in the 3D visualizations of the flapping envelope. That this case appears to be flapping in a more 2D manner is not entirely surprising. From a topological perspective, it would take higher local curvature to achieve the same out-of-span deflections for a narrower flag.

4.2.3 Comparison with 2D results

A common issue in simulating flapping and flutter of membranes and plates is the consistent discrepancies between 2D and 3D. Early on in the historical investigations into flapping and flutter of membranes, this manifested as a discrepancy between simulations and experiments because simulations were not capable of 3D FSI. However analytical work showed that the issue was in fact the difference in stability between 2D and 3D flags. Both finite span effects (Eloy et al., 2007) and spanwise confinement effects (Doaré et al., 2011) were shown to increase the stability of 3D flapping flags in analytical models. This sensitivity of the structural dynamics to the aspect ratio and the spanwise confinement essentially changes the effective reduced velocity. Further confounding the comparison between 2D and 3D for flutter mixers is the sensitivity of the fluid dynamics to these 3D parameters. As was shown, a significant portion of the mixing at the higher Reynolds numbers in the 3D cases was due to streamwise aligned vortices shed from the spanwise edges of the flag. These vortices could only exist in the 3D system. Thus, it is not surprising to find discrepancies between the 2D and 3D system. What is interesting is determining the source of these discrepancies as they shed light on the behavior of both the 2D and 3D models.

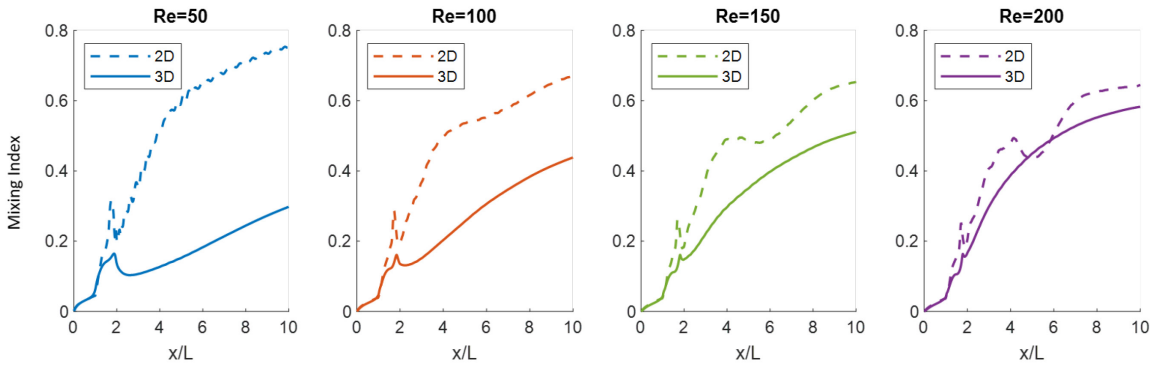

FIG. 4.17 – Mixing Index comparisons of the 2D and 3D systems. Each Re number is plotted separately.

FIG. 4.17 shows the differences in the key performance measure of the system, the Mixing Index. It is clear that at Re=50 the behavior is completely different, and this discrepancy diminishes with increasing Re. The way this decreasing discrepancy manifests is interesting. As was shown earlier, the Mixing Index increases with Re for the 3D system. But as shown in the earlier 2D mixing study, the Mixing Index actually decreases with increasing Reynolds number between Re=50 and Re=100. This is due to the strong sensitivity to the increase in Peclet number that the 2D system exhibits. In some sense this allows the 3D system to catch up to and overtake the 2D system with increasing Re. However, it is important to emphasize these results are dramatically different both in terms of the individual behavior as a function of x/L, as well as how that behavior changes with increasing Re.

Another key distinction is in the smoothness of these plots. It is interesting to point out that the 2D cases were averaged over many more cycles than the 3D cases (due to the computational expense of 3D simulations). Nevertheless, the 2D cases show very nonmonotonic behavior, particularly between x/L 4 – 6 whereas the 3D cases very smoothly increase and then plateauing, as is the case in the Re=200 figure. While it is not surprising that there are discrepancies, the very significant differences in the Re=50 and Re=100 cases bring into question if the flapping dynamics are too dissimilar to warrant comparison.

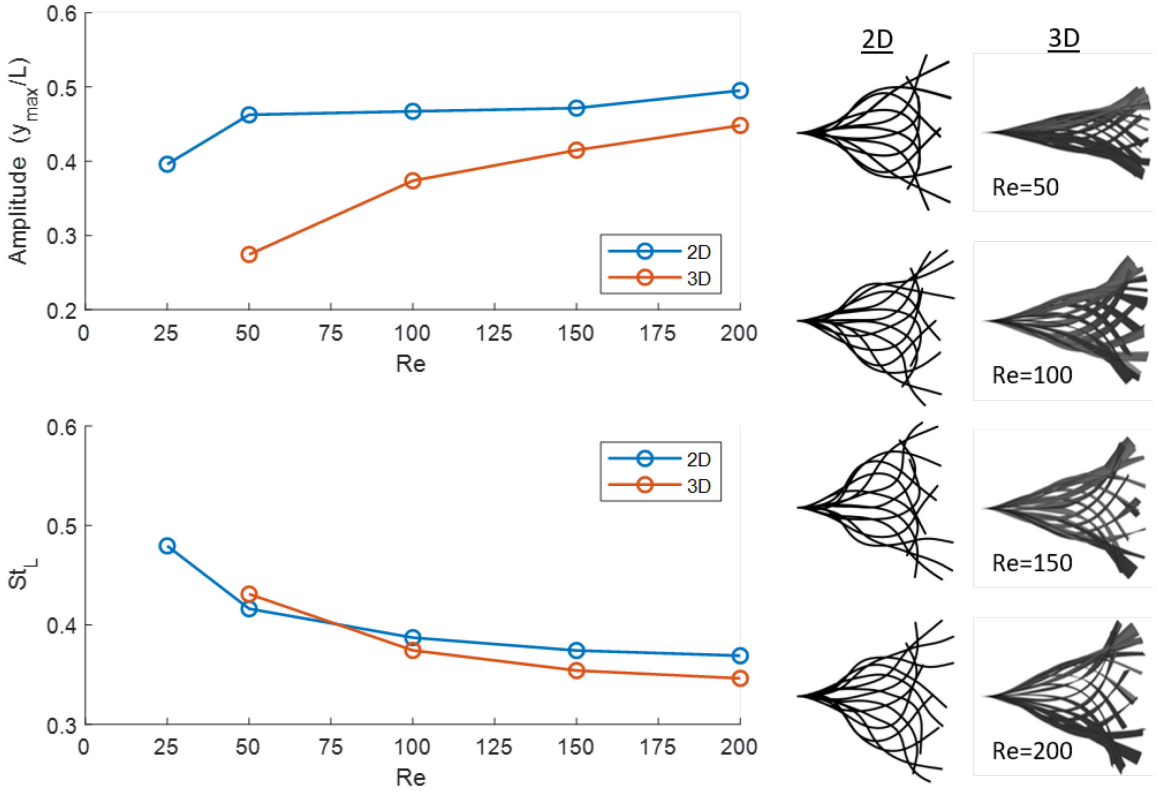

FIG. 4.18 – (Left) Amplitude and Strouhal number comparisons between the 2D and 3D cases as a function of Re number. (Right) Flapping Envelope comparisons between the 2D and 3D cases for each of the considered Re numbers.

FIG. 4.18 explores the comparison of flapping dynamics between 2D and 3D from three perspectives: mean flapping amplitude, Strouhal number, and side views of the flapping envelope. The flapping envelope figures are included to allow for the comparison of flapping regime and mode shapes. The amplitude results are not as dissimilar as would be expected considering the drastic discrepancy in mixing index. The greatest difference is at Re=50. We can see that the 2D case exhibits a plateau in the flapping amplitude with increasing Re, whereas the 3D case sees a smooth, seemingly asymptotic increase in amplitude. It should be noted that the maximum possible half amplitude is actually y/L=0.5 as that is when the flag would touch the walls. But while this explains the plateau in the 2D case, there is still a small increase in amplitude from Re=150 to 200. It does appear that the amplitudes are becoming increasingly more similar between 2D and 3D with

increasing Re. The Strouhal number results show far closer agreement with both cases following a decreasing asymptotic trend with Re. There is slight discrepancy though, especially at Re 150 and 200, and this can perhaps be explained by examining the differences in the flapping mode shapes.

Perhaps the most illuminating comparison of the dynamics can be seen in the flapping envelopes. In the 2D case we can see a fundamental transition in behavior with increasing Re, from two node symmetric flapping in the Re=50 case to three node, marginally asymmetric flapping by the Re=200 case. In contrast, the 3D flags appear to be exhibiting consistent two node flapping. This difference highlights a limitation of the flapping amplitude as a measure of the flutter intensity. While the 2D and 3D flags may have relatively similar amplitudes, in the Re=200 case (for example) the fundamental difference in flapping modes could mean the 2D case is imparting more energy to the flow, or in some way causing a more drastic disturbance to the flow. This is possibly a result of the difference in envelope shape midway along the flag, where we can see the 2D case exhibiting significantly greater deflection at the midpoint of the flag for all Re due to the higher mode flapping. This more energetic mode shape has previously been shown in work by Shoele & Mittal (2014) to create large persistent vortices as compared to the two-node flapping mode, and we have previously shown in the section on 2D mixing that those large persistent vortices are crucial for mixing performance in the 2D configuration.

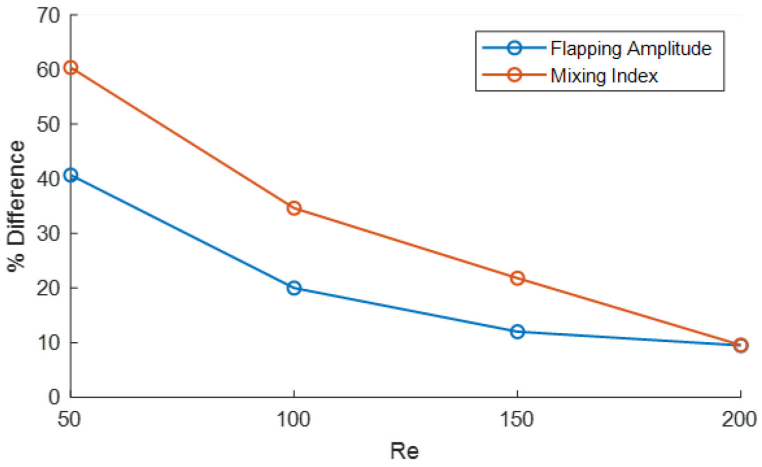

FIG. 4.19 – Percent difference of the 3D results from the 2D results for the flapping amplitude and the mixing index vs. Re.

While there is clearly a connection between the differences in flapping behavior from 2D to 3D and the differences in mixing index, it is important to investigate how much of this difference is simply the result of lower flapping amplitudes, as opposed to other mechanisms such as the flapping mode. To examine this, we compare the percent difference in the flapping amplitudes with the percent difference in the mixing index. FIG. 4.19 shows this comparison for the 2D and 3D cases as a function of Re. Here we can see there does seem to be some level of correlation between the amplitude discrepancy and the Mixing Index discrepancy. Without more Re samples, it is difficult to draw conclusions about the nature of these curves, however it is clear these curves have somewhat similar behavior in terms of slope and perhaps curvature. Regardless of the reason the cases are so different, it appears that if analogies are to be drawn between 2D models and 3D models for flutter mixers, specialized matching will be required. Here the various non-dimensional parameters were matched between 2D and 3D, which led to drastically different behavior. Perhaps a more useful analogy could be made if the 2D parameters were somehow systematically adjusted such that the flapping dynamics were matched. However, this sort of a-priori tuning without knowing the 3D flag dynamics would require fairly sophisticated analytic models of the 3D behavior.

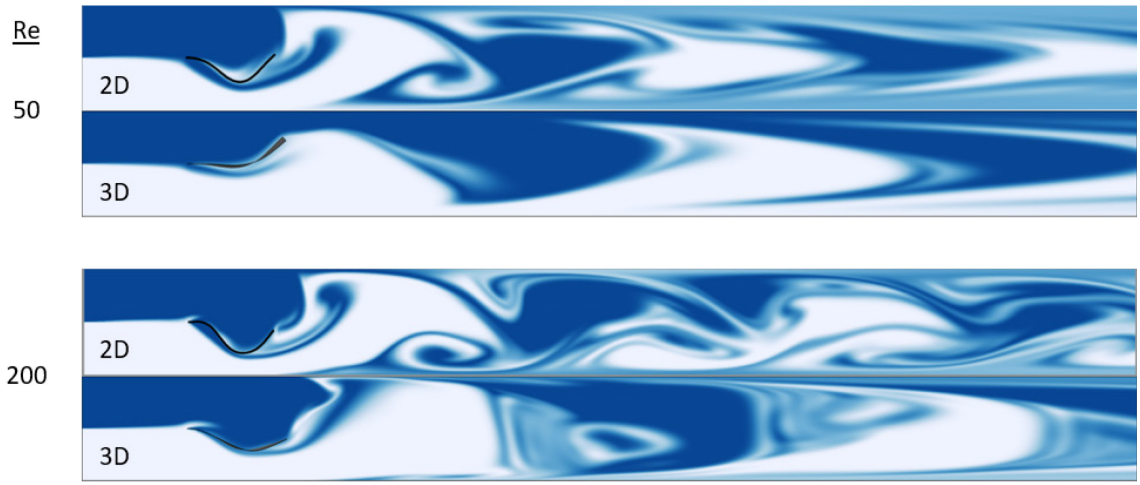

FIG. 4.20 – Snapshots of the scalar field for the 2D and 3D cases at Re=50 and Re=200. The plane shown for the 3D cases, is the mid-span plane.

To understand how these differences in dynamics affect the scalar distribution, FIG. 4.20 shows comparisons of the scalar field between the 2D case and the midplane of the 3D case. If the 2D configuration has any potential as a valid simplification for the 3D configuration, then these visualizations should at least have some qualitative similarities. What is interesting here is that Re=50 cases appear qualitatively more similar than the Re=200 cases, which is the opposite behavior to the mixing index results. Here the similarities between the 2D and 3D for the Re=50 case can be seen in that they both have alternating pockets of scalar and the interface between these pockets seems to be shaped similar to a channel flow profile. Notably, the 2D case shows indications of a distinct vortex shedding from the flag while the 3D case only shows the interface deflection pattern with no indication of spanwise vortices. Furthermore, it appears that the period of the alternating pattern is shorter for the 2D case than it is for the 3D case. It is important to point out that as discussed in FIG. 4.18, the flapping St number is nearly identical between the 2D and 3D cases, especially at Re=50. This difference in scalar spatial oscillation is thus not the result of differences in the flapping dynamics, but instead shows that there must be some sort of stretching or compressing phenomenon for this profile of the scalar field.

Finally, the difference in scalar concentration in the boundary layer along the channel walls shows why the 2D case sees such strong mixing performance even at this low Re number. It appears that the increase in Pe due to the relatively low Re is very effective at breaking down any sharp gradients in the scalar field. So that when large vortical structures are introduced to the flow creating sharp gradients, as can be seen near the channel walls immediately after the flag, they will be very rapidly diffused due to the comparatively high scalar diffusion coefficient. This rapid breakdown of sharp gradients is not visible in the 3D case. It is unclear from a 2D midplane view if that is simply because there isn't any spanwise vorticity being shed, or if it is because Pe number effects are felt differently in the 3D case. In any case, the fact that 2D the flag is able to shed vortices at these low Re numbers, and the subsequent rapid diffusion across the ensuing gradients, is the reason for the very strong mixing in the 2D and the corresponding large discrepancy compared to the 3D.

For the Re=50 case, the 2D and 3D snapshots appeared qualitatively similar, however careful inspection uncovered the key difference which was responsible for the drastic mismatch in mixing index. In contrast, the Re=200 case appears to have much greater qualitative discrepancy between the 2D and 3D snapshots, despite the mixing index results indicating these cases have fairly similar performance. Here again we can see the difference in apparent spatial frequency of oscillating patterns of the scalar field with the 3D case showing lower spatial frequency oscillations. It is important to again note that the St number between these cases is fairly similar as shown in FIG. 4.18. If we examine the third pocket for each configuration (the second white colored region after the flag), we can more clearly see what is happening. While it appears the third pocket for the 3D case is much longer than that of the 2D case, in fact, in the 2D case, it appears that this pocket has wrapped underneath the previous pocket of scalar. This is an interesting phenomenon and indicates that the frequency of the oscillatory patterns seen in the scalar field is subject to how the pockets of scalar are packed and overlap in the channel, suggesting complex inter-cycle interactions.

Furthermore, the 2D Re=200 case shows the characteristic swirling patterns resulting from large coherent vortices being shed from the 2D flag. Those swirl patterns are not visible in the 3D case, which is not surprising as our previous discussions have shown that the majority of the vorticity shed from in the 3D flag manifests as streamwise aligned vortical structures.

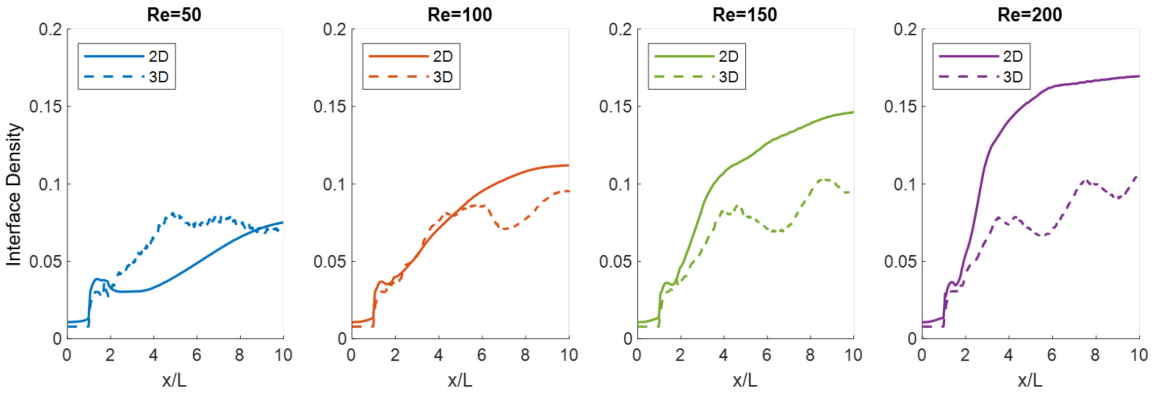

FIG. 4.21 – Interface Density comparisons of the 2D and 3D configurations. Each Reynolds number is plotted separately.

Comparisons of the Interface Density finally show one aspect where the 3D system does have features which can aide in mixing as compared to the 2D system. So far, the non-physical peculiarities of 2D flows have, somewhat surprisingly, aided in mixing. In theory, the 3D case has several fundamental differences over the 2D case which could seem a-priori like they should aide in mixing. In 3D, vortices break down more quickly as there is an entire extra dimension for diffusion to work. This means that vortices which seem to easily persist in a 2D simulation could in fact dissipate quickly in the corresponding 3D system, which is exactly what happened in this comparison. However, as it turns out, these vortices proved highly beneficial to mixing performance, so their persistence in 2D proved helpful.

Given the vortex persistence issue, one could expect the 2D case to exhibit a higher percentage of its domain occupied by areas of high scalar gradient (i.e. higher Interface Density) because the vortices persist longer and so should mix the fluid more. However, examining FIG. 4.21 shows that while the interface density is lower for 3D in the Re=50 case, by the Re=100 case, both systems

show similar interface density, and the 3D results continue to increase, significantly outperforming the 2D case for the Re=150 and Re=200 cases. This is expected as there is considerably more room in 3D for these interfaces to inhabit than in 2D. AS was discussed in the calculation of the Interface Density measure, in 3D a given pixel can be an interface in either or both the cross-stream and spanwise directions, while in 2D it can only be an interface in the cross-stream direction. Furthermore, observations of the interface field for both the 2D and 3D cases show that there appears to be a limit to how closely these interfaces can be packed. Essentially, there is a lower bound to the spatial scales exhibited in the scalar field. This manifests in FIG. 4.21 in that the interface percentage plots for Re=150 and Re=200 in the 2D appear identical, suggesting some sort of saturation effect is taking place.

Immediately this brings up a concern with using CFD in that one of the practical limitations of CFD is that we cannot resolve oscillations in any variable under the Nyquist limit of our grid. This is of course a concern when a lower bound of spatial frequencies is found. However, it is important to note that the grids used in these simulations were specifically verified with the intent of adequately resolving the scalar gradients. As was discussed earlier, these verification studies showed that for our major performance measures the results were adequately grid resolved.

4.2.4 Comparison with Post Mixers and Bluff Body Shedding

There exists a wide array of micromixer designs. Even among passive mixers there are many different approaches all with their own benefits and drawbacks and performance niches. Certainly, any new design is only meaningful when compared with the state-of-the-art. That being said, the goal of this study is not to present an optimized design, or even one that is ready for fabrication. The notional flutter mixer would likely have many flags in a tandem array, potentially with various optimization modifications such as varying or alternating flag lengths to introduce multiple length and time scales and perhaps to introduce some chaos inducing coupling between the flags. Those

and other nuances of the practical system are not of interest in this work, as we are simply exploring the viability and the flow physics of flutter mixers. To that point, instead of comparison against other fully realized mixers, a better comparison would be against other contemporary micromixers. Examples of this concept could be a single corner as the kernel for a zig-zag mixer, or as we studied in the 2D mixing case, a single cylinder as the core of a post mixer array. Comparison with a post mixer has the specific benefit of testing relatively the same fundamental mixing enhancement phenomenon, namely deformation and stretching of an interface due to vortex shedding.

Whereas this type of comparison was possible in 2D, the 3D configuration poses an interesting obstacle which provides interesting insight into the relative performance in its own right. Towards this comparison, we simulated a number of cylinder diameters in our channel flow all at our highest Reynolds number case, Re=200. In the 2D study, we found that only the cylinder with diameter D=H/2 experienced vortex shedding. However, in this configuration none of the cylinders exhibited any vortex shedding, meaning they did not improve the mixing performance at all. This result is perhaps not surprising, in general 3D vortex shedding would be more stable than 2D vortex shedding, which increase the critical Re. Also, spanwise confinement would further increase the critical Re. Recall that the Reynolds number based on the diameter for the D=H/2 case (the case which is most likely to exhibit vortex shedding of the cases we investigated) is half that of the channel flow, which means the combined effects serving to stabilize the vortex shedding including the three-dimensionality, the spanwise confinement, and of course the cross-stream confinement could easily raise the critical Re above our highest Re case. While this result fails in terms of providing a useful comparison for the flutter mixer, it is useful in showing one of the fundamental benefits to the flutter mixer which is that it can shed large coherent vortices at much lower Re than many other instability mechanisms that could be used for mixing enhancement. This allows mixing via vortices to be used at much lower Re than what is possible with other approaches.

4.2.5 Energy Loss

One key aspect towards understanding the true mixing performance improvements of a given micromixer is the notion of efficiency. In principle, any addition to the system which improves mixing performance will also necessarily lead to additional losses in mechanical energy. In the case of an active mixer, this energy is easy to measure as it is at least in part whatever external energy was needed to drive the active mixer. For passive mixers this additional energy is extracted from the flow in one way or another. For meandering path mixer that would manifest as higher head loss due to the corner flows; for a post type mixer it would be the drag on the posts; and for a flutter mixer it must be the energy required to flap the flag, the drag on the flag, and any energy that was lost to viscous dissipation due to the vorticity being generated and shed. We can examine this energy loss by plotting the nondimensional Head Loss.

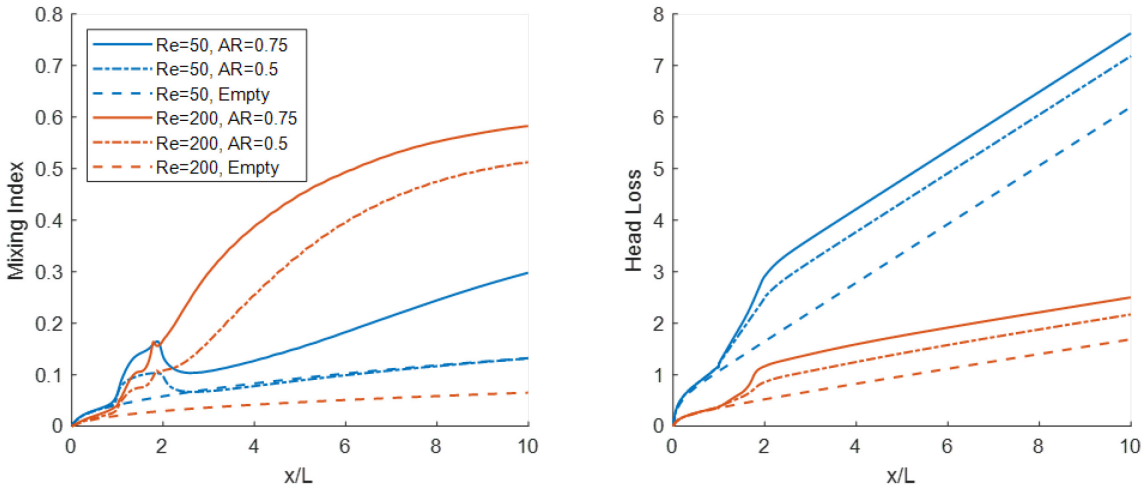

FIG. 4.22 – Mixing Index and Head Loss as a function of x/L for the AR cases at Re=50 and 200.

FIG. 4.22 shows the Mixing Index and Head Loss for the AR cases. The Head Loss plots show similar behavior as was seen in the 2D mixing study as well as the heat transfer enhancement study, wherein the Head Loss due to the flapping membrane appears to be almost entirely created in the region of the membrane itself. After the end of the membrane the Head Loss increases at the same

rate as the empty channel. This suggests the energy losses in the flow are completely dominated by the viscous drag on the membrane. This is clear because even though the AR=0.5, Re=50 case did not exhibit any flapping behavior, it still had a similar increase in Head Loss as the AR=0.5, Re=200 case which did exhibit large amplitude flutter. Comparing between the AR cases we can see the Head Loss is almost a linear function of the flag area, which would make sense considering the Head Loss appears to be only sensitive to the viscous drag term.

Chapter 5

Heat Transfer Enhancement

5.1 Background and Motivation

As discussed in the introduction, one avenue where fluttering flags showed promise to improve an existing engineering system is with heat transfer. Particularly forced convection heat exchangers, which are essentially the most aggressive available heat transfer tool in most applications. Aggressive in the sense that they represent the most complex solution to a heat transfer problem, including the addition of a working fluid, accompanying pumps and plumbing to move that fluid, and some sort of radiator to dissipate the heat away from the device being cooled. Despite the significant added complexity of the forced convection approach, it is often the only viable option in many applications from the smallest scales of microelectronics to the largest scales of air-cooled condensers used in power plants.

Even with the significant improvement in heat transfer rate afforded by forced convection, many systems that use this type of heat exchanger are still heat limited, meaning the performance and operation of the device are limited by the rate at which heat can be removed. Computer processors are one obvious example but there are many others, and this is a very common limiting factor on a design. Thus, ways by which heat transfer rate in a forced convection heat exchanger could be improved are valuable to myriad applications across the breadth of engineering, technological, and scientific applications.

The reason heat transfer rate is such a common limiting factor, even when forced convection is utilized, comes down to the basic physics of the simple system underlying all forced convection heat exchangers; flow through a heated channel. That system is subject to performance hinderances and diminishing returns, such that heat transfer rate plateaus with increasing pump power.

The fundamental limitation here is the boundary layers that develop along the walls of a heated channel. Fundamental solutions to the heated channel flow problem show similarity between the solution for momentum and the solution for a scalar such as heat. Given the typical boundary conditions of a forced convection heat exchanger, the scalar field will develop a channel flow profile, whose specific shape is determined by the specific boundary conditions and the channel shape. Common to all solutions though, is the general profile wherein a smooth gradient develops between the heated wall and the cold core of the channel. This profile means that the hottest fluid in the channel is sitting right next to the heated wall, and as heat transfer rate is a function of the temperature difference between the wall and the fluid next to the wall, this is then a very non-ideal configuration towards rapid extraction of heat. Thus, the key to improving the performance is in disrupting this boundary layer and mixing the flow such that the cold fluid in the core is brought near the wall and the recently heated fluid next to the wall is removed.

This is where the flapping flag comes into play. At its most basic, the flag is acting as a mixer in this configuration, generally disturbing the flow so as to let convection mix the flow. However, as will be shown in the following sections, the flapping flag is particularly well suited as it creates very specific vortical structures which accomplish more specific goals than simple mixing enhancement. The following sections will detail our examination of this system using a fully coupled 3D fluid-structure interaction solver.

Prior work done in our group examined the idea of using fluttering flags to improve heat transfer in a forced convection heat exchanger by looking at the system in its most simplified configuration, a 2D channel with heated walls. This work was published as Shoele & Mittal, (2014).

It comprised a brute force parametric sweep over several parameters to create performance maps of the 2D configuration. A review of those results is discussed in Appendix A. That prior work motivates both our 3D heat transfer study, as well as other sections such as the investigation into the low Re limit of flutter.

5.1.1 Motivating 3D FSI Studies

While the results of the prior 2D study (Shoele & Mittal, 2014) were valuable and informative, 2D models have significant limitations. First, vortex shedding phenomena in general begin to exhibit 3D behavior at relatively low Reynolds numbers. For an unconfined cylinder, intrinsic 3D effects emerge at a Reynolds number (based on the diameter) of about 190 (Williamson, 1996). The Reynolds numbers of interest in these heat exchanger type problems are usually much higher than that, and even the reduced Reynolds number used in the prior 2D study was 400.

However, beyond the intrinsic fluid dynamic instabilities which will lead 2D flows to become 3D, the flapping flag in a duct flow is itself intrinsically three dimensional. In addition, since the flag cannot extend across the entire span of the channel, side-edges and the gap between the membrane and the side-wall would be expected to generate strong three-dimensional effects. While the gaps to the sidewalls could be made very small, it will be shown in this work that these effects play a significant role in determining the dynamics of the flag and the heat transfer. Thus, one goal of this 3D study is to understand the sensitivity to various 3D parameters such as the flag aspect ratio and the spanwise gap.

In addition, there are other aspects of the real-world application of forced convection heat exchangers which cannot be tested in 2D. One important factor is the effect of duct shape on the effectiveness of the heat exchanger. The rectangular duct heat exchanger is a good canonical shape, but in practice, heat exchanger passages come in a variety of shapes. One of the practical considerations of this research is to assess the viability of retrofitting existing heat exchangers with

flapping flags. This presents a serious concern for this technology, because it need to be able to work in a variety of channel shapes for retrofitting to be possible.

Rectangular channels are ideal for the flapping flag as the symmetry of the flapping is aligned with one plane of symmetry of the channel. Furthermore, the shape of the rectangular flag matches that of the channel. However, it is not obvious that this system would be as effective, or perhaps if it would work at all in other duct geometries. One consideration is if there is enough room for the flag to flap. Another consideration is if the changes in channel geometry effect the vortex dynamics in the channel, and in so doing, effect the heat transfer performance. It is not practical to examine the flag in all possible duct shapes, nor would that be in-line with the goals of this study, as we are interested in more general and more fundamental questions than the particular nuances of a specific real-world heat exchanger. Instead, we seek to understand what effects different duct shapes have on the performance of the heat exchanger and how strong is this dependence on the duct shape.

5.2 Problem Configuration

We used fully coupled 3D FSI simulations to examine various configurations of a flapping flag in a heated channel flow. FIG. 5.1 shows a problem schematic of a channel flow with a membrane type flag. For all work done in this 3D study, the flag length is L and is kept constant. Multiple channel shapes are examined in this study, including a square channel, a rectangular channel, a circular channel, and a diamond shaped channel. FIG. 5.1 shows the square channel which will be used as a baseline wherein the height and width equal L. The other channel shapes will be described in more detail in subsequent sections. The flag is a so called “regular flag” wherein its leading edge is free and its trailing edge is fixed. Its leading edge is placed 2L downstream of the inlet. The 3D configuration of this problem includes a gap between the edge of the flag and the sidewalls which is called G. This gap will be examined in a subsequent section, but for the baseline square channel the gap is 0.2L making the flag width 0.6L.

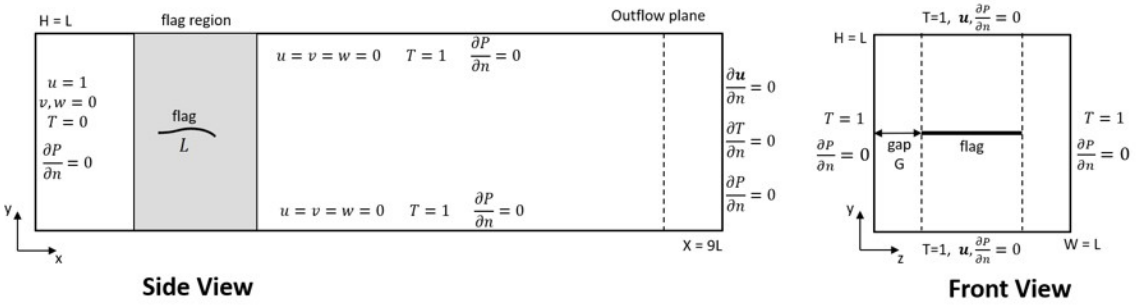

FIG. 5.1 – Configuration of the 3D flapping flag in a heated channel problem. This particular figure shows the square channel which functioned as a baseline for this this study.

This fluid-structure-thermal multiphysics system exhibits two-way coupling between the fluid and structure and one way coupling between the fluid and the temperature. The flow is governed by the incompressible Navier-Stokes equations. The equations governing the dynamics of the membrane are derived from the principle of virtual work (Huang & Sung, 2010) and are given in terms of the Lagrangian position vector $\mathbf{X}$ of the membrane. The scalar T is governed by an advection-diffusion equation. The governing equations and numerical methods used here are described previously in the Numerical Methods section of this thesis, so only a brief overview will be included for reference:

$$\frac{\partial \mathbf{u}}{\partial t} + \nabla \cdot (\mathbf{uu}) = -\nabla p + \frac{1}{\mathrm{Re}} \nabla^2 \mathbf{u} + \mathbf{f} \tag{5.1}$$

$$\nabla \cdot \mathbf{u} = 0 \tag{5.2}$$

$$\frac{\partial T}{\partial t} + \mathbf{u} \cdot \nabla T = \frac{1}{\mathrm{Re} \cdot \mathrm{Pr}} \nabla^2 T \tag{5.3}$$

$$\frac{\partial^2 \mathbf{X}}{\partial t^2} = \sum_{i,j=1}^{2} \left[\frac{\partial}{\partial s_i} \left(\sigma_{ij} \frac{\partial \mathbf{X}}{\partial s_j} \right) - \frac{\partial^2}{\partial s_i \partial s_j} \left(\frac{M^*}{U^{*2}} \frac{\partial^2 \mathbf{X}}{\partial s_i \partial s_j} \right) \right] + Fr \frac{\mathbf{g}}{\mathrm{g}} - \mathbf{F} \tag{5.4}$$

For the fluid governing equations (5.1) and (5.2), $\mathbf{u}$ is the velocity field, t is time, p is pressure, Re is the Reynolds number defined as $\mathrm{Re} = UL/\nu$ where U is the mean inlet velocity, L

is the characteristic length given by the length of the flag, and ν is the dynamic viscosity of the fluid. $\mathbf{f}$ is a forcing function associated with the fluid-structure interaction penalty method discussed in the numerical methods section. For the scalar equation (5.3), T is the temperature defined as 0 at the inflow and 1 at the walls, and Pr is the Prandtl number defined as $\mathrm{Pr} = c_p \mu / k$ where c_p is the specific heat, μ is the dynamic viscosity, and k is the thermal conductivity. Equation (5.4) governs the position the membrane. The key non-dimensional parameters governing the structure are the mass ratio M^* and reduced velocity U^*:

$$M^* = \frac{\rho L}{m_s}, \qquad U^* = UL\sqrt{\frac{m_s}{k_b}} \tag{5.5}$$

where k_b is the bending rigidity and m_s is the excess mass per unit area. In equation (5.4), $\mathbf{F}$ is the force density induced by the element on the surrounding fluid associated with the penalty forcing method, Fr is the Froude number defined as $Fr = U/\sqrt{gL}$ which is assumed to be 0 in this study, where $\mathbf{g}$ is the acceleration due to gravity, and $g = |\mathbf{g}|$.

5.2.1 Parameters and Boundary Conditions

In this study, we choose Re=600 based on the flag length L and Pr=1 to simulate a gas similar to air. While this Re number is significantly lower than what would be seen in our large scale applications such as an air cooled condenser, our prior 2D work (Shoele & Mittal, 2014) showed that the flapping dynamics for the 2D system were agnostic to Re above Re=200. Based on that same prior work, M^* and U^* were chosen as 0.5 and 15 respectively so as to generate large amplitude flutter at this Re number for the confined flapping flag configuration. The developing flow in the channel has a uniform inlet boundary condition $u(0,y,z,t)=1$, Dirichlet no-slip no-penetration boundary conditions on the sidewalls, Neumann boundary conditions at the outflow, and an initial value of $u(x,y,z,0)=1$ everywhere. The temperature boundary conditions are T=0 at

the inflow, constant temperature T=1 along the four side walls, a zero gradient outflow boundary condition, and a $T(x,y,z,0)=0$ initial condition. The leading-edge of the membrane is fixed and the trailing edge is free. The boundary condition equations for this type of configuration are presented in the Numerical Methods section. The membrane is initially deflected slightly (by a 2.5° angle to the incoming flow) to accelerate the attainment of stationary state. Verification studies have been performed to ensure that the dynamics are not sensitive to this small initial perturbation.

5.2.2 Numerical Method

The governing equations were solved using the in-house code ViCar3D which uses a second-order fractional step method on semi-staggered Cartesian grids (Mittal et al., 2008). The 2nd-order Crank-Nicolson fully implicit scheme is used for the convective and diffusion terms and the Pressure Poisson equation is solved with the biconjugate gradient (BiCGSTAB) scheme (Zhu et al., 2017). Further details of the method can be found in Mittal et al., (2008) and Seo et al., (2011) and validation and benchmarking for flow-induced flutter problems can be found in prior work using this solver (Shoele & Zhu, 2012; Shoele & Mittal, 2014). The membranes were coupled to the fluid using the penalty immersed boundary method discussed in the Numerical Methods section. In particular the modified expression for the coupling for was used according to:

$$\mathbf{F}(s,t) = -\kappa_p \frac{\rho U^2}{L}\left[\left(\tilde{\mathbf{X}} - \mathbf{X}\right) + \beta \Delta t\left(\tilde{\mathbf{U}} - \mathbf{U}\right)\right] \tag{5.6}$$

where κ_p and β are the penalty parameters, and Δt is the computational time step. Based on a prior sensitivity analysis (Shoele & Mittal, 2016), these parameters were chosen as $K_p = -10^5$, $\beta = 150$, and $dt = 1.0 \times 10^{-4}$.

The fluid-structure-scalar equations are discretized and solved following prior work (Shoele & Mittal, 2014; Shoele & Mittal, 2016). The fluid and scalar equations are solved on a Cartesian grids

in a 9*W* x *W* domain. The grid in the 2 cross-stream directions is uniform and the grid in the streamwise direction is uniform around the body and is then geometrically stretched towards the inlet and outlet with stretching ratios not exceeding 5% for the inflow and 2% for the outflow. While it was not possible to use streamwise grid stretching for the 3D mixing study, it is allowable in this study because the Prandlt number is so low, making the Peclet number only 600. For this low Pe, physical diffusion is much stronger than the numerical diffusion due to the expanding grid. The grid size in the uniform region is with $dx=dy=dz$=0.015L resulting in 384x64x64 total grid points. The membrane grid employs 80 points/L in both s_1 and s_2 directions which provides high resolution for the structural dynamics. The simulations were run for roughly 10 flow-through times ($O(10^6)$ time steps) and statistics accumulated over the last six flow-through times.

5.2.3 Performance Measures

Characterizing the performance of a forced convection heat exchanger is nuanced. Clearly the primary performance measure is the heat flux from the inflow to the outflow. However, this is not enough to fairly capture the relative performance. This is because while a heat transfer enhancement device should obviously improve the heat flux, depending on how it works, it will most likely also disturb the flow in some way. Physically this disturbance manifests as the device using some of the momentum in the flow, which practically manifests as increased pump power to operate at the same flow rate. Thus, there is a tradeoff between the amount of heat energy that can be extracted through the walls, and the amount of mechanical energy that needs to be supplied by the pump. This means that any improvement to the heat transfer performance is best described as a measure of how efficiently the system is using the momentum of the flow to extract energy from the walls. Thus, a performance measure must take into account both the heat flux and the momentum flux in the channel. The heat flux was calculated according to:

$$Q = \int_0^W \int_0^H \rho C_p u (T - T_0) dydz \tag{5.7}$$

Where ρ is the fluid density, C_p is the heat capacity, u is the fluid velocity, T is the temperature, and T_0 is the inlet temperature. This integration is performed at each X location to assess the performance with downstream position. The energy loss in the channel is measured as essentially a head loss between the inflow plane and a given downstream plane according to:

$$\dot{E} = \int_0^W \int_0^H (p - p_\infty) u dy dz \Big|_{x=0} - \int_0^W \int_0^H (p - p_\infty) u dy dz \Big|_x \tag{5.8}$$

Where p is the pressure, p_∞ is the ambient pressure, and the integrals are evaluated at the inflow plane and at each X plane. Combining these two measurements into a single performance metric allows for a parameter that assesses the configuration in terms of an efficiency. This combined metric is called the Thermal Enhancement Factor (TEF):

$$TEF = \frac{\bar{Q}}{\bar{Q}_0} \times \left(\frac{\bar{\dot{E}}_0}{\bar{\dot{E}}} \right)^{1/3} \tag{5.9}$$

Where the subscript 0 indicates the empty channel baseline configuration, and the overbar indicates a time average over many cycles. The method for arising at this expression for the TEF is described in the following papers (Gee & Webb, 1980; Ozceyhan et al., 2008; Promvonge et al., 2010; Tsia & Hwang, 1999). Essentially, the goal is to compare two systems (baseline and augmented) which are simulated at the same Re number, but have different energy loss, and so theoretically required different pump power to operate. In principle, the augmented case would have transferred less heat had it been given only the amount of pumping power which was used in the empty channel case. Thus, the heat flux improvement of the augmented case must be normalized such that both cases are considered at the same pump power.

A typical performance measure for Heat transfer is the Nusselt number defined as:

$$Nu = \frac{hL}{k} = \frac{\partial (T_w - T)/\partial n \big|_s}{\Delta T_w / L} \tag{5.10}$$

where h is the convective heat transfer coefficient, k is the thermal conductivity of the fluid, and n is the direction normal to a given wall. To obtain $\overline{\mathrm{Nu}}(x)$ at a given x location, Nu is integrated along the duct perimeter at that location. To characterize the dynamics of the fluttering membrane we can measure the key parameters of its motion. Assuming it is moving in a largely periodic behavior, then its motion can be well captured through it flapping amplitude and its Strouhal number St which is the nondimensional frequency. St is given by:

$$\mathrm{St} = \frac{fL}{U} \tag{5.11}$$

where f is the frequency of the captured motion. This could be identified via a Fourier transform type approach, however, in these cases, the motion here is not exactly sinusoidal, and while a Fourier approach does capture the frequency information of these cases, we found a peak identification method provided more consistent results with what could be directly measured by examining the tip position time series. In this method, we take time series of the Z position of points along the trailing edge of the flag, namely a point at each edge and a point on the midline. We then use a prominence based peak identification method to locate the local extrema of those signals by analyzing the z component of tip position information given by $|X_z(S_1, s, t)|$ where S_1 is the maximum Lagrangian position in the s_1 direction and equals L. The Δt_{peaks} between these identified extrema represents the local half-period, so the frequency can be given by $f = 1/\left(2 \cdot \overline{\Delta t_{peaks}}\right)$ where the overbar denotes a time average.

To find the amplitude of the tip position signal we can capture the value of $|X_z(S_1, s, t)|$. However, as will be seen later in the results, some of the cases exhibit significant spanwise deformation such that $|X_z(S_1, s, t)|$ varies as a function of s_2 location. Therefore, to most generally capture the motion of the flag, an average of the tip positions along s_2 is used. Thus, we create the dynamics measurement A_z which defines the deviation from the midline, it has a nondimensional

range of 0 to 0.5 and is called the Mean Tip Excursion. Another useful measure of the flag's amplitude information is $\mathrm{RMS}(|X_z(S_1,s,t)|)$.

These metrics are useful in understanding the dynamics of the flag, however, they do not fully capture the behavior of the system due to the spanwise deformations. There are many possible ways to characterize these spanwise deformations. We chose to examine these deformations in terms as differences between tip locations. Differences between the edge tip positions ($s_2 = 0, S_2$) and the midline tip position ($s_2 = S_2/2$) can give a description of the spanwise bending of the flag. Similarly, the difference between the edge positions ($s_2 = 0$ vs. $s_2 = S_2$) can give a sense of the twisting of the flag. This procedure results in time series of the difference in position. To get an overall perspective of the magnitude of this deviation, the RMS of those time series is taken. These RMS are then normalized against the RMS of the mean of all the tip positions to get a sense of the relative magnitude of these bending and twisting deflections. This procedure results in two measures of the flag's spanwise deflection which we call the Normalized Bending Anomaly (A_B) and the Normalized Twisting Anomaly (A_T). The mathematical description of the formulation is given:

$$A_B = \frac{\mathrm{RMS}\left(\left|X_z\left(S_1,\frac{S_2}{2},t\right)\right| - \left(\frac{|X_z(S_1,0,t)|+|X_z(S_1,S_2,t)|}{2}\right)\right)}{\mathrm{RMS}(Avg(|X_z(S_1,:,t)|))}\times 100\% \tag{5.12}$$

$$A_T = \frac{\mathrm{RMS}(|X_z(S_1,0,t) - X_z(S_1,S_2,t)|)}{\mathrm{RMS}(Avg(|X_z(S_1,:,t)|))}\times 100\% \tag{5.13}$$

These values are given as percentages of the RMS of the average across all points on the trailing edge of the flag. Low values represent relatively 2D flapping, and very high values mean the dynamics are dominated by the spanwise deformations compared to the streamwise flapping deformations.

Finally, there are many available methods to locate and identify vortices for a 3D flow. In this work we use the λ_2 vortex criterion. This method is a vortex core identification method (Jeong &

Hussain, 1995). To construct this criterion, we construct the velocity gradient tensor ∇u. We can then decompose this tensor into its symmetric and antisymmetric parts $\mathbf{S}$ and $\mathbf{Q}$. We then construct $\mathbf{S}^2 + \mathbf{Q}^2$ and order its eigenvalues $\lambda_1 \geq \lambda_2 \geq \lambda_3$. Finally, a point is only part of a vortex if two of the eigenvalues of $\mathbf{S}^2 + \mathbf{Q}^2$ are negative, so if λ_2 is negative we have successfully identified part of a vortex. A vortex is then defined as a connected region of negative λ_2. Plotting iso-surfaces of λ_2 shows a given 2D shell of a 3D vortex region.

5.3 Results

In this study, we examine in detail the baseline square duct configuration to investigate the heat transfer enhancement mechanism in 3D. By understanding how this system achieves heat transfer enhancement, it may be possible to further design the system to take better advantage of this mechanism. We then examine the effect of the spanwise gap parameter using a wider channel so as to be able to test a wider range of flag widths/spanwise gaps. Based on observations from this study, we examine two additional cases each with two flags in an abreast configuration with different inter-flag spacings. Finally, we examine the impact of channel shape on the flags flapping dynamics and on the heat transfer enhancement of the resulting system using the baseline square channel and two additional canonical configurations of a circular channel and a square channel at a 45 degree angle to the flag, which is essentially a diamond shaped channel.

For each part of the study we use flow visualization techniques to better understand the fluid dynamics and fluid structure interactions at play. We also use our performance measures from the prior 2D work to characterize the heat flux, energy loss, and thermal enhancement factor. New to this study, we examine these parameters as a function of downstream location. As compared to measuring the results only at a specified outflow measurement plane, it is useful to view the results as a function of the streamwise coordinate because these flags very rapidly lead to heat transfer

saturation. This means that a flow can only remove a certain amount of heat before the temperature of the flow itself is too close that of the wall. Due to this rapid heat transfer and saturation, it is often insufficient to examine only the outflow plain, as the cases which had different spatial transients may have converged to similar saturated results.

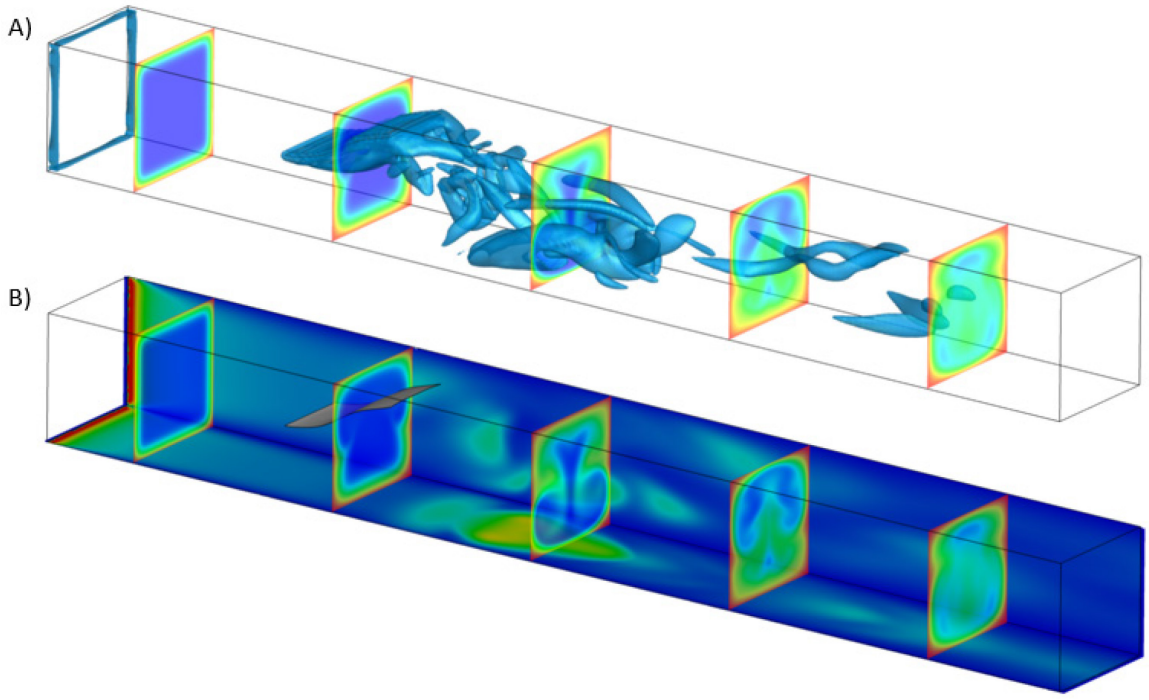

FIG. 5.2 – Snapshot of the 3D square channel configuration. In subplot A) the contours on the cross-stream planes show temperature and the iso-surfaces within the channel show the vortical structures shed by the flag identified by the λ_2 criterion. Subplot B) has cross-stream planes showing contours of the temperature profile and the contours on the interior of the channel walls shows the wall normal heat flux.

As an introduction to the 3D version of this system, FIG. 5.2 shows 2 views of the baseline square channel configuration. A) has cross-stream planes showing temperature contours, as well as iso-surfaces showing vortical structures as measured by the λ_2 criterion. B) has the same cross-stream planes showing temperature, and the contour on the inside channel walls shows the instantaneous heat flux through the wall. This snapshot shows most of the key phenomena at play in this system. From A) we can see a large packet of vorticity has been shed from the flag and is

traveling downstream. We can also see that it is very close to the lower channel wall. This vortical structure is crucial to the heat transfer enhancement mechanism due to the jetting of the cold fluid it induces towards the wall.

In B) we can see the impact of this vortical structure by examining the third cross-stream plane, which is the plane that the vortical structure is currently passing through in this snapshot. Here we can see that the temperature profile in that plane is taking on the shape of an inverted plume. At the surface underneath the jet, we can see a pronounced increase in heat transfer concentrated on the midline of the surface. The large vortical structure is observed to convect downstream, and the region of high heat transfer travels with it and remains prominent until about 4L downstream of the flag's trailing edge. In fact, in B) the remnants of the prior hotspot can still be seen between the 4^{th} and 5^{th} cross-stream planes. Each half-cycle of the flag flutter produces these vortex structures which travel alternatively along the top and bottom walls.

It is clear from the wall normal heat flux visualizations that this vortical structure is significant to the heat transfer enhancement mechanism. To examine exactly what is happening with this structure FIG. 5.3 shows a zoomed in version of the vortical structure. A) shows the sideview, B) shows the top view, and C) shows a front view with a cross-stream plane showing the temperature field. This zoomed in view is of the same cycle but a different time step than what was viewed in FIG. 5.2.

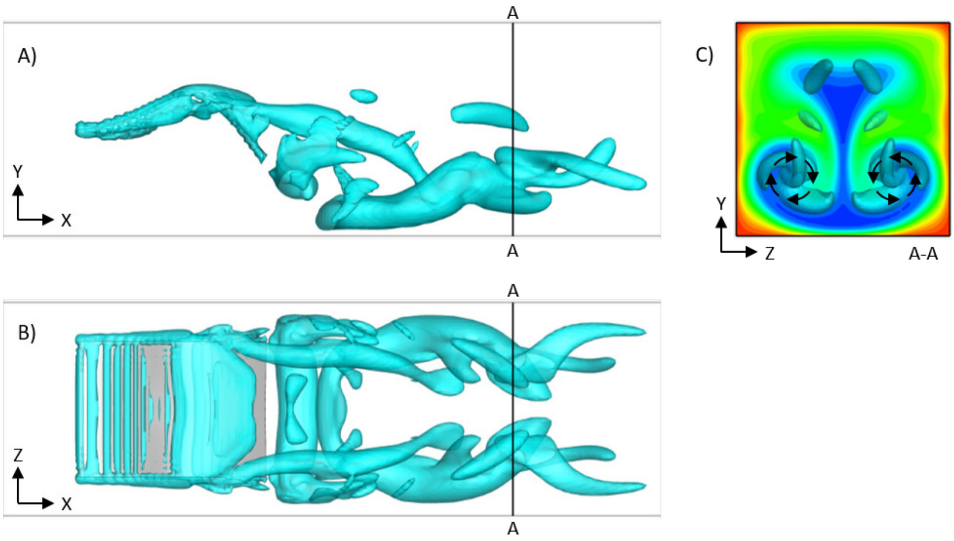

FIG. 5.3 – Zoomed in snapshot of the square channel configuration showing specific details of the key vortical structure responsible for heat transfer enhancement. A) is the side view (X-Y plane) and B) is the top view (X-Z plane) both with isosurfaces of the λ_2 criterion. C) shows a cross-stream view (Z-Y plane) taken at the location noted in A) and B) as A-A with contours showing temperature distribution.

In FIG. 5.3 we can see that this vortical structure is horseshoe shaped with two long streamwise arms followed by a cross-stream component which is aligned with the span. It is interesting to note that this shape is the mirror image of the free edge of the flapping flag, which is also a horseshoe. It is the mirror image insofar as the cross-stream piece follows the streamwise pieces in the vortical structure, while the free cross-stream edge of the flag is downstream of the free streamwise edges. This inversion of the flag edge is evidence of how it was created. The key pieces of this structure are the streamwise arms. These are the shed vortices which were once the vortices along the streamwise edges of the flag. These streamwise vortices are akin to tip leakage vortices. As the flag flaps downward (as in this snapshot) the bottom surface is the pressure side, and the top surface is the suction side, and due to this pressure difference the flow escapes around the side edges of the flag, creating tip leakage vortices. This formation method motivates the vorticity direction once they are shed.

Subplot C) has arrows indicating the direction of rotation for these streamwise vortical arms. We can see that in the center of the channel, the vortices both induce velocity pointing downward from the center of the channel towards the wall. If we examine the temperature contour, we can see the result of these vortices is a jetting phenomenon. Because these vortices are centered well below the midplane of the channel, they end up jetting fluid from the core of the flow towards the walls. It is this jetting behavior which is responsible for the heat transfer enhancement. Jetting cold core fluid towards the walls not only mixes the flow, but it also sharpens the gradient at the wall by placing cold fluid near the hot walls (changing the ΔT) and by decreasing the distance of this gradient by way of compression of the stratification due to the downwards V velocity component between the vortices. This mechanism is due to both the rotational direction of these vorticity arms, as well as their position below the midplane of the channel and so close to the bottom wall. This allows them to move cold fluid from the center of the channel right to the outer wall. It should be further noted that while this vortical structure begins as a horseshoe shape, visualizations show that the spanwise piece of the structure dissipates more quickly than the streamwise arms.

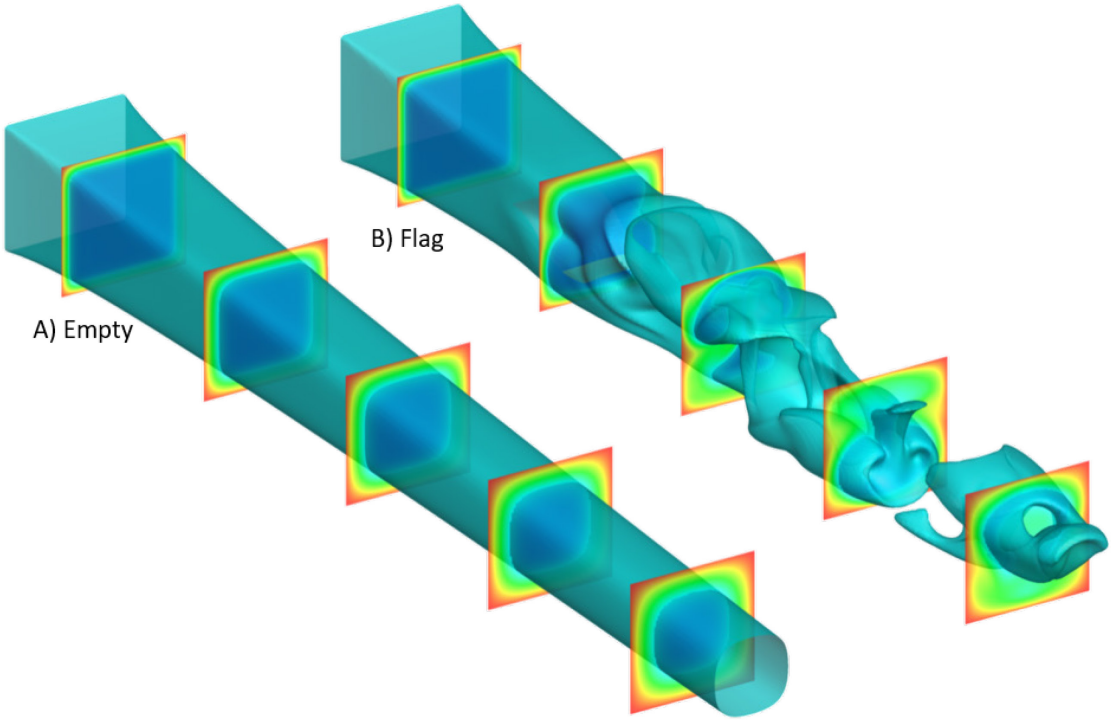

FIG. 5.4 – Isosurfaces of temperature T=0.25 for the A) empty channel and B) flapping flag cases.

Finally, to compare this baseline flapping flag case to the empty channel, FIG. 5.4 shows cross-stream planes with temperature contours as well as isosurfaces of temperature where T=0.25 for the empty channel and flapping flag cases. These temperature isosurfaces provide a qualitative visual indication of the interface between the heated boundary layer and the colder core fluid. For the empty case we see exactly what we would expect for a developing thermal boundary layer in a square channel. In contrast, the isosurface in the flapping flag case clearly shows results of the jetting phenomenon. The cold core fluid (fluid inside of the isosurfaces) is pushed towards the walls in large lobe-like structures which alternate in the top and bottom of the channel. The transitions between lobes is relatively short, as can be seen in between the 4th and 5th cross-stream planes. Also, those transition regions appear to be areas of very rapid heat transfer. This observation is supported by the separation between the lobes between the 4th and 5th cross-stream planes, indicating there is no more fluid at a temperature below T=0.25 in that region.

5.3.1 Comparison of 3D and 2D Heat Transfer Enhancement

One clear takeaway so far is that the streamwise vortices shed from the side edges of the flag play an important role in the heat transfer enhancement. However, this behavior is only possible in the 3D model (there are no streamwise edges in 2D). Yet heat transfer enhancement was seen in the prior 2D study. Furthermore, it was reported in that study that those results showed comparable performance to real world wind tunnel experiments. This 2D to 3D consistency must mean it is either incorrect to say that the 3D case sees the majority of the performance improvement due to these 3D exclusive streamwise vortices; or the 2D and 3D cases see heat transfer enhancement due to different mechanisms.

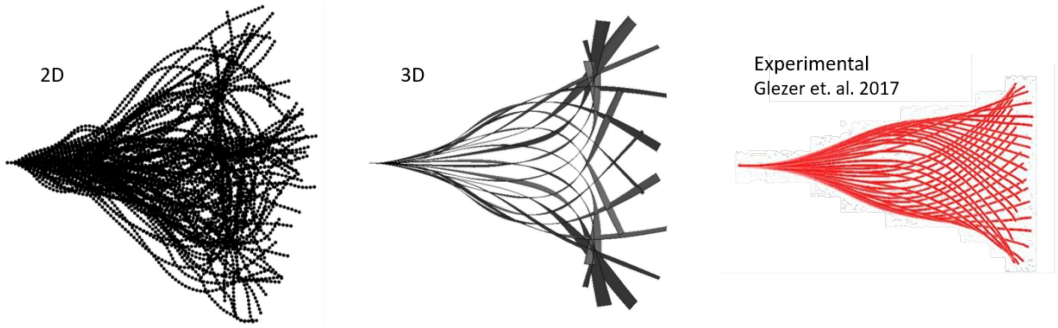

FIG. 5.5 – 2D and 3D flapping envelopes, experimental measurements from Prof. Ari Glezer's group at GA Tech are also included.

FIG. 5.5 shows the flapping envelopes for a 2D simulation and the 3D baseline case at the same U*. The experimental figure is from Prof. Ari Glezer's group at Georgia Tech (Private Communication, 2016). That data was of a flag with a different channel height and U*, however, it is still interesting to note that the mode shapes exhibited by the 3D flag are generally similar to the experiment. However, there are significant differences between the 2D and 3D simulation results. Significantly, the 2D model exhibits very complex and somewhat chaotic flutter. This type of behavior is described throughout the literature as being in the "chaotic flapping" regime (Shelley & Zhang, 2011). That we see chaotic flutter for the 2D model is not surprising given U* is much

higher than what was used in the prior 2D studies. This higher U* was required for the 3D flag to demonstrate large amplitude flapping. Herein we can already see one of the fundamental issues in comparing 2D and 3D flags flapping flags, which is 3D flags are consistently more stable than 2D flags (Eloy, Souilliez, & Schouveiler, 2007).

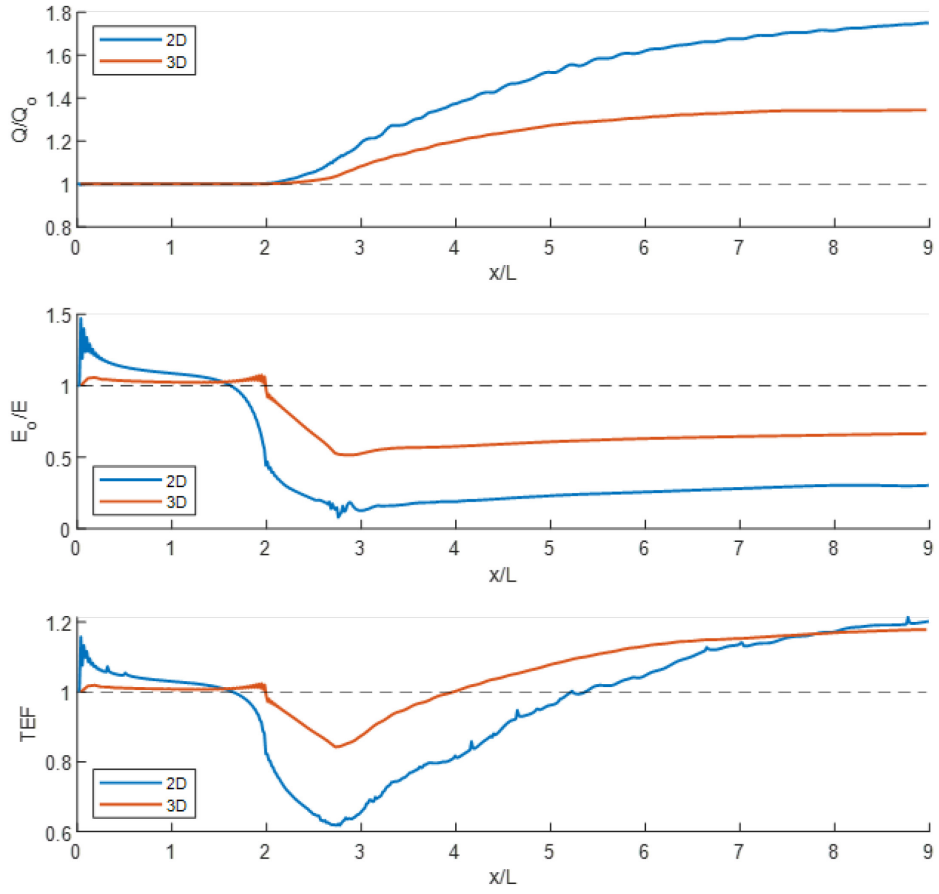

FIG. 5.6 – Performance comparison of 2D and 3D flag enhanced channel flow heat transfer.

FIG. 5.6 compares the results of the 2D and 3D versions of this problem. In both cases, Re=600, the flag length L equals the channel height, and the flag is placed 2L downstream of the inlet. It had been noted previously that the prior 2D study showed performance similar to real-world 3D experiments. However, plotting the performance parameters against the streamwise coordinate x/L shows that this result may be only true because both systems were measured once the performance improvement saturated. The heat flux Q/Q_0 shows that the 2D case is transferring far more heat

overall than the 3D case, and the heat flux appears to also be increasing more rapidly for the 2D case. Furthermore, whereas the 3D case seems to reach an asymptote within the simulated domain, the 2D case seems to still be increasing in relative heat flux. In contrast, the energy loss E_0/E is far worse for the 2D case than the 3D case, but the two curves do appear to follow a similar trend. These results when combined into the TEF show significant differences for most of the channel length simulated here. The increase in energy loss of the 2D flag drags the TEF below the 3D case for most of the domain. However, the increase in heat flux raises the TEF for the 2D case more rapidly than the 3D case such that they have equal TEF at around x/L=8. Thus, while the 3D flag generates a smaller net heat flux from the walls, it also generated a lower pressure loss, thereby leading to a TEF that rapidly exceeds that of the 2D flag and levels off to a value of about 1.2, which is similar to the 2D flag.

5.3.2 Sensitivity to Flag Aspect Ratio and Split Flags Experiment

Following on the evidence of the importance of the streamwise edges of the flag and the streamwise vortical structures they create, we examine the 3D parameter of the flag span and spanwise gap to the sidewalls. This will provide further insight into the interaction between these vortices and the sidewalls. It will also allow us to examine the tradeoff between energy loss and heat flux improvement. The notion here is that wider flags should create larger vortices which will potentially mix the flow more effectively and lead to more rapid heat transfer. However, wider flags would generate more drag leading to higher energy (pressure) losses. In addition, the energy required to flap and deform these larger flags would be higher, also leading to higher energy losses. Finally, we will also examine the relationship between flag aspect-ratio and the flapping dynamics of the flag. This topic has been studied previously by others (Eloy et al., 2007), and it is clear that it plays a significant role in this system as well.

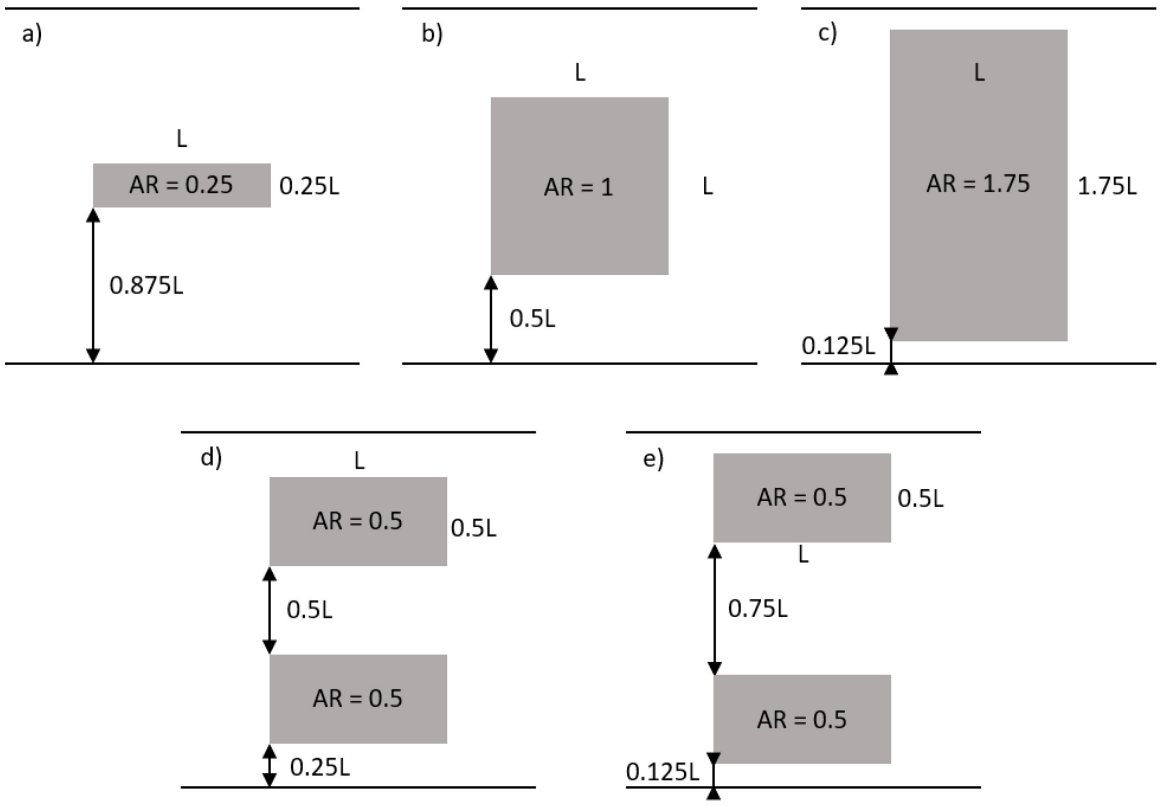

FIG. 5.7 – Schematic top views of the five cases explored in using the rectangular channel with channel aspect ratio 2. A-C cases explore the effect of flag aspect ratio, and confinement with AR=0.25, AR=1, and AR=1.75 respectively. D and E are the split flag cases which investigate any connection between spanwise edge length and heat transfer performance.

FIG. 5.7 shows schematics of the cases we used to investigate some of the 3D parameters. To have a wider range of possible flag spans and spanwise gaps, a wider rectangular shaped channel was used for these span studies wherein the channel width was 2L and the channel height was L. Three flags with widths 0.25L, L, and 1.75L were studied. Because it is clear that the effect of the vortices shed by the spanwise edges is important, we devised two additional simulations to test this effect with split flags. Each flag has AR=0.5 so that the combined total area is the same as the AR=1 case (to create comparable energy losses), but the split flag configurations have twice the spanwise edge length. The two cases we simulated had inter-flag spacings of 0.5L and 0.75L. The results will be presented with an examination of the flapping dynamics, an analysis of the heat

transfer performance, and an investigation into any differences in the heat transfer enhancing vortical structures.

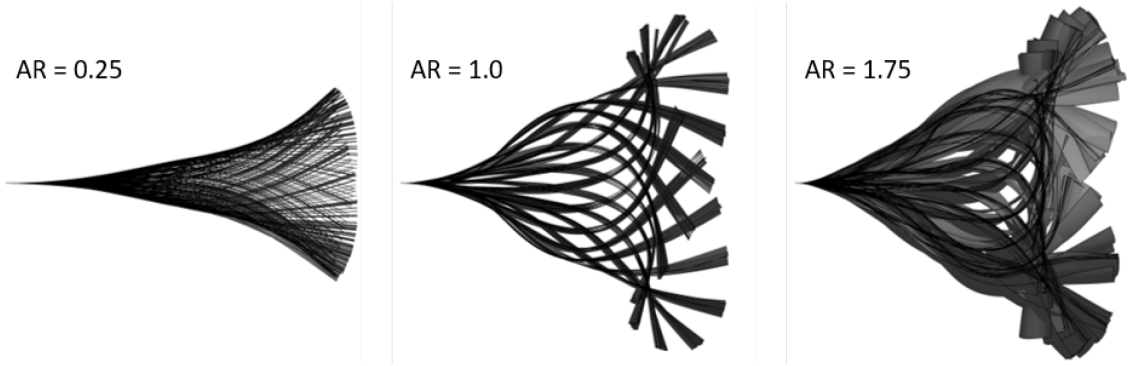

FIG. 5.8 – Flapping envelopes for the 3 aspect ratio cases showing a side view, visualized as a gray surface with a black edge.

FIG. 5.8 shows the side view of the flapping envelopes for the 3 aspect ratio tests. These envelopes show a jump in the flapping amplitude between AR=0.25 and AR=1 while the flapping amplitude appears to remain similar between AR=1 and AR=1.75. This change in amplitude can also be seen quantitatively in FIG. 5.10 on the flapping dynamics. It also appears that there is a change in mode shape between the AR=0.25 and AR=1 cases. Doare et al., (2011) studied the effect of spanwise confinement on a flag's flapping dynamics using an inviscid model. They found that the critical velocity as a function of the structural parameters U* and M* changed significantly from the theoretical 2D behavior for all but very small confinements (i.e. flags nearly in contact with the side walls behave in an almost 2D manner). However, the result here does not seem to be an effect of confinement per se as much as an effect of flag aspect ratio, as the transition in amplitude coincides with much larger spanwise gaps than what was studied in that work. Eloy et al., (2007) also used an analytic approach and characterized the dynamics of unconfined finite span flapping flags to understand the behavior as a function of aspect ratio.

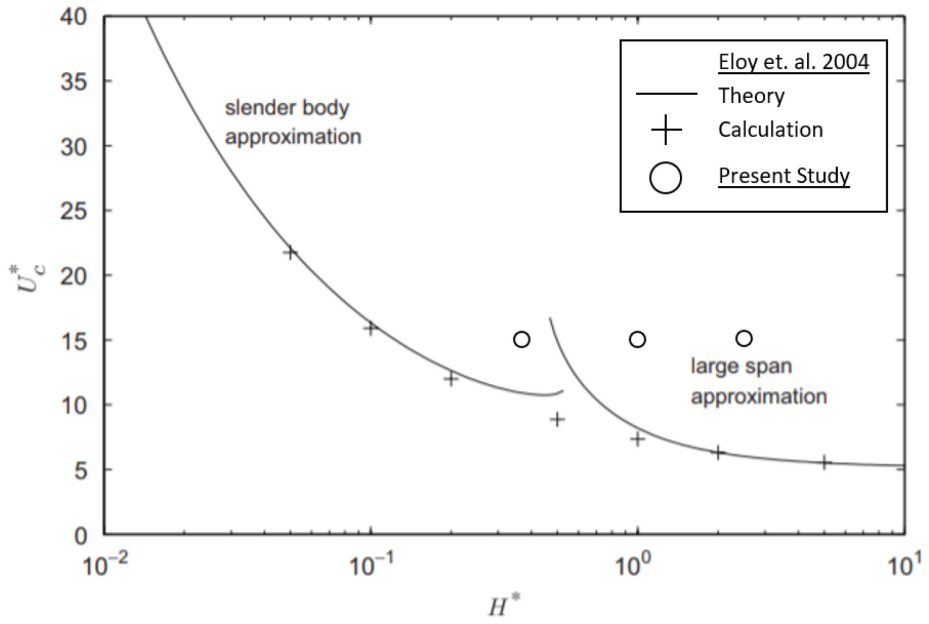

FIG. 5.9 - Critical velocity U_C of a theoretical 3D flapping plate as a function of its aspect ratio H* (Eloy et al., 2007).*

In general, they found that narrower flags (flags with smaller AR) are more stable, which is consistent with the behavior seen here. Crucially, they also found a transition in dynamics between the so called "slender body" and the "large span" approximations, as shown in FIG. 5.9. The results of this study seem to be in-line with this data. With decreasing AR, our cases are getting closer to the critical velocity. Furthermore, the AR=0.25 case appears to be under the predicted U_c^* via the large span approximation but above the U_c^* for the slender body approximation. Being between these regimes may explain why it shows a significantly different flapping mode. To get a more quantitative sense of the flag dynamics, we can also examine the four key measures of the dynamics. Those metrics are: the mean tip excursion, the Strouhal number, the normalized bending anomaly, and the normalized twisting anomaly:

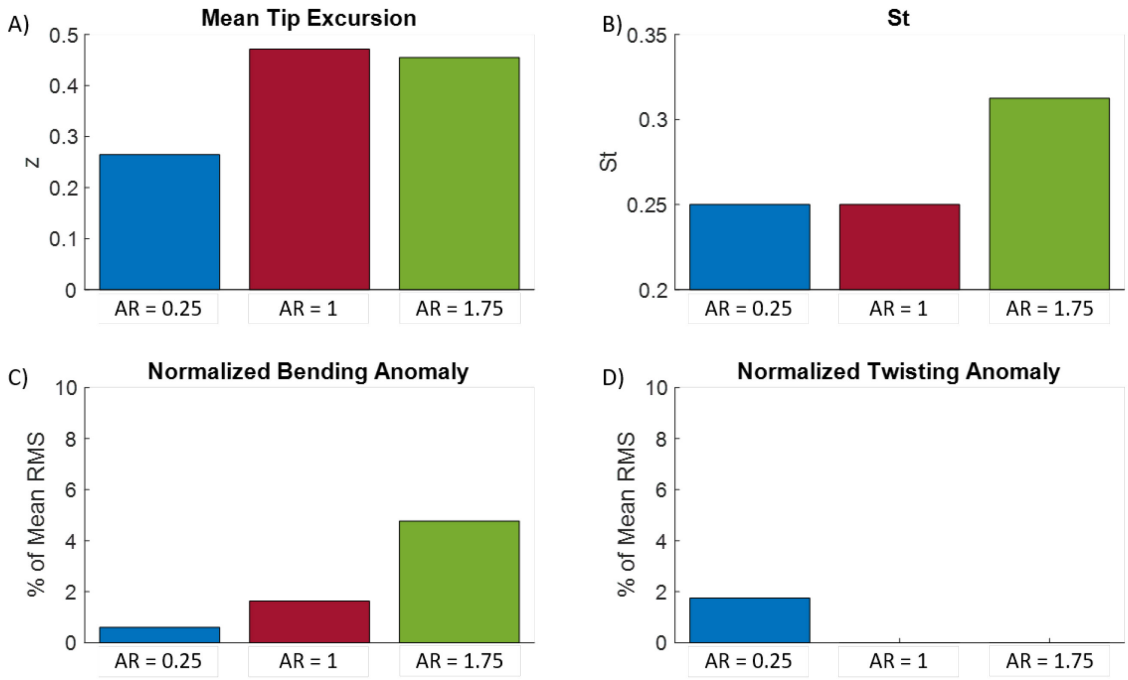

FIG. 5.10 – Bar graphs of the four measures of the overall flapping dynamics for the aspect ratio cases.

FIG. 5.10 shows these four measures of the dynamics. The amplitude information clearly shows what was noted in the observations of the flapping envelopes in that the AR=0.25 flag has a much lower amplitude. The St of the AR=1.75 case is 25% larger than for all other cases. This is an interesting result which will be seen the following cases as well, wherein confinement appears to increase the flapping frequency. A further observation of the dynamics is of the 3D transverse deformation of the flag. Here we can see with increased AR the normalized bending anomaly also increases. Without more AR samples it is difficult to know the nature of this growth; however according to this data, A_B appears to increase according to a power law.

This is not a surprising effect when considering the effect of the fixed leading-edge boundary condition on the spanwise bending moment. The specific boundary conditions of a plate clamped on one edge make a simple scaling analysis to predict this behavior difficult, especially considering the plate thickness is considered vanishingly small for these membranes. However, some intuition

can be developed from a simple geometric interpretation. A very narrow plate would require very high curvature to experience noticeable 3D deformation whereas a wide flag could exhibit higher deflection for the same curvature. This increase in A_B can also be seen by examining the 3D snapshots presented later in FIG. 5.14. There, we can see the narrowest flag (AR=0.25) seems to have no noticeable bending deformation, whereas the AR=1 case shows very small bending deformations. Finally, the AR=1.75 case shows significantly larger transverse deformation, and also appears to exhibit higher mode shape deformations than what appears in the AR=1 case.

The Normalized Twisting Anomaly stands in contrast, where only the narrowest flag exhibits any twisting. This is an interesting result in its own right. Observations of the movies of the membrane flapping for this case show that a twisting mode began to develop towards the end of the computational time, culminating in a large amplitude twisting event. This mode only began to grow several flapping cycles after the system had seemingly reached a stationary state and indicates some sort of twisting instability. It makes sense that the narrowest flag would be the most unstable to twisting modes. To understand this, we can consider the expression for the twist angle of a structure supported at one edge which is given by $\varphi = TL/\omega_\Gamma$ where φ is the twist angle, T is the applied torque (the result of asymmetric pressure forces due to a small spanwise-asymmetric perturbation) and L is the length of the plate. ω_Γ is the torsional rigidity given by $\omega_\Gamma = GJ_T$ where G is the shear modulus and J_T is the torsion constant. For our various aspect ratio cases the only variable is the torsion constant which is given by $J_T = \beta ab^3$ where β is a coefficient related to the aspect ratio of plate thickness to plate width, *a* is the plate width, and *b* is the plate thickness. This analogy breaks down for our membrane as we consider *b* to be vanishingly thin, however, this coefficient β monotonically increases with larger a/b aspect ratio. Furthermore, $J_T \sim a$ so J_T must increase for increasing *a* (i.e. wider membranes). This means that the torsional rigidity ω_Γ increases for wider membranes, which further implies that the twist angle for a given torque is smaller for

wider membranes. The results from the AR study seem to suggest that this twist instability has a bifurcation somewhere between AR=1 and AR=0.25.

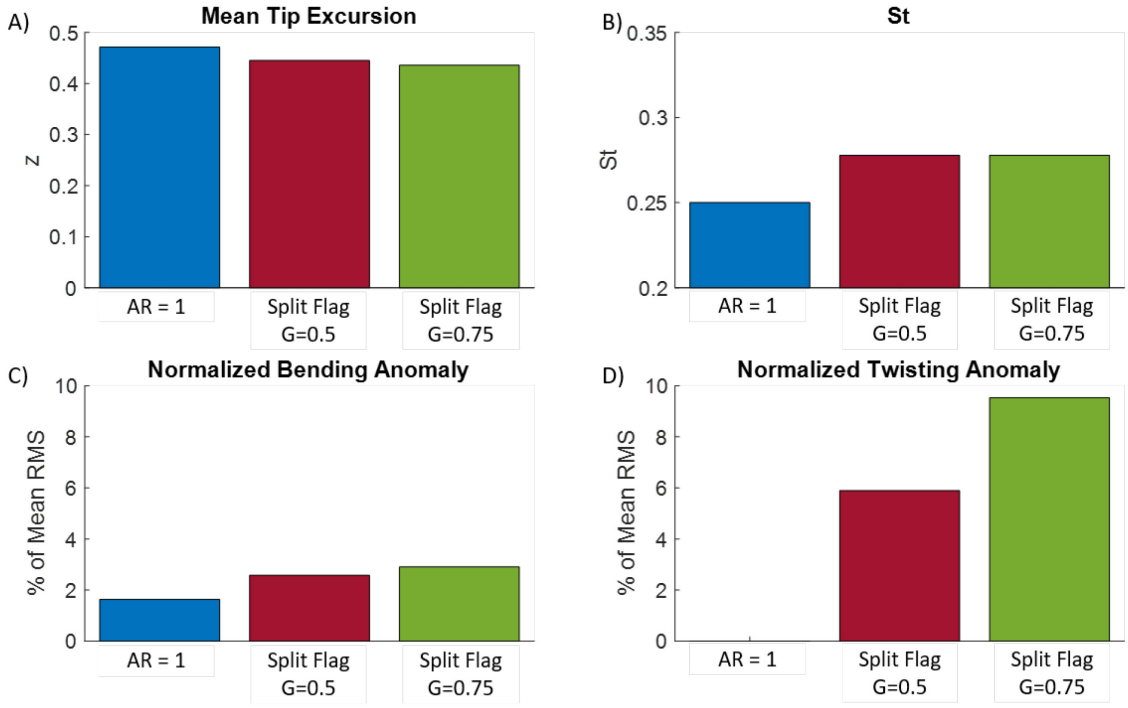

FIG. 5.11 – Bar graphs of the four measures of the overall flapping dynamics for the split flag cases compared to the AR=1 single flag case.

FIG. 5.11 shows the dynamics information for the split flag cases compared to the AR=1 case. This comparison is made because the AR=1 case has the same combined area. For these results, all values for the split flag cases are averaged between the flags. Here we can see there is a slight decrease in the flapping amplitude for the split flags, which due to their individually smaller aspect ratios. However, the tip excursion is still much larger than that of the AR=0.25 case shown before, and is very close to the results of the wider flags, which suggests there must be a bifurcation between AR=0.5 and AR=0.25 in terms of the flapping amplitude. Interestingly, the split flags have much higher St. This must be a result of the confinement, and not the aspect ratio. We know this because the AR=0.25 case exhibited the same St as the AR=1 case, whereas the highly confined AR=1.75 case showed increased St.

Examining the bending anomaly results, the split flags appear to exhibit higher bending than the AR=1 case, which is surprising considering they have smaller AR, meaning significantly more strain energy is needed to bend them to that degree. Observations of snapshots of the flags (as can be seen in FIG. 5.15) shows that this behavior is in fact physical, and not an artifact of the calculations. These observations show that the flags are bending such that the interior corners undergo larger amplitude flapping. Essentially it appears that the flags form a quarter-circular shape such that their curvature mimics the interior corners of the channel in some sense.

In addition to this spanwise bending, the flags also exhibit very significant twisting. Observations of the flapping behavior shows this twisting is consistent for all cycles (not the growth of an instability as was seen in the AR=0.25 case) and the result of this twisting is similar to the result of the bending. It appears that the interior corners are flapping more than the exterior corners and this is inducing bending and twisting deformations into the flags. This behavior is not surprising, though the amount of bending deformation is unexpected. It is unsurprising because of the asymmetric forcing for each flag introduced by the configuration. Each flag would feel a wall on their exterior edge, but on the interior edge they would experience the flow field from their neighbor, which apparently induces additional flapping energy. Thus, this behavior is the result of a combined effect of the interior corners getting a boost due to the coupling, and the exterior corners being dragged back by the confinement. We can see this combined behavior playout in the case with the larger inter-flag spacing, where the amplitude is slightly lower, but the twisting anomaly is much larger. To analyze the heat transfer performance of the system, we have a number of available performance measures including: Nu, Q, E, and TEF which are all described in the earlier section on the performance parameters.

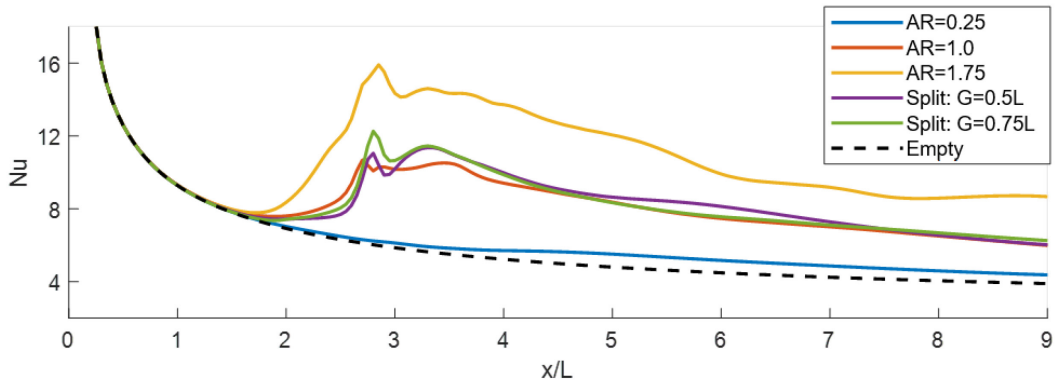

FIG. 5.12 – Nusselt Number vs. Streamwise coordinate for the 3 flag widths and the 2 split flag experiments.

FIG. 5.12 shows the Nusselt number as a function of the streamwise coordinate. Because the working fluid remains constant, improvement in the Nu number represents increased convective heat transfer. Here we can see the baseline empty channel follows exactly the trend that would be expected according to theory for developing heat transfer in a rectangular channel. That theory is that Nu decreases downstream as the boundary layers grow, and as the boundary layers merge to create a fully developed channel flow, the Nu number asymptotes to it fully developed value. We can see in this figure that the empty channel would likely not be considered fully developed by this point. The flag cases appear to lie in 3 groups. The AR=0.25 case shows almost no improvement over the baseline. It is also crucially different to the other cases in that it does not have a peak immediately after the flag. All of the cases that have the combined total surface area of the AR=1 case essentially collapse together with a sharp increase in Nu at the position of the flag followed by a decrease in Nu which is more rapid than the asymptotic decrease of the baseline. That downstream decrease is due to the dissipation of the heat transfer enhancing vortices, though even by the end of the channel, the effect of those vortices is still being felt.

The AR=1.75 case shows the same basic profile as the AR=1 cases, but with a higher magnitude increase over the baseline. One particularly interesting difference for the AR=1.75 case is the Nu improvement even at the flag location (the flag is from x/L =2 to3). The AR=1 cases only show improvement after the flag. The reasons for this earlier Nu increase can be seen in FIG. 5.14

(presented later), where there is clear evidence of high wall normal heat flux along the sidewalls due to the confinement. Overall, these results show that the flags drastically improve the convective heat transfer in the channel near the flag, and that improvement diminishes downstream but persists for several flag lengths (at least for the entire simulation domain). Presumably, at some downstream location the effects of the flag will no longer be felt and Nu will revert to the baseline channel flow. However, while the Nusselt number does provide significant insight into the relative benefit of a heat transfer enhancement device, it does not take into account the relative energy loss. As such, the normalized heat flux, normalized energy loss, and thermal enhancement factor are calculated.

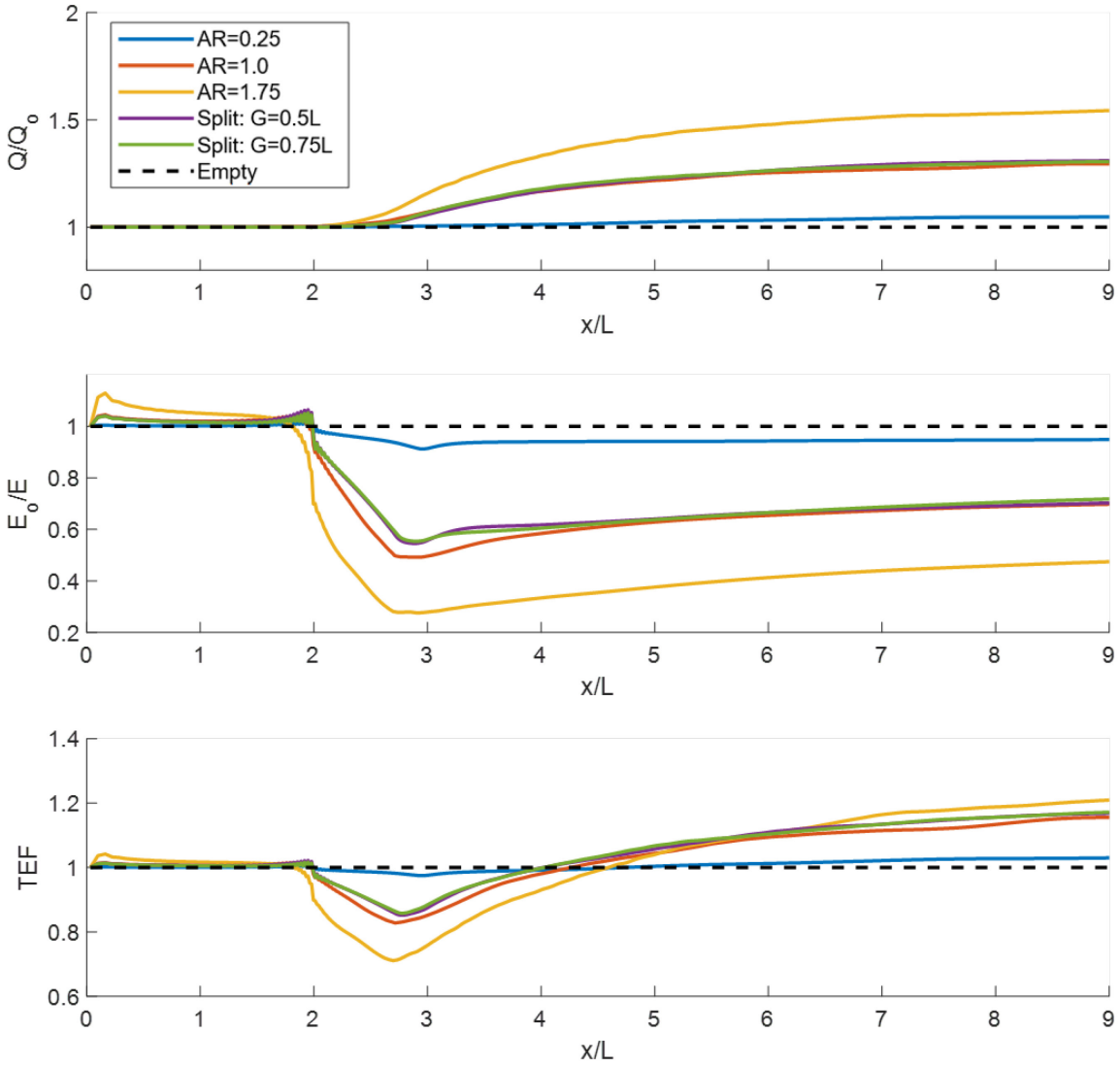

FIG. 5.13 – Time averaged performance measures for the 3 flag widths and the 2 split flag experiments showing the normalized heat flux Q/Q_0, energy loss E_0/E, and thermal enhancement factor TEF all as a function of streamwise position.

FIG. 5.13 shows the performance measures for the 5 cases which used the rectangular channel. The heat flux and energy loss plots behave mostly as expected. The heat flux clearly increases as a function of the flag span. This makes sense as the larger flags should create larger vortical structures and thus greater mixing and subsequent heat transfer enhancement. We can see that the AR=0.25 case has a negligible increase in heat flux, and the split flag cases appear to have nearly identical heat flux to the combined AR=1 case. There is perhaps a very minor improvement with the split

flags, however it is negligible. Finally, the increase in heat flux as measured at the outflow of the channel seems to be linearly increasing with the total flag area. The energy loss results follow a similar trend with minimal energy loss for the AR=0.25 case, similarity between the AR=1 case and the split flags, and a linear increase in energy loss as a function of the total flag area. What is interesting is that the combination of these results into the TEF leads to a collapse for the system performance, except for the AR=0.25 case. That case was shown earlier to be effectively more stable due to its very low aspect ratio, thus seeing lower amplitude oscillations. There is a slight improvement with the split flags though it is a very minor effect.

Also interesting is that the AR=1.75 case performs similarly to the AR=1 case. It appears that to first order, the significant improvement in heat flux is offset by the corresponding increase in energy loss due to the larger flag and larger blockage ratio. This suggests that to first order, the TEF may only be sensitive to the flapping amplitude. That being said, this similarity is not all encompassing, the AR=1.75 does display different behavior which could be relevant to a design, and these differences are evident in the TEF plot. We can see that immediately after the flag, the AR=1.75 case has significantly worse performance. All the cases show an initial TEF after the flag which is less than 1 and all the cases see an increase in TEF such that by X=2.5 they all have TEF>1. But while the AR=1.75 case lags behind the AR=1 case, its slope is greater, so that by X=6 it surpasses the AR=1 case and that improvement continues until the end of the computational domain such that by the end of the channel the AR=1.75 case is performing about 3% better. To understand the mechanism causing these differences based on aspect ratio, and the similarities for the split flag cases, we use visualizations similar to what was used for the square channel.

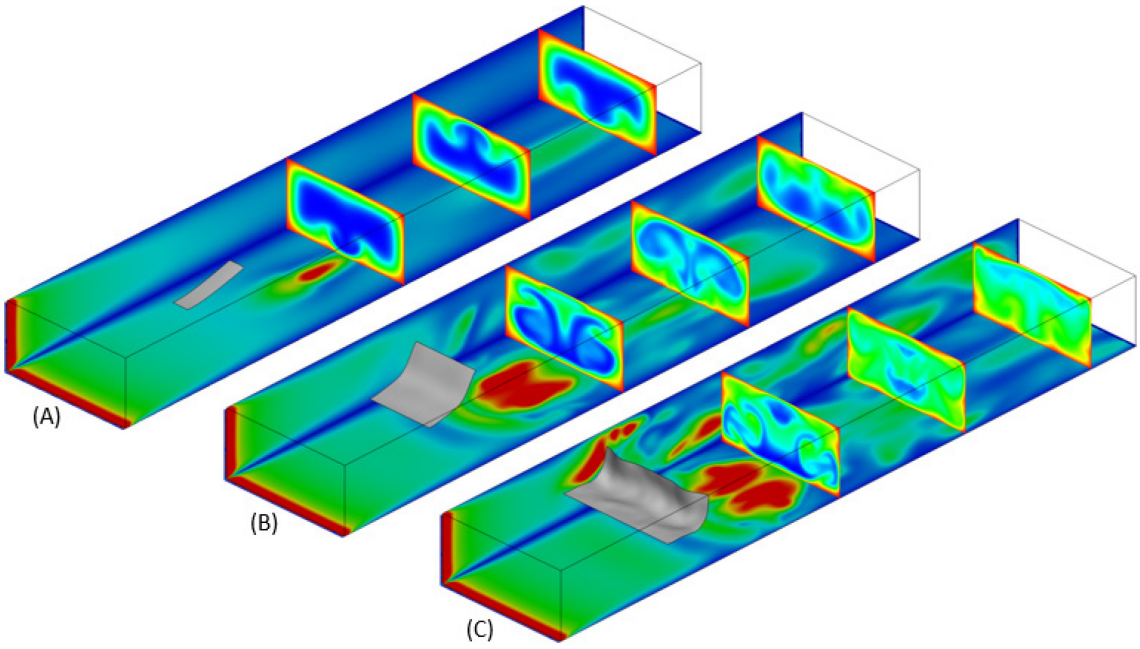

FIG. 5.14 – Snapshots of 3D results for 3 flag widths. A) is AR=0.25, B) is AR=1, and C) is AR=1.75. The channel's width is 2L. Contours on cross-stream planes show temperature distribution and contours on the interior channel walls show wall normal heat transfer.

FIG. 5.14 shows 3D visualizations of snapshots of the three AR cases. Here flags are shown as gray membranes, the cross-stream planes are the temperature contours, and the contours on the inside of the channel walls is the heat flux. We can see the jetting behavior seen in the square channel case is still present in some sense for all three AR cases. Even the narrowest flag (AR=0.25) does show a change in the temperature contours as seen in the cross-stream planes. We can see that in the center of the channel the cold core fluid is much closer to the walls in the center of the channel, though there is less clear indication of the plume shaped profiles seen in other cases. This behavior is visible in all three of the cross-stream planes (note: the phasing of the cross-stream planes was chosen so as to be similar to the shedding phase of the vortical structures). Just as in the square channel case, under this region where the cold fluid is much closer to the wall is a patch of high heat flux on the corresponding wall. However, comparing AR=0.25 with the higher AR cases, we can see that there is no evidence of increased heat flux on the sidewalls over the expected

developing channel flow profile. While there is a clear hotspot of heat flux in the AR=0.25 case, when considering how little of the channel is actually affected, it is not surprising that the improvements in the Nusselt number and TEF were so small.

The AR=1 case show contours similar to the expected jetting behavior seen in the square channel case. Interestingly, there is a split in the tail of the jet in the first cross-stream plane, but by the second cross-stream plane, this split appears to be closing. The result is that the tail also means cold core fluid is thrust towards the wall opposite the direction of the plume. This mean there is both the characteristic hotspot on the wall in the direction of the plume, as well as a narrower hotspot on the wall in the opposite direction. There are also smaller areas of moderately higher heat flux on the side walls in the immediate vicinity of the flag. This was also seen in the square channel case. These sidewall hotspots are the result of the mushroom shape the jet creates as it impinges on the top and bottom walls. Interaction with the wall causes it to spread out in both spanwise directions, thrusting the cold fluid from the core towards the spanwise sidewalls.

The AR=1.75 case shows significantly different behavior. While the jet is still visible in the cross-stream planes, its structure is more complex with what appear to be secondary jets which hit the sidewalls and create hotspots of high heat transfer on the side walls far stronger than what was seen in the AR=1 case, which is a potentially valuable side effect. Furthermore, the tail of the plume shape is much more complicated. So much so, that there is a pocket of cold core fluid very close to the wall on the opposite side from the plume.

Finally, it is interesting to qualitatively note how different the temperature profile is at the outlet between the cases. The AR=0.25 case appears to be only a slight variation of the expected channel flow, whereas for the AR=1.75 case, even by the 2nd cross-stream plane seems to already have no remaining pockets of fluid near the inflow temperature of T=0.

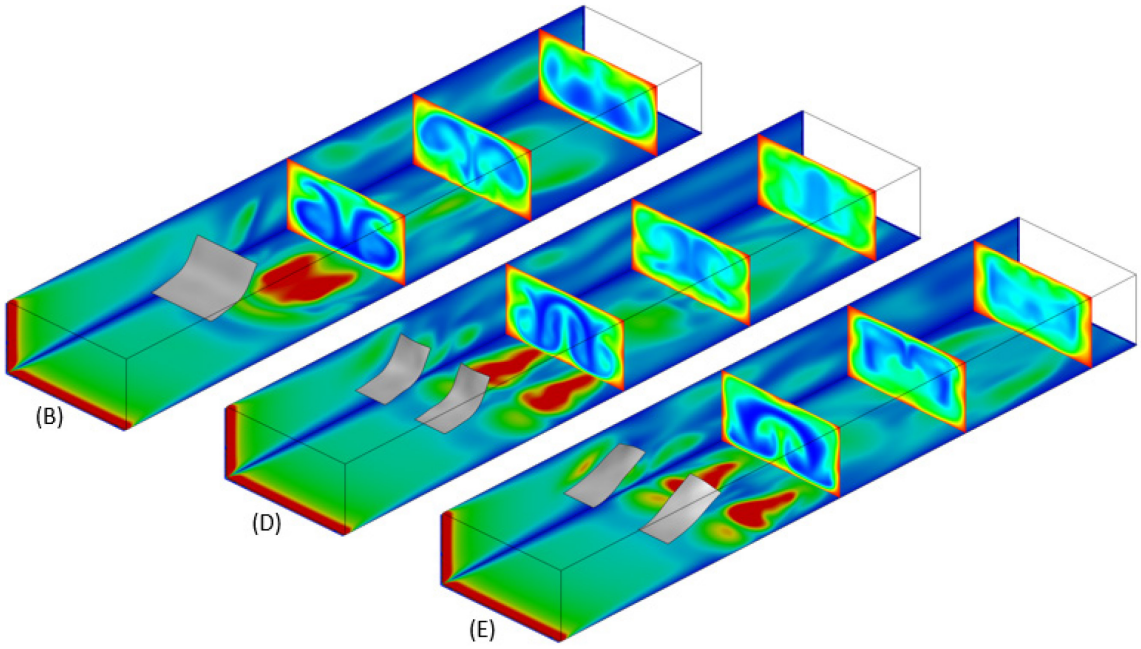

FIG. 5.15 – Snapshots of 3D results for the split flag experiment. B) is the W=L case shown before, D) has inter-flag spacing of 0.5L, and E) has inter-flag spacing of 0.75L. The channel width is 2L. Contours on cross-stream planes show temperature distribution and contours on the interior channel walls show wall normal heat transfer.

The results of the split flag simulations are shown in FIG. 5.15. The flow patterns created in these cases are understandably more complex due to interactions between the flags. Examining the first cross-stream plane, it is clear that in both split flag cases there are two jets of cold core fluid towards the bottom wall, as well as one jet in the midplane of the channel which is in the opposite direction, pulling hot fluid from the wall towards the core. This is theoretically also beneficial in that it helps mix the flow; however, this central jet also leads to a region of unusually low heat transfer in that patch as the temperature gradient is actually elongated in that region, meaning the heat transfer rate would be lower than the baseline empty channel.

It is important to note how dissimilar the split flags and combined AR=1 flag appear to be in terms of the heat flux and temperature visualizations considering how similarly they behaved in terms of Nu, Q/Q_0, E_0/E, and TEF. The convective patterns are grossly different, the heat flux

profiles on the walls are different, and the even the temperature profile at the outflow planes appear different even after having several flag lengths of distance to develop and homogenize. There is nothing in these visualizations that would indicate these cases would all have nearly identical performance. It is possible that the collapse of the performance measures is due in part to time averaging used in their calculation. Also, there may be more subtle similarities between these visualizations than what is immediately visually apparent.

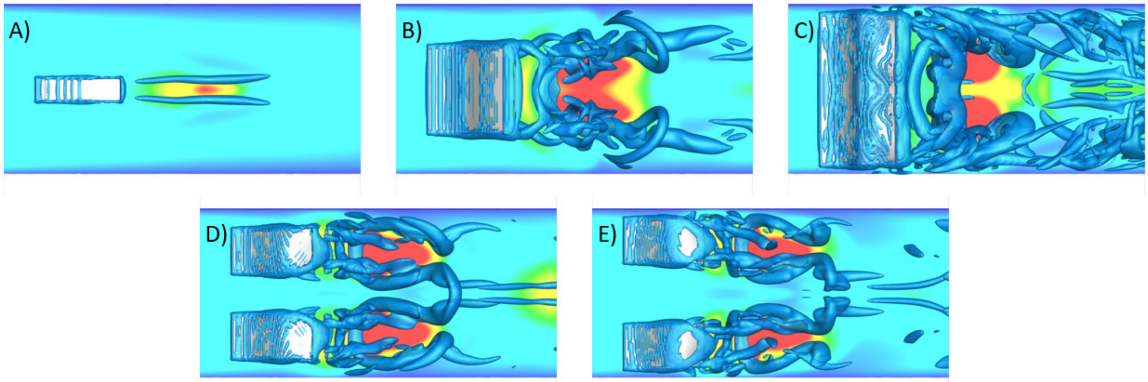

FIG. 5.16 – Top views of the vortical structures visualized by the λ_2 criterion, and the wall normal heat flux for the 3 flag width cases and the 2 split flag cases.

To more closely examine the vortical structures shed by the flags, FIG. 5.16 shows top views of the various rectangular channel cases. The AR=0.25 shows very little persistent vorticity is shed by the flag. The AR=1 case has the same 2 large streamwise vortical structures which were seen in the earlier square channel configuration; however, the decreased sidewall confinement means these vortices spread out with a wake angle which is likely the cause of the split jet noted in FIG. 5.14. The AR=1.75 case sheds significantly more vorticity which can be seen by noting the isosurface threshold for the λ_2 criterion is the same for all these snapshots, yet significantly more vortical structures are visible in the AR=1.75 case. Furthermore, the key streamwise vortices shed from the spanwise edges of the flag seem to be less coherent, which is most likely an effect of the confinement. In both split flag cases, the individual flags show vortex shedding behavior which is

similar to the solo flag cases, with the only distinction being that the interior streamwise vortices are connected.

5.3.3 Robustness to Channel Shape

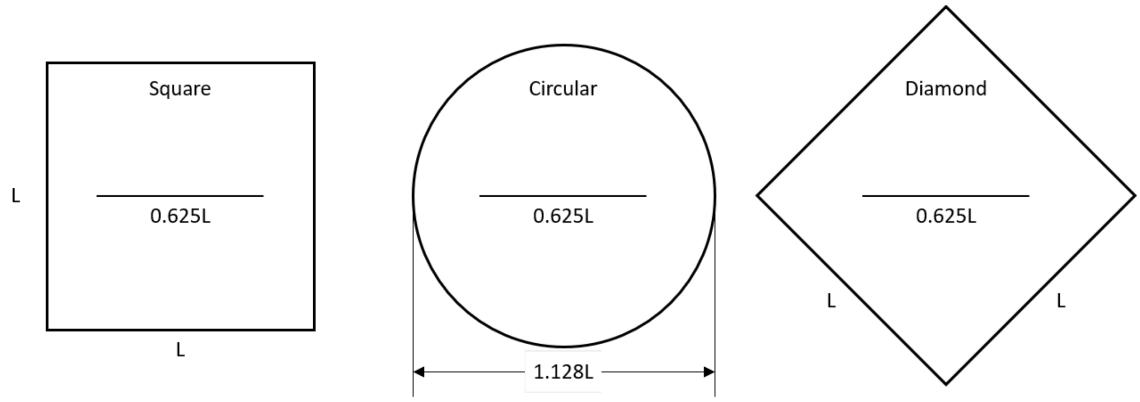

FIG. 5.17 – Front view schematics of the three channel shape cases.

As discussed previously, forced convection channel flow heat exchangers come in a wide variety of cross-section shapes. It is not practical to test this wide of a range of possible options. Instead we are interested to see how sensitive this system is to duct cross section. We chose two additional channels with canonical cross sections: a circular channel and a square channel with the flag rotated 45° such that the channel cross-section appears as a diamond to the flag. The diamond channel has the same cross-section as the original square channel and the circular channels size was chosen such that the cross-sectional area is the same as the square channel case, giving it a diameter of $D = 2L/\sqrt{\pi}$ or D=1.128L. It is not possible to match both the interior surface area (available heat) and the cross-sectional area (heat capacity). The 3 similarity options available are constant circumference D=1.273L (matching available heat), constant area D=1.128L (matching available heat capacity), or constant hydraulic diameter D=L. The constant cross-sectional area choice was made to preserve the total heat transfer capacity of the incoming flow. The first concern for non-square channels is whether the flag will have room to flap, and if so, how its dynamics will be affected by differential confinement along the span.

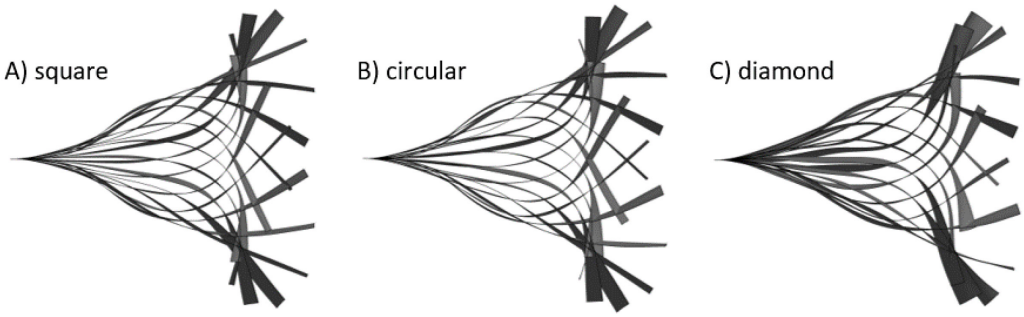

FIG. 5.18 – Flapping envelopes for the 3 channel shapes showing a side view, visualized as a gray surface with a black edge.

FIG. 5.18 shows side views of the flapping envelopes for the 3 channel shapes. Only one cycle is shown because the differences between the envelopes are subtle and are more easily identified with minimized clutter. In general, the flapping envelopes are very similar. The key difference is the behavior of the downstream corners. In the diamond case, the downstream corners are bent inward to avoid hitting the wall. This behavior is unsurprising, what is surprising is how little of the flag's span is affected, and for how little of the flapping cycle this effect is visible. Furthermore, the circular and diamond channels show very similar flapping amplitude, despite the fact that the unobstructed volume for them to flap being different.

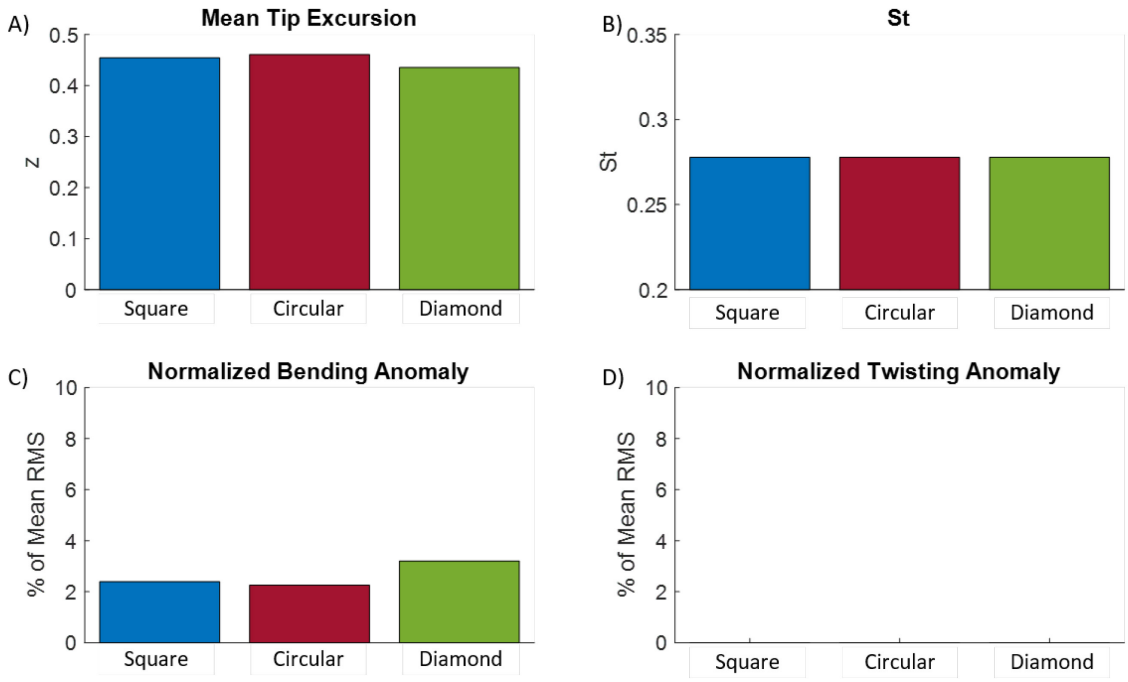

FIG. 5.19 – Bar graphs of the four flapping dynamics measures for the three channel shape cases.

FIG. 5.19 shows the flapping dynamic measures for the channel shape cases. St is similar for all three cases. We can see the circular channel has a very similar amplitude to the square channel, and the diamond case has only a marginal decrease in the amplitude. It appears that instead of the entire flag being affected by the variable confinement along the span, only the parts of the flag that are in regions of higher spanwise confinement show evidence of transverse deformation. This can be seen in the Normalized Bending Anomaly where the diamond case shows larger bending deformations. This is due to the smaller available unobstructed flapping envelope which means to flap at the same amplitude as the other cases, the corners must deflect out of the way of the walls. It should be noted that this observation is likely only relevant because the chosen channel shapes have a plane of symmetry which is coincident with the fixed leading edge. This result may very well breakdown given channels without even symmetry such as triangular cross-sections, which are often seen in applications. It is also important to note that the span of the flag for the square channel is considerably narrower than the channel, meaning even when the channel shape is

changed, the streamwise edges are still far from the sidewalls, implying the flag corners will only hit the sidewalls for large flapping amplitudes.

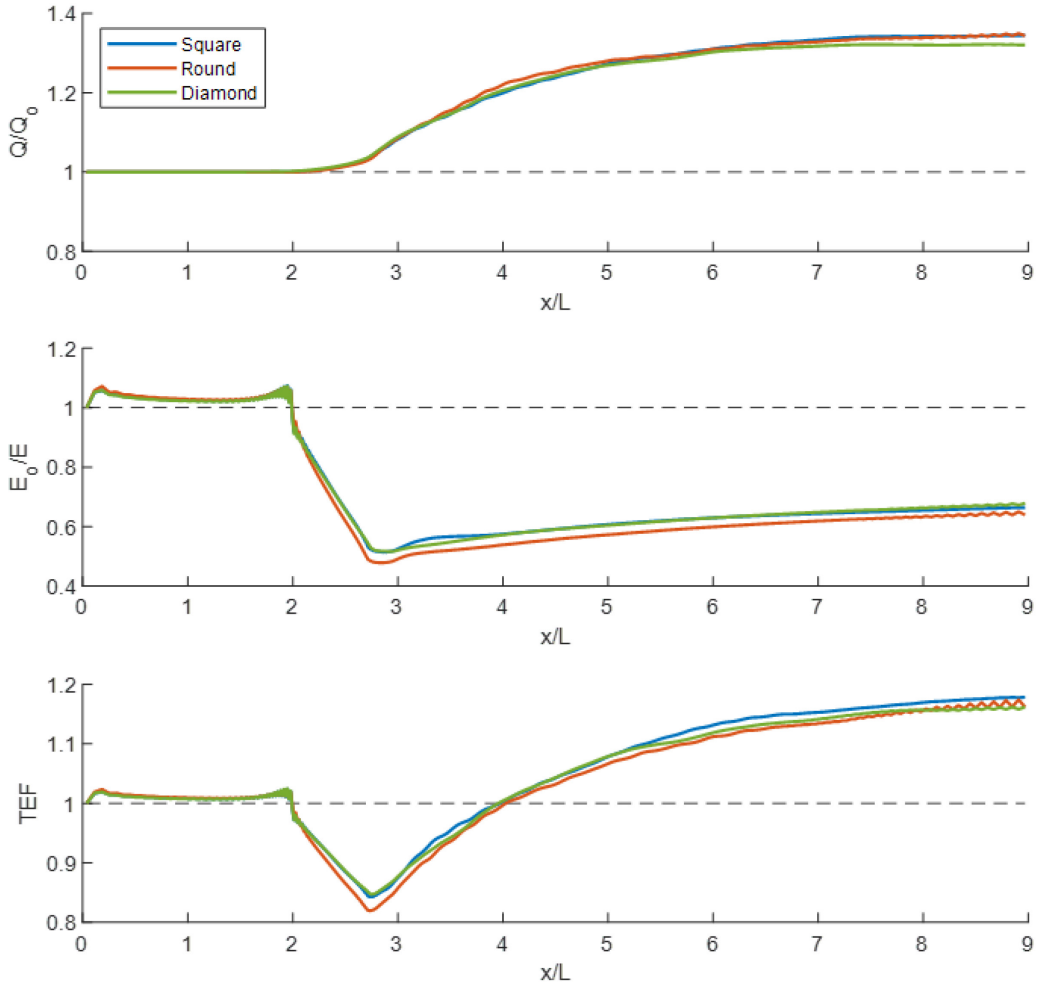

FIG. 5.20 – Time averaged performance measures for the 3 examined channel shapes showing the normalized heat flux Q/Q_0, energy loss E_0/E, and thermal enhancement factor TEF all as a function of streamwise position, where the heat flux and energy loss are normalized by the empty channel configuration for the corresponding shape.

FIG. 5.20 shows the three key performance metrics for the channel shape cases. Here we can see all three cases completely collapse, with only a miniscule increase in energy loss for the round channel case, which is most likely due to the hydraulic diameter mismatch. This similarity is

consistent with the observations of the flapping envelopes; however, it is still surprising how precisely similar these cases are. Part of the explanation is that these plots are the result of several procedures that include integrations and averages in both space and time. While, this would have the effect of smoothing the data and diminishing small relative differences, these results still show striking agreement. It appears this system is entirely agnostic to the channel shape. Some conditions on that result are that the channels in question have aspect ratios of 1 and have a symmetry plane coincident with the flags fixed edge.

To understand why this robustness exists, we can examine visualizations of the flow. We are interested in identifying similarities in the fluid dynamics despite the obvious differences in the boundaries. FIG. 5.21 shows temperature and heat flux contours for the three channel shapes. The jetting phenomenon seen in the square channel case is also clearly visible in the circular and diamond cross-section cases. The resultant heat flux hotspot pattern on the interior walls is differently shaped, but is still present in all three cases.

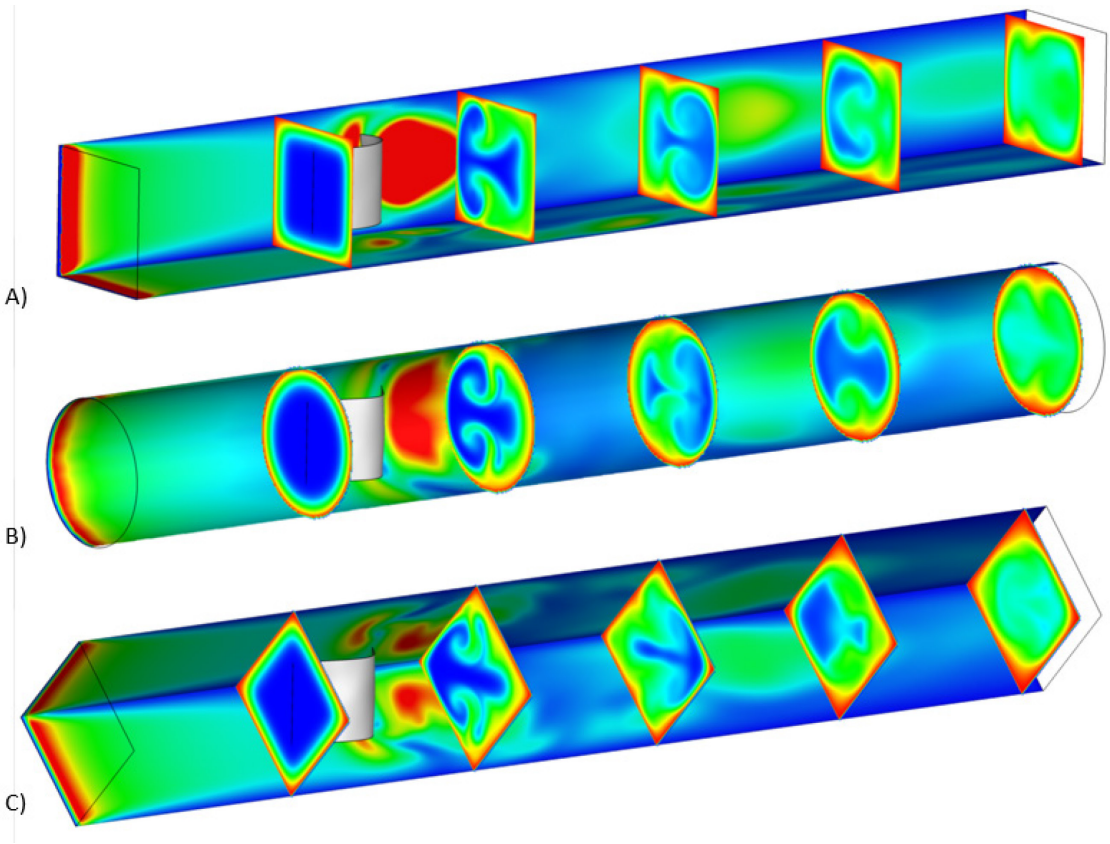

FIG. 5.21 – Snapshots of 3 channel shapes with a flapping flag. Contours on the cross-stream planes show temperature distribution and the contour on the inside surface of the channel shows wall normal heat flux.

This indicates the generation of these vortical structures is robust to channel shape. It appears that as long as the flag has room to flap, the tip leakage vortices along the streamwise edges will be shed to create the observed jetting phenomenon. Perhaps key to the robustness in the performance measures is how the jets change shape as they come in contact with the interior wall as can be seen in the 2nd plane for each case. We can see that as the jet impinges on the wall it creates a pocket of cold fluid which conforms to the shape of the wall as it mushrooms outwards. This behavior explains the similarity in the performance and may be due to the fact that in all three cases, the jet is impinging on a concave surface. Even the flat surface of the square channel is essentially concave considering the jet impingement region's spanwise extent is such that it must curl around the interior corners. This observation bodes well for other channel shapes not

investigated in this work, considering most regularly shaped channels will only have concave interior surfaces.

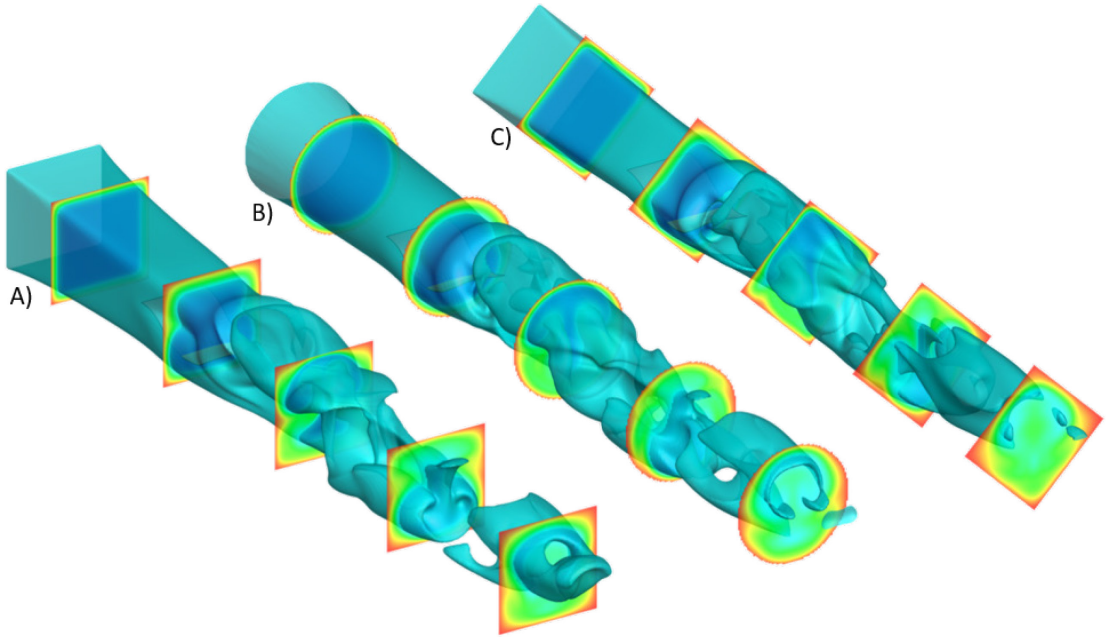

FIG. 5.22 – Temperature isosurfaces at T=0.25 for the 3 channel shapes.

To further assess the fluid dynamics and to understand the similarities between these cases, we again use temperature iso-surfaces, as can be seen in FIG. 5.22. Here we can see that after the flag, the developing thermal boundary layer completely gives way to the periodic lobed structures seen earlier in the square channel case. It is interesting how similar these isosurfaces appear to each other, despite being constrained by different boundaries. It appears as if there is a region in the core of each channel that is largely similar and the only differences are seen very close to the walls. This can especially be seen by examining the last lobed structure in each channel before the end of the computational domain. Within each lobed structure are pockets of fluid below T=0.25. All the pockets look very similar to each other with the caveat that they appear to have contoured themselves in some sense to the shape of the interior surface, which is consistent with the result seen by examining the jetting behavior in the cross-stream planes in FIG. 5.21.

5.4 Discussion

This analysis has shown that using a flapping flag undergoing aeroelastic flow-induced flutter as a heat transfer enhancement device has significant potential. This was shown by a 15-20% improvement in the overall system performance, as measured by the TEF. It has also answered several of the outstanding questions raised about this system which arose when it was modeled using 2D simulations. The first issue being the identification of differences in the heat transfer enhancement mechanism between 2D and 3D. This analysis showed very significant differences. We showed that in 3D, the primary vortices responsible for heat transfer enhancement were streamwise vortices which were the result of tip leakage flows around the spanwise edges from the pressure to the suction side of the flag. These vortices are not possible in the 2D configuration, making it unusual that the 2D and 3D cases seemed to show comparable TEF performance when measured at the end of the computational domain. However, by examining the three performance measures: normalized heat flux Q/Q_0, energy loss E_0/E, and TEF as a function of x/L, we were able to see the similarity in performance between 2D and 3D is only evident once the performance improvement has saturated with downstream position.

The second major question regarded the sensitivity to the 3D exclusive parameters such as spanwise confinement and aspect ratio. We saw both increasing confinement and aspect ratio served to increase the stability of the system as previously predicted in the literature (Doaré et al., 2011; Eloy et al., 2007), leading to more organized and lower amplitude flapping for the 3D case than the 2D case. This stabilizing phenomenon, particularly due to the finite span effects, significantly impacted the flag dynamics for the narrowest flag leading to almost no performance improvement. The split flag configurations introduced additional 3D features into the flow, but the systems' heat transfer performance was almost entirely insensitive to this change in terms of the time averaged performance measures. This leads to an interesting conclusion, which is the time

averaged performance parameters Q and E are only function of the total flag area. Going further, our simulations indicate that TEF is a strong function of the flapping amplitude, which is itself a function of the flag area. The final outstanding question was that of channel shape wherein we found the system to be agnostic to channel shape for symmetric channels with relatively low aspect ratios.

Chapter 6

Inverted Flag Energy Harvesting

As discussed in during the introduction, inverted flapping flags are well suited for piezo-electric energy harvesting due to the potential for very large amplitude deformations. In this work we investigate multi-inverted flag pairs to identify the behavior as a function of separation distance. To begin, we discuss the problem formulation and numerical method used for the simulations. Next, we present the results of the parameter sweep for both the tandem and side by side (abreast) configurations looking at both the flapping behavior and the fluid dynamics. We look carefully at the coupling modes and mechanism for the Tandem configuration, and at the distinct behavior regimes of the Abreast configuration. Then we use our three performance metrics (Phase shift, RMS of the amplitude, and Strouhal Number) to examine overall trends in the flapping dynamics and to assess the energy harvesting potential of the system.

6.1 Problem Configuration

As shown in FIG. 6.1A and FIG. 6.1B, we investigate the flow-induced flutter of flexible inverted membranes. This study examines two configurations: the Tandem and the Abreast configurations. The flags have length L and are placed in a uniform flow with velocity U and density ρ. The flags are assumed to be inextensible and are free at their leading edges and clamped at their trailing edges. The flow is governed by the 2D incompressible Navier-Stokes equations and the flags are governed by the nonlinear 2D Euler-Bernoulli equation. The position vector along the flag

is given by $\boldsymbol{X}(s,t)$ where t is time and s is arc-length along the filament with s=0 at the leading edge and s=L at the trailing edge.

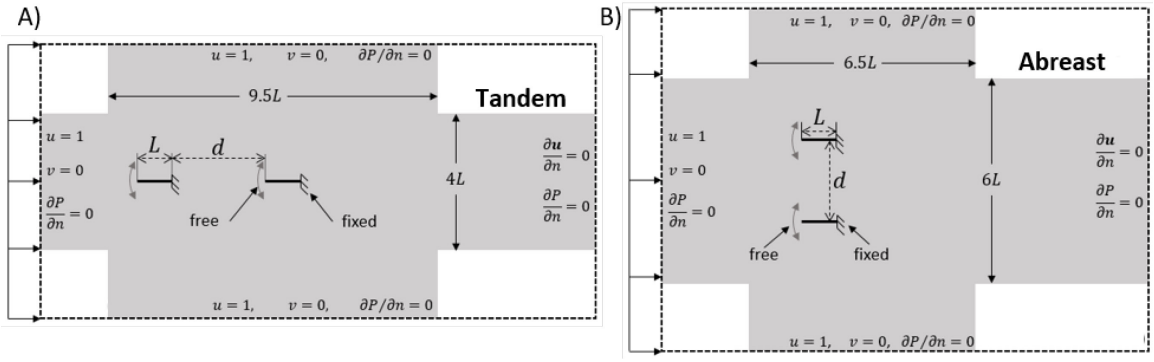

FIG. 6.1 – Computational Domain Figures. A) Tandem configuration and B) Abreast configuration.

FIG. 6.1A shows the tandem configuration with a leader flag and a follower flag. The separation d is measured as the horizontal distance from the trailing edge of the leader to the leading edge of the follower in the undeformed state. FIG. 6.1B shows the abreast configuration with "upper" and a "lower" flags. Here the separation distance d is measured as the vertical distance between the clamped trailing edges of the flags. For both configurations, the separation distance d can be nondimensionalized by the flag length to yield the key system parameter d/L. In both configurations, d/L = 0 represents the lower limit for this parameter. A series of 30 simulations were conducted for the tandem and abreast configurations where the parameter d/L was varied from 0.1 to 3.0 in increments of 0.1.

6.1.1 Governing Equations

The flow is governed by the non-dimensionalized incompressible Navier-Stokes equations which can be expressed as:

$$\frac{\partial \mathbf{u}}{\partial t} + \nabla \cdot (\mathbf{u}\mathbf{u}) = -\nabla p + \frac{1}{Re}\nabla^2 \mathbf{u} + \mathbf{f} \tag{6.1}$$

$$\nabla \cdot \mathbf{u} = 0 \tag{6.2}$$

where $\boldsymbol{x}$ is the positon vector in the fluid domain, $\boldsymbol{u}$ is the velocity vector, p is the dynamic pressure, and $\mathbf{f}$ is the momentum forcing associated with the immersed boundary condition on the surface of the flag. The Reynolds number is given by $Re = \rho UL / \mu$ with the density ρ, the free stream velocity U, and viscosity μ.

The flags are chosen to be inextensible using the constraint expressed as $d\left(\left|\partial \boldsymbol{X} / \partial s\right|\right) / dt = 0$ (Shoele & Zhu, 2012; Tornberg & Shelley, 2004). This leads to the non-dimensional governing equations for the position $\boldsymbol{X}$ of the flag and tension force σ:

$$m_s \frac{\partial^2 \mathbf{X}}{\partial t^2} = \frac{\partial}{\partial s}\left(\sigma \boldsymbol{\tau} + q\mathbf{n}\right) - \mathbf{F} \tag{6.3}$$

$$\frac{\partial^2}{\partial s^2}\left(\sigma \boldsymbol{\tau}\right) \cdot \boldsymbol{\tau} = \frac{m_s}{2}\frac{\partial^2}{\partial t^2}\left(\boldsymbol{\tau} \cdot \boldsymbol{\tau}\right) - m_s \frac{\partial \boldsymbol{\tau}}{\partial t} \cdot \frac{\partial \boldsymbol{\tau}}{\partial t} - \frac{\partial}{\partial s}\left(\frac{\partial\left(\gamma \mathbf{n}\right)}{\partial s} - \mathbf{F}\right) \tag{6.4}$$

where $\boldsymbol{\tau} = \dfrac{\partial \mathbf{X}}{\partial s}$ is the unit tangent vector along the Lagrangian coordinate s, $\mathbf{n}$ is the unit normal vector along the Lagrangian coordinate s, σ is the tension, and γ is the transverse stress. Furthermore, m_s is the excess mass per unit length of the flag defined as $m_s = m_f - \rho A_s$, where m_f is the mass per unit length of the flag, ρ is the density of the fluid, and A_s is the cross-sectional area of the flag. For the 2D case examined in this study, $A_s \to 0$ (the limit for a very thin flag), $m_s \sim m_f$. Finally, $\mathbf{F}$ is the force density applied by the flag on the surrounding fluid. The non-dimensional parameters governing the structure are the mass ratio m^*, and the reduced velocity U^* which are defined as:

$$m^* = \frac{\rho L}{m_s}, \qquad U^* = UL\sqrt{\frac{m_s}{k_b}} \tag{6.5}$$

Where $k_b = \dfrac{EI}{\rho_f U^2 L^3}$ is the bending stiffness, E as the modulus of elasticity and I is the 2nd moment of area. The free and clamped-end boundary conditions at the leading and trailing edges of the flag are:

$$M = \gamma = 0 \qquad \text{at } s = 0 \text{ (leading edge, free)} \tag{6.6}$$

$$\mathbf{X} = \mathbf{X}_0, \ \frac{\partial \mathbf{X}}{\partial s} = [1, 0] \qquad \text{at } s = L \text{ (trailing edge, fixed)} \tag{6.7}$$

where M is the total moment along the flag and γ is the transverse shear stress.

6.1.2 Numerical Method

The immersed boundary method used for this study follows implementation described by Shoele & Mittal (2016) for the single-inverted flag study. Here the Lagrangian velocity $\mathbf{U}(s,t)$ and the force density $\mathbf{F}(s,t)$ on the flag are translated to the fluid domain variables $\mathbf{u}(\mathbf{x},t)$ and $\mathbf{f}(\mathbf{x},t)$ using a delta function according to:

$$\mathbf{U}(s,t) = \int_{\Omega_F} \mathbf{u}(\mathbf{x},t)\,\delta\left[\mathbf{x} - \mathbf{X}(s,t)\right] d\mathbf{x} \tag{6.8}$$

$$\mathbf{f}(\mathbf{x},t) = \int_{\Gamma} \mathbf{F}(s,t)\,\delta\left[\mathbf{x} - \mathbf{X}(s,t)\right] ds \tag{6.9}$$

where Ω_F is the fluid domain, Γ the surface of the flag and δ the Dirac-delta function.

A penalty method is used to couple the flow and structural dynamics solvers where the equations for the fluid and structure are first solved independently, and their interaction force subsequently formulated as a penalty momentum forcing (Huang & Sung, 2009). The approach relies on two sets of points along the flag; the first set are the Lagrangian grid points used to

discretize the flag's structural equations and the second set are massless virtual points that are assumed to move with the fluid's local velocity. Coupling the structural solution with the fluid solution is then accomplished by "attaching" springs and dampers between the structure following points and the fluid following points. Thus, the momentum forcing equation for $\mathbf{F}(s,t)$ is expressed according to a spring-damper equation as follows:

$$\mathbf{F}(s,t) = -\mathrm{K}_p \frac{\rho U^2}{L}\left[\left(\tilde{\mathbf{X}} - \mathbf{X}\right) + \beta \Delta t\left(\tilde{\mathbf{U}} - \mathbf{U}\right)\right] \tag{6.10}$$

where K_p is a large penalty constant, β is a penalty constant, Δt is the computational time step, $\tilde{\mathbf{X}}$ and $\tilde{\mathbf{U}}$ are the position and velocity of massless fluid following points, and $\mathbf{X}$ and $\mathbf{U}$ are the position and velocity of the Lagrangian structure following points on the flag. $\tilde{\mathbf{X}}$ and $\tilde{\mathbf{U}}$ are computed from the current and previous fluid velocities as:

$$\frac{d\tilde{\mathbf{X}}}{dt} = \tilde{\mathbf{U}}(s,t) \;;\; \tilde{\mathbf{U}}(s,t) = \int_{\Omega_F} \mathbf{u}(\mathbf{x},t)\,\delta\left[\mathbf{x} - \tilde{\mathbf{X}}(s,t)\right] d\mathbf{x} \tag{6.11}$$

This formulation is in fact identical to the method proposed by Goldstein, et al., (1993) known as the feedback forcing scheme. Based on a study of the effect of penalty parameters on stability, accuracy and computational cost, similar to that done by Shoele & Mittal (2016), the final values chosen for the simulations were $K_p = -10^5$ and $dt = 1.0 \times 10^{-4}$.

The fluid-structure equations are discretized according to the prior work by Shoele & Mittal (2016) and the equations are solved using the in-house code ViCar3D which uses a semi-staggered, fractional step approach to decouple the Pressure Poisson equation from the momentum terms in Navier-Stokes equations. 2nd-order Crank-Nicolson fully implicit time step scheme is used for everything but the momentum forcing. The Pressure Poisson equation is then solved with the biconjugate gradient (BiCGSTAB) scheme (Zhu et al., 2017).

The ViCar3D code can be found described in detail in the papers Mittal, et al. (2008) and Seo & Mittal (2011). This code has been validated and verified for a variety of cases (SHOELE & ZHU, 2010; Shoele & Zhu, 2012; Shoele & Zhu, 2013; Shoele & Mittal, 2014). The FSI model used in this study has been previously verified during the Shoele & Mittal (2014) paper where flow-induced flutter of a flexible plate mounted behind a cylinder was compared to two other simulation techniques (Bhardwaj & Mittal, 2012; Turek & Hron, 2006). The work done in this study was computationally similar to the work done in the Shoele & Mittal (2014; 2016a) papers. No new features were added to either the FSI code specifically or the ViCar3D code in general to conduct this research. Therefore, we consider the prior verification and validation studies sufficient to validate the code at the chosen resolution.

6.1.3 Computational Domain, Boundary Conditions, and Grid

FIG. 6.1A-B show a schematic of the 2D computational domain and boundary conditions used in this study. The inflow and side wall boundary conditions assume a uniform flow and an outflow boundary condition was used for the rear wall. In the current study, parameters such as Reynolds number and the flag parameters are chosen so as to generate a robust, large-scale flutter in a solo flag and the primary parameters that are varied is the spacing between the two flags. The Reynolds number, m* and U* for this study were chosen as Re = 200, 1.0 and 2.2, which, based on the study of Shoele & Mittal (2016a), are in the range to generate large-scale symmetric flutter, while still allowing for a large number of adequately resolved simulations.

The computational domain for the tandem configuration was (-3L, 13L) in the x direction and (-4L, 4L) in the y direction. The domain for the abreast configuration was (-4L, 10L) in the x direction and (-5L, 5L) in the y direction. The simulations for the tandem configurations employ a grid of 768x384 and the abreast configuration grid used 576x512 points. Both configurations used a high resolution grid in a rectangular region around the flags and in the wake (with dx = dy =

0.016) and then stretched geometrically towards the boundaries as shown in FIG. 6.1A-B. The structural grid used 83 points per flag with a resolution of ds = 0.012. The time step used was dt = 0.0001 and the simulations were run for 300 non-dimensional time (NDT) units leading to 3×10^6 time steps. To quickly induce flapping, the flags were given a small initial 5° angle to the incoming flow.

This resolution and domain was guided by our previous work Shoele & Mittal (2016a). Similar to that work, extensive grid resolution and validation studies were carried out for a single inverted flag wherein the resolution of the fluid and structure were tested and subsequently chosen. Using those resolutions, the domains for the Tandem and Abreast configurations were then evaluated by examining the maximum separation case for each configuration. The domain chosen for the maximum separation for a configuration was then used for all cases in that configuration.

6.2 Data Analysis and Performance Metrics

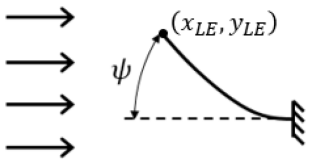

FIG. 6.2 – Tip Angle picture

In applications of these flags such as energy harvesting or mixing enhancement, the key metric that drives performance is the amplitude of the flutter (Shoele & Mittal, 2016a). Here, we use the angular deflection of the flag tip as a measure of the amplitude of flutter where the tip angle was computed as $\psi = \tan^{-1}\left(y_{LE} / x_{LE}\right)$ where x_{LE} and y_{LE} are the x and y locations of the leading edge of the flag.

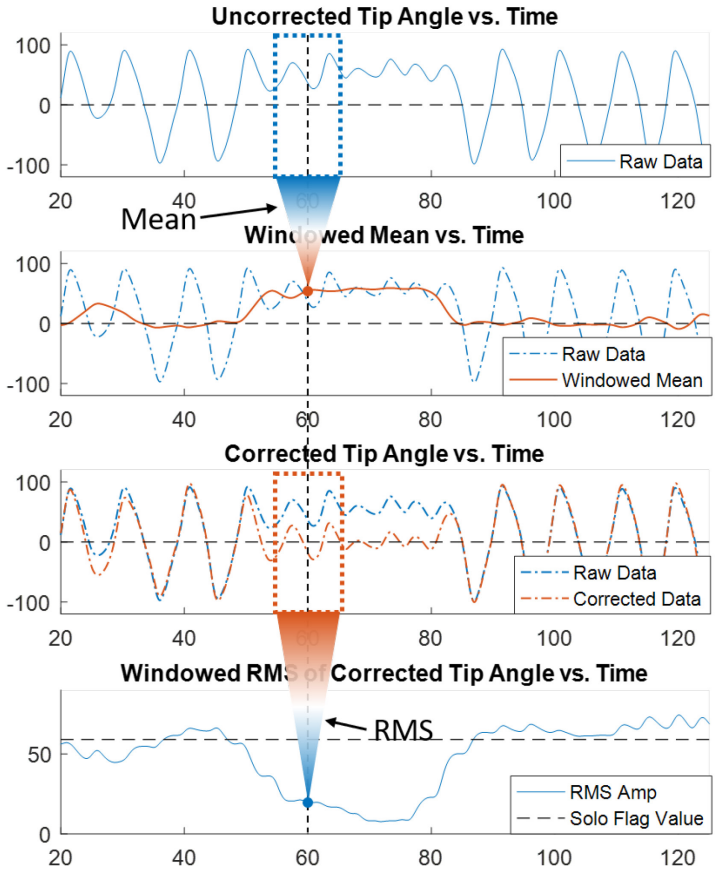

FIG. 6.3 – Examples of time series data depicting the windowed filtering procedure.

As will be shown later, these flags undergo extremely complex dynamics ranging from periodic to chaotic, as well as intermittent transition between different modes. Given this, we have defined a number of metrics to characterize this complex behavior of the flags. We call this procedure windowed filtering and FIG. 6.3 shows an example of how the various calculations effect the signal. First, the tip flutter amplitude is defined as follows: given the instantaneous angle subtended by the flag leading-edge, we define a moving average of this angle as:

$$\tilde{\psi}(t) = \frac{1}{\Gamma}\int_{t-\Gamma/2}^{t+\Gamma/2} \psi(t')dt' \tag{6.12}$$

where Γ is a suitably chosen period for the moving average. The root-mean-square of the flutter amplitude about this moving average can then be calculated as

$$\sigma_{\psi}(t) = \left[\frac{1}{\Gamma} \int_{t-\Gamma/2}^{t+\Gamma/2} \psi'^{2}(t')\, dt' \right]^{1/2} \tag{6.13}$$

where $\psi'(t) = \psi(t) - \tilde{\psi}(t)$. In the current study, this averaging window Γ is chosen to be T_D, where T_D is the time-period corresponding to the dominant frequency of flutter for the given case (as estimated below). The subtraction of the moving average was only performed for the abreast configuration and was employed to address that configurations tendency to remain at a non-zero angle for long periods with minimal motion. This correction then extracts the local flutter, instead of the global deflection. The correlation between two flags can be obtained by evaluating the function

$$\mathrm{C}_{12}(t;\tau) = \frac{1}{\Gamma} \frac{1}{\sigma_{\psi_1}(t)\sigma_{\psi_2}(t)} \int_{t-\Gamma/2}^{t+\Gamma/2} \psi_1'(t')\, \psi_2'(t'-\tau)\, dt' \tag{6.14}$$

where subscripts '1' and '2' refer to the two flags and τ is the time-shift between the two time-series. To obtain an estimate of the phase difference ϕ_{ψ} in the flutter of the two flags, we fix the window of one flag between and increase τ between $(-\Gamma/2, \Gamma/2)$, flag by small increments. The shift with the highest cross-correlation provides the most probable phase differences between the two which can be expressed as a phase angle ϕ_{ψ} given the most probable time-period of the flutter. The most probable time-period T_D (and corresponding Strouhal number: St= L/UT_D) for the flutter of a given flag is itself obtained by an autocorrelation (using Eq. 14 with both subscripts either 1 or 2) wherein the τ with the maximum autocorrelation (away from $\tau = 0$) gives the most probable time-period.

6.3 Solo Inverted Flag

The solo flag simulation was run for over 1000 time units in order to obtain highly converged statistics. FIG. 6.4B shows a snapshot of the generation of the 3 key vortices that comprise the

wake of the single flag. The vortex shedding behavior exhibited by the Solo inverted flag is as follows: at the beginning of a half cycle the flag presents a bluff body to the flow creating two counter-rotating vortices at the leading and trailing edges. As the flag begins the next half cycle the leading-edge vortex is shed and stretched, and is then split by the trailing edge vortex as can be seen in FIG. 6.4B. Thus, each half-cycle generates three vortices that arrange in one nearly symmetric vortex dipole (2P) and a single weaker ('S') vortex that forms a "2S-mode" Karman street with the other single vortices shed in the previous half-cycles.

The arrangement of these vortices has a significant impact on their convection speed. The arrows in FIG. 6.4B are a qualitative indication of the self-induced velocity of adjacent pairs of counter-rotating vortices (or dipoles) and it can be seen that the 2P vortex pairs self-induce a velocity which moves them away from the wake centerline and also slows them down. In contrast, the S vortices interacting with the opposite vortex of the adjacent 2P-pair, experience an induced velocity which moves them towards the centerline and also accelerates them. Vortex convection speeds determined by tracing the vortex centers are estimated to be $0.89\,U$ and $1.1\,U$ for the P and S vortices, respectively. As will be shown later, this behavior of the vortices plays an important role in the flutter of the downstream flag in the tandem flag arrangement.

It is useful to describe the role that these vortices play in driving the flutter. During the portion of the cycle after the flag has crossed the midplane, the flag presents a bluff body to the flow, thereby generating vortices from its two ends. These vortices generate a lower pressure region downstream of the flag which helps to further deflect the flag at the end of a half-cycle. However, once the flag has reached its maximum deflection and starts to move back towards its equilibrium position, these same leading edge-vortices in the near wake oppose the elastic recovery of the flag. The severing of the leading-edge vortex from its shear layer allows the vortex to convect away from the flag and removes this opposing effect. The interruption of this vortex separation by any

mechanism, can therefore interfere with the recovery of the flag, and alter the dynamics of flag flutter.

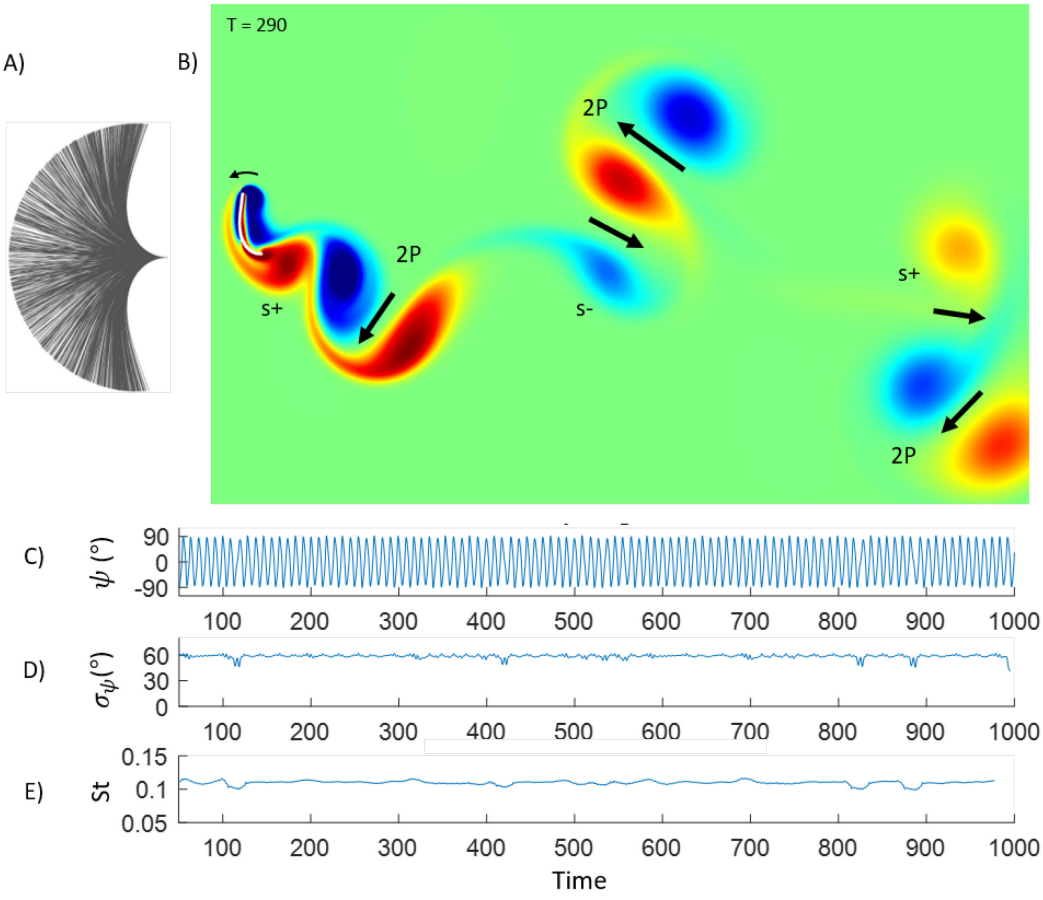

FIG. 6.4 – (A) shows the motion envelope and (B) shows the ω_z vorticity in the near wake for the solo flag baseline. The vortices are labeled per their vortex shedding mode and the vorticity induced jet direction between vortex pairs is labeled. (C-E) show time series for the solo flag configuration of the tip-angle ψ, the windowed RMS of the amplitude σ_ψ, and Strouhal number.

FIG. 6.4C-E shows the time series of three significant performance parameters: The tip angle ψ the RMS of the tip amplitude σ_ψ, and the Strouhal number for the flutter determined via autocorrelation. These figures indicate the following: first, the baseline value for the RMS amplitude σ_ψ is 59° and the baseline Strouhal number is 0.11, and second, the behavior is largely periodic, but not entirely so, with short lived transients appearing intermittently and infrequently.

This overall behavior is related to the Reynolds number of 200 that is chosen here, which is low enough to generate a mostly periodic behavior but high enough to be susceptible to other instabilities.

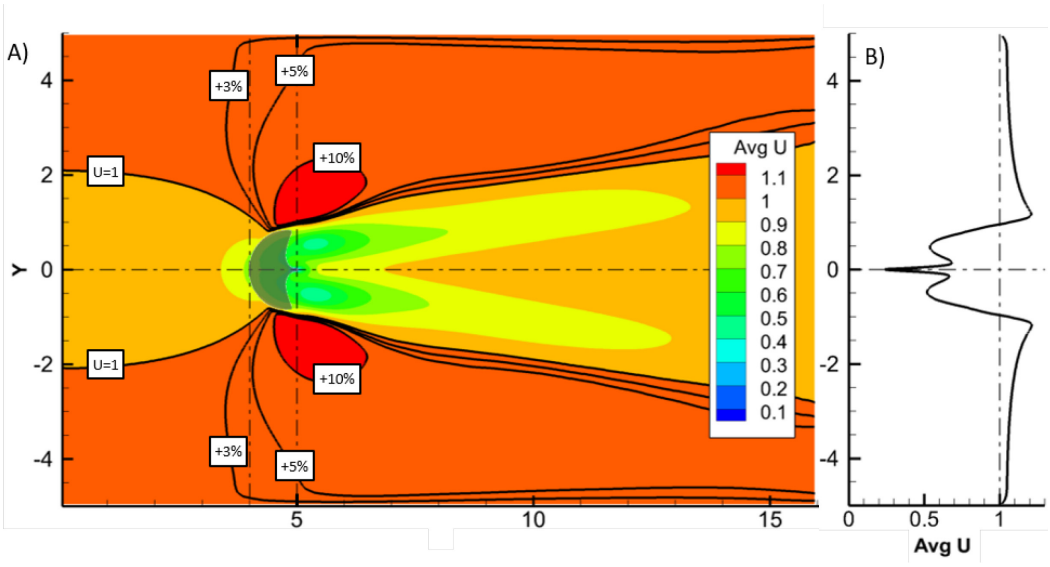

FIG. 6.5 – A) Mean U velocity contour plot with iso-lines at U = 1, 1.03, 1.05, and 1.1. B) shows vertical cross stream mean U profiles at the trailing edge of the flag.

Finally, FIG. 6.5 shows the time-averaged streamwise velocity for the solo flag. This plot shows that the flag has a bifurcated wake with two symmetric regions of momentum deficit that are associated with the velocity induced by the 2P vortices. The wake centerline is found to recover faster to the freestream velocity than these two regions of low-momentum in the wake and this is dissimilar to a typical bluff-body wake where the momentum deficit is maximal along the wake centerline. It is also noted that beyond a distance of about one flag length above and below the flag, the mean velocity is greater than the freestream velocity. The implication of these features on the paired flag configurations will be discussed later in the paper.

6.4 Tandem Inverted Flags

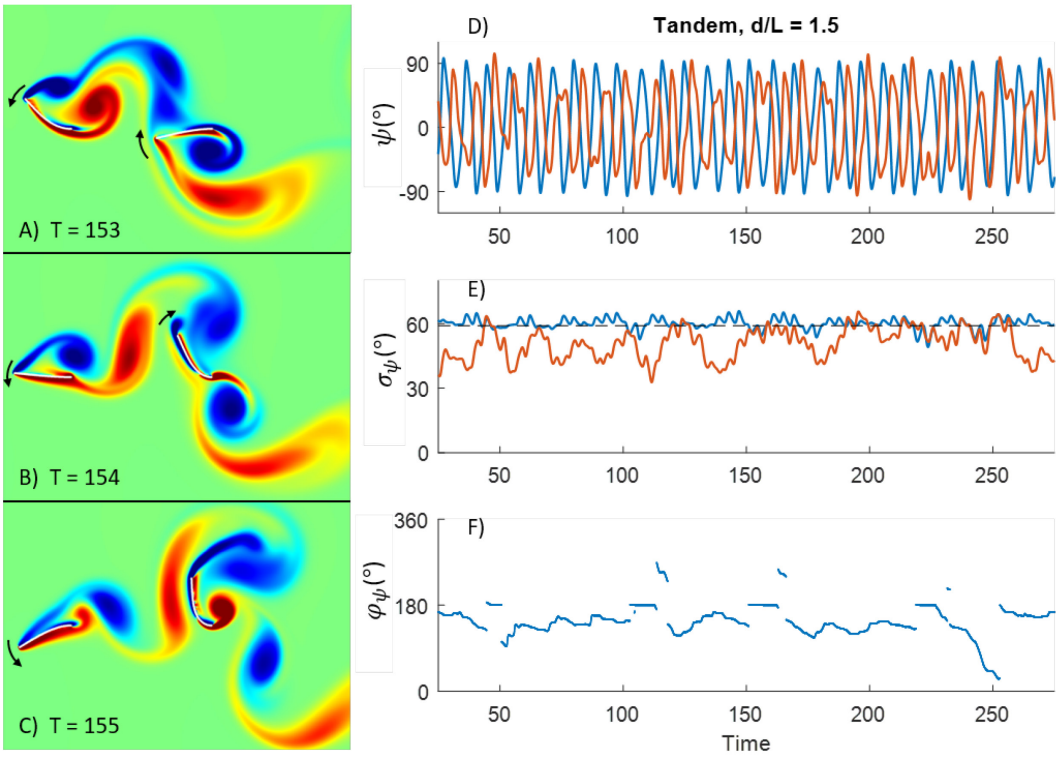

FIG. 6.6 – Snapshots of ω_z vorticity (A-C) and time series data (D-F) for the Tandem d/L = 1.5 configuration. For (A-B), arrows show the instantaneous flapping direction of the flags. (D-F) show the time series of the tip angle ψ, RMS of the amplitude σ_ψ, and phase difference φ_ψ. The Leader flag is shown in blue and the Follower is shown in red.

Simulations of the tandem flag configuration were conducted for flag distances in the range d/L = 0.1 – 3.0. Sample plots for the d/L = 1.5 configuration are shown in FIG. 6.6 including vorticity snapshots and time series for the Tip Angle ψ, RMS of the amplitude σ_ψ, and phase difference φ_ψ. Due to the interactions between the follower flag and the vortices shed from the leader, the flag kinematics, as evident from the time-series of ψ and σ_ψ, are significantly more complex. φ_ψ, however, indicates some degree of phase-locking between the two flags, an observation that will be discussed in detail in a following section.

FIG. 6.7 shows heatmaps of the probability density function (PDF) of σ_{ψ} for the 'leader' and 'follower' as a function of flag separation distance d/L for all the tandem cases simulated here. The heatmap for the leader shows that amplitude of flutter is initially lower than the Solo flag, but rises so that by d/L = 1.3, the Leader appears to be flapping with a slightly larger amplitude than the Solo flag. This behavior persists throughout the rest of the examined range of d/L, and for the largest separation, the upstream flag flutters with an amplitude which is about 2.5% larger than its baseline value. This upstream effect of the Follower on the Leader for such distance is unexpected. However, we note that regular tandem flags also exhibit an unexpected "inverted drafting" phenomenon (ALBEN, 2009; Ristroph & Zhang, 2008), wherein the Leader experiences drag reduction while the Follower experiences additional drag. It is possible that this anomalous behavior is a reflection of the elliptic nature of the pressure field in this incompressible flow wherein unsteady pressure variations generated by the downstream flag continue to produce a small effect on the upstream flag. However, given that this effect is small, we have not explored this issue further.

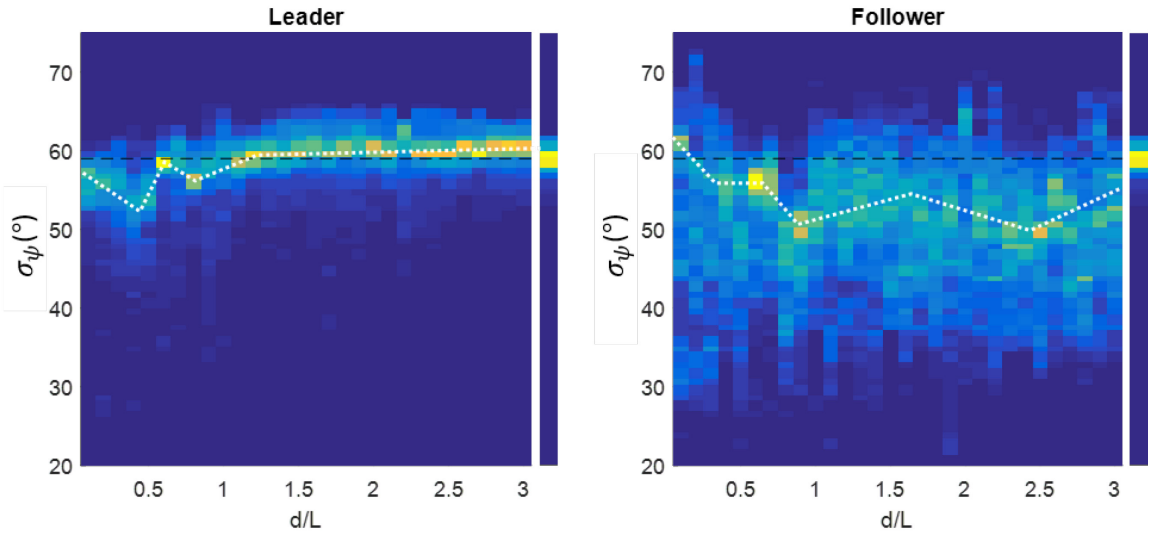

FIG. 6.7 – Heatmaps showing PDFs of the RMS of the Amplitude σ_ψ at each d/L for the Leader and Follower for the Tandem configuration. The average solo flag value of $\sigma_\psi = 60$ is noted with a dashed line. Beside each heatmap is a single bar showing the PDF of the solo flag baseline.

The behavior of the Leader flag for d/L smaller than about 1.2 is quite complex. In general, the amplitude of the Leader is smaller than the baseline for these spacings, but for the d/L = 0.6 case, the σ_ψ of the Leader is very near that of the Solo flag. The PDF for this case is also highly localized indicating that the flutter is quite coherent. This case will be discussed in some detail in the following sections. The behavior at the minimum spacing of d/L = 0.1 is also more localized, and just below the solo flag baseline. This case will also be discussed later.

FIG. 6.7B shows the PDF of σ_ψ for the Follower flag and as expected, this indicates significantly more complex and stochastic amplitude variations due to the strong influence of the vortices from the Leader. Aside from the d/L = 0.6 case and perhaps its neighbor 0.7, the Follower's σ_ψ heatmap is much more broadband, and is centered around a value noticeably below the Solo flag baseline. The value at d/L = 0.6 has a more localized histogram indicating more coherent behavior, and is centered at a value higher than its neighbors and near the solo flag baseline. The behavior at d/L = 0.1 is still quite broadband, but shows a hotspot above the solo flag baseline.

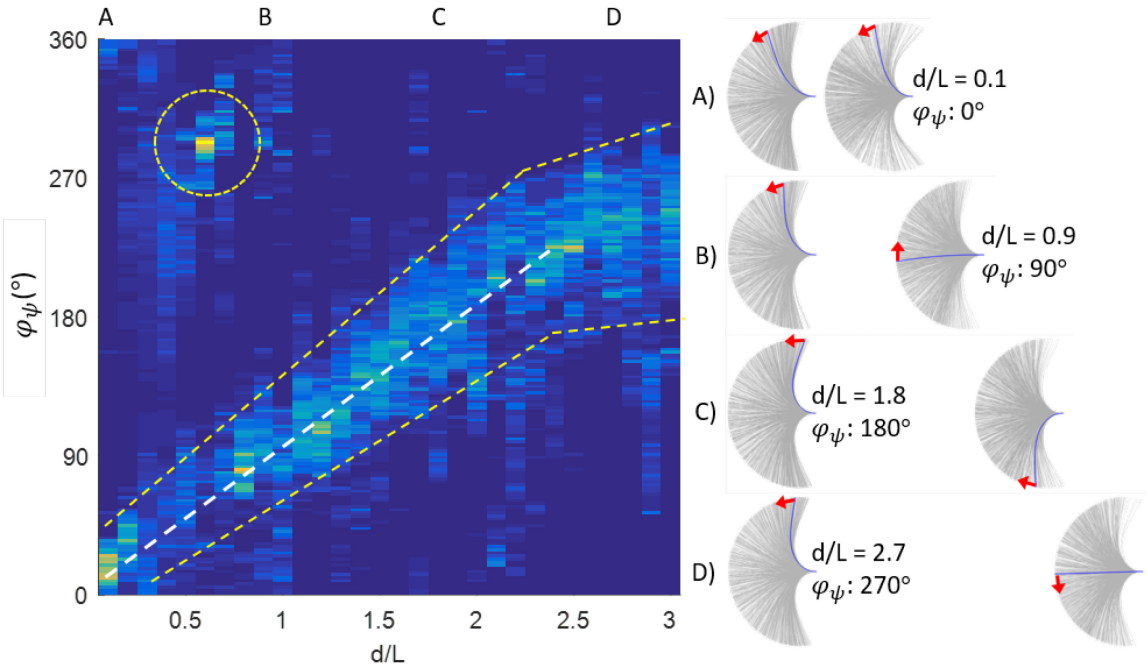

FIG. 6.8 – Heatmap of the PDFs of the phase difference φ_ψ at each d/L for the Tandem configuration. Locations A-D noted above the heatmap correspond to figures (A-D) showing the motion envelope of the flag in gray, instantaneous positions in blue, and arrows showing the direction of motion at that instant. The d/L and an approximate instantaneous φ_ψ are noted.

6.4.1 Phase Locking Trends

The phase difference φ_ψ between the two flags was computed using the procedure described in the section 'Data Analysis and Performance Metrics' and histograms of the φ_ψ time series at each d/L were stacked together to produce the heatmap shown in FIG. 6.8. Flutter movements of four selected cases are marked A-D (d/L = 0.1, 0.9, 1.8, 2.7) above the heatmap are also show in this figure. Three features are most apparent from the above flow: a linear trend in φ_ψ with flag separation; an 'elbow' in that linear trend at around d/L = 2.5, leading to a shallower slope and

widening PDFs; and an 'aberrant' behavior from d/L of about 0.5 to 0.7. We discuss these behaviors in some detail below.

The linear phase-difference trend evident from FIG. 6.8, represents the more dominant feature of this coupling. The most obvious hypothesis for this trend is that perturbations generated by fluttering of the leader flag convect downstream with a characteristic velocity and encounter the follower flag, and in doing so, establish the phase of the movement of the follower. Assuming that the convection velocity of the perturbation from the leader flag is V_p, the frequency of these perturbations is F_p, and the slope of the phase-shift is β, then the above hypothesis would suggest that $\beta / 360° = F_p / V_P$. Thus, the slope of the phase-shift is inversely proportional to the convection speed. In order to assess this hypothesis, we begin by estimating the slope of the phase-shift and this slope is found to be best estimated from the plot in FIG. 6.8 as $\beta = 87° / (d / L)$. Now, as shown in FIG. 6.4, each half cycle of the leader flag generates a set of 3 vortices (a 2P pair and a single S). Thus, given the cycle frequency of the flutter of the Solo flag of 0.11, the frequency of the perturbation experienced by the downstream flag is $F_p = 0.22$. With this value, and using the above expression, we obtain a perturbation convective velocity of $V_p = 0.91$. Previously, we estimated the convection velocity of the 2P and S vortices to be 0.89U and 1.1U respectively. Thus, the above estimate of V_p is quite in line with the convection speeds of the 2P vortices and this provides strong confirmation that the phase angle relationship between the two tandem flags is driven, for the most part, by the interaction of the Follower flag with the vortices generated by the Leader flag. Finally, the decrease in slope of the phase-shift beyond about d/L~2.5 is consistent with the fact that the streamwise velocity in the wake of the leader flag starts to recover back to the freestream velocity in this region (see FIG. 6.5 of the mean wake).

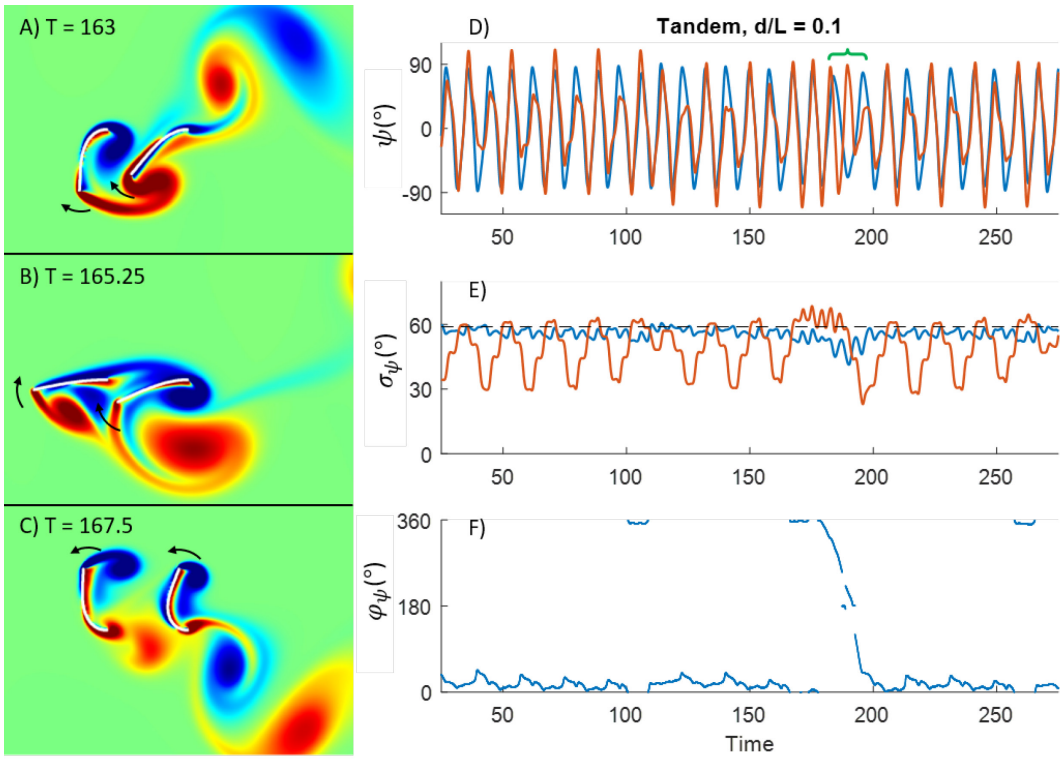

FIG. 6.9 – Snapshots of ω_z vorticity (A-C) and Time series data (D-F) for the Tandem d/L = 0.1 configuration, showing the minimum separation studied. For (A-B), arrows show the instantaneous flapping direction of the flags. (D-F) show the time series of the tip angle ψ, RMS of the amplitude σ_ψ, and phase shift φ_ψ. The Leader flag is shown in blue and the Follower is shown in red. Notice the flags are completely in phase except for a brief deviation shown with a bracket above plot (D).

An interesting special case of the linear phase locked flutter trend is the closest separation case d/L = 0.1. The phase locking trend indicates that at this minimum separation, the flags flap in-phase. FIG. 6.9 shows data for this case, and both the vorticity snapshots and the time series show that indeed the flags are completely in-phase. An interesting phenomenon here is the beating pattern, wherein the follower flag alternates between lower and higher amplitude oscillations than the leader every other cycle. We can see this beating reflected in the RMS Amp figure. A key feature of this minimum separation case is the robustness of this behavior in that any deviations from this behavior (as seen at around t/T=170 in the time-series plot) are "corrected" quite rapidly.

For flag distances d/L ranging from 0.5 to about 0.7, we observed a behavior that does not fit the linear-phase-locking type coupling seen for most of the range. In this particular range, the phase-shift PDF indicates that the Follower flag actually leads the Leader by a phase angle ranging between about 45 and 70 degrees. In contrast, in the adjacent ranges of d/L, the Leader always leads in phase with respect to the Follower by about 60 degrees. FIG. 6.10D shows the time series for the d/L = 0.6 case and this shows that in this mode, both flags flutter in a highly periodic manner for large periods, with intermittent periods of disorderly flutter. Similar behavior is also observed d/L = 0.5, and 0.7, although the d/L = 0.6 case shows the longest spans of uninterrupted periodic flutter.

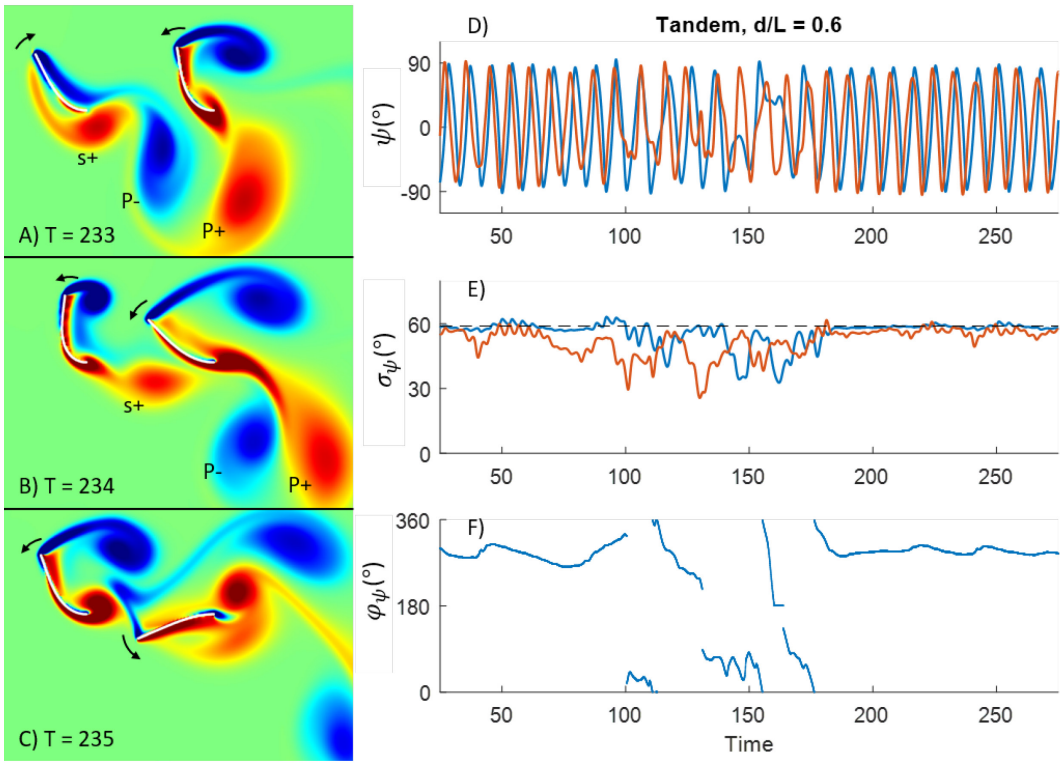

FIG. 6.10 – Snapshots of ω_z vorticity (A-C) and Time series data (D-F) for the Tandem d/L = 0.6 configuration. For (A-B), arrows show the instantaneous flapping direction of the flags. (D-F) show the time series of the tip angle ψ, RMS of the amplitude σ_ψ, and phase shift φ_ψ. The Leader flag is shown in blue and the Follower is shown in red. Note the intermittent periodic and chaotic behavior.

FIG. 6.10 depicting the vorticity snapshots and time variation of various flutter metrics shows that during the periodic fluttering mode, both flags flutter with an amplitude which is quite comparable to the Solo flag case. FIG. 6.10A-C shows snapshots of ω_z vorticity for the d/L = 0.6 case which provide insight into the mechanism that drives this aberrant behavior. This sequence demonstrates that for these flag separations, the Follower can mostly avoid being affected by the vortices shed from the upstream flag if it's flutter leads that of the upstream flag by approximately 45-70 degrees. Furthermore, despite the relative close spacing, this phase difference also seems to reduce any significant effect of the Follower on the Leader flag, allowing the Leader to flutter in a periodic manner for longer periods. This in turn allows the Follower flag to stay locked in this favorable phase relationship longer. Intermittently though, small variations in the phase of the flutter grow large enough so as to significantly perturb the vortex dynamics and the phase relationship. However, eventually, the system settles back in to this nearly periodic regime with the Follower leading in phase with respect to the Leader. Thus, despite their close proximity, the two flags are effectively decoupled from each at this distance, and we therefore refer to this as the 'proximal decoupling' behavior.

This 'decoupling' between the two flags appears to be the result of fortuitous spacing. Closer spacing than the lower limit of d/L = 0.5 has the Follower too close to the tail of the Leader, disrupting the flapping motion of the Leader. As a result, between d/L = 0.3-0.5 the Leader and Follower have different frequencies, with the Leader flapping at a lower frequency than the Solo baseline, and the follower flapping at a higher frequency than the baseline. For separations larger than the about d/L = 0.8, the vortices from the Leader occupy nearly all the space ahead of the Follower and the Follower is not able to miss all three vortices. As a result, the system does not find this periodic coupling mode.

6.4.2 Leader Decoupling

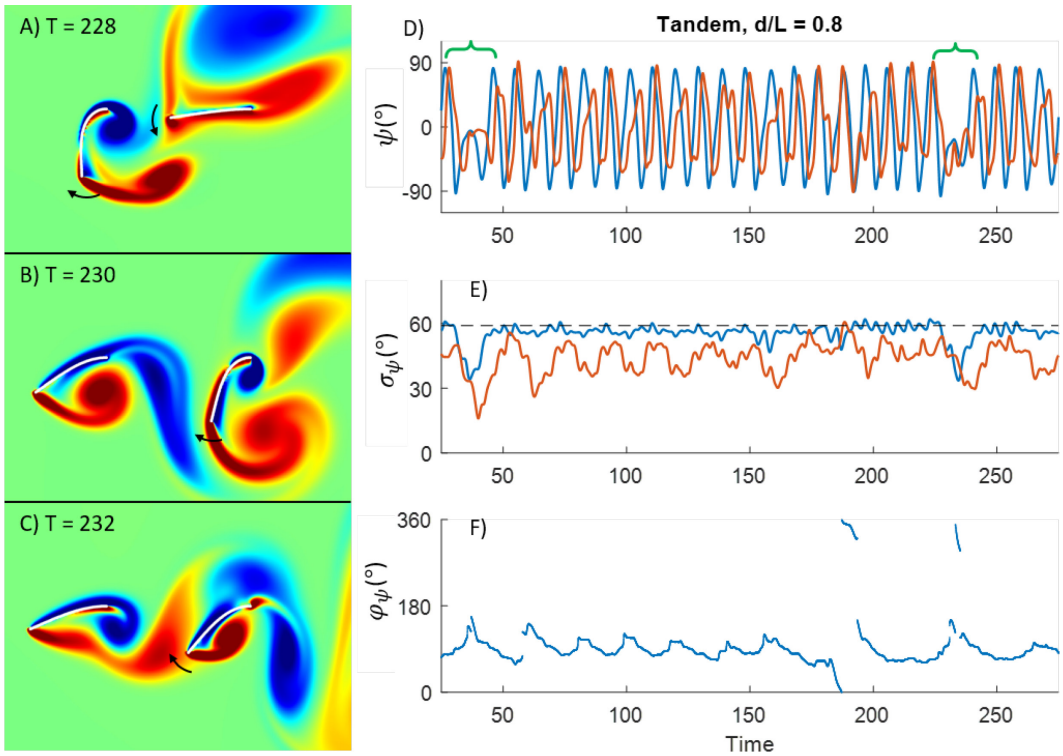

FIG. 6.11 – Snapshots of ω_z vorticity (A-C) and Time series data (D-F) for the Tandem d/L = 0.8 configuration. For (A-B), arrows show the instantaneous flapping direction of the flags. Notice that the leader flag does not move from (B) to (C). (D-F) show the time series of the tip angle ψ, RMS of the amplitude σ_ψ, and phase shift φ_ψ. The Leader flag is shown in blue and the Follower is shown in red. Examples of the Leader deviating from Solo flag behavior are noted with brackets above plot (D).

FIG. 6.7A showing PDFs of σ_ψ indicates that for flag separations of less than d/L=1.2, the Leader's behavior is significantly altered by the presence of the Follower. This upstream effect of the Follower on the Leader is interesting from a flow-physics perspective as well as from the perspective of energy harvesting. FIG. 6.11 shows a time series for the case with d/L=0.8. As can be seen, the Leader flag is observed to pause for durations that last about the length of one cycle, a behavior that is not observed for the Solo flag. The snapshots of vortex shedding for the various cases (d/L=0.6 in FIG. 6.10, d/L=0.8 in FIG. 6.11, and d/L=1.5 in FIG. 6.6) provide an indication

of the mechanism responsible for the coupling of the Leader to the Follower flag. For d/L=0.6 (see FIG. 6.10), we note that that the leading-edge of the Follower interferes significantly with the formation and shedding of the vortex at the trailing-edge of the Leader (see FIG. 6.11C). Such interference is absent for d/L=1.5 (see FIG. 6.6). The periodic formation and shedding of this trailing-edge vortex is essential for establishing and maintaining the periodic flutter of these flags and disruption of this process for d/L<1.2 is the cause for significant the complex flutter behavior of the Leader flag for the Tandem configuration.

6.5 Abreast Inverted Flags

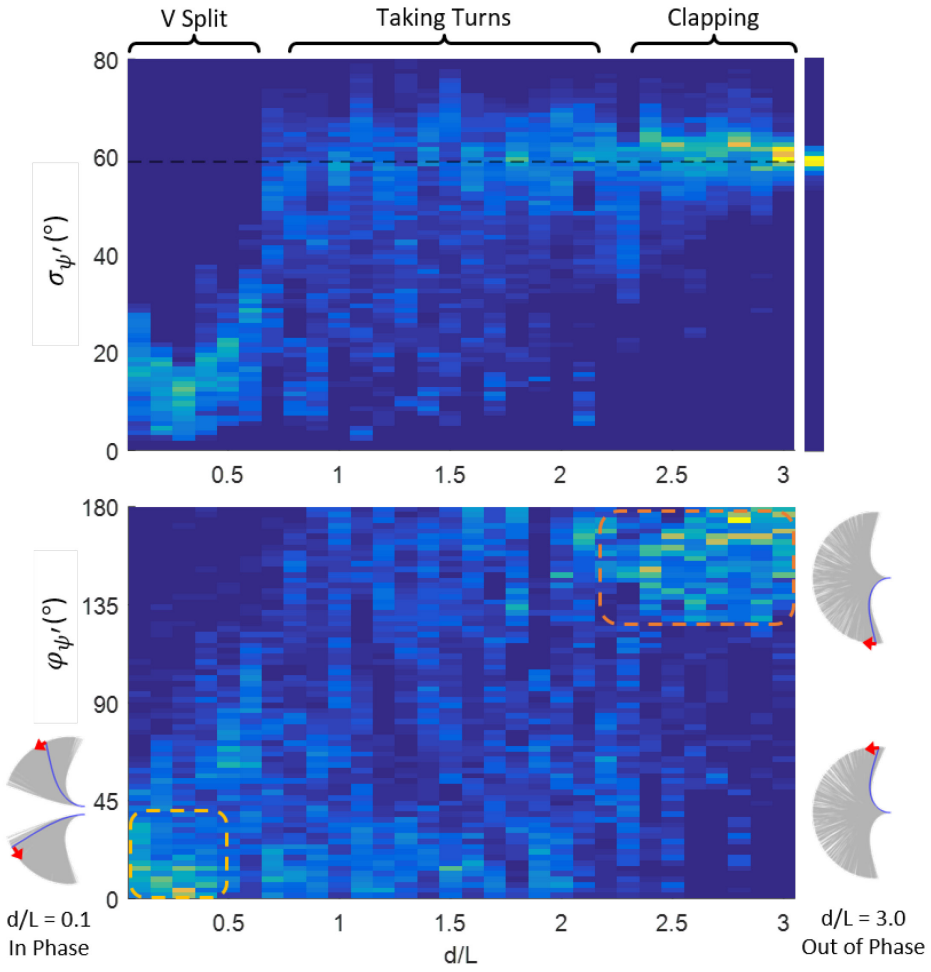

FIG. 6.12 – Heatmap of PDFs of the A) RMS of the amplitude $\sigma_{\psi'}$ and B) Phase Difference $\varphi_{\psi'}$ at each d/L for the Abreast configuration. The PDFs are of combined data from the upper and lower flags. In A) the Solo flag baseline behavior is shown as a dashed black line. The ambiguity in $\varphi_{\psi'}$ of the abreast configuration is removed by considering the 0° to 180° phase difference.

Simulations of the side-by-side or "Abreast" configuration were conducted for flag distances ranging from d/L = 0.1 – 3.0. Since in this configuration, both flags are expected to have the same statistical behavior, all the averages and PDFs combine data from both flags. FIG. 6.12 shows the heatmap of the PDF of the RMS of the amplitude $\sigma_{\psi'}$ and the phase-difference $\varphi_{\psi'}$

between the two flags. Using the 'corrected' tip angle ψ'. This figure, along with the flutter dynamics that we will describe shortly, shows evidence of three distinct behavior regimes which we refer to as: V-Split Flutter (d/L~ 0.1 – 0.5), Taking Turns (d/L ~ 0.5 – 2.3), and Clapping (d/L ~ 2.3 – 3.0+). Note that given the symmetry of the abreast configuration, the computed phase shift extends from 0° to 180°.

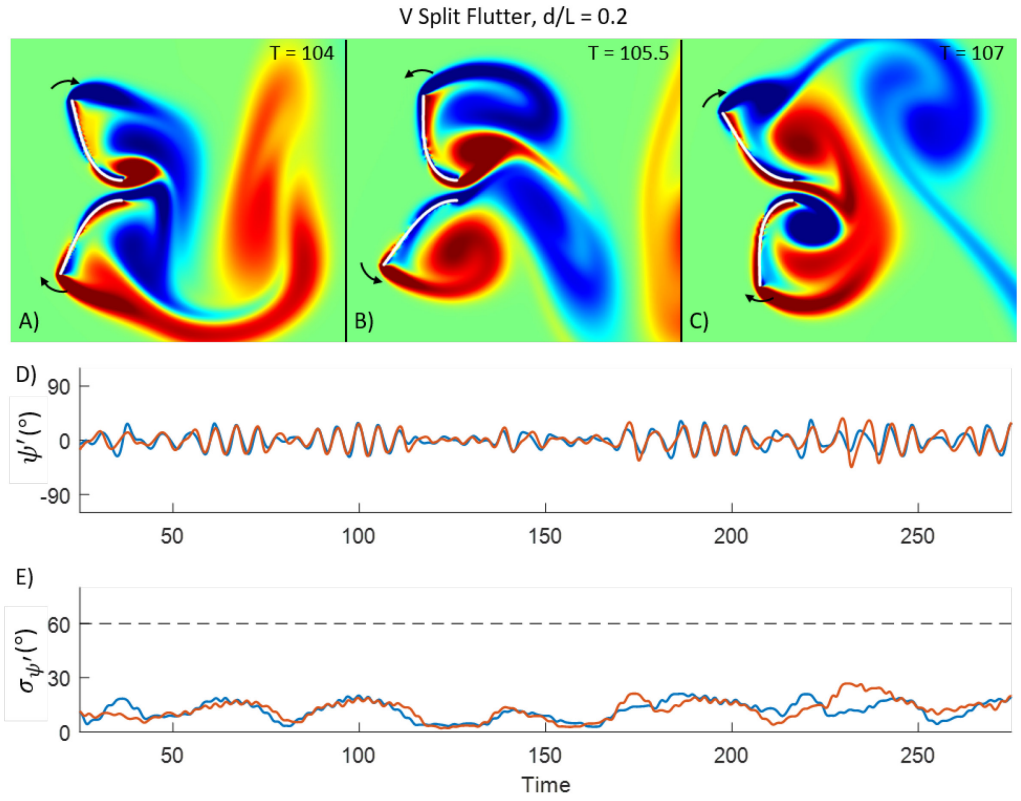

FIG. 6.13 – (A-C) Snapshots of ω_z and (D-E) time series of Corrected Tip Angle ψ' and RMS of the amplitude $\sigma_{\psi'}$ for the d/L = 0.2 Abreast case showing the V Split Flutter behavior. In (A-C), the flags are shown in white and the direction is noted with black arrows.

From d/L = 0.1 – 0.6, the $\sigma_{\psi'}$ of flutter is very low, indicating a significantly reduced energy harvesting potential. The phase-difference between the two flags is also small (mostly limited to the range 0-20 degrees) indicating that the flags move in the same direction as they flutter. The overall behavior becomes clear from the snapshots shown in FIG. 6.13, which show that the

flag split into a ‘V shape’ and oscillate back and forth with a small overall amplitude. The proximity of the two flags interferes significantly with the vortex shedding, especially from the trailing-edge of the flags and the flags essentially behave as a single entity in this flutter mode. We note that the frequency of the flutter in this mode is about 40% higher (St~0.15) than the Solo flag (see FIG. 6.17).

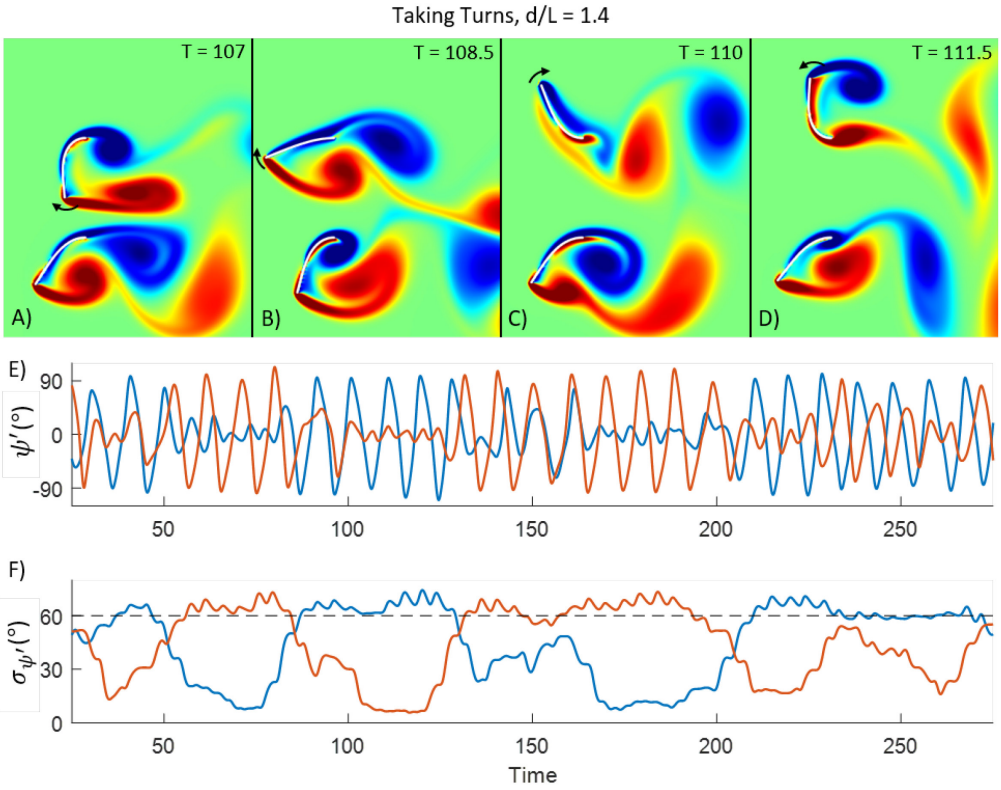

FIG. 6.14 – (A-D) Snapshots of ω_z and (E-F) time series of Corrected Tip Angle ψ' and RMS of the amplitude $\sigma_{\psi'}$ for the d/L = 1.4 Abreast case showing the Taking Turns behavior. In (A-D), the flags are shown in white and the direction is noted with black arrows. In (E-F) the Upper flag is blue and the Lower flag is red.

With separation increased beyond d/L=0.5, the flags are far enough apart that the vorticity from the trailing-edge of one flag does not directly interfere with the other, and the behavior transitions from the V-Split Flutter to another behavior we call `Taking Turns’. In this regime (very

clear in FIG. 6.14 showing vorticity snapshots and the time series of ψ' and $\sigma_{\psi'}$), one flag flaps vigorously while the other remains mostly stationary in a deflected state. After a few cycles, the flags switch roles, and this cycle of taking turns continues. The range d/L = 0.5 – 0.8 exhibits intermittent switching between V-Split flutter and Taking Turns behavior but beyond d/L ~0.8 to d/L~2.1, the flags lock on to the Taking Turns behavior. The PDF of the phase-difference for this regime are not meaningful since accurate estimation of the phase difference requires both flags to have a significant magnitude of flutter.

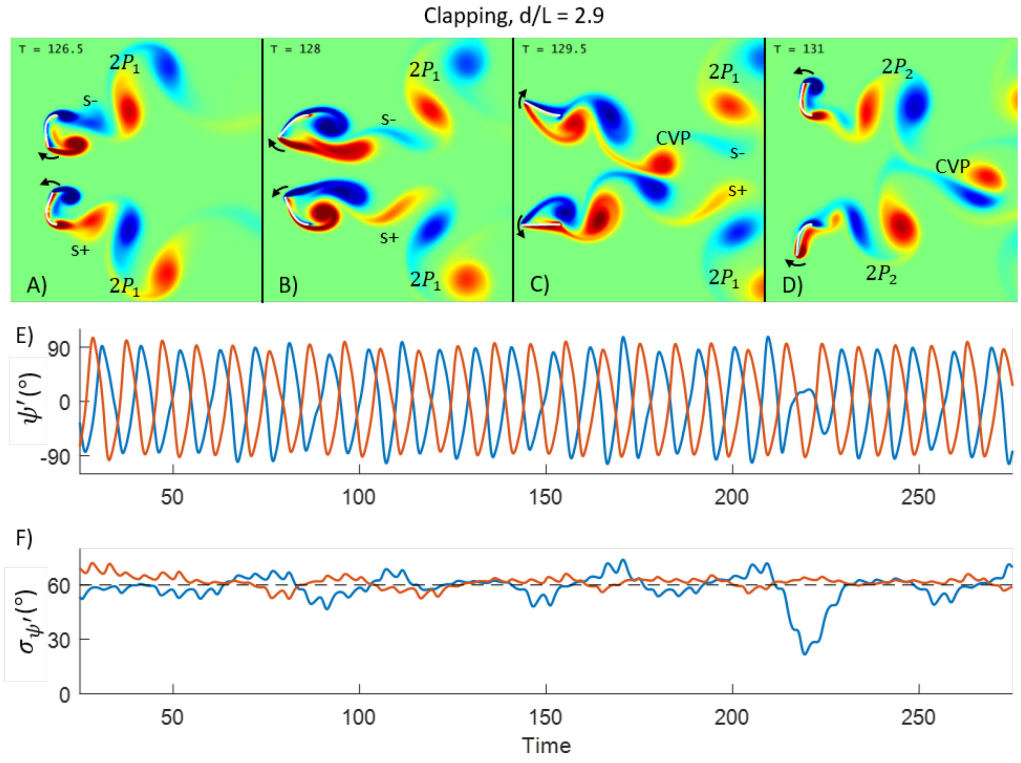

FIG. 6.15 – (A-D) Snapshots of ω_z and (E-F) time series of Corrected Tip Angle ψ' and RMS of the amplitude $\sigma_{\psi'}$ for the d/L = 1.4 Abreast case showing the Taking Turns behavior. In (A-D), the flags are shown in white and the direction is noted with black arrows. In (E-F) the Upper flag is blue and the Lower flag is red.

Once separation is increased beyond d/L=2.1, the flags develop what we refer to here as a `clapping' behavior (2.2 – 3.0+) The phase difference between the two flags (FIG. 6.12B) in this

regime ranges from about 135-180 degrees indicating that the flag mostly move in opposite directions. The Cerdeira, Fan, & Gharib (2018) paper focused on this separation range using wind tunnel experiments, examining d/L = 1.7 – 5.4, and also saw a clapping behavior for the specific U^* examined in this paper. FIG. 6.15 shows the sequence of flutter for one case (d/L = 2.9) and the vortices in the near wake. From FIG. 6.15A we can see the formation of the $2P_1$ vortex pairs and half of the 2S pair, which is similar to the Solo flag. In FIG. 6.15B the flags are flapping outside to inside, and as the leading edges get close, the leading-edge vortices combine together to create a Counter-Rotating Vortex Pair (CVP) as seen in FIG. 6.15B-C. The CVP is different than the 2P vortex pairs in that the jet between them is generally aligned to push them in the direction of the incoming flow, allowing them to be rapidly convected downstream as seen in FIG. 6.15C-D. This is a departure from the Solo flag vortex shedding behavior. Those vortices which make up the CVP would have each been half of the next 2P vortex pair in the Solo flag case, but instead they pair-up and convect downstream as a dipole. This leaves the other half of the expected 2P vortices and the expected S vortices to group together to make $2P_2$.

An interesting feature of clapping behavior is that in the range of d/L from 2.4-2.8, the amplitude of flutter is actually slightly larger ($\sigma_{\psi'}$ are up to 10% higher than the baseline). To explain this behavior, we refer back to FIG. 6.5 which shows the mean velocity profiles for the Solo flag. The mean velocity profile along the vertical line thorough the flag shows that beyond a vertical distance of about one flag length, the mean streamwise velocity actually exceeds the freestream velocity. The peak in this mean velocity value at the base of the flags is $\overline{u}/U = 1.22$ and is reached at about y/L=1.1 and then the velocity slowly decays back to the freestream velocity. Thus, any flag placed beyond a distance of about d/L=2.0, would generally experience a crossflow with momentum and kinetic energy that exceed that of a Solo flag. Furthermore, the mean velocity surplus also has a relatively large vertical gradient (i.e. shear) closer to the body, and this gradient introduces a significant asymmetry that would disrupt symmetric, large-amplitude flutter for a flag

in this region. Thus, the excess momentum available to the flag and shear are two competing mechanisms, and it is therefore not surprising that the highest amplitude consistent flutter occurs further out (2.4<d/L<2.8) where the shear is lower and the excess momentum is still available.

6.6 Strouhal Number Trends

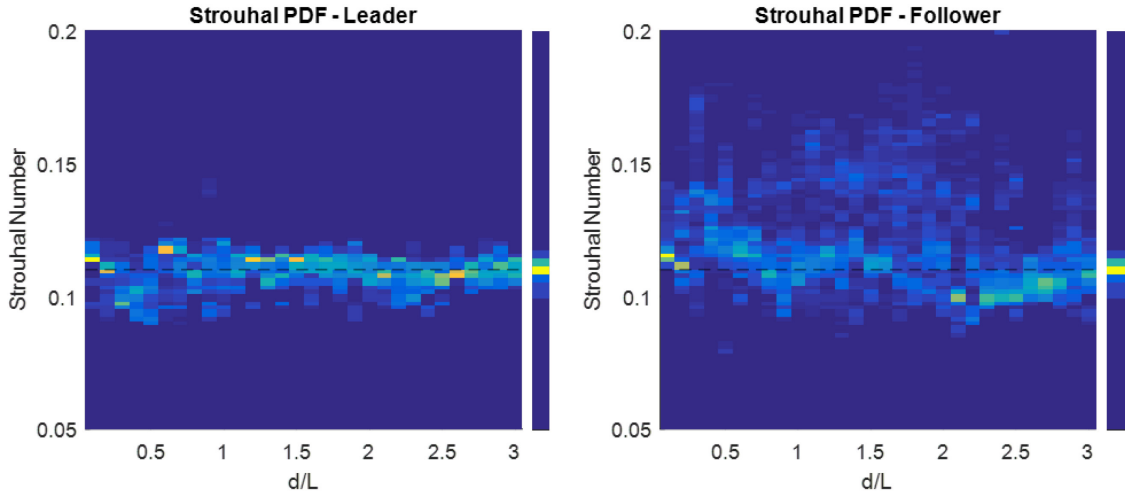

FIG. 6.16 – Heatmaps of the Strouhal number (which equals the nondimensional frequency) for the Leader and Follower flags for the Tandem configuration. The Solo flag baseline St = 0.11 is denoted with a dashed black line and the Solo PDF is shown beside the heatmaps.

FIG. 6.16 shows the heatmaps of the Strouhal number for the Leader and Follower. The Leader heatmap shows behavior which is consistent with the Solo flag. Throughout the range, the Follower shows a more broadband frequency spectrum.

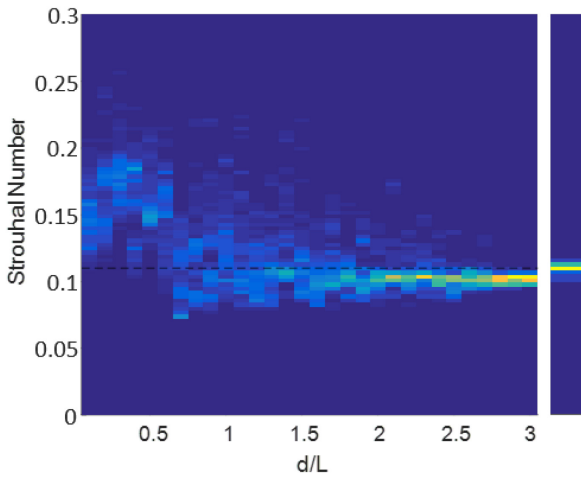

FIG. 6.17 – Heatmap of PDFs of the Strouhal number (i.e. the nondimensional frequency) for the Abreast configuration. The Solo flag baseline is shown as a black line and a PDF is shown next to the heatmap.

For the abreast configuration, the Strouhal number pdf was created by taking histograms of the combined Upper and Lower Flag data. FIG. 6.17 shows the heatmap of the Strouhal number versus d/L for the Abreast configuration. Here we can see the V-Split Oscillations appear to have a generally higher Strouhal number. Beyond d/L = 0.6, the PDFs center around the Solo flag baseline and converge to this value slowly with increased d/L.

6.7 Implications Towards Energy Harvesting

In the previous sections, we have outlined the effect of flag separation on the flutter dynamics for both tandem and the abreast configuration and connected this dynamical behavior with the underlying flow physics and vortex dynamics. In this section, we summarize the implications of the observed behavior for energy harvesting. According to Shoele & Mittal (2016a), the power extracted from the flutter of inverted flags/membrane made of piezoelectric materials scales as the square of the amplitude of the flutter. Thus, to assess the energy harvesting potential of these flag pairs, we have computed the mean squared amplitude for each flag and then taken an

average of this quantity for both flags. This quantity is then normalized by the corresponding quantity for the Solo flag and the PDFs of this quantity are shown in FIG. 6.18.

For the Tandem configuration, this quantity exhibits two major regimes. For d/L ranging from 0 to about 1.2, both flag exhibit diminished flutter amplitude (see FIG. 6.7) due to their proximity and this leads to a significant reduction in the energy harvesting potential. According to FIG. 6.18, the most probable value of the quantity is about 20% lower than the Solo flag. Within this range however is a narrow band between d/L=0.6 and 0.7 (referred to as the `Proximal Decoupling' range) where the energy harvesting potential is nearly back up to the level of the Solo flag. Additionally, the minimum spacing case of d/L = 0.1 shows robust in-phase flapping with performance only marginally lower at around 95% of the solo flag baseline. Beyond about d/L=1.2, the Leader recovers to its nominal flutter amplitude but the Follower exhibits reduced flutter. The net result is that the energy harvesting potential of the pair in this regime is centered between 80% to 90% of the nominal, Solo flag value.

The Abreast configuration shows three distinct regimes in its energy harvesting potential. For d/L less than about 0.7, the flag exhibits the V-Split oscillation with very small amplitude and consequently, the energy harvesting potential is between 0-20% of the nominal Solo flag value. Between d/L of about 0.7 and 2.2 is the Taking-Turns behavior where the two flags alternate between large and small amplitude flutter. Not surprisingly, this diminishes the energy harvesting potential of the pair and the plot indicates an energy harvesting potential of about 60-75% of the Solo flag. The clapping regime beyond d/L of 2.2 is where each flag is in the region of higher-speed flow generated by the other flag and this enhances the flutter and the energy harvesting potential by as much as 20% above the baseline value. This increase in amplitude is qualitatively similar that seen by Cerdeira, et al. (2018). Their result uses the maximum tip angle as an amplitude measurement and they show a 110° maximum tip angle at d/L = 2.8. They do not report a Solo flag tip angle in their paper, but they claim that this 110° tip angle is a 36% increase over the solo

flag. In our study, we saw a maximum tip angle for the abreast configuration of approximately 105 ° at d/L = 2.7 which is a remarkably similar result considering the gross differences between these approaches (e.g. Reynolds number, experimental vs. computational, 2D vs. 3D).

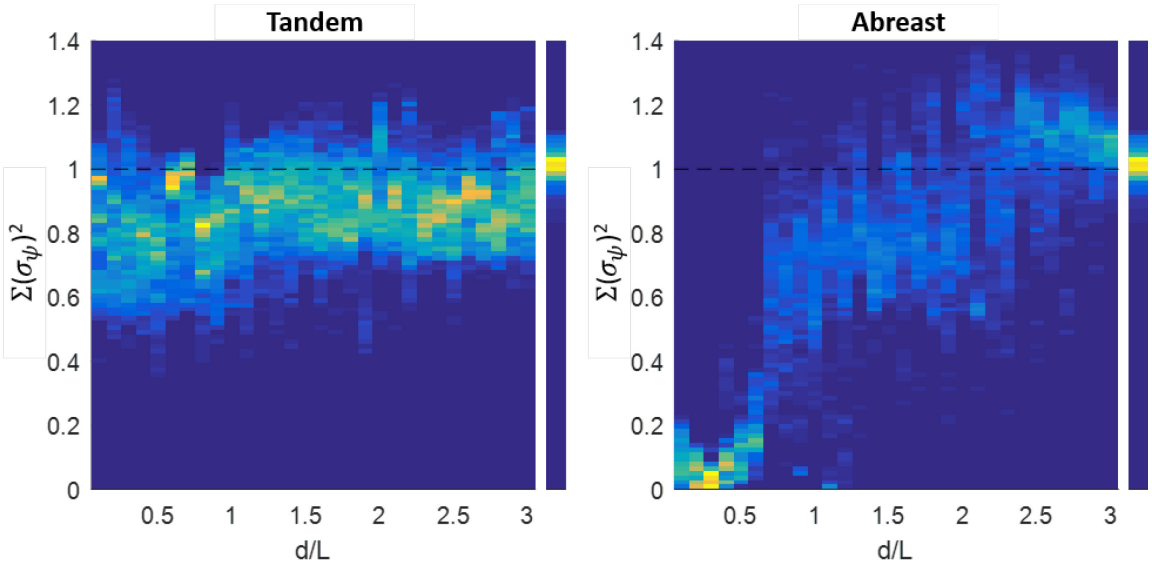

FIG. 6.18 – Heatmaps of the PDFs of the sum of the squared σ_ψ for the Tandem and Abreast configurations for each d/L. The values are normalized by twice the corresponding value of the Solo flag baseline. The Solo flag baseline value is depicted with a black line and a heatmap beside each figure.

Even though the scales are very different, it is worthwhile to compare the trends found here against those for horizontal axis wind turbine, which also extract energy from a freestream via induced movement of the rotor. Data on Abreast configuration of rotary turbines is not available for comparison and neither are systematic studies of the effect of rotary turbine spacing on turbine performance. However, one study (Pierella, Krogstad, & Sætran, 2014) for a Tandem wind turbine configuration at a fixed distance of three rotor diameters showed that the power coefficient of the downstream turbine was at most about 25% of the upstream rotor. Thus, the combined power of the two turbines is at most about 63% of two single turbines. For a similar setup with the current inverted flags, the overall energy harvesting potential is between 80 and 90% of the baseline value. Thus, the inverted flags seem to perform better than rotary turbines for similar spacing. The reason

for this is that while for rotary turbines, the rotational movement is driven by the mean lift force on the turbine blade, which is proportional to the square of the mean velocity, the inverted flags exploit a flow-induced flutter instability, which has a weaker dependence on the incoming flow velocity. As has been shown by Shoele & Mittal (2016a) and others, the flutter depends on the flow velocity via the reduced velocity parameter ($U^*=U/fL$) and the Reynolds number, and one advantage of the inverted flag configuration over regular flags is that its flutter behavior is relatively insensitive to U^* and Reynolds number over a wide range of these parameters. Thus, flow energy harvesting from multi-flag arrays offers some advantages over conventional rotary turbine arrays, for micro-scale energy harvesting applications.

Chapter 7

Conclusion

In this work we investigate applications where aeroelastic phenomena can be utilized to achieve a useful engineering objective. Specifically, we focus on a class of flow-induced flutter phenomena which encompasses flapping and fluttering membranes, flags, filaments, and plates. Using 2D and 3D coupled fluid-structure-scalar interaction simulations, we investigated these flapping membranes in three applications: A) scalar mixing enhancement in the inertial microfluidics regime, B) heat transfer enhancement in forced convection channel flow heat exchangers, and C) energy harvesting using multi-inverted flag configurations. In all three studies, we investigate the underlying fluid dynamics, structural dynamics, and fluid-structure coupling. We also use various performance measures and flow visualization techniques to understand how these fundamental fluid dynamics impact the design of these systems, and how they could be utilized to potentially improve the system for practical applications.

In these simulations we have used two immersed boundary method (IBM) based approaches for the different types of immersed boundaries in the flow. Stationary boundaries were modeled using a sharp-interface immersed boundary approach, while flexible bodies subject to fluid-structure interactions were modeled using a diffuse interface, penalty method approach. The flow solver, structural solver, and scalar solver were all discussed in terms of the underlying physics as well as in terms of the numerical methods. Finally, we also discussed ongoing work towards high fidelity 3D validation studies for 3D FSI problems. This work included the design, manufacture,

testing and implementation of a low speed 1ft x 1ft square test section wind tunnel. We used this wind tunnel to run preliminary analysis and qualitative comparisons using a newly developed validation configuration called the hanging banner.

The research related to inertial microfluidic mixing focused on three regimes: 2D single flag studies, 2D multi-flag studies, and 3D single flag studies. For analysis of the mixing, we used three key performance parameters to translate the fundamental physics into useful measures of engineering performance. The mixing performance was characterized by the mixing index, the energy losses by the head loss, and we formulated a new performance measure called the Interface Density to characterize the degree to which the interface is being stretched and folded by the perturbations introduced by the membrane.

In the 2D single flag studies we investigated the concept of using a flapping membrane as a so called "flutter mixer" in a simplified model of amicromixer. We first investigated the systems sensitivity to Reynolds number, where we found that beyond a critical Reynolds number, the flapping behavior and subsequent mixing performance transitions from lower Re behavior wherein mixing was accomplished via simple deformation of the interface between the fluids, to higher Re behavior wherein mixing was accomplished by the persistent shedding of vortices. The higher Reynolds number mixing mechanism resulted in very good mixing performance, particularly in the region immediately after the membrane. Stategies for extending downwards the Reynolds number where such system can we used were investigated Finally, we compared our higher Re mixing mechanism of vortex shedding with another canonical passive mixer which employs vortex shedding; the circular cylinder or "post mixer." That analysis showed that flutter mixers drastically outperform post mixers both in terms of mixing performance and in terms of energy expenditure.

The 2D multi-flag studies addressed tandem arrangements of membranes. We were interested in understanding the tandem configuration in part because a practical flutter mixer might employ many membranes in sequence. Furthermore, we were also interested in identifying potential

configurations that could take advantage of the complex coupling between the flows induced by the flags to enhance mixing performance. The results of the study were somewhat inconclusive since improves mixing was accompanied by increased pressure loss.

The 3D mixing study was our final investigation into microfluidic mixing. Due to the computational cost of 3D fully coupled FSI simulations, we used a small number of simulations to investigate the 3D system. The challenge is that 3D FSI simulations introduce new parameters which do not exist in the 2D model. A further challenge is that 3D fluttering and flapping behavior is typically more stable than 2D flapping. We sought to investigate the relevance of 3D parameters such as the flag aspect ratio and the spanwise confinement on the mixing performance. We were also interested in understanding the 3D mixing mechanism and mixing performance, and if and how it differed from the 2D model. We found significant differences between the 2D and 3D models, both in terms of fluid dynamics and mixing mechanism, as well as in terms of mixing performance. Whereas the 2D model was dominated by spanwise vortices, the 3D model was dominated by streamwise vortices.

Through these three inertial micromixing studies we demonstrated that the flutter mixer has significant potential to replace or augment existing passive mixers. The notion is that the flutter mixer is like a passive mixer in terms of complexity, cost, ease of manufacture and deployment, robustness to failure, and other engineering goals. However, it is like an active mixer in terms of adding temporal and spatial variations into the flow. In practice flutter mixers could exist on their own, or in a tandem arrangement with a few or many membranes. In addition, they could be placed at the inlet of a more typical passive or active micromixer to give an initial boost to the mixing performance.

The next major application area we investigated was heat transfer enhancement. This study is similar in many ways to the mixing investigation. In both cases a flapping membrane is being used to introduce large scale perturbations and deformations into the flow to achieve mixing and

boundary layer disruption. There are some differences in the physics and analysis, but in principle many of the lessons learned from one study can help motivate the other study. This investigation was motivated by prior work which examined a 2D model of the heat transfer problem. Following that study, we were interested in the systems sensitivity to several 3D specific parameters and configurations. First, we examined a baseline configuration of the 3D system with a square channel to develop a clear understanding of the physics at play and to understand the 3D heat transfer enhancement mechanism. We found that the primary cause of increased heat transfer was the shedding of a horseshoe shaped vortex at each flapping half cycle. This horseshoe vortex was aligned in such a way as to rapidly convect cold fluid from the core towards the heated channel walls creating a cross-stream jet, thereby sharpening the temperature gradient at the wall as well as mixing the flow.

We then investigated the systems sensitivity to 3D parameters such as spanwise confinement and membrane aspect ratio. Here we were able to show the system performance was sensitive to the flapping amplitude and the total membrane area. Finally, we examined ducts with non-square profiles including a circular duct and a diamond duct. These investigations were motivated by real world considerations. In principle, and particularly in the case of the large-scale air-cooled condensers, these flapping flags were meant as a retrofit to existing heat exchangers. This presented a challenge in that real-world heat exchangers come have a variety of duct shapes. However, the results for the two additional canonical duct shapes showed that for symmetric ducts with aspect ratios close to unity, the heat transfer performance is completely insensitive to the duct geometry. This robustness bodes well for practical applications.

Our final application was extracting energy from a flapping flag using piezoelectric energy harvesting. This application used an inverted flag. An inverted flag has a free leading edge and a fixed trailing edge, and is advantageous for energy harvesting due its lower critical velocity and large amplitude deflections. This investigation was also motivated by significant recent research

into inverted flags as piezo-electric energy harvesters. Our assessment was that practical energy harvesters might use arrays of fluttering membranes, so the coupling between those membranes would be important to understand to best design for an inverted flag array. We examined the multi-inverted flag system in the tandem and abreast configurations. In the tandem configuration, we found generally that the follower flag exhibited reduced energy harvesting potential, except for very narrow ranges where the vortex shedding and inter-flag spacing lined up such that the follower flag was essentially masked and decoupled from the leader. For the abreast configuration, we identified interesting dynamics exhibiting multiple distinct behavior regimes.

In summary, we investigated the engineering utility of aeroelastic flutter of membranes and flags. We showed that regular flags have the ability to create large amplitude perturbations with relatively low energy losses when placed in channel/duct flows. We showed that this behavior could be utilized to achieve significant mixing enhancement or heat transfer enhancement in these flows. We also showed that the coupling between multiple inverted flags can be utilized to enhance energy harvesting. While the work on fluid structure interaction is not over, and in many ways has just begun, it is our hope that this dissertation showed the utility, potential applications, and rich underlying physics of this complex phenomenon.

Appendix – A

Prior 2D Heat Transfer Enhancement Study

A.1 Methods and Performance Measures

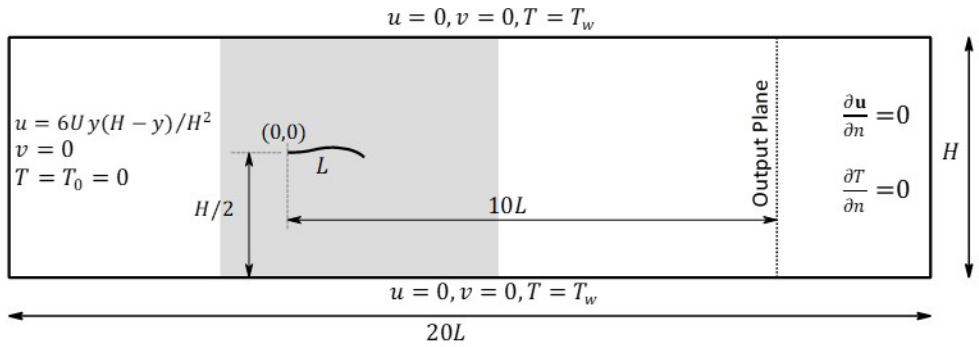

FIG. 7.1 – Simulation configuration of 2D heat transfer problem from Shoele & Mittal, 2014 (1)

To study this simplified 2D configuration, the 2D version of the solver described earlier was utilized. FIG. 7.1 shows the computational domain, which consists of a flag in a channel. The fluid has fully developed inflow boundary conditions and no slip, no penetration boundary conditions on the walls. The scalar has a uniform inflow and constant temperature boundary conditions on the walls. The choice to use constant temperature for the walls was made because in most forced convection heat exchangers, the material used to create the walls has very high thermal conductivity, so from the perspective of the fluid, the wall is essentially all at the same temperature.

A.2 Results

This prior 2D study examined many aspects of this system. Some of the results are of direct relevance to the work done in this dissertation, both in this section about heat transfer enhancement,

as well as in the section on 3D mixing enhancement. Those relevant results will be presented here in an effort to give context to the following 3D studies. The particular aspects of the original study that are of relevance here are A) the behavior of the vorticity and the scalar heat of a flapping flag in a heated channel, B) the sensitivity of the system to Re number, and C) the structural parameter space wherein this flapping phenomenon is possible. First, the 2D heat transfer enhancement mechanism is examined and shown to be particular vortical structures that are shed. FIG. 7.2 shows the temperature and vorticity of one configuration at a few Re.

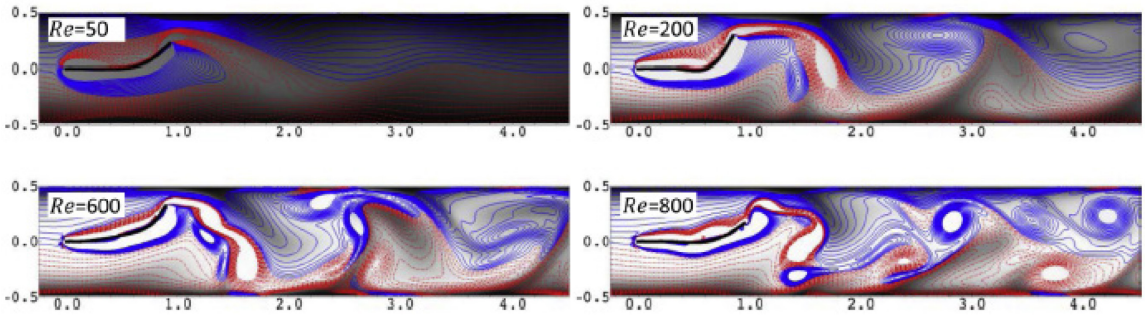

FIG. 7.2 – Vorticity (colored lines) and temperature contours (background black and white field) of a flapping flag in a heated channel at different Re numbers with M=1 and U*=12. Taken from* **(1)**

In this figure we can see many similarities to the familiar vortex shedding phenomenon of flapping flags in channel flow. Namely, we can see that at a sufficiently high Re, the flag sheds vortices that remain close to the walls. This should be beneficial as it will disrupt the boundary layers. This benefit can be seen qualitatively in the Re=200, 600, and 800 cases. For all three cases, between X=2.0 and X=3.0 we can see vortices interacting such that they cause a plume of heat to be ejected from the wall, and across the entire channel. This accomplishes one of the desired goals towards improving heat transfer in that it is pulling hot fluid away from the heated walls.

A.2.1 Sensitivity to Re Number

However, it is evident from FIG. 7.2 that this flow is sensitive to Re. The Re = 50 and 200 cases look very different from the Re = 600 and 800 cases. One goal of this study was to make

analogies between this 2D simulation and practical experiments carried out by our collaborators at Georgia Tech working in Prof. Ari Glezer's group. This presented a few challenges. First, one of the desired goals was to thoroughly explore the structural parameter space. This was to be accomplished by a brute force parametric sweep of the space requiring over 700 simulations in total. This made 3D simulations practically impossible, so 2D simulations were chosen which presents several issues.

The second problem was the practical experiment ran at an Re several orders of magnitude larger than what was reasonable for a DNS approach. However, observations of the system showed that it seemed to have a saturation of the dynamics with Re, such that above a certain threshold the system seemed to be largely agnostic to Re number. If that threshold could be identified, then the simulations for the parametric sweep could be performed at a Re above that threshold, allowing for analogies to be made from this relatively low Re simulation to the practical experiment.

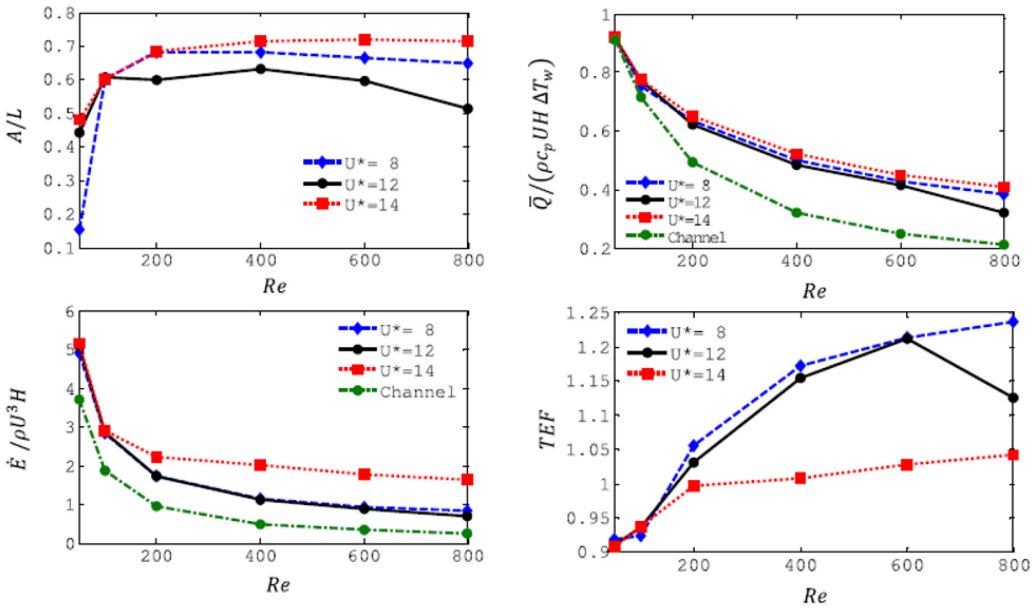

FIG. 7.3 – Plots showing the flapping amplitude, heat flux, energy loss, and thermal enhancement factor as a function of Re number for 3 U cases. Taken from (1).*

FIG. 7.3 shows the flapping amplitude A/L, Q, E, and TEF as a function of Re. This is an interesting set of results. On the one hand the A/L and E plots seem to show a clear saturation with Re. In particular, the A/L plots show that after Re = 200, the dynamics are Re agnostic. This behavior is echoed in the E plots, which further supports the result that the dynamics of the flag saturate after Re=200. On the other hand, the Q and TEF plots do show persistent sensitivity to Re even after Re = 200. This may be due to a changing Peclet number issue. If the Prandlt number is kept fixed, and the Re number is changing, then the Peclet defined as Pe = Re*Pr is also changing which is the key nondimensional parameter governing the diffusion term in the heat advection-diffusion equation. This would affect the Q and TEF results but not the A/L or E results. This explanation was sufficient to conclude Re=200 was the dynamic sensitivity threshold and the subsequent parametric sweeps were conducted at Re=400.

A.2.2 Exploration of the Structural Parameter Space of U* and M*

Another goal of this study was to examine the structural parameter space. Partly, this was to identify any optimal parametric configurations. Also, it was important to determine if the ranges wherein this system provided any significant benefit also coincided with material properties that were practical in terms of manufacturing and heat resistance. This was accomplished with a brute force parametric sweep of the U* and M* parameters governing the structure's dynamics.

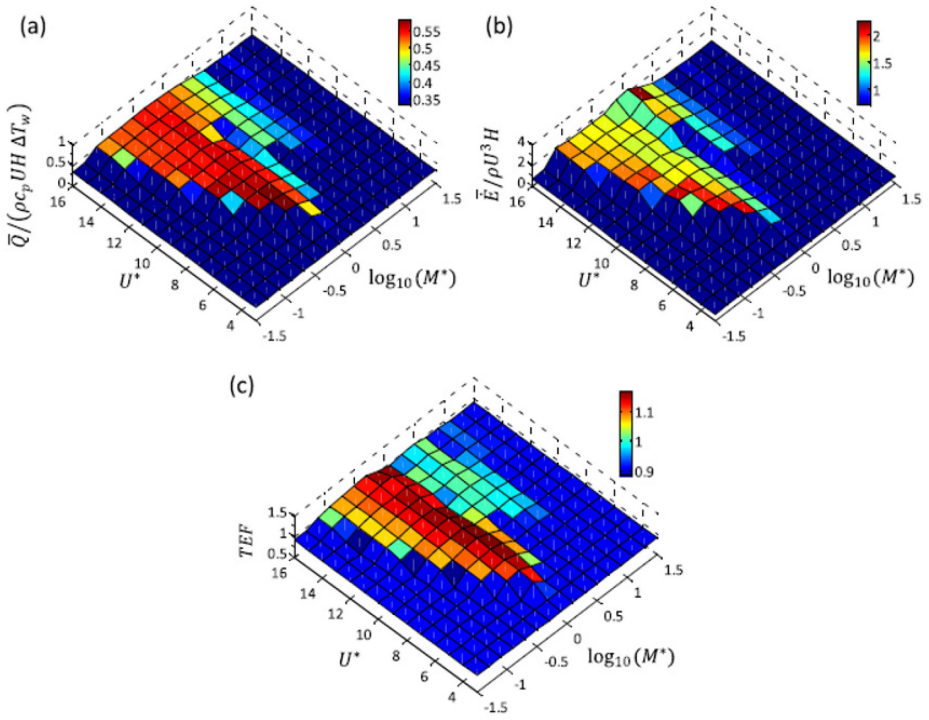

FIG. 7.4 -Effect of structural parameters U and M* on a) the non-dimensional heat flux, b) the non-dimensional energy loss, and c) the thermal enhancement factor (TEF). Taken from (1).*

FIG. 7.4 shows carpet plots of the time averaged Q, E, and TEF. The results show similar behavior across all three measures, wherein for a narrow range of mass ratios, there is a relatively wide range of reduced velocities that show similar performance. This result acted as a starting point for all the studies in this thesis which featured a regular flapping flag insofar as choosing the structural parameters. A possible issue with conducting parametric sweeps using simulations is that it is possible to encounter parameter spaces that are not physically viable or meaningful, but nevertheless can exist with no issues in simulations. Thus, the next step in that work was to calibrate the plateau seen in the carpet plots to identify what existing materials had those properties, if any. In the paper, it was noted with the proper processing and manufacturing materials such as copper, aluminum and mylar would all work, which bodes well for this device's viability for heat transfer applications.

References

Afzal, A., & Kim, K. (2012). *Passive split and recombination micromixer with convergent–divergent walls* doi://doi.org/10.1016/j.cej.2012.06.111

Afzal, A., & Kim, K. (2015). *Convergent–divergent micromixer coupled with pulsatile flow* doi://doi.org/10.1016/j.snb.2015.01.062

Ahmed, D., Mao, X., Shi, J., Juluri, B. K., & Huang, T. J. (2009). A millisecond micromixer via single-bubble-based acoustic streaming. *Lab on a Chip, 9*(18), 2738. doi:10.1039/b903687c

Ait Abderrahmane, H., Païdoussis, M. P., Fayed, M., & Dick Ng, H. (2012). *Nonlinear dynamics of silk and mylar flags flapping in axial flow* doi://doi.org/10.1016/j.jweia.2012.04.021

Akaydin, H. D., Elvin, N., & Andreopoulos, Y. (2010). Energy harvesting from highly unsteady fluid flows using piezoelectric materials. *Journal of Intelligent Material Systems and Structures, 21*(13), 1263-1278. doi:10.1177/1045389X10366317

Alam, M. K., Koomson, E., Zou, H., Yi, C., Li, C., Xu, T., & Yang, M. (2018). *Recent advances in microfluidic technology for manipulation and analysis of biological cells (2007–2017)* doi://doi.org/10.1016/j.aca.2018.06.054

Alben, S. (2008). The flapping-flag instability as a nonlinear eigenvalue problem. *Physics of Fluids, 20*(10), 104106. doi:10.1063/1.3000670

ALBEN, S. (2008). Optimal flexibility of a flapping appendage in an inviscid fluid. *Journal of Fluid Mechanics, 614*, 355-380. doi:10.1017/S0022112008003297

ALBEN, S. (2009). Wake-mediated synchronization and drafting in coupled flags. *Journal of Fluid Mechanics, 641*, 489-496. doi:10.1017/S0022112009992138

Alben, S. (2015). Flag flutter in inviscid channel flow. *Physics of Fluids, 27*(3), 033603. doi:10.1063/1.4915897

Alben, S., & Shelley, M. J. (2008). Flapping states of a flag in an inviscid fluid: Bistability and the transition to chaos. *Physical Review Letters, 100*(7), 074301. doi:10.1103/PhysRevLett.100.074301

Allen, J. J., & Smits, A. J. (2001). Energy harvesting eel. *Journal of Fluids and Structures, 15*(3-4), 629-640.

Amini, H., Lee, W., & Di Carlo, D. (2014). Inertial microfluidic physics. *Lab on a Chip, 14*(15), 2739-2761. doi:10.1039/c4lc00128a

Argentina, M., & Mahadevan, L. (2005). Fluid-flow-induced flutter of a flag. *Proc Natl Acad Sci U S A, 102*(6), 1829. doi:10.1073/pnas.0408383102

Bhardwaj, R., & Mittal, R. (2012). Benchmarking a coupled immersed-boundary-finite-element solver for large-scale flow-induced deformation. *AIAA Journal, 50*(7), 1638-1642.

Cai, G., Xue, L., Zhang, H., & Lin, J. (2017). A review on micromixers. *Micromachines, 8*(9), 274.

Capretto, L., Cheng, W., Hill, M., & Zhang, X. (2011). Micromixing within microfluidic devices. *Microfluidics* (pp. 27-68) Springer.

Collar, A. R. (1946). The expanding domain of aeroelasticity. *The Journal of the Royal Aeronautical Society, 50*(428), 613-636. doi:10.1017/S0368393100120358

CONNELL, B. S. H., & YUE, D. K. P. (2007). Flapping dynamics of a flag in a uniform stream. *Journal of Fluid Mechanics, 581*, 33-67. doi:10.1017/S0022112007005307

Cui, W., Zhang, H., Zhang, H., Yang, Y., He, M., Qu, H., . . . Duan, X. (2016). Localized ultrahigh frequency acoustic fields induced micro-vortices for submilliseconds microfluidic mixing. *Applied Physics Letters, 109*(25), 253503.

Danckwerts, P. V. (1952). The definition and measurement of some characteristics of mixtures. *Applied Scientific Research, Section A, 3*(4), 279-296.

Deshmukh, S. R., & Vlachos, D. G. (2005). Novel micromixers driven by flow instabilities: Application to post-reactors. *AIChE Journal, 51*(12), 3193-3204.

Dessi, D., & Mazzocconi, S. (2015). *Aeroelastic behavior of a flag in ground effect* doi://doi.org/10.1016/j.jfluidstructs.2015.03.006

Doaré, O., Sauzade, M., & Eloy, C. (2011). Flutter of an elastic plate in a channel flow: Confinement and finite-size effects. *Journal of Fluids and Structures, 27*(1), 76-88. doi:10.1016/j.jfluidstructs.2010.09.002

Dong, D., Chen, W., & Shi, S. (2016). Coupling motion and energy harvesting of two side-by-side flexible plates in a 3D uniform flow. *Applied Sciences, 6*(5), 141.

Dong, H., Mittal, R., & Najjar, F. M. (2006). Wake topology and hydrodynamic performance of low-aspect-ratio flapping foils. *Journal of Fluid Mechanics, 566*, 309-343.

Dou, Z., Rips, A., Welsh, N., Seo, J., & Mittal, R. (2018). Flow-induced flutter of hanging banners: Experiments and validated computational models. *2018 fluid dynamics conference* () American Institute of Aeronautics and Astronautics. doi:10.2514/6.2018-3081 Retrieved from https://doi.org/10.2514/6.2018-3081

Dowell, E. H., Curtiss, H. C., Scanlan, R. H., & Sisto, F. (1989). *A modern course in aeroelasticity* Springer.

Eloy, C., Souilliez, C., & Schouveiler, L. (2007). *Flutter of a rectangular plate* doi://doi.org/10.1016/j.jfluidstructs.2007.02.002

Eloy, C., Kofman, N., & Schouveiler, L. (2012). The origin of hysteresis in the flag instability. *Journal of Fluid Mechanics, 691*, 583-593. doi:10.1017/jfm.2011.494

ELOY, C., LAGRANGE, R., SOUILLIEZ, C., & SCHOUVEILER, L. (2008). Aeroelastic instability of cantilevered flexible plates in uniform flow. *Journal of Fluid Mechanics, 611*, 97-106. doi:10.1017/S002211200800284X

Farnell, D. J. J., David, T., & Barton, D. C. (2004). *Coupled states of flapping flags* doi://doi.org/10.1016/j.jfluidstructs.2003.10.001

Favier, J., Revell, A., & Pinelli, A. (2015). *Numerical study of flapping filaments in a uniform fluid flow* doi://doi.org/10.1016/j.jfluidstructs.2014.11.010

Garrick, I. E., & Reed III, W. H. (1981). Historical development of aircraft flutter. *Journal of Aircraft, 18*(11), 897-912. doi:10.2514/3.57579

Gee, D. L., & Webb, R. L. (1980). *Forced convection heat transfer in helically rib-roughened tubes* doi://doi.org/10.1016/0017-9310(80)90177-5

Gibbs, S. C., Sethna, A., Wang, I., Tang, D., & Dowell, E. (2014). *Aeroelastic stability of a cantilevered plate in yawed subsonic flow* doi://doi.org/10.1016/j.jfluidstructs.2014.05.006

Glasgow, I., & Aubry, N. (2003). Enhancement of microfluidic mixing using time pulsing. *Lab on a Chip, 3*(2), 114-120.

Goldstein, D., Handler, R., & Sirovich, L. (1993). Modeling a no-slip flow boundary with an external force field. *Journal of Computational Physics, 105*(2), 354-366.

Herrault, F., Hidalgo, P. A., Ji, C. -., Glezer, A., & Allen, M. G.Cooling performance of micromachined self-oscillating reed actuators in heat transfer channels with integrated diagnostics. Paper presented at the *IEEE 25th International Conference on Micro Electro Mechanical Systems (MEMS),* 1217-1220. doi:10.1109/MEMSYS.2012.6170408

Hossain, S., Ansari, M. A., & Kim, K. (2009). Evaluation of the mixing performance of three passive micromixers. *Chemical Engineering Journal, 150*(2-3), 492-501.

Huang, W., Shin, S. J., & Sung, H. J. (2007). Simulation of flexible filaments in a uniform flow by the immersed boundary method. *Journal of Computational Physics, 226*(2), 2206-2228. doi:10.1016/j.jcp.2007.07.002

Huang, W., & Sung, H. J. (2009). *An immersed boundary method for fluid–flexible structure interaction* doi://doi.org/10.1016/j.cma.2009.03.008

Huang, W., & Sung, H. J. (2010). Three-dimensional simulation of a flapping flag in a uniform flow. *Journal of Fluid Mechanics, 653*, 301-336.

Huertas-Cerdeira, C., Fan, B., & Gharib, M. (2018). *Coupled motion of two side-by-side inverted flags* doi://doi.org/10.1016/j.jfluidstructs.2017.11.005

Jacobi, A. M., & Shah, R. K. (1995). *Heat transfer surface enhancement through the use of longitudinal vortices: A review of recent progress* doi://doi.org/10.1016/0894-1777(95)00066-U

Jeong, J., & Hussain, F. (1995). On the identification of a vortex. *Journal of Fluid Mechanics, 285*, 69-94. doi:10.1017/S0022112095000462

Jia, L., & Yin, X. (2008). Passive oscillations of two tandem flexible filaments in a flowing soap film. *Physical Review Letters, 100*(22), 228104. doi:10.1103/PhysRevLett.100.228104

Khatavkar, V. V., Anderson, P. D., den Toonder, J. M., & Meijer, H. E. (2007). Active micromixer based on artificial cilia. *Physics of Fluids, 19*(8), 083605.

Kim, D., Cossé, J., Huertas Cerdeira, C., & Gharib, M. (2013). Flapping dynamics of an inverted flag. *Journal of Fluid Mechanics, 736* doi:10.1017/jfm.2013.555

KIM, S., HUANG, W., & SUNG, H. J. (2010). Constructive and destructive interaction modes between two tandem flexible flags in viscous flow. *Journal of Fluid Mechanics, 661*, 511-521. doi:10.1017/S0022112010003514

Kinsey, T., & Dumas, G. (2008). Parametric study of an oscillating airfoil in a power-extraction regime. *AIAA Journal, 46*(6), 1318-1330. doi:10.2514/1.26253

Kockmann, N., Kiefer, T., Engler, M., & Woias, P. (2006). Convective mixing and chemical reactions in microchannels with high flow rates. *Sensors and Actuators B: Chemical, 117*(2), 495-508.

Kornecki, A., Dowell, E. H., & O'Brien, J. (1976). *On the aeroelastic instability of two-dimensional panels in uniform incompressible flow* doi://doi.org/10.1016/0022-460X(76)90715-X

Lee, C., Chang, C., Wang, Y., & Fu, L. (2011). Microfluidic mixing: A review. *International Journal of Molecular Sciences, 12*(5), 3263-3287.

Lee, C., Wang, W., Liu, C., & Fu, L. (2016). *Passive mixers in microfluidic systems: A review* doi://doi.org/10.1016/j.cej.2015.10.122

Leonard, B. P. (1988). Simple high-accuracy resolution program for convective modelling of discontinuities. *International Journal for Numerical Methods in Fluids, 8*(10), 1291-1318. doi:10.1002/fld.1650081013

Li, S., Yuan, J., & Lipson, H. (2011). Ambient wind energy harvesting using cross-flow fluttering. *Journal of Applied Physics, 109*(2), 026104. doi:10.1063/1.3525045

Lighthill, J. (1975). *Mathematical biofluiddynamics* Society for Industrial and Applied Mathematics. Retrieved from https://books.google.com/books?id=wGRdvQEACAAJ

Liscinsky, D., True, B., & Holdeman, J. (1993). (1993). Experimental investigation of crossflow jet mixing in a rectangular duct. Paper presented at the *29th Joint Propulsion Conference and Exhibit,* 2037.

MATSUMOTO, M. (1999). *Vortex shedding of bluff bodies: A review* doi://doi.org/10.1006/jfls.1999.0249

Michelin, S., & Doaré, O. (2013). Energy harvesting efficiency of piezoelectric flags in axial flows. *Journal of Fluid Mechanics, 714*, 489-504. doi:10.1017/jfm.2012.494

Michelin, S., & Llewellyn Smith, S. G. (2009). Resonance and propulsion performance of a heaving flexible wing. *Physics of Fluids, 21*(7), 071902. doi:10.1063/1.3177356

Mittal, R., Dong, H., Bozkurttas, M., Najjar, F. M., Vargas, A., & von Loebbecke, A. (2008). A versatile sharp interface immersed boundary method for incompressible flows with complex boundaries. *Journal of Computational Physics, 227*(10), 4825-4852.

Mittal, R., Erath, B. D., & Plesniak, M. W. (2013). Fluid dynamics of human phonation and speech. *Annual Review of Fluid Mechanics, 45*(1), 437-467. doi:10.1146/annurev-fluid-011212-140636

Mittal, R., & Iaccarino, G. (2005). Immersed boundary methods. *Annual Review of Fluid Mechanics, 37*(1), 239-261. doi:10.1146/annurev.fluid.37.061903.175743

Nguyen, N., & Wu, Z. (2004). Micromixers—a review. *Journal of Micromechanics and Microengineering, 15*(2), R1.

Oddy, M. H., Santiago, J. G., & Mikkelsen, J. C. (2001). Electrokinetic instability micromixing. *Analytical Chemistry, 73*(24), 5822-5832.

Orrego, S., Shoele, K., Ruas, A., Doran, K., Caggiano, B., Mittal, R., & Kang, S. H. (2017). Harvesting ambient wind energy with an inverted piezoelectric flag. *Applied Energy, 194*, 212-222.

Ozceyhan, V., Gunes, S., Buyukalaca, O., & Altuntop, N. (2008). *Heat transfer enhancement in a tube using circular cross sectional rings separated from wall* doi://doi.org/10.1016/j.apenergy.2008.02.007

Pierella, F., Krogstad, P., & Sætran, L. (2014). Blind test 2 calculations for two in-line model wind turbines where the downstream turbine operates at various rotational speeds. *Renewable Energy, 70*, 62-77.

Promvonge, P., Chompookham, T., Kwankaomeng, S., & Thianpong, C. (2010). *Enhanced heat transfer in a triangular ribbed channel with longitudinal vortex generators* doi://doi.org/10.1016/j.enconman.2009.12.035

Rips, A., Shoele, K., Glezer, A., & Mittal, R. (2017). (2017). Efficient electronic cooling via flow-induced vibrations. Paper presented at the *Thermal Measurement, Modeling & Management Symposium (SEMI-THERM), 2017 33rd,* 36-39.

Ristroph, L., & Zhang, J. (2008). Anomalous hydrodynamic drafting of interacting flapping flags. *Physical Review Letters, 101*(19), 194502. doi:10.1103/PhysRevLett.101.194502

Ryu, J., Park, S. G., Kim, B., & Sung, H. J. (2015). *Flapping dynamics of an inverted flag in a uniform flow* doi://doi.org/10.1016/j.jfluidstructs.2015.06.006

Ryu, K. S., Shaikh, K., Goluch, E., Fan, Z., & Liu, C. (2004). Micro magnetic stir-bar mixer integrated with parylene microfluidic channels. *Lab on a Chip, 4*(6), 608-613.

Sader, J. E., Cossé, J., Kim, D., Fan, B., & Gharib, M. (2016). Large-amplitude flapping of an inverted flag in a uniform steady flow – a vortex-induced vibration. *Journal of Fluid Mechanics, 793*, 524-555. doi:10.1017/jfm.2016.139

Sahin, M., & Owens, R. G. (2004). A numerical investigation of wall effects up to high blockage ratios on two-dimensional flow past a confined circular cylinder. *Physics of Fluids, 16*(5), 1305-1320.

Seo, J. H., & Mittal, R. (2011). A sharp-interface immersed boundary method with improved mass conservation and reduced spurious pressure oscillations. *Journal of Computational Physics, 230*(19), 7347-7363.

Seo, J. H., Vedula, V., Abraham, T., Lardo, A. C., Dawoud, F., Luo, H., & Mittal, R. (2014). Effect of the mitral valve on diastolic flow patterns. *Physics of Fluids, 26*(12), 121901. doi:10.1063/1.4904094

Shelley, M., Vandenberghe, N., & Zhang, J. (2005). Heavy flags undergo spontaneous oscillations in flowing water. *Physical Review Letters, 94*(9), 094302. doi:10.1103/PhysRevLett.94.094302

Shelley, M., & Zhang, J. (2011). Flapping and bending bodies interacting with fluid flows. *Annual Review of Fluid Mechanics, 43*(1), 449-465. doi:10.1146/annurev-fluid-121108-145456

Shoele, K., & Mittal, R. (2014). Computational study of flow-induced vibration of a reed in a channel and effect on convective heat transfer. *Physics of Fluids, 26*(12), 127103. doi:10.1063/1.4903793

Shoele, K., & Mittal, R. (2016a). Energy harvesting by flow-induced flutter in a simple model of an inverted piezoelectric flag. *Journal of Fluid Mechanics, 790*, 582-606.

Shoele, K., & Mittal, R. (2016b). Flutter instability of a thin flexible plate in a channel. *Journal of Fluid Mechanics, 786*, 29-46. doi:10.1017/jfm.2015.632

Shoele, K., & Mittal, R. (2016c). Flutter instability of a thin flexible plate in a channel. *Journal of Fluid Mechanics, 786*, 29-46.

SHOELE, K., & ZHU, Q. (2010). Flow-induced vibrations of a deformable ring. *Journal of Fluid Mechanics, 650*, 343-362. doi:10.1017/S0022112009993697

Shoele, K., & Zhu, Q. (2012). Leading edge strengthening and the propulsion performance of flexible ray fins. *Journal of Fluid Mechanics, 693*, 402-432. doi:10.1017/jfm.2011.538

Shoele, K., & Zhu, Q. (2013). Performance of a wing with nonuniform flexibility in hovering flight. *Physics of Fluids, 25*(4), 041901. doi:10.1063/1.4802193

Stone, H. A., Stroock, A. D., & Ajdari, A. (2004). Engineering flows in small devices: Microfluidics toward a lab-on-a-chip. *Annu.Rev.Fluid Mech., 36*, 381-411.

Stroock, A. D., Dertinger, S. K., Ajdari, A., Mezić, I., Stone, H. A., & Whitesides, G. M. (2002). Chaotic mixer for microchannels. *Science, 295*(5555), 647-651.

Tai, C., Yang, R., Huang, M., Liu, C., Tsai, C., & Fu, L. (2006). Micromixer utilizing electrokinetic instability-induced shedding effect. *Electrophoresis, 27*(24), 4982-4990.

Tanda, G. (2004). *Heat transfer in rectangular channels with transverse and V-shaped broken ribs* doi://doi.org/10.1016/S0017-9310(03)00414-9

Taneda, S. (1968). Waving motions of flags. *Journal of the Physical Society of Japan, 24*(2), 392-401. doi:10.1143/JPSJ.24.392

Tang, D. M., Yamamoto, H., & H. Dowell, E. (2003). *Flutter and limit cycle oscillations of two-dimensional panels in three-dimensional axial flow* doi://doi.org/10.1016/S0889-9746(02)00121-4

Taylor, G. W., Burns, J. R., Kammann, S. A., Powers, W. B., & Welsh, T. R. (2001). The energy harvesting eel: A small subsurface ocean/river power generator. *IEEE Journal of Oceanic Engineering, 26*(4), 539-547.

Theodorsen, T. (1935). *General theory of aerodynamic instability and the mechanism of flutter.* (). Langley, VA: US National Advisory Committee for Aeronautics. Retrieved from https://ntrs.nasa.gov/search.jsp?R=19930090935

Tornberg, A., & Shelley, M. J. (2004). *Simulating the dynamics and interactions of flexible fibers in stokes flows* doi://doi.org/10.1016/j.jcp.2003.10.017

Tretheway, D. C., & Meinhart, C. D. (2002). Apparent fluid slip at hydrophobic microchannel walls. *Physics of Fluids, 14*(3), L12. doi:10.1063/1.1432696

Tsia, J. P., & Hwang, J. J. (1999). *Measurements of heat transfer and fluid flow in a rectangular duct with alternate attached–detached rib-arrays* doi://doi.org/10.1016/S0017-9310(98)00300-7

Turek, S., & Hron, J. (2006). (2006). Proposal for numerical benchmarking of fluid-structure interaction between an elastic object and laminar incompressible flow. Paper presented at the *Fluid-Structure Interaction,* 371-385.

Van Phan, H., Coşkun, M. B., Şeşen, M., Pandraud, G., Neild, A., & Alan, T. (2015). Vibrating membrane with discontinuities for rapid and efficient microfluidic mixing. *Lab on a Chip, 15*(21), 4206-4216.

WATANABE, Y., ISOGAI, K., SUZUKI, S., & SUGIHARA, M. (2002). *A theoretical study of paper flutter* doi://doi.org/10.1006/jfls.2001.0436

Webb, R. L. (1981). *Performance evaluation criteria for use of enhanced heat transfer surfaces in heat exchanger design* doi://doi.org/10.1016/0017-9310(81)90015-6

Williamson, C. H. K. (1996). Vortex dynamics in the cylinder wake. *Annual Review of Fluid Mechanics, 28*(1), 477-539. doi:10.1146/annurev.fl.28.010196.002401

Wu, Z., & Nguyen, N. (2005). Convective–diffusive transport in parallel lamination micromixers. *Microfluidics and Nanofluidics, 1*(3), 208-217.

Xia, Q., & Zhong, S. (2013). Liquid mixing enhanced by pulse width modulation in a Y-shaped jet configuration. *Fluid Dynamics Research, 45*(2), 025504.

Zhang, J., Childress, S., Libchaber, A., & Shelley, M. (2000). Flexible filaments in a flowing soap film as a model for one-dimensional flags in a two-dimensional wind. *Nature, 408*(6814), 835-839. doi:10.1038/35048530

Zhang, J., Yan, S., Yuan, D., Alici, G., Nguyen, N., Warkiani, M. E., & Li, W. (2016). Fundamentals and applications of inertial microfluidics: A review. *Lab on a Chip, 16*(1), 10-34.

Zhou, Z., & Mittal, R. (2018). Swimming performance and unique wake topology of the sea hare (aplysia). *Physical Review Fluids, 3*(3), 033102. doi:10.1103/PhysRevFluids.3.033102

Zhu, C., Seo, J. H., Vedula, V., & Mittal, R. (2017). (2017). A highly scalable sharp-interface immersed boundary method for large-scale parallel computers. Paper presented at the *23rd AIAA Computational Fluid Dynamics Conference,* 3622.

Zhu, L., & Peskin, C. S. (2002). Simulation of a flapping flexible filament in a flowing soap film by the immersed boundary method. *Journal of Computational Physics, 179*(2), 452-468.

Zhu, L., & Peskin, C. S. (2003). Interaction of two flapping filaments in a flowing soap film. *Physics of Fluids, 15*(7), 1954-1960. doi:10.1063/1.1582476

Vita

Aaron Rips was born in January 1992 in Santa Monica, California. He attended The Whiting School of Engineering at The Johns Hopkins University where earned a degree of Bachelor of Science in Mechanical Engineering with a concentration in Aerospace in 2014. He continued at Johns Hopkins in the 5th year master's program where he pursued the Fluid Dynamics focus. During his 5th year master's program he applied for and was accepted to the PhD program at Johns Hopkins studying Computational Fluid Dynamics under Professor Rajat Mittal. His research focused on Fluid-Structure Interaction and Flow Induced Flutter as discussed in the precedent dissertation. During his time as an Undergraduate and Graduate student Aaron was a teaching assistant for a number of courses including Thermodynamics, Aerospace Structures and Materials, Undergrad Fluid Mechanics 2, Biofluid Mechanics, Fluids Lab, and Heat Transfer Lab both to further his understanding in those areas and to develop experience as a teacher. Aaron's expertise is in Fluid-Structure Interactions, both in terms of the complex physics and fluid dynamics, as well as in the challenges of computationally modeling these coupled multi-physics systems. His focus is in making complex fluid dynamics phenomena sufficiently intuitively understandable so as to characterize their potential applications and engineering impact.